Universitat de València

(Estudi General)

Departament de Física Atòmica, Molecular i Nuclear

DOCTORAL THESIS

High precision measurement of $\Gamma(Z \to b\bar{b})/\Gamma(Z \to hadrons)$ with the DELPHI detector at LEP collider

Fernando Martínez-Vidal
November 1997

ProQuest LLC
789 East Eisenhower Parkway
P.O. Box 1346
Ann Arbor, MI 48106-1346

The work described in this thesis is part of the research program of the Departament de Física Atòmica, Molecular i Nuclear/Instituto de Física *Corpuscular* (IFIC) in Valencia (Spain), of the Laboratoire de Physique Nucléaire d'Hautes Energies (LPNHE) in Paris VI (France) and of the DELPHI Collaboration at CERN (Geneva, Switzerland). The author was partially supported by a fellowship of the Generalitat Valenciana in Spain.

Dr. Christian DE LA VAISSIÈRE, Directeur de Recherche del CNRS (Francia), Prof. Victoria CASTILLO GIMENEZ y Prof. Emilio HIGÓN RODRIGUEZ, Profesores Titulares del Departamento de Física Atómica, Molecular y Nuclear de la Facultad de Ciencias Físicas de la Universidad de Valencia,

CERTIFICAN:

que la presente memoria

High precision measurement of $\Gamma(Z \to b\bar{b})/\Gamma(Z \to hadrons)$ with the DELPHI detector at LEP collider

ha sido realizada bajo nuestra dirección en el Departamento de Física Atómica, Molecular y Nuclear de la Facultad de Ciencias Físicas de la Universidad de Valencia por D. Fernando Martínez Vidal, constituyendo su tesis para optar al grado de Doctor en Ciencias Físicas por la Universidad de Valencia.

Y para que así conste, en cumplimiento de la legislación vigente, firmamos el presente Certificado en Valencia a ...17 de ...Octubre de 1997.

Fdo. Prof. Victoria CASTILLO GIMENEZ

Fdo. Dr. Christian DE LA VAISSIÈRE

Fdo. Prof. Emilio HIGÓN RODRIGUEZ

A Carmen
A mis padres

Abstract

Among the measurements available at the Z pole center-of-mass energy, the ratio of the Z partial width into $b\bar{b}$ quark pairs and its total hadronic partial width,

$$R_b^0 = \frac{\Gamma(Z \to b\bar{b})}{\Gamma(Z \to hadrons)},$$

has currently an exciting particular interest. Most electroweak and QCD radiative corrections cancel in the ratio, leaving R_b^0 sensitive essentially to corrections to the $Z \to b\bar{b}$ vertex, like the large CKM coupling to the top quark. Due to the high quality of the agreement between the Standard Model and most of precise observations, together with the recent top quark discovery and its direct mass measurement, the parameters of the Standard Model become better constrained. A precise measurement of R_b^0 at 0.5% level tests thus not only the Standard Model but also the presence of novel radiative vertex corrections. In this way, R_b^0 is currently one of the most interesting windows in the search for physics beyond the Standard Model. Experimentally, R_b^0 can be obtained with only very small corrections from the ratio of cross-sections $R_b = \sigma(e^+e^- \to b\bar{b})/\sigma(e^+e^- \to hadrons)$. These small corrections are due to the photon propagation contribution.

This thesis reports on the measurement of R_b performed with the DELPHI detector at CERN's LEP collider, using the full LEP 1 statistics, recorded between the 1991 and 1995 years. About 60% of these data were taken with a high precision double sided silicon microvertex detector, and all the rest with a single sided silicon detector providing high resolution only in the plane transverse to the colliding beams. A total of about 4.2M hadronic Z decays were recorded and analyzed, together with about twice the data sample statistics of simulated hadronic events. In addition, dedicated $Z \to b\bar{b}$ samples were used, corresponding to an equivalent amount of also twice the data sample size.

The precise measurement of R_b relies on high purity/efficiency hemisphere b tagging techniques. Due to the particular multihadronic topology of Z events at LEP 1 energies, multivariate methods provide efficient tools for performing a global flavour tagging by hemispheres, especially b identification. To optimize the event information and the high tracking resolution of the DELPHI detector, the following features are included in the algorithms:

- three-dimensional and independent primary vertex reconstruction for each hemisphere of the event, reducing hemisphere-hemisphere tagging efficiency correlations;
- three-dimensional secondary vertexing and invariant mass reconstruction;
- three-dimensional impact parameters and related quantities;
- event shape properties, like transverse and total momenta of decay products, rapidity of tracks and sphericity.

For the precise determination of R_b, events are divided into hemispheres by the plane perpendicular to the thrust axis. Each hemisphere is then classified between six mutually exclusive tagging categories or tags ordered by decreasing b purity: b-tight, b-standard, b-loose, charm, uds and no-tag. There are 20 different observables (combinations of two hemisphere tags) and 17 independent unknowns: R_b, R_c and 15 *uds*, c and b tagging efficiencies. The direct fit of this double tag matrix is degenerated and additional constraints are needed. Two kinds of solutions were investigated. In the first one, the b efficiencies are estimated from the fraction of hemispheres tagged in one category while the opposite hemisphere is tagged as b as a function of a purity cut. The shape of the *uds* and c backgrounds is taken from the Monte Carlo simulation of the experiment, but the parameters themselves are measured directly from data. R_c is taken from electroweak theory. This solution was proven to be systematically powerful but statistically limited due to the large number of free parameters in the fit. In the second approach, the *uds* and c backgrounds of the b-tight tag are estimated from simulation and introduced in the fit, taking as before R_c from electroweak theory. This approach resolves all problems of the first one. The quoted result was

$$\frac{\Gamma(Z \to b\bar{b})}{\Gamma(Z \to hadrons)} = 0.21658 \pm 0.00076(stat.) \pm 0.00087(syst.) - 0.025 \times (R_c - 0.172)$$

where the first error is statistical and the second one systematic. The explicit dependence with the assumed value of R_c is also given. This number is still preliminary.

Within a 0.53% relative precision, the result is in good agreement with the current Standard Model expectation, $R_b^0 = 0.2158 \pm 0.0003$, as predicted for a top quark mass of 175.6 ± 5.5 GeV/c^2 as measured at FNAL. If the radiative corrections (dominated by top quark effects) were left out of the electroweak calculation, the expected result would be $R_b^0 = 0.2183 \pm 0.0001$. Therefore, this measurement shows evidences of the top quark dominated radiative vertex correction in the $Z \to b\bar{b}$ vertex.

This experimental result is consistent with other precise determinations performed at LEP/SLC colliders, but it is the most precise one.

Resumen

Entre las medidas disponibles a la energía en centro de masas correspondiente al polo del bosón Z, la fracción de la anchura parcial a pares de quarks $b\bar{b}$ y su anchura parcial hadrónica,

$$R_b^0 = \frac{\Gamma(Z \to b\bar{b})}{\Gamma(Z \to hadrons)},$$

tiene actualmente un excitante y especial interés. Prácticamente todas las correcciones radiativas electrodébiles y de QCD cancelan al realizar el cociente, de forma que R_b^0 es esencialmente sensible sólo a las correcciones al vértice $Z \to b\bar{b}$, como el fuerte acoplamiento CKM al quark top. Dado el excelente acuerdo entre el Modelo Estándar y la mayor parte de las observaciones de precisión, junto con el reciente descubrimiento del quark top y la determinación directa de su masa, los parámetros del Modelo Estándar quedan muy restringidos. Por ello, una medida de precisión de R_b^0 al 0.5% no solamente examina el Modelo Estándar sino que además prueba la presencia de nuevas correcciones radiativas al vértice. De esta forma, R_b^0 es actualmente una de las vías mas interesantes en la búsqueda de física más allá del Modelo Estándar. R_b^0 puede obtenerse experimentalmente, con muy pequeñas correcciones, a partir del cociente de secciones eficaces $R_b = \sigma(e^+e^- \to b\bar{b})/\sigma(e^+e^- \to hadrons)$. Estas correcciones se deben a la contribución del propagador fotónico.

Esta tesis presenta la medida de R_b realizada con el detector DELPHI del colisionador LEP del CERN, utilizando la estadística completa de LEP 1, registrada entre los años 1991 y 1995. Alrededor del 60% de estos datos fueron tomados con un detector de microvértices de silicio de doble cara, y los restantes con uno equivalente pero de simple cara, suministrando información de precisión sólo en el plano transverso a los haces del colisionador. En total, cerca de 4.2M de desintegraciones hadrónicas del Z han sido analizadas, junto con aproximadamente el doble de estadística de sucesos hadrónicos simulados. Además se han utilizado muestras dedicadas de sucesos $Z \to b\bar{b}$, cuyo tamaño equivalente es similar al del resto de los sucesos simulados.

La medida precisa de R_b está estrechamente relacionada con el desarrollo de técnicas de alta pureza/eficiencia para el etiquetado por hemisferios de quarks b. Debido a la particular topología multihadrónica de los sucesos Z a las energías de LEP 1, los métodos multivariados ofrecen amplias posibilidades para realizar un etiquetado global de sabores por hemisferios, con especial énfasis en la identificación del sabor b. Con el fin de optimizar la información del suceso y la elevada resolución en la reconstrucción de trazas del detector DELPHI, los algoritmos desarrollados incluyen las siguientes características:

- reconstrucción tridimensional e independiente para cada hemisferio del vértice primario del suceso, con la consiguiente reducción de correlaciones hemisferio-hemisferio en las eficiencias de identificación;
- reconstrucción tridimensional de vértices secundarios y masas invariantes;

- parámetros de impacto tridimensionales y cantidades relacionadas;
- propiedades topológicas del suceso, como momento transverso, momento total, *rapidity* y esfericidad de los productos de la desintegración.

Para la determinación precisa de R_b, los sucesos son inicialmente divididos en dos hemisferios utilizando para ello el plano perpendicular al eje *thrust*. Cada hemisferio es entonces clasificado en una de entre seis excluyentes categorías de etiquetado (*tags*) ordenadas por decreciente pureza de sabor *b*: *b-tight, b-standard, b-loose, charm, uds* y *no-tag*. De esta forma hay 20 observables distintos (combinaciones de dos categorías de hemisferio) y 17 incógnitas independientes: R_b, R_c y 15 eficiencias de identificación de quarks *uds*, *c* y *b*. El ajuste directo de esta matriz de doble classificación está degenerado, con lo que se require información adicional. Dos soluciones han sido investigadas. En la primera de ellas, las eficiencias *b* se estiman a partir de la fracción de hemisferios clasificados en una categoría mientras el hemisferio opuesto es clasificado como *b* en función de un corte de pureza dado. La forma del ruido de fondo *uds* y *c* se toma de la simulación Monte Carlo del experimento, pero los parámetros se ajustan a los datos. R_c se fija a su valor predicho por la teoría electrodébil. Esta solución es potente desde el punto de vista sistemático pero está estadísticamente limitada debido al elevado número de parámetros que el ajuste requiere. En la segunda solución, el ruido de fondo *uds* y *c* de la categoría *b-tight* se calcula con la ayuda de la simulación Monte Carlo antes de introducirlo en el ajuste. Como antes, R_c se fija a su valor predicho por la teoría electrodébil. Esta segunda solución resuelve todos los problemas de la primera. El resultado que finalmente se obtiene es

$$\frac{\Gamma(Z \to b\bar{b})}{\Gamma(Z \to hadrons)} = 0.21658 \pm 0.00076(stat.) \pm 0.00087(syst.) - 0.025 \times (R_c - 0.172)$$

donde el primer error es estadístico y el segundo sistemático. El último término de este resultado es la dependencia explícita con el valor tomado de R_c. Este valor es todavía preliminar.

Dentro de una precisión relativa del 0.53%, el valor obtenido está en buen acuerdo con la predicción actual del Modelo Estándar, $R_b^0 = 0.2158 \pm 0.0003$, para una masa del quark top de 175.6 ± 5.5 GeV/c^2, tal como se ha medido al FNAL. Si las correcciones radiativas (dominadas por los efectos del quark top) se omiten en los cálculos electrodébiles, el resultado que se obtendría es $R_b^0 = 0.2183 \pm 0.0001$. Por lo tanto, esta medida muestra evidencias de que el vértice $Z \to b\bar{b}$ está dominado por correcciones radiativas debidas al quark top.

Este resultado experimental es consistente con otras determinaciones precisas realizadas en los colisionadores LEP/SLC, pero es la más precisa de todas ellas.

Contents

Chapter 1

Introduction

The *Standard Model* (SM) of the electroweak and strong interactions [1] is the present theory describing the fundamental constituents of matter and their interactions being theoretically consistent and in agreement with all known experimental data. The Standard Model is the Glashow-Salam-Weinberg model of leptons [2], extended via the GIM mechanism [3] to the hadronic sector, thus incorporating the Cabbibo mixing [4] and the concept of color [5]. Actually, the Standard Model is supporting extremely stringent quantitative experimental tests at LEP and SLC colliders [6], which have provided increasing evidence of the correctness of the model at present energy scales and distances, down to 10^{-16} cm.

In the Standard Model the fundamental constituents of matter can be grouped into three generations (or families) of fundamental (point-like) spin-$\frac{1}{2}$ quarks and leptons, as shown in table 1.1 [7, 8, 9]. For each fermion there is an antiparticle with the same mass but opposite electric charge. For ordinary matter only particles from the first generation are necessary, but all of them were decisive 10000 million years ago, just 1000 millionth of a second after the Universe was born in the Big Bang, according to the conventional wisdom in cosmology. If the number of quark-lepton generations is equal to the number N_ν of light neutrinos (with masses not above half the Z boson mass), then there are no more than these three. This statement comes from the precision measurements of the Z lineshape at LEP collider (see figure 1.1), which imply $N_\nu = 2.993 \pm 0.011$ [6] in the Standard Model. This also provides an important check of cosmological models [10].

In 1897, electrons were discovered from cathodic ray experiments by J.J. Thomson at the Cavendish Laboratory. In 1931, W. Pauli predicted the existence of the electronic neutrino to resolve the energy crisis in the β decay [11]. Only after 22 years, Reines and Cowan detected for the first time these elusive particles in a nuclear reactor experiment [12]. Although protons and neutrons were discovered as constituents of the atomic nucleus in 1919 by E. Rutherford and in 1932 by J. Chadwick respectively from scattering experiments with α particles, it was only in 1968 when J. Friedman and H. Kendall at SLAC (on the basis of deep inelastic electron scattering experiments) obtained evidences on the behavior of point-like

Table 1.1: The three generations of the fundamental spin-$\frac{1}{2}$ constituents of matter, their electric charges (Q_f) in units of the positron charge and masses.

Generation	Fermion	Q_f	Mass (MeV/c^2)	Type
1	up	2/3	2 to 8	quark
	down	-1/3	5 to 15	quark
	ν_e	0	$< 15 \times 10^{-6}$, $CL = 95\%$	lepton
	e^-	-1	$0.51099907 \pm 0.00000015$	lepton
2	charm	2/3	1000 to 1600	quark
	strange	-1/3	100 to 300	quark
	ν_μ	0	< 0.17, $CL = 90\%$	lepton
	μ^-	-1	105.658389 ± 0.000034	lepton
3	top	2/3	175600 ± 5500	quark
	bottom	-1/3	4100 to 4500	quark
	ν_τ	0	< 24, $CL = 95\%$	lepton
	τ^-	-1	$1777.00^{+0.30}_{-0.27}$	lepton

charged structures inside the nucleon [13], the so-called 'partons'. This was in fact the discovery of the quark (up and down). The detailed study of cosmic rays in the 1930's triggered a shower of spectacular discoveries. Among them, C. Anderson observed in 1932 the positron (the antimatter partner of the electron), predicted by P. Dirac in 1929. Four years later, C. Anderson together with S. Neddermeyer discovered the muon [14]. In addition, the break-up of cosmic ray muons suggested that the neutrino might also come in different kinds. In 1962, using a neutrino beam produced from pions decaying in flight at Brookhaven, L. Lederman, J. Steinberger and M. Schwartz discovered the muon neutrino [15]. In the 1950's, a new family of peculiar and unstable particles was found. All of them lived for about 10^{-8} s producing in their decays two tracks emerging from a common point, giving an inverted V shape. By this common properties they were called 'strange' particles. Again, the first evidences for these particles were obtained from the analysis of cosmic rays. The first strange particle to be discovered by J. Rochester and C. Butler in 1947 [16] and confirmed by C. Anderson in 1950 was the kaon. In the early 1950's, a new generation of experiments using particle accelerators starts. The discoveries of strange particles were confirmed and extended. Later in 1964 M. Gell-Mann explained the observed properties of the strange particles: they carried another quark, the 'strangeness'.

Because of their much higher masses, the charm quark and the members of the third generation have been studied in detail only recently. Charm was initially suggested by S. Glashow and J.D. Bjorken in 1964, but there was no need at the time for an additional quark to build any known particle. However, S. Glashow, L. Maiani and J. Iliopoulos showed how the unification of electromagnetism and

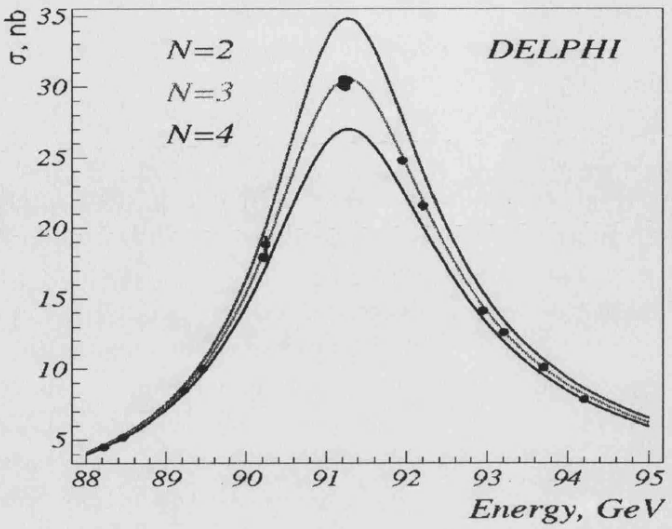

Figure 1.1: The LEP hadronic cross-section around the Z boson peak measured with the DELPHI detector as a function of the center-of-mass energy. Superimposed is the Standard Model prediction for 2, 3 or 4 light neutrino species.

the weak nuclear force (initially involving only leptons) could be extended also to quarks, but only if there were four [3]. The charm quark was finally discovered in 1974 through the production of the $J/\Psi(3.1)$ resonance simultaneously in a fixed target experiment at Brookhaven and in an e^+e^- collider experiment at SLAC [17]. The discovery of the τ lepton followed in 1975 [18] and the observation of open charm was published in 1976 [19]. In 1977, first evidence for the bottom quark was reported through the discovery of the Υ family of resonances in a fixed target experiment at FNAL [20] and the first evidence for open bottom production was published in 1980 [21]. The first evidence for the direct production of the top quark was obtained at Tevatron of FNAL in 1994 [22], and its discovery and mass measurement was published in 1995 [8, 9]. There is strong indirect evidence for the τ neutrino from τ decay combined with neutrino reaction data [7].

The three generations of leptons and quarks are represented in left-handed weak isospin doublets and right-handed weak isospin singlets:

$$\begin{pmatrix} \nu_e \\ e^- \end{pmatrix}_L \begin{pmatrix} \nu_\mu \\ \mu^- \end{pmatrix}_L \begin{pmatrix} \nu_\tau \\ \tau^- \end{pmatrix}_L \tag{1.1}$$

$$\left(e^- \right)_R \left(\mu^- \right)_R \left(\tau^- \right)_R \tag{1.2}$$

and

$$\begin{pmatrix} u \\ d \end{pmatrix}_L \begin{pmatrix} c \\ s \end{pmatrix}_L \begin{pmatrix} t \\ b \end{pmatrix}_L \tag{1.3}$$

$$\left(\begin{array}{c} u \end{array}\right)_R \left(\begin{array}{c} d \end{array}\right)_R \left(\begin{array}{c} c \end{array}\right)_R \left(\begin{array}{c} s \end{array}\right)_R \left(\begin{array}{c} t \end{array}\right)_R \left(\begin{array}{c} b \end{array}\right)_R . \tag{1.4}$$

This phenomenological structure can be embedded in a gauge invariant field theory of the electromagnetic and weak interactions by interpreting $SU(2)_L \otimes U(1)_Y$ as the group of gauge transformations under which the Lagrangian is invariant locally at each point in space-time [23]. Right-handed fermions transform under $U(1)_Y$ only. Y represents the weak hypercharge introduced below. No right-handed massless neutrinos are introduced. Left-handed fermions transform under both $SU(2)_L$ and $U(1)_Y$. The requirement of local invariance implies that there is one spin-1 gauge boson for each generator of the symmetry group and it restricts their couplings, so that the theory is renormalizable and calculations can be done in perturbation theory and the model can be confronted to experiment. The four generators of $SU(2)_L \otimes U(1)_Y$ introduce four vector fields which will correspond to the massless photon and the massive $W^{\pm}$ and Z bosons responsible for electroweak interactions. If the gauge symmetry of the group is exact, all the gauge bosons and fermions remain massless. It is possible, however, to introduce a mechanism that breaks the symmetry *spontaneously* while preserving the good behavior of the gauge theory. This is the well-known *Higgs mechanism* [24]. In the most simple configuration, known as Minimal Standard Model (MSM), the generation of particle masses is realized by introducing a single complex doublet under $SU(2)_L$ of scalar fields

$$\Phi = \begin{pmatrix} \phi^+ \\ \phi^0 \end{pmatrix}$$

coupled to the gauge fields with two self-interacting coupling constants (μ, λ). Three of the four real field components are identified as massless Goldstone bosons corresponding to the spontaneous breakdown of $SU(2)_L$. The three degrees of freedom associated with the Goldstone bosons are absorbed as degrees of freedom for three of the four gauge fields, thus giving mass to the three corresponding gauge $W^{\pm}$ and Z bosons. The fourth real component of the scalar doublet remains and acquires a vacuum expectation value $v = 2\mu/\sqrt{\lambda}$, thus breaking the symmetry. This physical scalar massive particle, with mass $M_H = \sqrt{2}\lambda$, is the Higgs boson. Lepton and quark masses arise in this model through a Yukawa coupling of the lepton and quark fields to the Higgs field vacuum expectation value, i.e. $m_f = g_f v/\sqrt{2}$, where the Yukawa couplings g_f are arbitrary numbers fixed by the experimentally determined masses of particles. The vacuum expectation value can be related to the Fermi constant G_F via $v^2 = (\sqrt{2}G_F)^{-1} \approx (246\ GeV)^2$. The specific gauge chosen for the Lagrangian provides us the vector boson propagators which describe the propagation of four-vector field components whereas only three polarization states are physical. On the other hand, it is not possible to define a propagator without imposing a gauge-fixing condition, introducing the fourth component. In the case of non-abelian gauge fields (as it is the case of $SU(2)_L$), the introduction of the unphysical components would give rise to consequences like gauge dependent physical quantities, unless additional unphysical states, called *ghosts*, are introduced. Ghosts together with the unphysical Higgs components of the complex doublet render physical matrix elements gauge

independent. Only in the unitary gauge these unphysical degrees of freedom seem to vanish but essentially reappear in the gauge field sector, where they provide the longitudinal component modes of $W^{\pm}$ and Z when they acquire masses. However, in general, calculations can be done more easily in the t'Hooft-Feynman gauge.

The strong interactions are invariant under the gauge group $SU(3)_C$, which is known as 'color', the analogous of the electric charge in strong interactions. Under $SU(3)_C$, the quarks are triplets and the leptons are singlets. In other words, each quark specie exists in three different colors and leptons are colorless. The eight generators of the group correspond to the eight massless gluons of Quantum Chromodynamics (QCD) which are responsible of the strong interactions. Gauge invariance requires that they interact. These self-interactions produce a potential energy which grows linearly with distance between isolated quarks or gluons. Consequently, quarks are permanently confined into experimentally observed hadrons. At short distances (large momentum transfers) the strong interactions are weak so that perturbation theory can be used, whereas at low momentum transfers non-perturbative effects dominate.

The interaction of quarks and leptons in the Standard Model is therefore constructed by requiring the Lagrangian $\mathcal{L}_{SM}$ [1, 23] to be locally invariant under the gauge group

$$SU(3)_C \bigotimes SU(2)_L \bigotimes U(1)_Y. \tag{1.5}$$

The matter fields f entering in the Lagrangian are fermions belonging to the fundamental representation of the gauge group. The local invariance generates a total of 12 gauge bosons belonging to the adjoint representation of the group with coupling constants:

gluons	$SU(3)_C$	α_s
weak bosons	$SU(2)_L$	g
abelian boson	$U(1)_Y$	g' .

All gauge bosons are responsible for all known interactions except gravity, for which there is no fully satisfactory quantum theory. The requirement of $U(1)$ gauge invariance does not lead to any constraint on the coupling constants of the abelian boson with the left-handed fermion doublets and the right-handed fermion singlets. Making use of this freedom, these constants can be chosen so that the weak and the electromagnetic interactions are unified in the electroweak interaction. This can be done taking as abelian coupling constants the product of g' and the weak hypercharge Y_f, defined according to the Gell-Mann-Nishijima relation

$$Q_f = I_3^f + Y_f/2. \tag{1.6}$$

Q_f and I_3^f are, respectively, the fermion electric charge in units of the positron charge and the third weak isospin component (table 1.2). The group $U(1)$ is called the weak hypercharge group $U(1)_Y$. However, in the case of the $SU(2)_L$ invariance,

when several spinor field doublets are present, the coupling constants g of these fields with the Yang-Mills vector gauge fields ought to be identical. Hence the couplings in the $SU(2)_L \otimes U(1)_Y$ group of the matter fields and gauge bosons are only given by two constants, g and g', and the weak hypercharge Y_f defined by the Gell-Mann-Nishijima relation. Table 1.2 summarizes the assignment of all electroweak quantum numbers Q_f, I_f, I_f^3 and Y_f to the fundamental fermions. The same arguments are also applied to the QCD coupling constant α_s.

Table 1.2: Assignment of the electroweak quantum numbers Q_f, I_f, I_f^3 and Y_f to the fundamental fermions. Q_f, I_f and I_f^3 are, respectively, the fermion electric charge in units of the positron charge, the weak isospin and third weak isospin component. The weak hypercharge Y_f is defined by the Gell-Mann-Nishijima relation.

Fermion			Q_f	I_f	I_f^3	Y_f
ν_{eL}	$\nu_{\mu L}$	$\nu_{\tau L}$	0	1/2	1/2	-1
e_L	μ_L	τ_L	-1	1/2	-1/2	-1
u_L	c_L	t_L	2/3	1/2	1/2	1/3
d'_L	s'_L	b'_L	-1/3	1/2	-1/2	1/3
e_R	μ_R	τ_R	-1	0	0	-2
u_R	c_R	t_R	2/3	0	0	4/3
d'_R	s'_R	b'_R	-1/3	0	0	-2/3

Due to the diagonalization of the gauge boson mass matrix after the symmetry breaking and after the identification of the photon field coupling via the electric charge e to fermions (allowing the electroweak unification), the non-abelian and abelian coupling constants are related to the electric charge e through the relations

$$g = \frac{e}{\sin\theta_W}, \quad g' = \frac{e}{\cos\theta_W}. \tag{1.7}$$

θ_W is the electroweak mixing angle (Weinberg angle) which originates from the diagonalization of the gauge boson mass matrix, whose definition is

$$\cos\theta_W = \frac{g}{\sqrt{g^2 + g'^2}} = \frac{M_W}{M_Z}. \tag{1.8}$$

The masses of the vector bosons are

$$M_W = \frac{1}{2}vg, \quad M_Z = \frac{1}{2}v\sqrt{g^2 + g'^2}. \tag{1.9}$$

Finally, the Yukawa coupling terms are

$$m_f = g_f\frac{v}{\sqrt{2}} = \sqrt{2}\frac{g_f}{g}M_W. \tag{1.10}$$

These relations allow to replace the original set of parameters given by the gauge couplings (g, g', α_s), the Yukawa couplings (g_f) and the Higgs self-interacting couplings (μ, λ) by the following equivalent set of more physical parameters: strong coupling constant (α_s), electromagnetic coupling constant α, masses of the vector bosons (M_W and M_Z), Higgs mass (M_H) and fermion masses (m_f). All the other parameters of the theory, in particular, the number of matter fields (generations) and the quark mixing matrix (V_{CKM}) remain unchanged. Each of these parameters can (in principle) directly be measured by a suitable experiment.

The requirement of Lorentz invariance of $\mathcal{L}_{SM}$, via the minimal substitution rule, together with the fact that electroweak interactions between leptons and quarks are mediated by the photon and the $W^{\pm}$ and Z bosons, generates the following interaction Lagrangian of the fundamental fermions with gauge vector bosons:

$$\mathcal{L}_I = \left(-\frac{e}{2\sqrt{2}\sin\theta_W} J_\mu^{CC} W^\mu + h.c. \right) - \frac{e}{2\cos\theta_W \sin\theta_W} J_\mu^{NC} Z^\mu - e J_\mu^{EM} A^\mu. \quad (1.11)$$

J_μ^{NC} and J_μ^{EM} are the neutral currents which couple to the Z and to the photon neutral weak vector boson fields (Z^μ and A^μ respectively). J_μ^{CC} are the charged currents, which couple to the $W^{\pm}$ charged weak vector boson fields (W^μ).

The charged current (CC) is given by

$$J_\mu^{CC} = J_\mu^{lept} + J_\mu^{quark} = 2(\bar{\nu}_e, \bar{\nu}_\mu, \bar{\nu}_\tau)_L \gamma_\mu \begin{pmatrix} e^- \\ \mu^- \\ \tau^- \end{pmatrix}_L + 2(\bar{u}, \bar{c}, \bar{t})_L \gamma_\mu V_{CKM} \begin{pmatrix} d \\ s \\ b \end{pmatrix}_L \quad (1.12)$$

where V_{CKM} is a 3×3 complex unitary matrix in flavour space which accounts for the fact that the weak eigenstates of quarks are linear superpositions of the mass eigenstates, thus generating family mixing. The matrix can be expressed in terms of four physically independent parameters [7]: three rotation angles and one complex phase which introduces the possibility of CP violation in charged current weak decays. Quarks of one generation can decay into quarks of another generation. Since there are no right-handed fields for neutrinos, the charged lepton mass matrix is already diagonal and there are no family changing leptonic currents. Hence the charged current has a pure V-A structure.

The matrix V_{CKM} relating the quark mass eigenstates with the weak eigenstates was introduced by Kobayashi and Maskawa [25] and is a generalization of the Cabbibo rotation matrix [4]. The matrix elements are conveniently labeled by the quark flavours linked by them. By convention, the family mixing is assigned to the $I_3^f = -1/2$ states:

$$\begin{pmatrix} d' \\ s' \\ b' \end{pmatrix}_L = \begin{pmatrix} V_{ud} & V_{us} & V_{ub} \\ V_{cd} & V_{cs} & V_{cb} \\ V_{td} & V_{ts} & V_{tb} \end{pmatrix} \begin{pmatrix} d \\ s \\ b \end{pmatrix}_L \quad (1.13)$$

and hence the quark weak eigenstates become:

$$\begin{pmatrix} u \\ d' \end{pmatrix}_L \begin{pmatrix} c \\ s' \end{pmatrix}_L \begin{pmatrix} t \\ b' \end{pmatrix}_L \tag{1.14}$$

$$\begin{pmatrix} u \end{pmatrix}_R \begin{pmatrix} d \end{pmatrix}_R \begin{pmatrix} c \end{pmatrix}_R \begin{pmatrix} s \end{pmatrix}_R \begin{pmatrix} t \end{pmatrix}_R \begin{pmatrix} b \end{pmatrix}_R . \tag{1.15}$$

Neutral currents (NC) couple to the Z and the photon and they are given by

$$J_\mu^{NC} = \sum_f \bar{f}\gamma_\mu [v_f - a_f\gamma_5] f \tag{1.16}$$

and

$$J_\mu^{EM} = \sum_f \bar{f}\gamma_\mu Q_f f. \tag{1.17}$$

a_f and v_f are the vector and axial-vector coupling constants defined as

$$\begin{aligned} a_f &= I_3^f \\ v_f &= I_3^f - 2Q_f \sin^2\theta_W \end{aligned} \tag{1.18}$$

In terms of pure left-handed and right-handed components, the neutral currents can be written as

$$J_\mu^{NC} = 2\sum_f \bar{f}\gamma_\mu \left[g_L^f \frac{1-\gamma_5}{2} + g_R^f \frac{1+\gamma_5}{2} \right] f \tag{1.19}$$

being

$$g_L^f = \frac{v_f + a_f}{2}, \quad g_R^f = \frac{v_f - a_f}{2}. \tag{1.20}$$

The Z boson interaction transmutes singlets and the upper and lower members of doublets into themselves, preserving quark and lepton flavours. The neutral current is flavour diagonal and all fiavour changing transitions in the Standard Model (at tree level) are confined to the charged current sector. While the electromagnetic interaction conserves C, P and CP separately, the Z exchange violates C and P but conserves CP. Neutral currents were discovered from $\nu_\mu e$ scattering in the Gargamelle bubble chamber at CERN in 1973 [26].

The Standard Model, as a gauge invariant quantum field theory, uses perturbation theory on the coupling constants to compute cross-sections and decay widths. To simplify the matrix element calculations, the Lagrangian $\mathcal{L}_{SM}$ is written in a way which shows directly the fermions, propagators and vertices (Feynman diagrams), and can be applied, for instance, to the estimation of the muon lifetime at lowest order. Moreover, the Fermi current-current model of weak interactions with an effective constant G_F yields an expression for the muon lifetime from which the value of

G_F is determined. Taking into account mass effects and the electromagnetic corrections (QED) to the muon decay in the Fermi model [27], and using the very precise measurement of the muon lifetime [7], the numerical value of G_F can be determined with high precision. Consistency of the Standard Model at low transfer momentum ($q^2 \ll M_W^2$) with the Fermi model gives

$$G_F = \frac{\pi\alpha}{\sqrt{2}\sin^2\theta_W M_W^2} \tag{1.21}$$

and similarly

$$G_F = \frac{\pi\alpha}{\sqrt{2}\sin^2\theta_W \cos^2\theta_W M_Z^2}. \tag{1.22}$$

These equations allow to predict the vector boson masses in terms of the parameters α, G_F and $\sin^2\theta_W$. In 1983, ten years after the discovery of the neutral currents, the predicted existence of the $W^\pm$ and Z bosons together with the theoretical estimations of their masses (using for $\sin^2\theta_W$ determinations from neutrino scattering data) was spectacularly confirmed on the $p\bar{p}$ collider at CERN [28].

The Minimal Standard Model as outlined above contains only one complex scalar doublet. However, symmetry breaking can also be achieved by the introduction of more complicated structures. It is useful to introduce the ρ parameter by the ratio of neutral and charged current coupling strengths as

$$\rho = \frac{M_W^2}{M_Z^2 \cos^2\theta_W}. \tag{1.23}$$

The ρ parameter is unity in the Standard Model with one Higgs doublet and the introduction of further isospin doublets does not modify its value. Therefore, the ρ parameter is determined by the Higgs structure of the theory. Deviations from $\rho = 1$ in the Minimal Standard Model can only be originated from radiative corrections. Using relations (1.8) and (1.23) the mixing angle can be written generally as

$$\sin^2\theta_W = 1 - \frac{M_W^2}{\rho M_Z^2} \tag{1.24}$$

with $\rho = 1$ at tree (first order) level. To see deviations from $\rho = 1$, one can write $\rho = \frac{1}{1-\Delta\rho}$, in which case

$$\sin^2\theta_W = 1 - \frac{M_W^2}{M_Z^2} = 1 - \frac{M_W^2}{M_Z^2} + \frac{M_W^2}{M_Z^2}\Delta\rho. \tag{1.25}$$

Consequently, relation (1.22) has to be modified according to

$$G_F = \frac{\pi\alpha}{\sqrt{2}\rho\sin^2\theta_W \cos^2\theta_W M_Z^2} \tag{1.26}$$

whereas relation (1.21) remains unchanged.

The physical observables to be confronted with the electroweak theory at the Z pole are the measured cross-sections for various final states, forward-backward and polarization asymmetries [29]. At tree level in perturbation theory, they can all be expressed in terms of the vector and axial-vector couplings. The $Z \to f\bar{f}$ partial width is given by

$$\Gamma_{ff} = \Gamma(Z \to f\bar{f}) = 4N_C^f \frac{G_F M_Z^3}{24\sqrt{2}\pi} \left\{v_f^2 + a_f^2\right\} \tag{1.27}$$

where N_C^f is 1 for leptons and 3 for quarks, and the total width is the sum over all open channels. Around the Z pole, the total cross-section for the process $e^+e^- \to f\bar{f}$ is dominated by Z exchange. The peak cross-section σ_f^0 can be expressed through the total and partial widths of the Z:

$$\sigma_f^0 = \frac{12\pi}{M_Z^2} \frac{\Gamma_{ee}\Gamma_{ff}}{\Gamma_Z^2}. \tag{1.28}$$

The angular dependence of the cross-section for the process $e^+e^- \to f\bar{f}$ with $f \neq e$ is given by

$$\frac{d\sigma(s)}{d\cos\theta} \sim 1 + \cos^2\theta + \frac{8}{3} A_{FB}(s) \cos\theta \tag{1.29}$$

where θ is the polar angle between the directions of the incoming e^+ and the outgoing antifermion $\bar{f}$. For $f = e$, a more complicated expression arises from the t-channel involved. The parameter $A_{FB}(s)$ is the forward-backward asymmetry defined for unpolarized beams. The experimental information about forward-backward asymmetry is expressed in terms of a single number, the peak asymmetry $A_{FB}^{0,f}$, defined as

$$A_{FB}^{0,f} = A_{FB}^f(s = M_Z^2) = \frac{3}{4} \mathcal{A}_e \mathcal{A}_f \tag{1.30}$$

with

$$\mathcal{A}_f = \frac{(g_L^f)^2 - (g_R^f)^2}{(g_L^f)^2 + (g_R^f)^2} = \frac{2v_f a_f}{v_f^2 + a_f^2}. \tag{1.31}$$

Fermions in Z decays are produced polarized and in the decay into $\tau^+\tau^-$ pairs this polarization can be measured experimentally from the analysis of the τ decay properties. Mean τ polarization is a measurement of $\mathcal{A}_\tau$, while as a function of the polar production angle provides both, $\mathcal{A}_\tau$ and $\mathcal{A}_e$, thus allowing to test lepton universality. If longitudinal beam polarization is available, the left-right asymmetry at the Z peak provides a direct access to $\mathcal{A}_e$, the electron couplings to the Z. The forward-backward polarized asymmetry for the process $e^+e^- \to f\bar{f}$ gives access to $\mathcal{A}_f$. However, before one can make predictions from the theory, a set of independent parameters has to be determined from experiment. All the practical calculational

schemes choose the same physical input quantities α, G_F, M_Z, m_f and M_H for fixing the free parameters of the Standard Model (see next chapter for more details). In terms of this set of quantities, M_W and all the observables at the Z resonance can be calculated as predictions depending on m_t and M_H, together with the strong coupling constant α_s.

One can classify the Z measurements in two classes:

- first, measurements providing tests of the $SU(2)_L \otimes U(1)_Y$ gauge structure. The main consequence of the $SU(2)_L \otimes U(1)_Y$ invariance is *universality* in a global sense: the couplings of particles with the same quantum numbers should be the same, independently of their family, which can be better tested with leptons. Furthermore, the couplings of the Z to fermions should all obey the formulae (1.18). After correction for radiative effects, the same value of $\sin^2\theta_W$ should match all measured couplings;

- second, measurements which probe the perturbative effects of the theory, in other words, radiative effects. Besides QED radiative effects (emission of real or virtual photons), Z observables are sensitive to heavy particles (some of them undiscovered), such as the top quark or the Higgs boson. Chapter 2 is devoted to a detailed summary of all such radiative corrections, with special emphasis in the specific decay channel of the Z into $b\bar{b}$ quarks, which has special features with respect to all the other processes in neutral currents. As it is shown there, one effect of the electroweak radiative corrections is the redefinition of the coupling constants ($v_f \rightarrow g_v^f$, $a_f \rightarrow g_a^f$) and of the electroweak mixing angle ($\sin\theta_W \rightarrow \sin\theta_W^{f,eff}$) to effective quantities.

So far the most stringent tests of the Standard Model are performed by the LEP collider at CERN and the SLC collider at SLAC. Running around the Z pole center-of-mass energy, they have precisely measured the Z lineshape, asymmetries and polarizations. Both experimental setups are complementary: whereas LEP provides high statistics with unpolarized beams, SLC provides small statistics with longitudinally polarized beams. For the Z lineshape determination, two kind of fits are usually performed. First, a nine parameter fit (M_Z, Γ_Z, σ^0_{had}, R_e, R_μ, R_τ, $A^{0,e}_{FB}$, $A^{0,\mu}_{FB}$ and $A^{0,\tau}_{FB}$) is performed to verify lepton universality, where σ^0_{had} is the peak hadronic cross-section. The ratios R_l are defined as $R_l = \Gamma_{had}/\Gamma_{ll}$, where Γ_{had} is the hadronic partial decay width and Γ_{ll} the leptonic width for $l = e, \mu, \tau$. Second, once lepton universality is verified, one can accomplish a five parameter fit with M_Z, Γ_Z, σ^0_{had}, one leptonic width Γ_{ll} and one asymmetry $A^{0,l}_{FB}$. The latest preliminary results obtained by the LEP experiments for the lineshape and forward-backward asymmetries are given in table 1.3. To see details about how these quantities are experimentally determined, see [6] and references therein. The couplings $\mathcal{A}_f$ measured by the LEP and SLC asymmetries and polarizations determine the ratio g_v^f/g_a^f and can be combined into a single observable, the effective leptonic electroweak mixing angle $\sin\theta_W^{l,eff}$. Used in combination with the partial

widths of the Z into leptons, which give access to the sum of squares of the coupling constants, the effective leptonic coupling constants can be determined. The most recent preliminary LEP/SLC averages for the effective mixing angle and the effective vector and axial-vector coupling constants are given in table 1.4[1]. The precision on $\sin^2\theta_W^{l,eff}$ is of the order of 10^{-3}.

Table 1.3: Average lineshape and forward-backward asymmetry parameters from the LEP experiments, with and without assumption of lepton universality.

Parameter	Measurement with total error
$M_Z(GeV)$	91.1867 ± 0.0020
$\Gamma_Z(GeV)$	2.4948 ± 0.0025
$\sigma^0_{had}(nb)$	41.486 ± 0.053
R_e	20.757 ± 0.056
R_μ	20.783 ± 0.037
R_τ	20.823 ± 0.050
$A^{0,e}_{FB}$	0.0160 ± 0.0024
$A^{0,\mu}_{FB}$	0.0163 ± 0.0014
$A^{0,\tau}_{FB}$	0.0192 ± 0.0018
R_l	20.775 ± 0.027
$A^{0,l}_{FB}$	0.0171 ± 0.0010

Table 1.4: Effective mixing angle and effective vector and axial-vector coupling constants assuming lepton universality from LEP and SLC data.

	LEP	LEP+SLC
g^l_v	-0.03681 ± 0.00085	-0.03793 ± 0.00058
g^l_a	-0.50112 ± 0.00032	-0.50103 ± 0.00031
$\sin^2\theta_W^{l,eff}$	0.23196 ± 0.00028	0.23152 ± 0.00023

These precise electroweak measurements can be used to check the validity of the Standard Model and, within its framework, to infer information about its fundamental parameters. The accuracy of the measurements can be used to constraint m_t and $\alpha_s(M_Z)$ in the Standard Model and to a lesser extend, M_H and $\alpha(M_Z^2)$, through loop corrections [6]. As it will be explained in chapter 2, the leading m_t dependence is quadratic and allows a determination of m_t. The main dependence

[1] In practice, polarized and unpolarized forward-backward asymmetries at LEP and SLC for b and c quarks are also included. This is justified by the fact that all these asymmetries have a reduced sensitivity to corrections particular to the hadronic vertex.

on M_H is logarithmic and therefore the constraints on M_H are weak. The m_t values derived from different observables at the Z can be compared to the direct measurement from the FNAL $p\bar{p}$ collider [8]. In addition, the top quark mass inferred from electroweak measurements can be expressed in terms of a $W^{\pm}$ mass value which can be compared to the direct measurement of M_W from $p\bar{p}$ and LEP 2 colliders. A very good agreement is found for both, m_t and M_W, from electroweak data [6] and direct measurement [9, 28, 30].

As a first example of the impressive agreement between observations and Standard Model predictions, figure 1.2 shows the leptonic partial width measured at LEP versus the effective electroweak mixing angle from LEP and SLC, compared with the Standard Model expectations. The star shows the prediction when only the photon vacuum polarization is included among all the electroweak radiative corrections. One can see that electroweak corrections are required to reproduce the LEP/SLC data. Note that the error on $\alpha(M_Z^2)$ is as large as the error on $\sin^2\theta_W^{l,eff}$ from LEP/SLC. As a second example of the agreement between the Standard Model and the experimental data, figure 1.3 compares the most recent measurements of M_W from direct observation with the value estimated from precision electroweak data at LEP 1/SLC colliders (where the W's are not produced directly). Finally, the value of $\alpha_s(M_Z^2)$ from electroweak precision tests within the Standard Model framework (which depends essentially on R_l, Γ_Z and σ^0_{had}) is also in good agreement with that obtained from event-shape measurements at LEP [31] and of similar precision.

Even if the Standard Model is extraordinary successful (there is no experiment that contradicts it until now), it has drawbacks:

- why the gauge group is $SU(3)_C \otimes SU(2)_L \otimes U(1)_Y$?;
- the large number of free parameters, for instance, the number of generations;
- the unification of the strong interaction with the electroweak interactions remains formal. How to incorporate gravity in an unified theory?;
- the problem of CP violation is not well understood;
- one of the main problems of the Standard Model is the origin of the mass spectrum. While there is strong experimental evidence supporting the 'gauge' theoretical part of the model, there is as yet no evidence for the Higgs mechanism for electroweak symmetry breaking. The Higgs particles have not yet been observed and it is not clear whether they are fundamental or composite. Nor there are data to indicate the mechanism by which finite number of generations and unequal fermion masses are generated (flavour symmetry breaking).

Understanding these questions, specially how the masses are produced, is the central problem of particle physics today. From a theoretical point of view, several scenarios just beyond the Standard Model have been proposed:

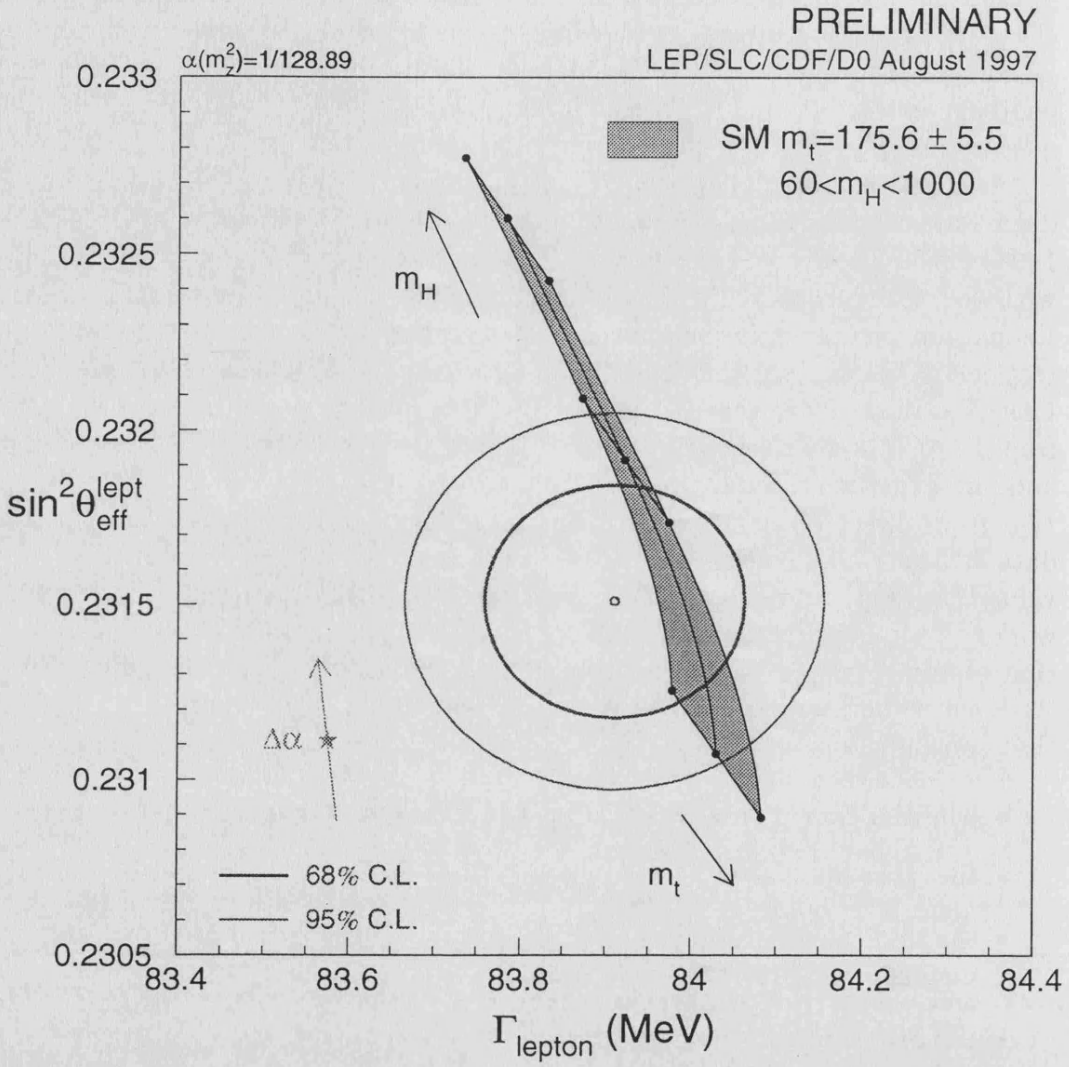

Figure 1.2: The LEP/SLC measurements of $\sin^2\theta_W^{l,eff}$ and leptonic widths and the Standard Model prediction. The star shows the prediction if, among the electroweak radiative corrections, only the photon vacuum polarization is included. The corresponding arrow shows variation of this prediction if $\alpha(M_Z^2)$ is changing by one standard deviation. This variation gives an additional uncertainty to the Standard Model prediction shown in the figure. The agreement with the latest determination of the top quark mass is striking.

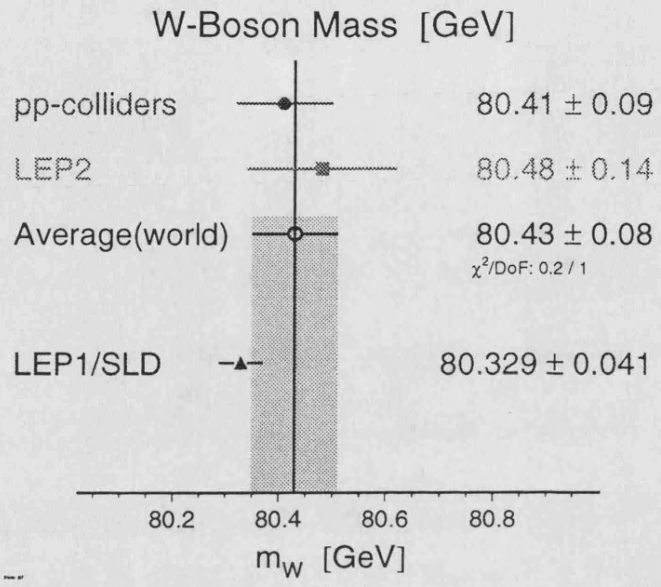

Figure 1.3: Comparison between the measurements of the W boson mass from direct observation in $p\bar{p}$ and LEP 2 colliders and from precision electroweak data in LEP 1/SLC colliders.

- standard Higgs models containing more than one elementary Higgs boson multiplet, generally complex weak doublets. The Mininal Standard Model has only one complex weak doublet with a single neutral boson;
- Supersymmetry, where there are two Higgs doublets and each known particle has a superpartner;
- models of dynamical electroweak and flavour symmetry breaking, like Technicolor;
- composite models, in which quarks and leptons are built of more fundamental constituents.

Other scenarios have been proposed far beyond the Standard Model, like Grand Unified Theories, Supergravity, Superstrings, etc. However, none of these proposals is fully satisfactory and more experimental data becomes crucial.

The situation at the moment is that no observation of an effect beyond the Minimal Standard Model has been made. Therefore, the indirect observation through loop effects of potential 'new physics' appearing as anomalies in well known Standard Model processes becomes very important.

May be one of the most interesting processes of this kind available today is the $Z \to b\bar{b}$ decay. This is the subject of the experimental analysis presented in this

thesis. Chapter 2 is just devoted to a detailed description of the special features of this process. It will appear in the discussion that the physical observable experimentally sensitive to those special effects is the ratio of partial decay widths $\Gamma(Z \to b\bar{b})/\Gamma(Z \to hadrons)$. Then it is shown that a precision better than 0.5% is needed in order to be sensitive to new phenomena. Such a very precise determination of $\Gamma(Z \to b\bar{b})/\Gamma(Z \to hadrons)$ requires:

- a high statistics of hadronic Z decays, which can only be obtained in a Z factory, as is the case of the high luminosity LEP 1 collider;
- a high quality tracking system for detection of the Z decay products. This is fulfilled by DELPHI, one of the four detectors operating at LEP collider, in particular thanks to the installation of a high resolution silicon microvertex detector;
- efficient classifiers of the hadronic events in their flavours, especially for b quarks;
- a method for self-calibrating the classifier, reducing dependences on simulation models (physics and detector).

Chapter 3 will present a brief description of the experimental setup, the LEP collider and the DELPHI detector.

To accomplish the difficult task of identifying $Z \to b\bar{b}$ events among the $Z \to q\bar{q}$ produced at LEP, one requires a good knowledge of all the properties of heavy quarks. The complexity is mainly due to the fact that quarks are not observed as such. According to the present view, the $e^+e^- \to hadrons$ annihilation process can be summarized into four phases:

- In a first step, the e^+e^- pair annihilates into a virtual photon or a Z boson, which subsequently decays into a primary quark-antiquark pair (*hard process*). The amplitudes of these decays are predicted by electroweak theory, as given in chapter 2.
- In a second step, the primary quarks radiate gluons (*final state radiation*), which can radiate further gluons or convert into quark-antiquark pairs, generating a parton cascade. Quark-antiquark pairs can also be created by the radiation of photons by the primary quarks. It is the nature of this process that determines the topological characteristics of the event. Three approaches exist to the modeling of these perturbative corrections: *matrix element* [32], *parton shower* [32] and *color dipole* [34]. The matrix element approach can only handle a maximum of four partons at the end of the cascade. Hence, its applicability at Z pole is strongly limited.

- In a third phase, since only colorless states show up as physical particles (confinement), the partons interact, dress themselves with other partons from the *sea* and rearrange in order to create observable meson or baryon states. If the energy of the primary quark is much larger than its mass (as it is the case of LEP), the quark pair creation can repeat many times resulting ultimately in *jets* of hadrons whose direction follows closely the primary quark direction. This phase is known as *hadronization* or *fragmentation process.* The three most extended models used when describing the hadronization phase in e^+e^- annihilation are the following: *string model* with Lund symmetric fragmentation for light quarks [35] or with Peterson et al. fragmentation for heavy quarks [36], *independent fragmentation* [37] and *cluster model* [38].

- In the fourth phase, unstable hadrons decay. In particular, weak decay of heavy mesons and baryons containing c or b quarks into lighter particles. These decays are governed by the CKM charged current of the weak interaction. Figure 1.4 shows the various contributions to the decay of the b quark. For mesons composed of a light and a heavy quark, the energy released in the heavy quark decay is much larger than the typical quark binding energies. One expects therefore that the light constituents of a heavy meson or baryon play a rather passive role and the heavy quark decays quasi independently of the other constituent(s). This approximation is called the *spectator model* of heavy hadron decays. The model can be refined [29] by taking into account phase space corrections due to finite quark and lepton masses and QCD corrections arising from virtual gluon exchange and real gluon emission. As expected from asymptotic freedom, for b quarks these corrections are considerably smaller than for c quarks. Table 1.5 summarizes the masses, lifetimes and semileptonic branching ratios of bottom and charm hadrons, taken from [7].

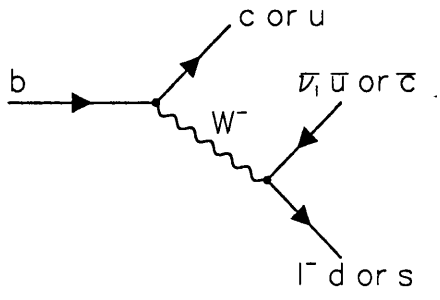

Figure 1.4: The various contributions to the decays of the b quark.

At present, three 'standard' simulation programs reproduce reasonably well the $e^+e^- \rightarrow$ *hadrons* annihilation process. The Lund Parton Shower JETSET Monte Carlo program [32], based on string fragmentation (including also independent fragmentation); the HERWIG Monte Carlo program [33], based on the decay of mass

Table 1.5: Masses, lifetimes and semileptonic branching ratios of bottom and charm hadrons.

Particle	Mass (MeV/c^2)	τ (10^{-12} s)	$c\tau$ (μm)	$Br(X \to e^+ anything)$ (%)
B^+	5278.9 ± 1.8	1.62 ± 0.06	462	10.1 ± 2.3
B^0	5279.2 ± 1.8	1.56 ± 0.06	468	10.3 ± 1.0
B_s^0	5369.3 ± 2.0	1.61 ± 0.10	483	7.6 ± 2.4
D^+	1869.3 ± 0.5	1.057 ± 0.015	317	17.2 ± 1.9
D^0	1864.5 ± 0.5	0.415 ± 0.004	124.4	7.7 ± 1.2
D_s^+	1968.5 ± 0.6	0.467 ± 0.017	140	< 20 *at* $CL = 90\%$

clusters; and the ARIADNE Monte Carlo program [34], interfaced with JETSET and including the color dipole approximation for final state QCD radiation. The JETSET and HERWIG programs use the parton shower approach for final state QCD radiation. JETSET includes also the matrix element option for final state radiation.

From table 1.5 one can see that hadrons containing charm or bottom quarks have the following characteristic properties in common. They have large mass, sizeable semileptonic decay branching ratios and relatively long lifetimes. All these properties can be used, alone or in combination using multivariate techniques, to tag the presence of b quarks in the decay of the Z boson. Final state radiation and fragmentation will difficult the identification, being sources of backgrounds.

The relatively large mass of the decaying hadron has advantageous effects which are related. Since the fragmentation function of a heavy quark favors a harder spectrum, the heavier quark produces the larger momentum of the heavy meson and hence also the momentum of the decay products. The differences in the fragmentation function of charm and bottom should reflect in the momentum distribution of the decay products. At LEP 1, B hadrons will carry, in average, between 70% and 80% of the beam energy (compared to about 50% in D hadrons), whereas the rest will be distributed among the other fragmentation particles. As a fundamental consequence, the two B or D hadrons fly in opposite directions and their decay products will appear inside two different hemispheres in an jet-like topology. Fragmentation particles will spread out in an isotropic-like topology. It is then natural to perform the heavy flavour identification independently for each of both hemispheres. This phenomenological fact can be compared at $\Upsilon(4S)$ energies, where B hadrons are produced almost at rest with no accompanying additional hadron, and where the decay products of the two B hadrons are confused in an isotropic-like topology. The decay products momentum transverse to the jet axis of the jet containing the decaying heavy meson can be as large as $p_\perp \leq 1/2m_Q$. Thus charm decays give $p_\perp \leq 0.8$ GeV/c and bottom decays give $p_\perp \leq 2.5$ GeV/c, assuming $m_c \sim 1.6$ GeV/c^2 and $m_b \sim 4.9$ GeV/c^2. Moreover, B hadrons decay have a mean charged multiplicity of

about 5.5, whereas for charm hadrons it is about 2.5. Due to this difference in track multiplicity, the average track momentum in B decays is lower than in D decays. Therefore, the differences in track transverse momentum and multiplicity lead to different distributions of track rapidity $y = 1/2 \ln \left[(E + p_{\parallel})/(E - p_{\parallel})\right]$, where E is the energy of the track and $p_{\parallel}$ its longitudinal momentum with respect to the jet axis. The tracks from D decays are more 'rapid' than the tracks from B decays.

The sizeable semileptonic decay branching ratio combined with the large mass of heavy quarks make the $p_{\perp}$ of identified leptons a good separation variable for $b\bar{b}$ events. Misidentified leptons, fake leptons, electron-positron pairs from gamma conversions, hadronic punchthrough, pion and kaon decays are strongly suppressed by requiring a high momentum (typically $p > 3$ GeV/c) for the lepton. The remaining backgrounds consist of $c\bar{c}$ and light quark pairs [39]. To obtain a sample of events enriched in charm will require other techniques, because a selection based on lifetimes suffers from an overwhelming background from bottom production [40]. However, there is a considerable price to pay since one looses a factor of five to ten in statistics due to the semileptonic branching ratio.

The long lifetime of heavy flavour particles is by far the experimentally most crucial characteristic property to tag heavy hadrons. The flight distance at LEP 1 ($L = \gamma\beta c\tau$) is of the order of 2.5 mm, if a value around 1.6 ps is taken for the mean B lifetime. The lifetime information in $Z \rightarrow b\bar{b}$ events can be extracted by following two complementary techniques: a) by measuring the impact parameter (shortest distance between the track and the Z boson production vertex) of the tracks; and b) by determining the possible presence of a secondary decay vertex (B decay point) displaced from the primary vertex (Z production point). The presence of a tertiary vertex (originating from the preferred CKM b decay cascade $b \rightarrow c \rightarrow s$ or u) can also be exploited (provided a high resolution tracking) to tag the presence of B hadrons.

The discussion presented above underlines that the e^+e^- annihilation into hadrons is a complex process. The high precision determination of the primary branching of the Z into $b\bar{b}$ quark pairs is a difficult task and truly an experimental challenge. To reach with success this goal, one is interested in reducing as much as possible the dependence of the result on the models assumed. Thus the event classification will be twofold. On one hand, one is interested in having as pure and efficient as possible subsamples of a given flavour. In this case, one needs a classifier with high efficiency for the flavour one wants to enrich, and low efficiency for the complementary flavours. The description of such a classifiers, as developed by the DELPHI Collaboration, is the purpose of chapter 4. Experimentally, the signatures which will be used to identify $Z \rightarrow b\bar{b}$ events are: large track impact parameters, presence of secondary vertices and event shape or topological properties. The main advantage of the lifetime behavior with respect to the event shape properties (connected with the large mass of heavy hadrons), other that the difference in performances, is that it has a very small sensitivity to the energy of the particles. Thus, the impact parameters and secondary vertices, being directly connected to the lifetime, have a

small sensitivity to the complex fragmentation processes. The signature of high $p_\perp$ identified leptons is not used in the analysis presented here because does not improve the results and increase the complexity in the study of systematic errors (assumptions on semileptonic models and branching ratios, lepton identification efficiency and purity, etc.). On the other hand, when one wishes to determine a branching fraction of the Z (specially for the $b\bar{b}$ channel), one is interested in having a classifier for which the efficiencies are well known. In other words, it is extremely important to be able to determine efficiencies and backgrounds of the classifier directly from data, reducing dependences on simulation models (self-calibrating tagging). The description of such a method will be the purpose of chapter 5.

Chapter 6 will be dedicated to the $\Gamma(Z \to b\bar{b})/\Gamma(Z \to hadrons)$ measurement itself and to the study of systematic errors. Finally, chapter 7 reviews other precise determinations of $\Gamma(Z \to b\bar{b})/\Gamma(Z \to hadrons)$ performed at LEP/SLC experiments, giving the preliminary DELPHI and world average results with some conclusions on the Standard Model check, as well as some future prospects on the final results.

Chapter 2

$\Gamma(Z \to b\bar{b})/\Gamma(Z \to hadrons)$, Standard Model and beyond

As outlined in chapter 1, the Standard Model requires several input parameters not theoretically predicted which are compelled to be determined from experiment. Given the electromagnetic constant α and the two vector boson masses M_W and M_Z, and neglecting fermion masses, all observables in $e^+e^- \to f\bar{f}$ reactions can be formulated in lowest order. In particular, the weak mixing angle is defined by the ratio of the $W^\pm$ and Z masses. However, beyond tree level, electroweak calculations get contributions from loop diagrams, for which the masses of all the fermions as well as the Higgs boson need to be incorporated. The loop diagrams lead to 'shifts' in the parameters of the theory, which are made finite through mass and charge renormalizations. Owing to the renormalization technique, the residual finite parts are dependent on the choice of basic parameters. This is what one usually denotes as a *renormalization scheme.* The renormalized parameters are all, in general, functions of the energy scale. The specification in terms of α, M_Z and M_W is called *on-shell scheme.* In the on-shell scheme, the $W^\pm$ and Z masses define $\sin^2\theta_W$ according to expression (1.24) with $\rho = 1$, which is valid in all orders. This definition was the most natural and practical in the 1980's when the most precise electroweak measurements were the $W^\pm$ and Z masses and the NC/CC ratio from neutrino scattering. The advent of LEP, with the high statistics of produced Z bosons together with the high precision energy calibration of the machine, has allowed a Z mass measurement to 10^{-4}. The parameter M_Z is therefore redundant with the $W^\pm$ mass itself. In practice, the parameters used in the calculations are

$$\alpha,\ M_Z,\ G_F. \tag{2.1}$$

In addition to the on-shell renormalization scheme, several other schemes have been used in the interpretation of the LEP data. A detailed discussion can be found in [29, 41]. In the *Minimal Subtraction scheme* ($\overline{MS}$), $\sin^2\theta_W$ is defined according to the expression

$$\sin^2\theta_{\overline{MS}}(M_Z^2) = \frac{\hat{e}^2}{\hat{g}^2}(M_Z^2). \tag{2.2}$$

$\hat{e}^2$ and $\hat{g}^2$ are, respectively, the QED and $SU(2)_L$ running coupling constants at the M_Z scale. This definition is probably the most appropriate for the discussion of the extrapolation of coupling constants in Grand Unified Theories to large energy scales. Finally, in the *star-scheme*, running coupling constants are defined such that the results at LEP are a measure of these couplings at a scale $q^2 = M_Z^2$. In this scheme, the effective structure of the Born-level formulae is maintained (improved Born approximation).

2.1 Radiative corrections

The α constant is measured at low momentum transfer (Thomson scattering limit) with high precision [7]. The Fermi coupling constant G_F can be experimentally determined very accurately from the muon lifetime (because of this accuracy, G_F if generally considered instead of M_W). Theoretical calculations include mass effects and electromagnetic corrections to the lowest order diagram of the muon decay (figure 2.1.a). Radiative corrections other than QED are not accounted for in expressions (1.21) and (1.22). Therefore, an additional Δr term describing the electroweak radiative corrections has to be introduced in the definition of the parameters [29]:

$$G_F = \frac{\pi\alpha}{\sqrt{2}\sin^2\theta_W M_W^2}\frac{1}{1-\Delta r}. \tag{2.3}$$

In general, the one loop corrections to the Standard Model processes can be subdivided into the following subclasses:

- QED corrections, which consist of diagrams with an extra photon added to the Born (tree level) diagrams either as a real bremsstrahlung photon or a virtual photon loop. The sum of the virtual loop graphs is ultraviolet finite but infrared divergent because the massless photon. However, the infrared divergence is canceled by adding the cross-section with real photon bremsstrahlung (after integrating over the phase space for experimentally invisible photons), which always accompanies a realistic scattering process. Since the phase space for invisible photons is a detector dependent quantity, the QED corrections can in general not be separated from the experimental device, and depend on experimental cuts applied to the final state photons and to the event selection.

- Weak corrections, which collect all other one-loop diagrams: the subset of diagrams involving corrections to the vector boson propagators (γ, $W^\pm$ and Z), which are usually known as 'oblique corrections', and the set of vertex corrections and box diagrams with two massive boson exchanges. The weak corrections are independent of experimental cuts and they include the more

subtle part of the electroweak theory beyond tree level. They are also sensitive to novel physics contributions outside the Standard Model.

The Δr correction term can be parameterized as

$$\Delta r = \Delta\alpha - \frac{\cos^2\theta_W}{\sin^2\theta_W}\Delta\rho + \Delta r_{remainder} \tag{2.4}$$

where $\Delta\alpha$ includes the QED corrections due to the running of the electromagnetic coupling constant α and $\Delta\rho$ comprises the main weak corrections. The $\Delta r_{remainder}$ term incorporates the small corrections that are not included in $\Delta\alpha$ and $\Delta\rho$. Each one of these terms is briefly discussed in the following.

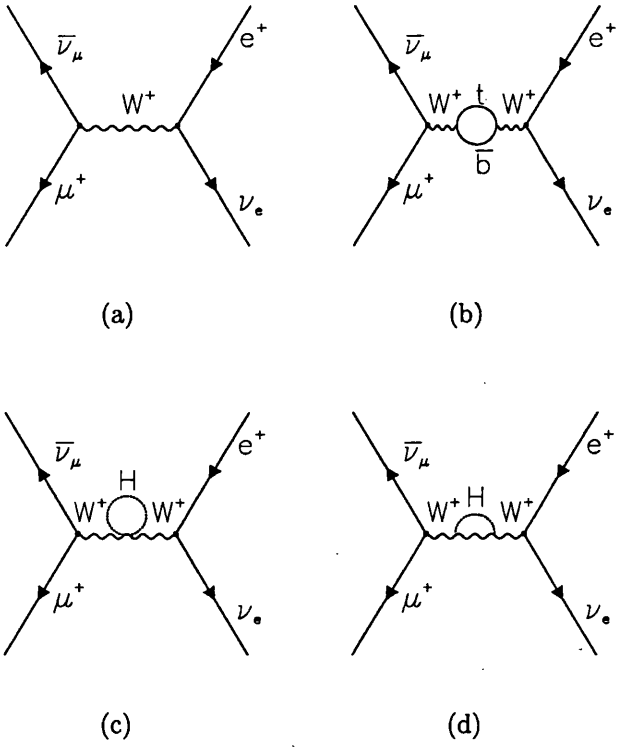

Figure 2.1: (a) Muon decay in lowest order, (b) $W^\pm$ vacuum polarization involving the top quark, and (c,d) $W^\pm$ vacuum polarization from the Higgs boson.

$\Delta\alpha$ contains the large QED corrections due to the running of the α constant from its definition at low momentum transfer to the scale of the heavy gauge bosons:

$$\alpha(M_Z^2) = \frac{\alpha}{1-\Delta\alpha}. \tag{2.5}$$

This can be pictured as the change in the electron charge e when approaching it from large distances. The determination of $\alpha(M_Z^2)$ requires the calculation of the self-energy of the photon (photon propagator correction). The contributions to $\Delta\alpha$ are for light ($m_f \ll M_Z$) fermions

$$\Delta\alpha_f = \frac{\alpha}{3\pi} Q_f^2 N_C^f \left\{ \ln \frac{M_Z^2}{m_f^2} - \frac{5}{3} \right\} \quad , \; m_f \ll M_Z \tag{2.6}$$

and for heavy fermions

$$\Delta\alpha_t = \frac{\alpha}{3\pi} \frac{4}{15} \frac{M_Z^2}{m_t^2} \to 0 \quad , \; m_t \gg M_Z. \tag{2.7}$$

The contribution of leptons can be determined because their masses are precisely measured [7]. The contribution of the top quark is small and in addition its mass has recently been measured [8, 9]. But the five other lighter quark flavours represent a problem since their masses are not unambiguously defined [1]. The total contribution of the five lighter quarks is finally evaluated using experimental cross-sections for $e^+e^- \to hadrons$ at low energies. The final result for $\alpha(M_Z^2)$ differs by about 6% from its definition at low momentum transfer, what is very large compared to the precision of the electroweak observables at LEP.

The main cause of the $\Delta\rho$ weak corrections is the $W^\pm$ vacuum polarization diagram ($W^\pm$ propagator correction) shown in figure 2.1.b. The contribution of these kind of diagrams is proportional to the difference of the squared masses of the two loop fermions. Thus, the by far most important diagram is the virtual decay of the $W^\pm$ into a top and bottom quark which gives rise to large corrections due to the mass difference in this isospin doublet. Weak isospin symmetry breaking by fermion doublets with large mass splitting modifies hence the ρ parameter. In the limit $m_b \to 0$, the leading contribution due to isospin symmetry breaking is quadratic in m_t:

$$\Delta\rho = N_C \frac{\alpha}{16\pi \sin^2\theta_W} \frac{m_t^2}{M_W^2} = N_C \frac{G_F}{\sqrt{2}} \frac{m_t^2}{8\pi^2} \tag{2.8}$$

where N_C is the number of colors. The $\Delta\rho$ term will be the main correction to the $Zb\bar{b}$ vertex.

There are other electroweak radiative corrections present in the $W^\pm$ exchange, for instance vertex corrections and box diagrams. In general, these corrections are small and do not give rise to large m_t^2 dependence terms. All these smaller corrections are included in the $\Delta r_{remainder}$ term. Among them, of particular interest are the electroweak radiative corrections from virtual exchange of a Higgs boson. Since the coupling of the Higgs is proportional to the mass of the particle, only diagrams where the Higgs appears coupling to the heavy gauge bosons $W^\pm$ and Z matter

[1] Only the b quark mass at M_Z scale has recently been measured [42].

(figures 2.1.c-d). The purely bosonic vacuum polarization gives contribution to the ρ parameter, which depends only logarithmically on the Higgs boson mass [29]:

$$\Delta r^{Higgs}_{remainder} = \frac{\alpha}{16\pi \sin^2\theta_W} \frac{11}{3} \left(\log \frac{M_H^2}{M_W^2} - \frac{5}{6} \right) + ... \tag{2.9}$$

It should be noted that $\Delta r_{remainder}$ also contains a term logarithmic in the top mass:

$$\Delta r^{top}_{remainder} = \frac{\alpha}{4\pi \sin^2\theta_W} \left(\frac{\cos^2\theta_W}{\sin^2\theta_W} - \frac{1}{3} \right) \log \frac{m_t^2}{M_W} + ... \tag{2.10}$$

As a result, the dependence of the Standard Model predictions on the unknown Higgs mass is much smaller than on the top quark mass m_t.

Inverting equation (2.3), we can define the quantity Δr=$\Delta r(\alpha, M_W, M_Z, M_H, m_t)$ as a physical observable:

$$\Delta r = 1 - \frac{\pi\alpha}{\sqrt{2}G_F} \frac{1}{M_W^2 \left(1 - \frac{M_W^2}{M_Z^2}\right)}. \tag{2.11}$$

Experimentally, it is determined by M_Z, M_W, α and G_F. Theoretically, it can be computed from M_Z, G_F and α, specifying the masses M_H, m_t and adjusting M_W such that (2.3) yields the experimental value for G_F. In practice, equation (2.3) is solved for M_W by iteration. In this way, the theoretical prediction of Δr can be estimated as a function of the Higgs and top masses.

2.2 First order corrections to $Z \to f\bar{f}$

Previously described electroweak corrections define the loop diagrams contributing to the Δr correction. Nevertheless, the tree level $e^+e^- \to f\bar{f}$ process (figure 2.2) has additional contributions. Due to the smallness of the electron mass, the lowest order Higgs exchange diagram can be neglected, as well as diagrams with Higgs. In spite of that, the propagator corrections involve all particles of the model. As in the case of the muon decay, the contribution comes from isospin symmetry breaking by fermion doublets with large mass splitting, and only the top mass term matters. A residual logarithmic dependence on M_H also appears (expression 2.10). In contrast to the propagator corrections the vertex corrections are not universal, depending in general on the fermion species. Figure 2.3 visualizes all the weak vertex corrections in the t'Hooft-Feynman gauge. For light final fermions ($f \neq b, t$), the vertex corrections contain only $W^\pm$ and Z in virtual states (figure 2.3.a-c). The contributions are small and practically independent of the parameters m_t and M_H. Vertex corrections due to heavy fermions depend on the Higgs-fermion Yukawa couplings, arising from the presence of unphysical Goldstone bosons (figure 2.3.d-g). The external fermions self-energies, which are visualized in figure 2.3.h, are also included in the vertex corrections.

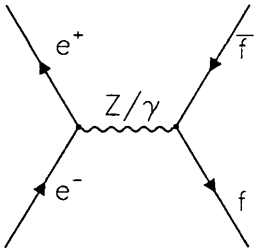

Figure 2.2: The tree level Feynman diagram for the process $e^+e^- \to f\bar{f}$.

Besides the running α coupling constant, there are other higher order electromagnetic processes contributing to Δr in $e^+e^- \to f\bar{f}$ process. These corrections are due to higher order diagrams with additional real of virtual photons and are known, as outlined above, as pure QED radiative corrections [29]. The presence of initial state bremsstrahlung has a huge impact on the cross-section because the radiated photons removes some fraction of the center-of-mass energy, $\sqrt{s}$, in such a way that the production of the Z takes place at a reduced effective energy, $\sqrt{s'} \approx \sqrt{s} - 112$ MeV, where the cross-section is smaller[2]. This effect produces an asymmetric cross-section curve below and above the Z pole (see figure 1.1). The QED radiative corrections are large compared to the experimental error achieved by the experiments, so that QED calculations are taken into account up to α^2 order (two-loop diagrams). The involved technique used to correct for these rather large effects is well under control, and can be found for instance in reference [43].

In hadronic final states, the strong coupling constant α_s enters through QCD radiative corrections. They consist of gluons exchanged between or radiated from the quarks in the final state, in a similar way as additional photons lead to QED radiative corrections (figure 2.4) [29]. The radiation of gluons alters the event shape of hadronic Z decays and the hadronic decay width and the total cross-section $e^+e^- \to hadrons$ are also modified by QCD corrections as a function of α_s. This fact can be used for precision measurements of strong coupling constant α_s [31]. The quark mixing, given by V_{CKM}, is not important for total hadronic cross-section in neutral current interactions considered here.

After the inclusion of all diagrams and the renormalization procedure, it happens that effects of all weak radiative corrections at leading order appear in terms of a fermion dependent form factor ρ_f in the Z neutral current normalization factor, which is proportional to $M_Z\sqrt{G_F}$ in the Born approximation,

$$M_Z\sqrt{G_F} \to M_Z\sqrt{G_F\rho_f} \tag{2.12}$$

and of a form factor κ_f in the mixing angle

[2]The reduction of the peak cross-section is about 74%.

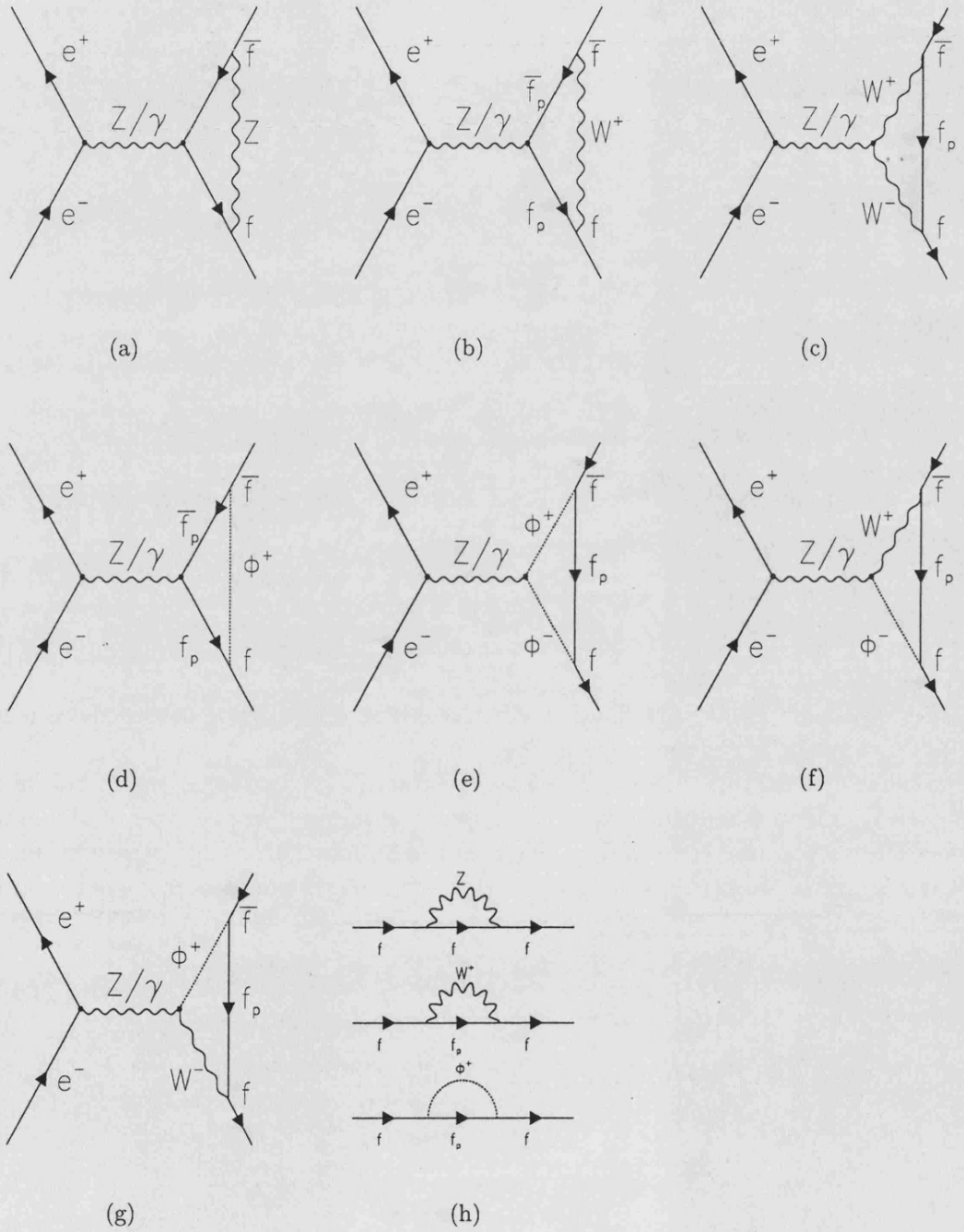

Figure 2.3: Weak vertex correction energies for the $\gamma f\bar{f}$ and $Zf\bar{f}$ vertices in the t'Hooft-Feynman gauge. The diagrams arising from Higgs-fermion Yukawa couplings are negligible for light fermions ($f \neq b, t$). f_p denotes the isospin doublet partner of f.

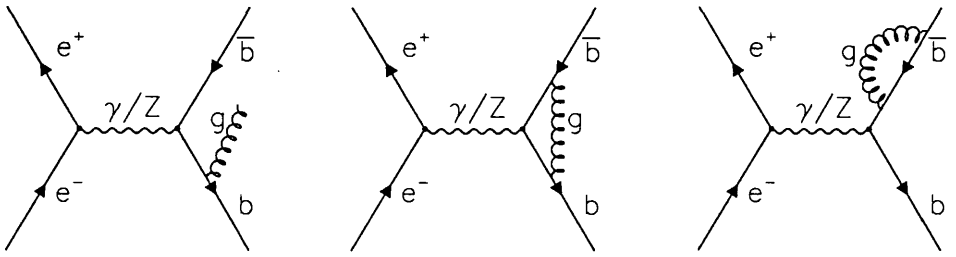

Figure 2.4: Examples of QCD radiative processes in $e^+e^- \to hadrons$.

$$\sin^2\theta_W \to \sin^2\theta_W^{f,eff} = \kappa_f \sin^2\theta_W. \tag{2.13}$$

The vector and axial-vector coupling constants can be expressed in terms of the form factors

$$\begin{aligned} a_f &\to g_a^f = \sqrt{\rho_f} I_3^f \\ v_f &\to g_v^f = \sqrt{\rho_f}(I_3^f - 2Q_f \sin^2\theta_W^{f,eff}). \end{aligned} \tag{2.14}$$

The left-handed and right-handed effective coupling constants can be defined in the same way as it was done in equation (1.20).

The form factors ρ_f and κ_f have *universal* parts (independent of the fermion species) and *non-universal* parts (dependent explicitly on the type of the external fermions). The universal parts arise from the oblique corrections, the non-universal parts from the vertex corrections and the fermion self-energies in the external lines:

$$\begin{aligned} \rho_f &= 1 + (\Delta\rho)_{univ} + (\Delta\rho)_{non-univ} + (\Delta\rho)_{remainder} \\ \kappa_f &= 1 + (\Delta\kappa)_{univ} + (\Delta\kappa)_{non-univ} + (\Delta\kappa)_{remainder}. \end{aligned} \tag{2.15}$$

In the leading terms, the universal contributions are given by

$$\begin{aligned} (\Delta\rho)_{univ} &= \Delta\rho \\ (\Delta\kappa)_{univ} &= \frac{\cos^2\theta_W}{\sin^2\theta_W}\Delta\rho \end{aligned} \tag{2.16}$$

where $\Delta\rho$ is provided by equation (2.8). Contrary to the case of Δr, here there is no logarithmic top quark mass term in the universal part of the form factors. The non-universal contributions arising from vertex corrections and contributing only to $b\bar{b}$ final states are specified by

$$(\Delta\rho)^b_{non-univ} = -\frac{4}{3}\Delta\rho - \frac{\alpha}{4\pi \sin^2\theta_W}\left(\frac{8}{3} + \frac{1}{6\cos^2\theta_W}\right)\log\frac{m_t^2}{M_W^2}$$

$$(\Delta\kappa)^b_{non-univ} = -\frac{1}{2}(\Delta\rho)^b_{non-universal}. \tag{2.17}$$

Both leading and leading-log terms of $(\Delta\rho)^b_{non-univ}$ are of the same order of magnitude, and they are connected with the large CKM bottom-top quark coupling together with the large isospin symmetry breaking of the 3rd quark family. These contributions overcompensate the top dependence of $(\Delta\rho)_{univ}$. Other possible contributions are negligible.

If we restrict to the leading order terms $\mathcal{O}(\alpha)$ in the form factors, we have a simple recipe to write down an *improved Born approximation* which contains all large corrections from light and heavy fermions. Once purely QED corrections have been accounted for, to a very good approximation, the Born level formulae of the Standard Model can be used in the analysis of the LEP data, provided that the coupling constants are replaced by the effective constants. On these results, higher order corrections (certainly much more smaller) can then be introduced. The analytical calculations of leading and higher order radiative corrections (including experimental cuts on the event and particle selections) and their effects on the physical observables is performed by programs used by the LEP experiments. In general, all these codes include electroweak radiative corrections to $\mathcal{O}(\alpha)$ in the improved Born approximation, as well as a treatment of the initial and final state bremsstrahlung. Therefore, the different realizations agree at the $\mathcal{O}(\alpha)$ and the differences may start at $\mathcal{O}(\alpha^2)$ and $\mathcal{O}(\alpha\alpha_s)$. An extensive study and comparison between some of them (BHM, LEPTOP, TOPAZ0, WOH and ZFITTER) can be found in [41] and references therein.

The definition of the effective mixing angle $\sin^2\theta_W^{f,eff}$ of equation (2.13) is closely related with the $\sin^2\theta_W$ definition in the star renormalization scheme. The only difficulty is for $Z \to b\bar{b}$ final states, where a term Δ_v^f including the non-universal vertex corrections is present:

$$\sin^2\theta_W^{f,eff} = \sin^2\theta_W^{l,eff} + \Delta_v^f. \tag{2.18}$$

For all fermions except for b quarks Δ_v^f is small and essentially independent of the top quark mass. As all asymmetry measurements essentially measure the ratio of couplings g_v^f/g_a^f, the agreed definition of the mixing angle in the star-scheme is

$$\sin^2\theta_W^{l,eff}(M_Z^2) = \frac{1}{4\mid Q_f \mid}\left(1 - \frac{g_v^f}{g_a^f}\right). \tag{2.19}$$

The advantage of choosing the effective mixing angle as a definition relating it to the measurements of the ratio of vector to axial-vector coupling of leptons is that all asymmetries at LEP can be expressed in terms of this variable, thus simplifying the comparison between them.

Finally, the $Z \to f\bar{f}$ partial decay width in the improved Born approximation is described by the following equation:

$$\Gamma(Z \to f\bar{f}) = 4N_C^f \frac{G_F M_Z^3}{24\sqrt{2}\pi} \left\{ (g_v^f)^2 R_v^f + (g_a^f)^2 R_a^f \right\} \tag{2.20}$$

where g_v^f and g_a^f are the effective electroweak coupling constants, and $N_C^f = 1$ or 3 for leptons or quarks respectively ($f = l, q$). The factors R_v^f and R_a^f describe the final state QED and QCD interactions, taking into account the fermion masses m_f [41]. The QCD contribution has been calculated up to $\mathcal{O}(\alpha_s^3)$. Expression (2.20) must be compared to the tree level equation (1.27).

2.3 Higher order universal corrections to $Z \to f\bar{f}$

The inclusion of higher than one-loop effects from top quark insertions in the gauge boson self-energies requires the modification of equations (2.3) and (2.4) according to [41]:

$$\frac{1}{1-\Delta r} = \frac{1}{(1-\Delta\alpha)\left(1 + \frac{\cos^2\theta_W}{\sin^2\theta_W}\Delta\bar{\rho}\right) - (\Delta r)_{remainder}} \tag{2.21}$$

with

$$\Delta\bar{\rho} = N_C^f \frac{G_F}{\sqrt{2}} \frac{m_t^2}{8\pi^2} \left\{ 1 + \frac{G_F}{\sqrt{2}} \frac{m_t^2}{8\pi^2} \rho^{(2)}\left(\frac{m_t^2}{M_H^2}\right) + \delta\rho_{QCD}. \right\} \tag{2.22}$$

Therefore, $\Delta\bar{\rho}$ contains the higher than one-loop corrections, while $\Delta\rho$ incorporates only first order weak loops. As always, $\Delta\alpha$ embodies the QED corrections due to the running α constant. $\rho^{(2)}(m_t^2/M_H^2)$ is the electroweak two-loop function, which can be found in [44, 45], describing the $\mathcal{O}(\alpha^2 m_t^4/M_W^4)$ corrections to $\Delta\rho$. $\delta\rho_{QCD}$ is a QCD correction up to $\mathcal{O}(\alpha\alpha_s^2 m_t^2/M_W^2)$ [46]:

$$\delta\rho_{QCD} = c_1 \frac{\alpha_s(m_t^2)}{\pi} + c_2 \frac{\alpha_s^2(m_t^2)}{\pi^2}. \tag{2.23}$$

The c_1 and c_2 coefficients describe the first and second order QCD corrections for the leading contribution to $\Delta\rho$. The complete $\mathcal{O}(\alpha\alpha_s)$ corrections to the self-energies beyond the m_t^2/M_W^2 approximation are also available [47]. Writing

$$\rho = \frac{1}{1-\Delta\bar{\rho}} \tag{2.24}$$

expression (2.21) is compatible with the following form of the M_Z-M_W interdependence:

$$G_F = \frac{\pi}{\sqrt{2}} \frac{1}{M_W^2\left(1 - \frac{M_W^2}{\rho M_Z^2}\right)} \frac{\alpha}{1-\Delta\alpha}[1 + (\Delta r)_{remainder}]. \tag{2.25}$$

It is interesting to compare this result with the expressions (1.23) and (1.24), which represent the M_Z-M_W interdependence in a more general model with tree level ρ parameter $\neq 1$. The tree level ρ in a general model enters in the same way as the ρ from a heavy top in the Minimal Standard Model. Hence, up to the small quantity $(\Delta r)_{remainder}$, they cannot be distinguished from an experimental point of view. In the minimal model, however, ρ is calculable in terms of m_t whereas in other models it is an additional free parameter. Further information on the top quark mass, like the direct m_t measurement and the $Zb\bar{b}$ vertex corrections, will allow to disentangle the different sources. Replacing $\Delta\rho$ by the two-loop quantity $\Delta\bar{\rho}$, the next order universal leading terms are correctly incorporated:

$$\begin{aligned} \rho_f &= \frac{1}{1-\Delta\bar{\rho}} + \ldots \\ \kappa_f &= 1 + \frac{\cos^2\theta_W}{\sin^2\theta_W}\Delta\bar{\rho} + \ldots \end{aligned} \tag{2.26}$$

2.4 Standard Model features of the $Zb\bar{b}$ vertex

The partial decay width $\Gamma(Z \to b\bar{b})$ contains an additional and specific m_t^2 dependence due to the vertex diagrams of figure 2.3 in t'Hooft-Feynman gauge, whose main contributions are also shown in figure 2.5 in the unitary gauge. The complete one-loop approximation, given by expressions (2.17), was calculated in references [48, 49] and it is embedded in the effective coupling constants. Following references [44, 50], the two-loop order QCD and electroweak leading terms in the $Zb\bar{b}$ vertex are implemented by an additional redefinition of universal effective couplings ρ_b and κ_b of equations (2.26):

$$\begin{aligned} \rho_b &= \rho_d(1+\tau_b)^2 \\ \kappa_b^2 &= \frac{\kappa_d^2}{1+\tau_b} \end{aligned} \tag{2.27}$$

with the quantity $\tau_b = \Delta\tau_b^{(1)} + \Delta\tau_b^{(2)} + \Delta\tau_b^{(\alpha_s)}$ calculated perturbatively, at the present level comprising:

- the complete one-loop term containing the leading $\mathcal{O}(\alpha m_t^2/M_W^2)$ term and also the logarithmically enhanced term $\mathcal{O}[\alpha\log(m_t^2/M_W^2)]$, whose contribution is comparable to the leading one (expressions 2.17):

$$\Delta\tau_b^{(1)} = -2\frac{G_F}{\sqrt{2}}\frac{m_t^2}{8\pi^2} - \frac{\alpha}{8\pi\sin^2\theta_W}\left(\frac{8}{3} + \frac{1}{6\cos^2\theta_W}\right)\log\frac{m_t^2}{M_W^2}; \tag{2.28}$$

- the electroweak two-loop contribution $\mathcal{O}(\alpha^2 m_t^4/M_W^4)$:

$$\Delta\tau_b^{(2)} = -2\left(\frac{G_F}{\sqrt{2}}\frac{m_t^2}{8\pi^2} - \frac{\alpha}{8\pi\sin^2\theta_W}\right)^2 \tau^{(2)}\left(\frac{m_t^2}{M_H^2}\right) \tag{2.29}$$

where $\tau^{(2)}$ is a two-loop function, with $\tau^{(2)} = 9 - \pi^2/3$ for $M_H \ll m_t$ [51, 45];

- the QCD corrections to the leading term, $\mathcal{O}(\alpha\alpha_s m_t^2/M_W^2)$ [50]:

$$\Delta\tau_b^{(\alpha_s)} = 2\frac{G_F}{\sqrt{2}}\frac{m_t^2}{8\pi^2}\frac{\pi}{3}\alpha_s(m_t^2). \tag{2.30}$$

QCD corrections were also calculated for the leading-log term $\mathcal{O}\left[\alpha_s\alpha\log(m_t^2/M_W^2)\right]$ [52]. However, this correction can be nearly completely absorbed into the final state QCD corrections. What remains is approximately one hundred times less than the QCD correction for the leading term of τ_b.

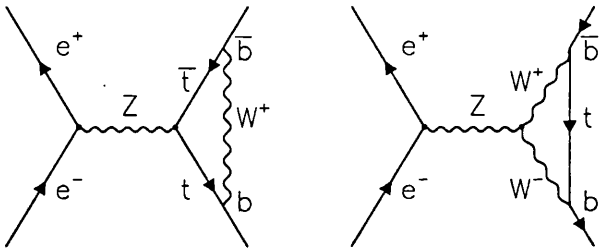

Figure 2.5: Main Minimal Standard Model contributions to the $Zb\bar{b}$ vertex in the unitary gauge.

One feature of the Standard Model calculations is of particular importance. The self-energies of the charged and neutral $SU(2)_L$ gauge bosons as well as the vertex corrections do not go to zero as $m_t \to \infty$, that is, the contribution does not decouple in m_t. The reason for this is that the couplings of the longitudinal gauge bosons (in the limit $m_b \to 0$)[3] to t_R and b_L are proportional to m_t. Hence the decoupling theorem does not apply [53].

2.5 The branching ratio $\Gamma(Z \to b\bar{b})/\Gamma(Z \to hadrons)$

From equations (2.16) and (2.17), one realizes that the vertex correction is of opposite sign and, owing to the non-negligible logarithmic term, of larger size than the oblique correction. In fact, for $m_t \sim 2M_Z$, the vertex correction is nearly twice as large as the oblique term. This suggests that isolating the full vertex component

[3] In the limit $m_b \to 0$ the Standard Model correction to the $Zb\bar{b}$ vertex does not involve the Higgs boson, only the longitudinal gauge bosons.

would be an interesting way in the Minimal Standard Model of searching for virtual top effects in measurable quantities, compared to the way of isolating the oblique effect from asymmetries.

The deviation between $\Gamma(Z \to b\bar{b})$ and the partial decay widths of light quarks can be parameterized as

$$\Gamma(Z \to b\bar{b}) = \Gamma(Z \to d\bar{d}) + N_C \frac{\sqrt{2} G_F M_Z^3}{12\pi} \Delta_b^{vertex}. \tag{2.31}$$

From equation (2.20), the deviation Δ_b^{vertex} contains:

- the b quark specific electroweak contributions to the $Zb\bar{b}$ vertex corrections, of equations (2.28) and (2.29);
- the QCD correction $\mathcal{O}(\alpha\alpha_s m_t^2/M_W^2)$ to the leading electroweak one-loop contribution, equation (2.30):

$$\Delta_b^{vertex,\alpha\alpha_s} = N_C \frac{\sqrt{2} G_F M_Z^3}{12\pi} \left(1 - \frac{2}{3}\right) \frac{G_F}{\sqrt{2}} \frac{m_t^2}{4\pi^2} \alpha_s \frac{\pi^2 - 3}{3} \tag{2.32}$$

- the b quark finite mass terms and QCD corrections through the factors R_v^f and R_a^f [4]:

$$R_v^b = 12 \frac{m_b^2}{M_Z^2} \left\{ \frac{\alpha_s}{\pi} + (6.07 - l) \frac{\alpha_s^2}{\pi^2} + (2.38 - 24.29l + 0.083l^2) \frac{\alpha_s^3}{\pi^3} \right\} \tag{2.33}$$

$$R_a^b = 6 \frac{m_b^2}{M_Z^2} \left\{ -1 + (2l - l) \frac{\alpha_s}{\pi} + \mathcal{A}\left(\frac{m_t^2}{M_Z^2}, l\right) \frac{\alpha_s^2}{\pi^2} + \frac{1}{3} \mathcal{I}\left(\frac{M_Z^2}{4m_t^2}\right) \frac{\alpha_s^2}{\pi^2} \right\} \tag{2.34}$$

where

$$\mathcal{A}\left(\frac{m_t^2}{M_Z^2}, l\right) = 17.96 + \log \frac{m_t^2}{M_Z^2} + 14.14l - 0.083l^2$$

$$l = \log(M_Z^2/m_b^2) \tag{2.35}$$

and

$$\mathcal{I}(x) = -9.25 + 1.037x + 0.0632x^2 + 6 \log(\sqrt{2}x); \tag{2.36}$$

So long as the first two contributions are embodied in the b specific coupling constants, the third one is not part of it. The top dependence of Δ_b^{vertex} is essentially contained in the first of the above contributions. Now we are interested in isolating the top mass dependence occurring in Δ_b^{vertex}. This can be done by taking appropriate branching ratios. As it is discussed in detail in [48], the normalization

[4] QED corrections cancel because at one-loop level they are proportional to $1 + \frac{3\alpha}{4\pi} Q_f^2$.

of $\Gamma(Z \to b\bar{b})$ to the total hadronic decay width $\Gamma(Z \to hadrons)$ is the most interesting one. QCD corrections and top and Higgs dependences from the oblique corrections basically cancel in this ratio. However, some of the sensitivity to the top quark mass, with respect to other ratios like $\frac{\Gamma(Z\to b\bar{b})}{\Gamma(Z\to c\bar{c})}$ or $\frac{\Gamma(Z\to b\bar{b})}{\Gamma(Z\to s\bar{s})}$, is lost because the $b\bar{b}$ channel represents an important fraction of the hadronic decays. Nevertheless, from the experimental point of view, the hadronic width is much better known. Only the $b\bar{b}$ channel is needed to be separated from the rest of the very clear hadronic decays, while for the ratios $\frac{\Gamma(Z\to b\bar{b})}{\Gamma(Z\to c\bar{c})}$ and $\frac{\Gamma(Z\to b\bar{b})}{\Gamma(Z\to s\bar{s})}$ one is confronted with the difficult experimental task of measuring the charm and strange fractions.

2.6 R_b and R_b^0

A quantity which is very related with $\Gamma(Z \to b\bar{b})/\Gamma(Z \to hadrons)$ and closer to experiment is the ratio of cross-sections $\sigma(e^+e^- \to b\bar{b})/\sigma(e^+e^- \to hadrons)$. The only difference between both quantities is the photon propagation contribution to the ratio of cross-sections, which is not present in the ratio of partial decay widths. However, at Z pole center-of-mass energy, basically only the Z propagator contributes and only residual effects of photon exchange appear. The effect can be estimated with the codes used to compute radiative corrections, for instance ZFITTER [43]. The correction to be applied to the cross-section ratio in order to obtain the decay width ratio is only $+0.0002$[5]. For up-type quarks the correction has opposite sign, -0.0002. The quantity which finally can experimentally be determined is just the cross-section ratio, known as R_b:

$$R_b = \frac{\sigma(e^+e^- \to b\bar{b})}{\sigma(e^+e^- \to hadrons)}. \tag{2.37}$$

The ratio of partial decay widths is known in the literature as R_b^0:

$$R_b^0 = \frac{\Gamma(Z \to b\bar{b})}{\Gamma(Z \to hadrons)} = R_b + 0.0002. \tag{2.38}$$

All corrections to R_b vary from a little less than 1.5% to a little less than 2.5% as the top mass varies from 150 to 200 GeV (figure 2.6). Therefore only a precise measurement, to better than 0.5%, is useful to constraint the Standard Model and thus to get information from the $Zb\bar{b}$ vertex. As claimed in [48], although this is certainly not an easy experimental task, the obvious importance of checking the Minimal Standard Model, independently of QCD corrections and top and Higgs dependences from oblique corrections, asks for a strong effort in this direction. Only

[5]This correction corresponds to a cut on the hadronic selection of $\sqrt{s'/s} > 0.1$, which is the one used in the hadronic selection of this analysis. For a cut of $\sqrt{s'/s} > 0.0$, the corresponding acceptance correction is $+0.0003$. s and s' are, respectively, the nominal and effective center-of-mass energies at which the production of the Z takes place.

an excellent self-calibrated identification of bottom quarks and a high luminosity performance for LEP [54] can provide such an accurate measurement.

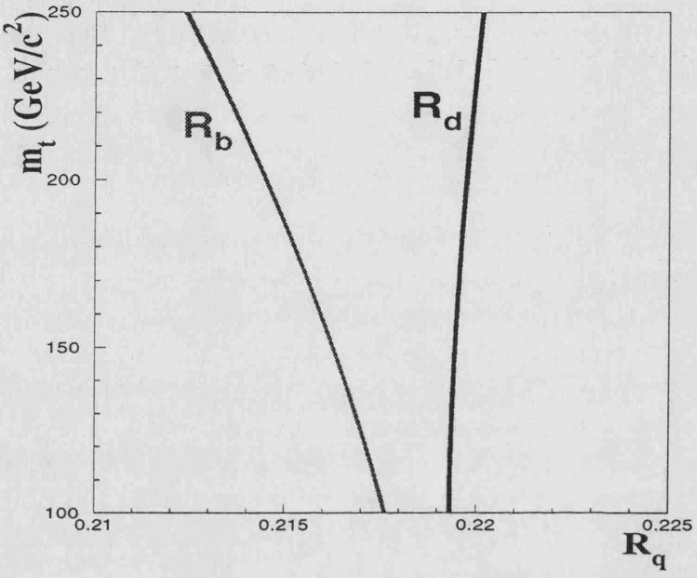

Figure 2.6: The variation of the hadronic partial decay widths R_b and R_d as a function of the top quark mass in the Minimal Standard Model. The line width includes the change in the Higgs mass from 50 GeV/c^2 to 1 TeV/c^2.

The precision of the Standard Model prediction is very good. Dominant sources of uncertainty are: a) the top quark mass error, $m_t = 175.6 \pm 5.5$ GeV/c^2, leads to ΔR_b less than 0.0003; b) the uncertainty in the b quark mass corrections, $\Delta m_b = 0.5$ GeV gives $\Delta R_b = 0.0002$; c) the QCD corrections essentially cancel in R_b, residual ones are estimated to give an error smaller than $\Delta R_b = 0.0001$. The total theoretical uncertainty is finally $\Delta R_b = 0.0003$.

2.7 Effects of physics beyond the Standard Model on the $Zb\bar{b}$ vertex

As soon as one considers extensions of the Minimal Standard Model, the differentiation between universal and non-universal correction becomes deeper. A great variety of models beyond the Standard Model is at our disposal. One can distinguish between the following classes:

- models in which new $Zb\bar{b}$ couplings appear at tree level, through Z or b quark mixing with new undiscovered particles (models with extra families, extra gauge vector bosons, Technicolor, etc.);

- models which introduce 'new physics' at the one-loop level. This type includes top quark mixing and models with new scalars and fermions, like two scalar doublet models, Supersymmetry and extra families.

The possible contamination by any kind of 'new physics' in the $Zb\bar{b}$ vertex is much more restricted and in any case different than in the self-energy propagator. Models with extra families, non-standard Higgses, extra vector bosons, might all contribute (both at tree level and radiative corrections) to a single effective quantity

$$\Delta\bar{\rho} = \Delta\bar{\rho}^{MSM} + \Delta\bar{\rho}^{new\ physics}. \tag{2.39}$$

However, such additional terms are completely independent of m_t and thus in models with 'new physics' a substantial value of $\Delta\bar{\rho}$ does not necessarily imply a correspondingly large value of m_t. Conversely, provided that m_t is known from direct observation, one might try to derive, from a measurement of $\Delta\bar{\rho}$, information on its possible novel content. The number of possible contributing models would make this task a not easy one, unless some extra information is added. In the case of non-universal corrections, non-canonical neutral Higgses and extra Z bosons would not contribute, whereas charged Higgses would contribute. Various extensions of the Minimal Standard Model retaining $\rho = 1$ at tree level, like a fourth generation, a second Higgs doublet and Supersymmetry, contribute to $\Delta\rho$ in the same way as a heavy top quark, whether large mass splittings in $SU(2)_L$ doublets are present. Also, such contributions cannot be separated from the top effect if only the boson mass relation is studied. Therefore, the $Zb\bar{b}$ vertex becomes a crucial to look indirectly for novel physics contributions.

In the following, the highlights of effects on R_b of the most extended models just beyond the MSM proposed in the literature are briefly presented. For a detailed description as well as a summary of other models, see reference [55].

2.7.1 Tree level effects

Technicolor

The $SU(2)_L \otimes U(1)_Y$ electroweak model has many arbitrary parameters associated with the elementary Higgs field, in addition to the coupling constants of the gauge symmetry. These parameters are the Yukawa couplings of the Higgs boson to fermions and the self-couplings in the Higgs potential. Technicolor models represent an attempt to avoid this arbitrariness by replacing the elementary Higgs scalar by composite ones. The composite scalars are meson bound states of a new strong interaction between new fermions. The gauge group is

$$G_{TC} \bigotimes SU(3)_C \bigotimes SU(2)_L \bigotimes U(1)_Y \tag{2.40}$$

where G_{TC} is the gauge group of the Technicolor (TC) interaction. The usual quarks and leptons are TC singlets, and the new fermions on which G_{TC} acts are called

technifermions. Their TC singlet bound states are technimesons. It is assumed that Technicolor is confined with all physical states being technicolor singlets, like QCD.

In technicolor theories, the electroweak symmetry is broken due to the vacuum expectation value of a fermion instead of a fundamental scalar particle (dynamical electroweak symmetry breaking). In the simplest theory [56], one introduces a doublet of massless technifermions

$$T_L = \begin{pmatrix} U \\ D \end{pmatrix}_L$$
$$\begin{pmatrix} U \end{pmatrix}_R \begin{pmatrix} D \end{pmatrix}_R \tag{2.41}$$

which are members of the technicolor gauge group $SU(N)_{TC}$. This doublet is embedded in an $SU(2)_L \otimes SU(2)_R$ chiral symmetry. If with the left-handed technifermions forming a weak doublet, we identify hypercharge with a symmetry generated by a linear combination of the third isospin component in $SU(2)_R$ and technifermion number (similarly to electroweak theory), then symmetry breaking will result in the electroweak gauge group. The Higgs mechanism then produces the appropriate masses for the $W^{\pm}$ and Z bosons if the coupling constant of the technicolor theory is about 246 GeV. However, this mechanism does not account for the non-zero masses of the ordinary fermions. In order to do that, one introduces additional gauge interactions, called 'extended technicolor' (ETC) interactions [57], which couple the chiral symmetries of the technifermions to those of the ordinary fermions.

The ETC interactions produce corrections to the $Zb\bar{b}$ branching ratio which do not decouple with m_t. At energies below the technicolor chiral symmetry breaking scale, this results in a change of g_L^b. Assuming that technicolor is QCD-like, we can estimate the size of this effect as

$$\frac{\delta R_b}{R_b} = -5.1\%\xi^2 \left(\frac{m_t}{175\ GeV}\right) \tag{2.42}$$

where ξ is a model-dependent coefficient equal to one in the simplest models. For a top quark mass of 175 GeV, we find $\delta R_b^{ETC} = -0.011\xi^2$. For $\xi = 1$, this results in a total $R_b \approx 0.205$, i.e., a change of -5.1% [58] with respect to the Standard Model. In ordinary technicolor theories, assuming that the gauge bosons of the ETC theory do not carry electroweak quantum numbers, the effect is about a factor two smaller and in the same direction [59]. Recent technicolor theories contains ETC bosons which carry weak charge [60]. Such a theories include also extra Z' bosons with flavour dependent couplings. In this case, it is possible for the correction to be of the same order of magnitude, but positive.

Extra gauge bosons

At tree level, the $Zb\bar{b}$ couplings can also be modified if there is mixing amongst down quarks, or the neutral colorless vector bosons. Being a tree level effect, it is relatively easy to analyze and compare different scenarios.

The first considered scenario of possible physics beyond the Standard Model concerns theories with extra weak gauge bosons. For simplicity, let us consider theories with an extra $U(1)$ gauge symmetry, resulting in an extra Z' boson which will mix with the ordinary Z [61]. The rotation to the mass basis modifies the physical $Zb\bar{b}$ couplings to become

$$g^b_{L,R} = g^b_{Z_{L,R}} c_Z^2 + g^b_{Z'_{L,R}} s_Z^2 \tag{2.43}$$

where $g^b_{Z_{L,R}}$ is the Standard Model coupling in the absence of Z mixing and $g^b_{Z'_{L,R}}$ is the b quark coupling to the new Z' boson. c_Z and s_Z are the cosine and sine of the corresponding diagonalization mixing angle. In addition, the mixing results in a change in the width of the Z going to various fermions and in potentially dangerous changes in the relationship between $\sin^2\theta_W$ to α, G_F and M_Z.

In extra gauge boson models inspired on Superstring and GUT models, the Z' is usually assumed to couple to up and down quarks in a flavour universal way. In the limit $M_{Z'} \to \infty$, the theory reduces to the Standard Model. The limits on the mixing angle of the extra gauge bosons coupling universally to the fermions are so strong that the mixing effect on the $Zb\bar{b}$ vertex cannot exceed the 1%. However, in ETC/TC models the Z' can be related to the gauge boson responsible for generating the top quark mass. In this kind of theories, such a gauge boson couples more strongly to b_L, t_L and t_R than to the other fermions. The implications of these models is that it is not possible to take $M_{Z'} \to \infty$ since the mass of the Z' is related to the size of m_t, and the contributions are again completely non-decoupling. In general, the effects of an extra family gauge boson are model dependent. In theories where the ETC gauge boson responsible for generating the top quark mass carries electroweak quantum numbers, the extra gauge boson follows in a decrease of R_b. In some ETC models, the theory does not give rise to an ETC contribution as described previously, and the extra weak singlet Z' boson can increase R_b [62, 63].

Extra families: bottom mixing

The second mixing scenario we consider are theories with extra families, where one has pure b quark mixing with no new neutral gauge bosons. Without much loose of generality, it suffices to consider the case where the Standard Model b quark mixes with only one new b' quark. Let us denote the flavour eigenstates by b_1 and b'_1 and the mass eigenstates by b and b'. Assuming the b' too heavy to be directly produced, the mixing modifies the tree level $Zb\bar{b}$ couplings to be

$$g^b_{L,R} = g^{b_1}_{L,R} c^2_{L,R} + g^{b'_1}_{L,R} s^2_{L,R} \tag{2.44}$$

where $c_{L,R}$ and $s_{L,R}$ are the cosine and sine of the two corresponding mixing angles, one for each helicity state. The differentiation between left-handed and right-handed mixing angles is due to the fact that to diagonalize the mass matrix one has to rotate

the left-handed and right-handed fields separately. Neglecting the b quark mass, m_b, the Z width to $b\bar{b}$ is proportional to

$$\Gamma_{bb} \propto (g_L^b)^2 + (g_R^b)^2 = \left(-\frac{c_L^2}{2} + \frac{\sin^2\theta_W}{3} + s_L^2 I'_{3L}\right)^2 + \left(\frac{\sin^2\theta_W}{3} + s_R^2 I'_{3R}\right)^2 \quad (2.45)$$

$I'_{3L,R}$ is the third component of the weak isospin of the b'_1 quark. Looking at equation 2.45, to increase (decrease) R_b one either needs to make g_L^b more negative (positive) and/or g_R^b more positive (negative). These requirements lead to some conditions on the third components of the b'_1 weak isospins, different for small and large mixing. In order to find all possible solutions, one simply starts out by enumerating all weak representations that b'_1 can have [64, 65].

2.7.2 Radiative effects

Two scalar doublet models

The simplest extension of the Minimal Standard Model is one in which the electroweak symmetry breaking sector involves two fundamental scalar complex doublets, $\Phi_1 = \begin{pmatrix} \phi_1^{0*} \\ -\phi_1^- \end{pmatrix}$ and $\Phi_2 = \begin{pmatrix} \phi_2^+ \\ \phi_2^0 \end{pmatrix}$, instead of one [66]. The neutral members of the doublets acquire vacuum expectation values v_1 and v_2. Diagonalization of the mass matrices requires two mixing angles (α and β), generating five physical Higgs boson states: a pair of charged scalars $H^\pm$, two neutral scalars (one the Minimal Standard Model Higgs state H and the other an additional boson h^0) and one pseudo-scalar particle A^0. The relationship between the charged scalar fields in the mass eigenstate fields is

$$H^- = -\phi_1^- \sin\beta + \phi_2^- \cos\beta = (H^+)^*. \quad (2.46)$$

In addition, a charged 'ghost' Goldstone boson appears

$$\phi^- = \phi_1^- \cos\beta + \phi_2^- \sin\beta = (\phi^+)^*. \quad (2.47)$$

In order to be correct the $W^\pm$ and Z masses, the expectation values of the two scalars (v_1, v_2) should verify that $v_1^2 + v_2^2 = v^2 = (\sqrt{2}G_F)^{-1}$. Given this relation, it is natural to define an angle β such that

$$v_1 = v\cos\beta, \qquad v_2 = v\sin\beta. \quad (2.48)$$

Hence, the relation $\tan\beta = v_2/v_1$ is verified. The angle α depends on the parameters appearing in the Higgs potential. In the most general model, these angles and the physical Higgs boson masses are all independent parameters.

Conventionally, it is expected that only one of the original scalar doublets (which we take to be Φ_1) couples to the right-handed top to avoid flavour changing neutral currents. This results in the charged current Yukawa couplings to the mass eigenstate fields (in the limit $m_b \to 0$)

$$\frac{m_t}{v \sin\beta} \bar{t}_R \left[\phi^+ \sin\beta + H^+ \cos\beta\right] b_L. \tag{2.49}$$

The Goldstone boson field ϕ^+ couples to $\bar{t}_R b_L$ with the same strength as in the Standard Model, while the coupling of the H^+ differs from this by a factor $\cot\beta$. Since the coupling of the Goldstone boson field is the same as in the MSM, the Standard Model calculations still apply. This is a general result: in the limit $m_b \to 0$, the correction to the $Zb\bar{b}$ vertex does not involve the Higgs boson, only longitudinal gauge bosons.

There are, however, additional contributions coming from the exchange of the extra charged scalars. These corrections are shown in figure 2.7. These diagrams

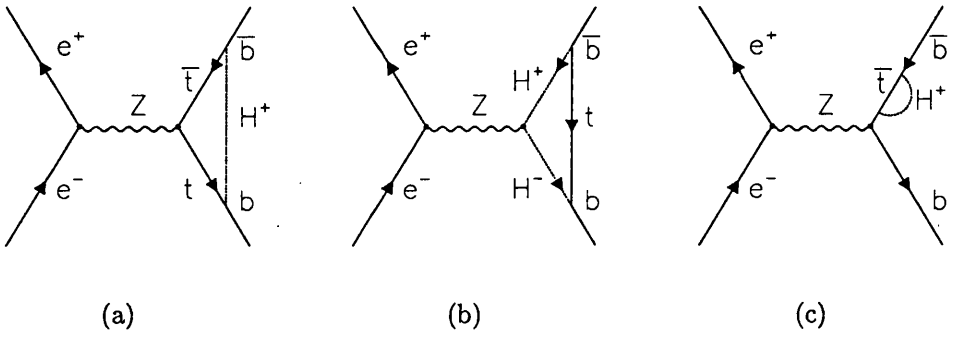

Figure 2.7: Contributions from two doublets of Higgses to the $Zb\bar{b}$ vertex.

are, in fact, a subset of the diagrams shown in figure 2.3, with the replacement $\phi^+ \to H^+$. It results in the change of the coupling by a factor $\cot^2\beta$ and in the replacement of M_W by M_{H^+}. For $\tan\beta \approx 1$ and $M_{H^+} \approx M_W$, we expect an impact of the same order of magnitude as in the top quark MSM effect [67]. Note that, as in the MSM, it tends to reduce the width $Z \to b\bar{b}$. This tendency holds except in the limit where $\tan\beta$ is very large ($\tan\beta \geq m_t/m_b$). There, the Yukawa coupling of the b quark can be comparable to that of the top quark. So the process involving intermediate b quarks and neutral scalars become important, and can result in an increase of R_b [68].

Two features are of particular interest. First, because of the Yukawa coupling of the charged scalar is proportional to m_t, $\sim \frac{m_t}{v \tan\beta}$, the effect on R_b does not decouple in m_t. Second, the effect of R_b does vanish in the limit $m_{H^+} \to \infty$. Consequently,

the extra contributions can arbitrarily be small, independent of the top quark and $W^{\pm}$ masses.

Supersymmetry

May be the most popular extension of the Standard Model is Supersymmetry (SUSY) [69]. SUSY is a kind of symmetry which interrelates fermions and bosons. In the minimal version of this scenario (MSSM), one introduces superpartners (a fermionic partner for every boson and vice versa) for all the ordinary Standard Model particles. In addition, Supersymmetry requires that the theory involves (at least) two weak-doublet superfields to perform the role of the Standard Model Higgs doublet. In a supersymmetric world, the number of fermion and boson degrees of freedom must match. At M_W scale, the $SU(2)_L$ and $U(1)_Y$ gauginos (superpartners of the gauge bosons) mix with the higgsinos (superpartners of the scalar bosons), receiving additional mass contributions from the Higgs vacuum expectation values (v_1,v_2) and from a supersymmetric higgsino mixing mass term. The mass eigenstates are called neutralinos and charginos, for the neutral and charged sectors respectively. In the MSSM, the conditions on the Higgs potential imposed by Supersymmetry reduces the number of parameters (with respect to the general two scalar doublet model) to three, which may be chosen to be M_W, v_2/v_1 and $M_{H^{\pm}}$. The other masses and the angle α are given in terms of these three parameters. A local Supersymmetry is called Supergravity (SUGRA). If Supersymmetry were exact (unbroken), the sparticle states would have the same mass as their corresponding particle states. None of the extra particles required by the model have been observed. Therefore, Supersymmetry cannot be exact. If Supersymmetry is softly broken, the radiative corrections to the Higgs masses are proportional to the masses of the supersymetric partners. Since one wishes the Higgs to 'naturally' have a mass of order 1 TeV, Supersymmetry is relevant if the masses of the superpartners are of order 1 TeV (or less).

In SUSY theories, besides the contributions of the Minimal Standard Model and the two scalar doublet models, we have contributions coming from intermediate states involving the superpartners. The relevant vertices, which include loops with charginos and stop quarks, are shown in figure 2.8. These vertices have two kinds of contributions depending on the weak eigenstate component. For gaugino component to the chargino mass eigenstate, the contribution is proportional to m_t/v, while for the higgsino component it is proportional to $m_t/v \tan\beta$. These couplings are non-decoupling in m_t, but decoupling in the superpartners (top squark and chargino) masses. In the limit where the superpartner masses are large, but the charged scalar masses are small, the total effect on R_b can approach that of the two scalar model presented above. The overall contribution could be anywhere between the two scalar and MSSM genuine contributions. For relatively light superpartner masses (of the order of M_W), the results are of the same order of magnitude as the correction in the Standard Model, but have opposite sign. The effects of radiative corrections

involving superpartners tend to increase R_b.

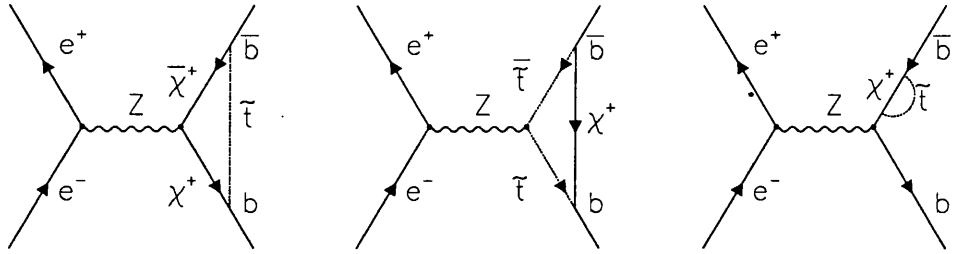

Figure 2.8: Genuine Minimal Supersymetric Standard Model contributions to the $Zb\bar{b}$ vertex, including loops with charginos and stop quarks.

Finally, we should note that there are other contributions to R_b in Supersymmetry, even some strong corrections involving the gluino. They have been calculated and are very small: the contributions are entirely decoupling and vanish in the limit where there is no $\tilde{b}_L - \tilde{b}_R$ mixing, which is the only $SU(2)_L \otimes U(1)_Y$ breaking contribution to this process [70].

For a full analysis of the R_b values inside the MSSM framework see [63, 71, 72].

Extra families: top mixing

In a very analogous way to the bottom mixing, one can list all possible models of top mixing, depending on the weak isospin quantum numbers of the t' as well as on the left-handed and right-handed mixing angles. A new aspect arises from the presence of a b'_1 in these models, since tree level b mixing could potentially dominate any loop induced by the corrections due to top mixing. According to the nature of the involved b'_1, models for top mixing fall into four categories: a) those in which the B' is SM-like, i.e. it has the same quantum numbers as the Standard Model b_1) and hence does not affect R_b; b) those in which the b'_1 is exotic (not SM-like) but in which gauge invariance imposes a constraint on the $b_1 - b'_1$ mass matrix that forbids b mixing; c) those in which the b'_1 is exotic and mixes, in which case one imposes that b mixing vanishes in order to isolate the loop effect; d) and those models that do not contain a b'_1. For a detailed discussion and complete list of models, see [64]. As for b mixing, R_b can finally increase or decrease according with the third component of the weak isospin of the t' and the left-handed and right-handed mixing angles, which depend on the assumed model.

2.8 R_b and QCD

R_b is also important in the context of QCD. All determinations of the strong coupling constant α_s suffer from one of the following weakness: non-perturbative corrections, hadronization effects, missing higher orders, imprecision of experimental data. However, $R_l = \Gamma_{had}/\Gamma_{ll}$ offers a clean, high statistics and low systematics third order determination of α_s [73]:

$$R_l = R_l^0 \left(1 + 1.06\frac{\alpha_s}{\pi} + 0.9\frac{\alpha_s^2}{\pi^2} - 15\frac{\alpha_s^3}{\pi^3} + ...\right). \tag{2.50}$$

R_l^0 is the value of R_l including electroweak corrections but without the QCD corrections. Considering all observables connected with the hadronic width of the Z, R_l, σ_{had}^0 and Γ_Z, the best Standard Model fit gives $\alpha_s = 0.123 \pm 0.003$ for a Higgs boson mass of 300 GeV [6]. The central value shifts to 0.121 for a Higgs mass of 60 GeV, and 0.125 for a Higgs boson mass of 1 TeV. The result is in good agreement with the world average $\alpha_s(M_Z^2) = 0.118 \pm 0.003$ [7]. The strong coupling constant can also be determined from the parameter R_l alone. For $M_Z = 91.1867$ GeV, and imposing $m_t = 175.6 \pm 5.5$ GeV/c^2 as a constraint, $\alpha_s = 0.126 \pm 0.004 \pm 0.002$ [6], where the second error accounts for the variation of the result when varying the Higgs mass in the range 60 GeV $\leq M_H \leq$ 1000 GeV. The sensitivity to the top quark mass is much smaller because to a cancelation between the radiative effect on the $Z \rightarrow b\bar{b}$ vertex and the effective mixing angle $\sin^2\theta_w^{eff}$ which enters in the vector couplings. This determination of α_s is largely independent of fragmentation models, jet algorithms, etc., in contrast with other methods like, for instance, the rate of 3-jet events [74].

However, if R_b is affected by 'new physics', so it is R_l, and the precise measurement of α_s from R_l becomes unreliable. According to this scenario, the relative changes of R_b and R_l due to this potential new effect are [63]:

$$\frac{\delta R_b}{R_b} = \frac{\delta\Gamma_{bb}}{\Gamma_{bb}} - R_b, \qquad \frac{\delta R_l}{R_l} = \frac{\delta\Gamma_{bb}}{\Gamma_{bb}} R_b. \tag{2.51}$$

From equations (2.50) and (2.51), the corresponding change in α_s is

$$\delta\alpha_s = +4.005\delta R_b. \tag{2.52}$$

If a reliable α_s value (which does not include R_l) were available, one could test the R_b value with R_l. From the difference between the α_s determination including and not including R_l, one can compute a value of $\delta\alpha_s$ and then estimate a possible deviation in R_b beyond the Standard Model and QCD. Such an evaluation of α_s is available from τ decays and lattice QCD calculations of the Quarkonium spectra. The discrepancy between $\alpha_s = 0.123 \pm 0.004$ obtained from hadronic width and the world average 0.118 ± 0.003 can be translated in a possible deviation of R_b. Using equation (2.52),

$$\delta\alpha_s = 0.005 \pm 0.005 \Rightarrow \delta R_b = 0.0012 \pm 0.0013. \tag{2.53}$$

With the current available data and QCD calculations, that value corresponds to the possible deviation of R_b from new effects with respect to the Standard Model predictions (compatible with QCD) [63].

One realizes therefore that the direct measurement of R_b together with the determination of R_l provides a powerful test of the following question: is there something new in the $Z \to b\bar{b}$ vertex?

2.9 Comments and remarks

From all previous discussion, it appears that after the top quark discovery, R_b is a very powerful test of the Minimal Standard Model and an exciting window for possible 'new physics'. That implies a strong effort in the direction of a precise direct determination of R_b. Nevertheless, if finally some significant deviation of R_b is found with respect to the Standard Model prediction, all theories beyond the standard electroweak theory need to be studied in great detail, to be able to determine whether they can be consistent with the experimentally measured value of R_b.

It should be stressed here that since the first precision measurements, R_b was above the Standard Model prediction, showing some evidences of novel vertex corrections [63] (see chapter 7 for more details on the time evolution of R_b). However, although the analyses from the experiments do not exploited the full available LEP 1 statistics, the preliminary results were systematically limited. For this reason, to resolve the question of whether this deviation was real or only an experimental effect, especial efforts were done by the experiments to reduce as much as possible the errors, in particular the rather large and dominant systematic errors. This thesis is part of these efforts performed during the last five years inside the DELPHI Collaboration.

Chapter 3

The experimental setup

3.1 The LEP collider

LEP is the Large Electron Positron collider [75] placed between the Jura mountains and the Geneva lake, on both sides of the border between France and Switzerland (figure 3.1), at CERN, the European Laboratory for Particle Physics. The main ring is situated in an underground tunnel with a circumference of 26.7 km, and is in operation since 1989. Two beams consisting of bunches of electrons and positrons move in opposite directions in one beam pipe, which is kept at high vacuum.

The LEP collider is used to produce e^+e^- collisions at high energy and with high luminosity. Since 1989 until 1995, LEP has been operated at the center-of-mass energy of the Z resonance, corresponding to about 91.2 GeV (LEP 1 phase). Since November 1995, the accelerating power is being increased progressively with the addition of superconducting cavities (LEP 2 phase). In the last period of the 1995 run, the energy was increased up to about 136 GeV. In the 1996 run the energy was about 161 GeV (just the threshold for the production of $W^\pm$ pairs) and also 172 GeV. For the 1997 run, more cavities were added to reach a center-of-mass energy of about 185 GeV. At the energy of the Z resonance, LEP has provided about 16M Z bosons to the experiments. Among other things, LEP has been an excellent laboratory for the study of bottom physics, which is abundantly produced through $Z \to b\bar{b}$ decays.

Before the particles are injected into the LEP ring, they are accelerated up to an energy of 20 GeV by a chain of preaccelerators (figure 3.2):

- the LIL1, a 200 MeV electron LINAC, produces positrons through the bombardment of an $e^- \to e^+$ converter;
- the LIL2, a second LINAC, accelerates the electrons and positrons (injected with a mean energy of 10 MeV) up to 600 MeV;
- the 600 MeV electrons and positrons are then injected in the electron-positron accumulator (EPA), where the beams are stoked to increase their intensity

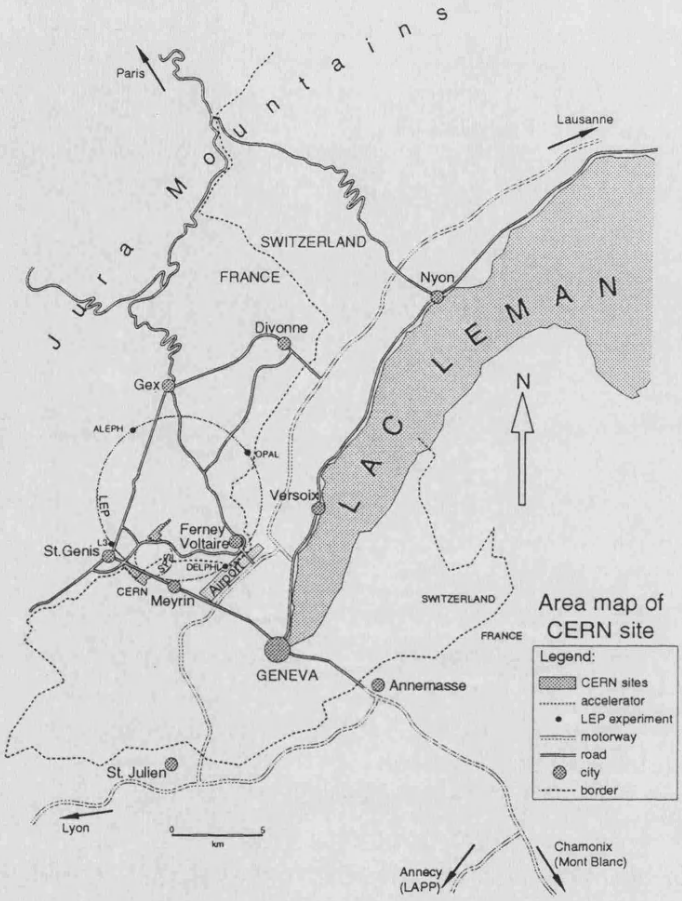

Figure 3.1: Geographical situation of LEP, the CERN's Large Electron Positron collider.

and to reduce their dimensions;

- the Proton Synchrotron (PS) and Super Proton Synchrotron (SPS) increase the energy up to 3.5 GeV and 20 GeV respectively, for the final injection into LEP.

After this injection, the beams are accelerated to an energy of about 45 GeV (LEP 1 phase) or higher (LEP 2 phase). This acceleration is done in the straight sections of the tunnel, using radio frequency cavities, while dipole magnets guide the beams through the curved sections (arcs). Quadrupole and sextupole magnets are used to focus the beams. At four points in the ring (located in four of the eight right sections of 2 km each one) the beams collide with a frequency of about 45000 Hz, which means a beam crossing each 22 μs (assuming a configuration of four bunches per beam). At these interaction points huge detectors have been built, in large underground caverns, to record the product of the collisions (figure 3.3):

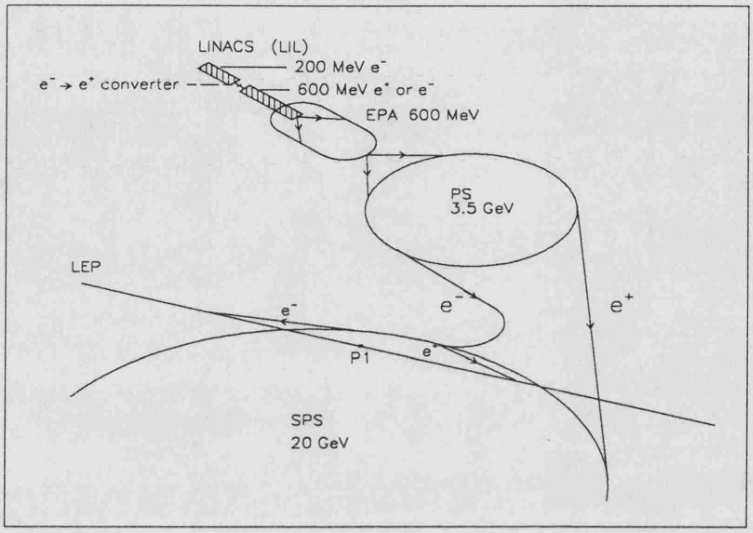

Figure 3.2: LEP injector system.

ALEPH (**A**pparatus for **LE**p **PH**ysics), DELPHI (**DE**tector with **L**epton, **P**hoton and **H**adron **I**dentification), L3 (**L**etter of intent **3**) and OPAL (**O**mni **P**urpose **A**pparatus for **L**ep).

The data used in this work were collected with the DELPHI detector from 1991 to 1995 around the Z resonance. During these years the luminosity of LEP has been continuously improved, increasing the number of events considerably. The luminosity of an e^+e^- storage ring is often written in the form

$$\mathcal{L} = \frac{N_e^2 n_b f}{4\pi\sigma_x\sigma_y} \tag{3.1}$$

where N_e is the number of particles per bunch, n_b the number of bunches per beam, f is the rotation frequency and $4\pi\sigma_x\sigma_y$ is the transverse beam area. Superconducting quadrupole magnets are installed around the experimental regions to reduce the size σ_x and σ_y of the beams and therefore to increase the luminosity ('Squeezing'). Typical values of the interaction size region are 150 μm and 10 μm in the transverse plane (x and y respectively) and 1 cm in the longitudinal direction to the beam (z). At the beginning of LEP, n_b was four and the mean luminosity was 3×10^{30} cm^{-2}s^{-1}, far beyond the nominal luminosity of the machine at the Z peak, 1.7×10^{31} cm^{-2}s^{-1}. With the nominal luminosity, the expected number of recorded Z bosons is 3 millions by experiment per year of 1500 hours of running. However, in 1991, the recorded statistics was only about 275K Z decays, and 125K events in 1990. At that time, much activity was devoted to raising that number while avoiding unwanted collisions.

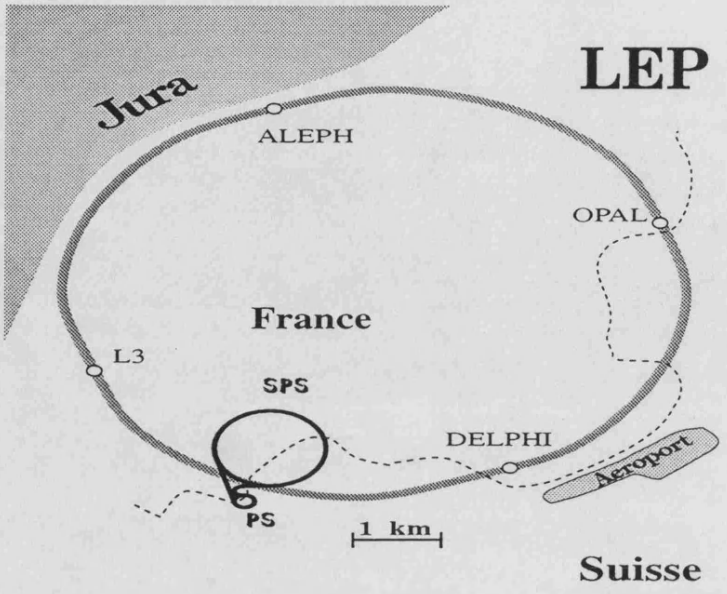

Figure 3.3: The LEP collider and the different experiments: ALEPH, DELPHI, L3 and OPAL.

As stated in chapter 1, the high luminosity is one of the fundamental points of a precise measurement of R_b.

In practice, the only way to improve the luminosity is to increase the number of bunches stored in the ring [76]. But with n_b bunches per beam, spaced equidistantly around the circumference, there are $2n_b$ points where bunches encounter each other and will collide, unless the e^+ and e^- bunches are separated. With the $n_b = 4$ configuration there are eight crossing points, four are occupied by experiments requiring therefore head-on collisions. At the other four crossing points, the beams are separated vertically by local, closed and vertical orbit bumps generated by electrostatic separators[1]. If more bunches are added, unwanted collisions will take place also in the arcs of the ring. The vertical separation in the arcs is impractical by technical reasons, including the serious limitations of physical space in the arcs. The solution found was a 'pretzel' configuration [76] with eight bunches. It started at the end of the 1993 run and was used during all the 1994 run, providing a luminosity up to 2.2×10^{31} cm^{-2}s^{-1}. In this way, the luminosity exceeded the design value. In the pretzel technique, bunches of electrons and positrons are deviated on the trajectory plane by installing horizontal electrostatic plates where there are neither experimental areas nor accelerating cavities, generating a closed orbit distortion in each arc of opposite sign for each beam so that bunches miss each other except at the interaction points (figure 3.4). In principle, the pretzel scheme can be extended to

[1] This creates a fully compensated local deformation of the closed orbit.

more bunches but it was restricted to eight. With eight bunches the beam crossing is already 11 μs and a higher colliding frequency would impose limitations on the trigger rates of the LEP detectors. With the pretzel technique, the collisions are no more head-on as for the initial n_b configuration, and take place with a given angle (see figure 3.4). During accumulation and acceleration any collision in the eight interaction points of LEP is avoided with the help of the electrostatic vertical separators. At top energy, the bunches will be brought into collision in the experimental interaction points, whereas they will be kept separated elsewhere via the combined effect of the pretzel separators and the electrostatic vertical separators. In 1994, the luminosity was 65 pb^{-1} per experiment.

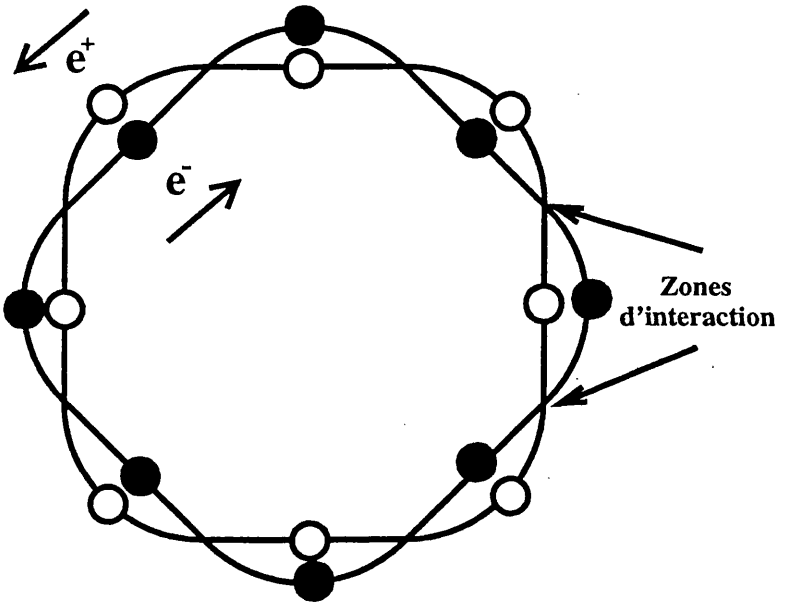

Figure 3.4: Orbits described by the electrons and positrons inside LEP with the 'pretzel' technique.

Since 1995, a bunch train solution was used to increase again luminosity, with $n_b = 4 \times n$, $n = 2, 3, 4$. In this technique, electrons and positrons are grouped into n_b trains of n bunches inside the same closed orbit. For $n = 4$, the time separation between bunches is 248 ns, what is almost negligible when compared to the time separation between trains. To reduce parasitic collisions, the bunch train method requires to duplicate the vertical electrostatic separators in the straight regions of the ring. The collision is performed between the same bunch number of electrons and positrons inside a train. Other collisions are considered parasitic collisions.

Accurate energy calibration of the machine has been a key factor for the accurate measurement of M_Z and Γ_Z. It has been done using a high precision resonant depolarization method based on the transverse polarization of the beams [77]. Such

a precise calibration has shown some spectacular correlations between the LEP energy and: a) the tidal forces, b) the level of water in the Geneva lake, and c) the timetable of the electric trains passing through the LEP region. However, for the R_b determination such an accurate calibration has no a major impact: the ratio of the $Z \to b\bar{b}$ to the total hadronic cross-sections varies very little at the center-of-mass energy around the Z pole.

3.2 The DELPHI detector

DELPHI is one of the four detectors operating at LEP collider since 1989. It was designed as a general purpose detector for e^+e^- physics with special emphasis on precise tracking and vertex determination and on powerful particle identification. The number of hadronic Z decays recorded each year at LEP 1 is summarized in table 3.1.

Table 3.1: Number of hadronic Z decays recorded by DELPHI in each year of operation at LEP 1, in a running period normally lasting from May to November.

Year	1989	1990	1991	1992	1993	1994	1995	Total
	13K	125K	275K	751K	755K	1484K	750K	4153K

In the standard DELPHI coordinate system, the z axis is along the electron LEP beam direction, the x axis points towards the center of LEP, and the y axis points upwards. The polar angle to the z axis is called θ and the azimuthal angle around the z axis is called ϕ; the radial coordinate is $R = \sqrt{x^2 + y^2}$.

DELPHI is installed in a cavern 100 m underground. The ensemble consists of a cylindrical section covering the 'barrel' region of θ (typically from 40° to 140°) and two endcaps covering the 'forward' regions. The endcaps can be moved to allow access to the subdetectors. Figure 3.5 schematically shows the layout of the barrel and one endcap. A description in detail of all the components (subdetectors) of DELPHI and its performance have been done in [78]. In the following we shall give only a summary of the detector characteristics from 1989 to the end of 1995, corresponding to the experimental setup of the data taking during the LEP 1 phase. Moreover, only the details most relevant to the analysis reported here will be described, in particular, detectors and algorithms concerning the tracking.

The superconducting solenoid (7.4 m long, 5.2 m inner diameter) provides a highly uniform magnetic field of 1.23 T (5000 A) parallel to the z axis through the central tracking volume, namely: the microvertex detector (VD), the Inner Detector (ID), the Time Projection Chamber (TPC) and the Outer Detector (OD) and also the forward tracking chambers (Forward Chambers A and B). The superconducting cable consists of 17 wires made of 300 Nb-Ti filaments (25 μm Ø) embedded in

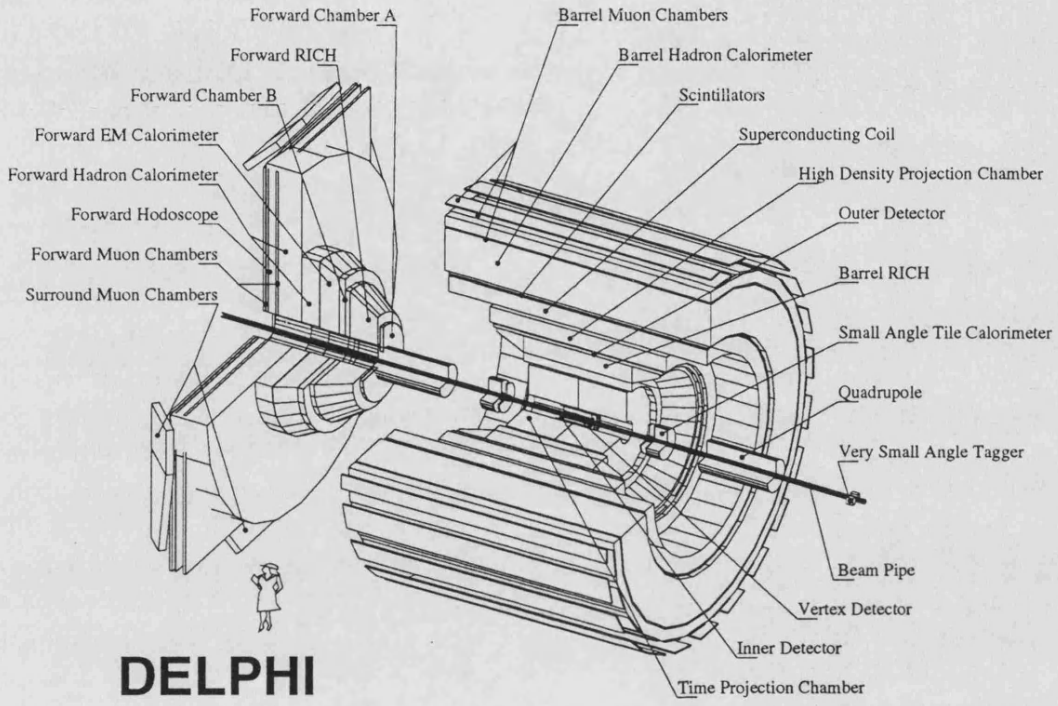

Figure 3.5: Schematic layout of DELPHI.

copper and cooled by liquid helium at 4.5 K. There is a second short end layer of cable (35 cm) to improve field homogeneity at the ends. The goal of the magnetic field is twofold: to curve the trajectory of charged particles, allowing the momentum track measurement, and to insure the correct performance of the TPC.

3.2.1 Tracking devices

The tracking detectors are the responsible to reconstruct the trajectories of the particles, allowing the evaluation of their momenta and impact parameters. They are close to the interaction region to avoid the effects of the material, being the most relevant subdetectors for the R_b analysis reported here. We shall describe the detectors and their performances in an ordered way, starting from the innermost to the outermost.

Microvertex detector (VD)

The purpose of the VD in DELPHI is the study of heavy flavour physics containing short-lived particles (lifetimes in the order 10^{-12} to 10^{-13} s), by means of improving the determination of both primary and secondary vertices. By far it is the detector with a major impact on the analysis presented here. Its intrinsic resolution has to be as high as possible. This is made possible with microstrip silicon detectors [79]. In addition, the first detector layer has to be as close as possible to the interaction point.

For the startup in 1989, the VD was installed with two silicon strip layers in the barrel region, at radii 9 cm (Inner layer) and 11 cm (Outer layer) around the beam pipe. Each layer was formed by 24 modules (23.6 cm long) containing four detector plates each, with about 10° overlap in ϕ. The modularity was chosen to avoid the intrinsic resolution degradation by inclined tracks. The overlap region was designed to improve the relative alignment of neighboring modules. In April 1991 the 8 cm radius aluminium LEP beam pipe was replaced by a 5.6 cm radius berilium one, and the VD was upgraded [80] by adding a third (Closer) layer of silicon strips. The strips are parallel to the beam direction and the readout pitch is 50 μm in the $R\phi$ plane perpendicular to the beam direction. The polar angle coverage for charged particles hitting all three layers of the detector is 44° to 143°. The average association efficiency of VD points to reconstructed tracks by other DELPHI tracking chambers in multihadronic events is about 96%.

In April 1994, the VD was further upgraded [81] by adding z readout to the Outer and Closer layers, provided by diodes on the n side of the detectors orthogonally oriented to those on the p side. On the n side, the signals are carried to the ends of the modules by an extra layer metal strips parallel to those on the p side. With this arrangement there is negligible extra material in the sensitive region of the detector, and both coordinates may be read out at the end of the detector. At the same time, the polar angle coverage of the Closer layer was extended to $25° \leq \theta \leq 155°$. For the z coordinate in the Closer layer, the readout pitch of 49.5 μm used near $\theta = 90°$ is increased to 99 and 150 μm for larger $\mid z \mid$ values, in order to optimize the number of electronic channels. Similarly, the pitch values for the Outer layer are 42 and 84 μm. The geometrical layout of this double sided detector is shown in figure 3.6. The large overlap of detectors in the same layer can be seen in the transverse view. These overlaps amount to about 10% of the sensitive region in the Closer and Outer layers and about 20% in the Inner layer. A particle traversing the detector can therefore register up to 6 (4) hits in $R\phi$ (Rz). This design results in a high detector efficiency, as well as it provides extra constraints for the software alignment of the detector [82].

Intrinsic resolution for a single hit of the detector can be estimated from the residual distributions of hits from the fit in the overlap regions. Such a distributions include contributions from remaining alignment uncertainties. They contain a central Gaussian together with non-Gaussian tails which are due to different cluster

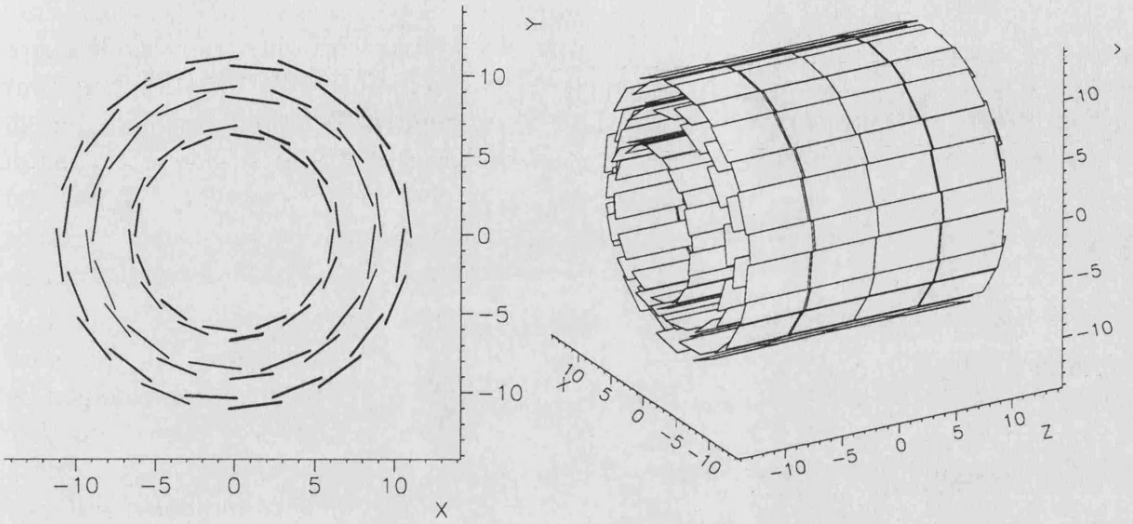

(a) Transverse $R\phi$ view. (b) Three dimensional view.

Figure 3.6: Schematic cross-sections of the DELPHI double sided vertex detector in the 1994-1995 configuration.

characteristics (size, pulse height, noise) and incidence angles. For all layers, the microstrip detectors provide hits in the $R\phi$ plane with a measured intrinsic resolution of about 8 μm. The single hit resolution in z is a function of the incidence angle of the track, reaching a value of 9 μm for tracks perpendicular to the modules.

The alignment of the VD uses particle tracks from Z decays, taking as starting points the results of a mechanical survey and a very precise optical measurement of the individual modules, which leads a precision of 25 μm. The rest of the alignment uses hadron tracks passing through the overlap regions, isolated tracks with 3 hits contained within a sector, and tracks from $Z \rightarrow \mu^+\mu^-$ (dimuon events). Tracks in the overlaps are used to refine the $R\phi$ rotations and translations of the modules in a layer; tracks in dimuon events and 3-hit tracks constrain the relative positions of modules in different layers. A similar procedure is used for the z alignment. With that procedure, only the momenta of the hadrons are taken from measurements of other detectors. A full description of the alignment procedure may be found in [80, 81, 82].

Inner detector (ID)

Up to the 1994 run, the ID consists of two concentric parts: a drift jet-chamber to measure accurately the trajectory of outgoing particles in the $R\phi$ plane and five layers of MWPC which measure also the z coordinate. The inner jet-chamber has

24 azimuthal sectors, each providing up to 24 $R\phi$ points per track between radii 12 and 23 cm. For polar angles in the range $23° \leq \theta \leq 157°$, a track crosses a volume of the detector sensed by a minimum of 10 wires. Each MWPC has sense wires spaced by about 8 mm (192 wires per layer) and with circular cathode strips giving Rz information. The $R\phi$ measurements are mainly used for triggering, but also provide the possibility of resolving the left/right drift ambiguities inherent in the jet-chamber. The polar angle coverage is $30° \leq \theta \leq 150°$. The precisions of the parameters for the local track element in dimuon events are $\sigma(R\phi)$=50 μm and $\sigma(\phi)$=1.5 mrad. The two track resolution is about 1 mm. The z precision from a single MWPC layer for an isolated track varies from 0.5 to 1 mm, depending on θ.

At the beginning of 1995, a new longer ID has been operational. The inner drift chamber has exactly the same wire configuration as the previous one, but the polar angle acceptance is now $15° \leq \theta \leq 165°$. The old five MWPC have been changed by five cylindrical layers of straw tube detectors (192 tubes per layer) measuring $R\phi$. The polar angle acceptance is now $15° \leq \theta \leq 165°$, but there is no longer any z measurement. The precisions of the local track parameters are now $\sigma(R\phi)$=40 μm and $\sigma(\phi)$=0.89 mrad.

Time projection chamber (TPC)

The TPC is the central tracking detector in DELPHI, and it has therefore the main responsibility (together with the VD) for track reconstruction and for measurement of particle momenta. An schematic layout of the TPC is shown in figure 3.7. Both end-plates of the TPC are divided into 6 azimuthal sectors, each with 192 sense wires and 16 circular pad rows with constant spacing (with a total of 1680 pads per sector). The size of the TPC is limited (R=120 cm, $L = 2 \times 150$ cm) by the inclusion of the RICH detector, but other track chambers were added (OD, FCA and FCB) to improve momentum resolution. The detector provides up to 16 space points per particle trajectory at radii of 40 to 110 cm between polar angles of $39° \leq \theta \leq 141°$. At least three pad rows are crossed down to polar angles of $20° \leq \theta \leq 160°$.

The single point resolution is determined by extrapolating tracks from dimuon events from the VD to the TPC pad rows. The width of the distributions of distances between reconstructed and extrapolated points is a direct estimate of the hit resolution. Since 1994, each muon track is separately extrapolated from the two Rz hits in the VD, while for previous years the z information of the cathode strips in the MWPC layer of the ID was used. The quoted values are 250 μm in the $R\phi$ plane and 880 μm in the Rz plane. The two point resolution is about 1 cm in both directions.

The magnetic field of DELPHI (which is parallel to the electric field in the TPC) serves to confine the drifting electrons along the field direction, reducing the diffusion in the perpendicular direction to a factor 5-10.

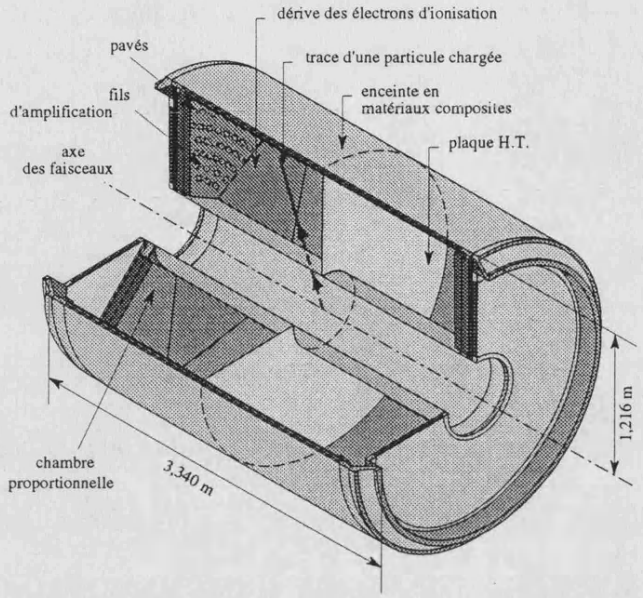

Figure 3.7: Schematic layout of the TPC of DELPHI.

Outer detector (OD)

The OD consists of five layers of drifts tubes, operated in the limited streamer mode, located between radii of 197 and 206 cm. Successive layers are staggered and adjacent modules of the 24 azimuthal sectors overlap, giving full azimuthal coverage. Three layers read the z coordinate by timing the signals at the ends of the anode wires. The active length of the detector corresponds to polar angles of $42° \leq \theta \leq 138°$. The single point precision is $\sigma(R\phi)$=110 μm, independent of the drift distance. The OD is complementary to the TPC because in front of each dead zone of the TPC an OD module is placed, improving the geometrical acceptance.

Forward Chambers (FCA and FCB)

The FCA is placed at both ends of the TPC at a distance from the interaction point of about $\pm$160 cm in z. On each side there are three chambers, each one with two staggered layers and split into half discs with an outer radius of 103 cm, operated in the limited streamer mode. The chambers are rotated with respect to each other by 120°, thus providing 2×3 coordinates. The chambers cover polar angles of $11° \leq \theta \leq 32°$ and $148° \leq \theta \leq 169°$. The reconstructed track elements have precisions of $\sigma(x)$=290 μm, $\sigma(y)$=240 μm, $\sigma(\theta)$=8.5 mrad, and $\sigma(\phi)$ averaged over θ is 24 mrad.

The FCB is a drift chamber also segmented in two half discs (of dodecagonal shape) in each arm, with an inner radius of 48 cm and outer radius of 211 cm,

and is placed behind the Forward RICH, at an average distance of $z = \pm 275$ cm from the interaction point. It consists of 12 wire planes separated by 1.1 cm and rotated in pairs by 120° with respect to each other. The chamber covers polar angles of $11° \leq \theta \leq 36°$ and $144° \leq \theta \leq 169°$. The precision achieved on the parameters of the reconstructed track elements are $\sigma(x, y)$=150 μm, $\sigma(\theta)$=3.5 mrad and $\sigma(\phi) = 4.0/\sin\theta$ mrad.

3.2.2 Other detectors

Muon chambers

The muon detection system consists of chambers in the barrel (MUB) and in the forward region (MUF). In the barrel there are three layers: the inner one inside an iron surface (after the hadron calorimeter), the outer one on the one surface of the iron and one peripheral. Each detector layer is constructed of two staggered planes of flat drift chambers operated in proportional mode with a central anode. A delay line determines the coordinate along the anode wire. In the forward region there are two planes of chambers, one behind of the hadron calorimeter and the other behind a layer of iron and the forward hodoscope (HOF). The chambers are operated in streamer limited mode. In 1994 a layer of Sourronding Muon Chambers (SMC) was installed outside the endcaps to fill the gap between the barrel and forward regions. The recent addition of the SMC has improved the hermeticity of the DELPHI muon identification.

Calorimeters

The energy reconstruction carried out by the outgoing charged particles and the detection of neutral particles is done in DELPHI by the electromagnetic and hadron calorimeters. The electromagnetic calorimetry system of DELPHI is composed of a barrel calorimeter, the High Projection Chamber (HPC), a Forward Electromagnetic Calorimeter (FEMC) and two very forward calorimeters, the Small angle TIle Calorimeter (STIC) -which replaced the Small Angle Tagger (SAT) in April 1994- and the Very Small Angle Tagger (VSAT).

The aim of the HPC is to measure the three-dimensional charge distribution induced by electromagnetic showers and by hadrons with very high granularity in all coordinates, with an acceptable number of readout channels. It consists of azimuthal modules arranged in rings inside the magnetic field. Each module is a small TPC with layers of high density material (lead) in the gas volume. The FEMC consists of two discs of Cherenkov lead glass counters. The counters are blocks of truncated pyramidal shape arranged in an appropiate way to provide a quasi-pointing geometry towards the interaction region, allowing the reconstruction of the electromagnetic showers. The SAT was optimized for luminosity measurements counting Bhabha events and consists of a track detector and a calorimeter. The calorimeter consists of lead layers and plastic scintillation fibres parallel to the beam. The STIC

is a sampling lead-scintillator calorimeter formed by two cylindrical detectors placed on either side of the DELPHI interaction point having a geometry quasi-projective. The VSAT is made of four rectangular calorimeter modules on either side of the DELPHI interaction point. The calorimeter modules are assembled of tungsten absorbers interspaced with three silicon detectors planes for energy measurement. The VSAT detector is designed also to measure the background of beam gas produced off-momentum electrons and of synchrotron radiated X rays. These measurements provide checks of orbit calculations for the LEP machine and a measure of the background to the Bhabha process. Before 1994, the absolute luminosity was measured using the SAT detector and the VSAT was used to measure the relative luminosities at different energies. Since 1994, after installation of the STIC, the luminosity measurement is completely based on STIC measurements. The STIC (SAT) and VSAT are also essential for detecting e^+ and e^- from $\gamma\gamma$ processes.

The HCAL is installed in the return yoke of the DELPHI solenoid. Its geometry is projective: the calorimeter is arranged in small towers pointing to the interaction region in order to be optimized for neutral detection and to give good energy flow estimate. The HCAL has the same modularity in ϕ as the HPC and its sensitive part is based on limited streamer tubes.

Scintillators

The time of flight counter in the barrel (TOF) consists of a single layer of scintillator counters and occupies the small region between the external surface of the magnet and the hadron calorimeter. It serves as fast trigger for beam events and cosmics and may be used to veto cosmic muons during beam crossings. The TOF counters are also used to provide information for those particles (mainly photons) that go in the dead regions of the inner-most detector layers of DELPHI. The forward hodoscope (HOF) is also used in the muon detection and trigger for beam events and cosmics, in particular for trigger on beam related halo muons which are very useful for alignment. It consists of a single layer of plastic scintillators placed just behind the end-cap hadron calorimeter. Recently, in order to achieve complete hermeticity for high energy photon detection, important at LEP 2, additional lead-scintillators have been installed to cover the gap between the HPC and the FEMC at $\theta \approx 40°$ and 90° and also ϕ cracks ('ϕ taggers') between the HPC modules not covered for this purpose by the Time of Flight (TOF) scintillators.

RICH detectors

The Ring Imaging CHerenkov (RICH) detectors of DELPHI provide charged particle identification in both the barrel (BRICH) and forward (FRICH) regions. They contain two radiators of different refractive indices. The liquid radiator is used for particle identification in the momentum range from 0.7 to 8 GeV/c. The gas radiator is used for particles from 2.5 GeV/c to 25 GeV/c. With both radiators the identification of charged particles over most of the momentum range at LEP 1

is practically assured. Though the main structures were installed before startup in 1989, the radiators, fluid systems, chambers and electronics were installed and brought into operation in stages during 1990 to 1993. The BRICH became fully operational during 1992 and the FRICH at the beginning of 1994. The positions of the mirrors and drift-tubes of the RICH counters are determined after alignment of the full tracking system (section 3.2.6), using extrapolated tracks from the dimuon sample.

3.2.3 Particle identification

The combination of the DELPHI subdetectors allows a good particle identification.

Identification of electrons in the barrel of DELPHI is performed using the specific ionization energy loss per unit length (dE/dx) in the TPC and the energy deposition in the HPC. The identification of electrons is complicated because of electromagnetic interactions in front of the calorimeters. The iron of the hadron calorimeter provides a filter which gives a first level of separation between muons and hadrons. Most hadrons are stopped by this material, whereas all muons of momenta above 2 GeV/c are expected to penetrate into the muon chambers. Muon identification is achieved by comparing the extrapolations of the reconstructed tracks with the hits in the Barrel (MUB), the Forward (MUF) muon drift chambers and the Sourronding Muon Chambers (SMC).

Photons produced before the electromagnetic calorimeters (about 40%) are identified using showers in the HPC and FEMC which cannot be associated to tracks (neutral particles). Photons converted in front of the TPC (about 7%) creating pairs e^+e^- are reconstructed with good efficiency using tracking techniques. π^0's are reconstructed either by pairing photons and by calculating the invariant $\gamma\gamma$ mass or by analyzing the internal structure of energy depositions in the calorimeters, taking advantage of the very fine granularity of the HPC.

The identification of charged particles in DELPHI relies on the dE/dx measurement in the TPC, on the RICH detectors, and on the electron and muon identification. Particle identification in the RICH detectors is based on the fact that charged particles traversing a dielectric medium faster than the speed of light in that medium produce a cone of Cherenkov light. The emission angle θ_c depends on the mass m and momentum p via the expression $\cos\theta_c = 1/n \times \sqrt{1 + m^2/p^2}$. The number of photons emitted per unit length is proportional to $\sin^2\theta$. Both informations together with the momentum of the reconstructed track are the information used for identifying the particle mass.

3.2.4 The trigger and data acquisition systems

As said in section 3.1, the time between beam crossings at LEP 1 is 11 μs (22 μs) when operating at eight (four) bunches. But only a small fraction $\sim 10^{-5}$ of the beam crossings produces an e^+e^- annihilation. The goal of the DELPHI trigger

system [83] is to select these events with high efficiency through four successive trigger levels (T1, T2, T3 and T4). T1 and T2 operate synchronously with the Beam Cross Over signal (BCO) provided by LEP, selecting on-line candidate to Z decays. These triggers use a combination of individual fast subdetector signals, providing sufficient redundancy and geometrical overlap to achieve an efficiency close to one and making possible to determine both the trigger efficiency and its maximal error with good precision. The T1 and T2 trigger decisions are taken 3.5 μs and 39 μs after the BCO respectively, and they have been active since the LEP startup. T3 and T4 are software filters performed asynchronously with respect the BCO, and their aims are to reject background. T3 has a similar logic as T2 but using more detailed information from detectors. T4 is a tailored version of the DELPHI reconstruction program DELANA (see section 3.2.5) rejecting basically events with no track pointing towards the interaction region and no energy release in the calorimeters. T3 was implemented in 1992 and T4 in 1994. After the T3 and T4 triggers, the data acquisition system (DAS) [78] reads out asyncronically the digitized data from the detectors and records it on data tapes with a frequency of about 2 Hz. The DELPHI DAS is based on standard Fastbus connected over an Ethernet network to a VAX cluster. An on-line monitoring via event reconstruction (DelPit) is also available for control of data quality.

In addition to the trigger and data acquisition systems, the slow control system monitors and controls the operation of the detector (voltages, fastbus power supplies, etc.) reporting and acting on changes in the detector or its environment (temperatures, pressures, etc.), recording such changes and maintaining the safety of the equipment.

3.2.5 Reconstruction packages

The resulting raw data tapes recorded by the DAS system are processed off-line by the DELphi ANAlysis package DELANA [84], based on the Track ANAlysis and GRAphics package TANAGRA [85] which provides a well defined data structure for storing track and vertex information in a format independent of the subdetectors. DELANA, running on the 'DELPHI farm', performs local pattern recognition for every subdetector to reconstruct track elements (for instance single two-dimensional points in $R\phi$ or Rz for the VD and fully reconstructed track segments for the TPC) and energy clusters from the calorimeters. A database (CARGO) provides calibration and alignment constants for each subdetector.

The individual track elements and energy clusters are then linked to form tracks [86]. The main search algorithm in the barrel region (which is the one used in the analysis presented in this thesis) starts with TPC segment tracks and extrapolates them inwards and outwards to form candidates of tracks with the ID and OD elements. Algorithms combining ID and VD or VD and TPC tracks elements are also used. After this track search, all strings found are passed through the full track fitting algorithm [87] and any remaining ambiguities are resolved. Tracks are then

extrapolated through the detector and VD hits are associated to the tracks using a χ^2 method. Tracks are finally refitted including associated hits from all tracking detectors. A new algorithm has been recently implemented with the main difference that it starts the track search using both, TPC and VD hits. This algorithm enhances greatly the tracking efficiency and resolution. Calorimetric clusters are then associated to tracks, as well as hits in the muon chambers to provide the muon identification.

After reconstruction, a new event filter is used to select interesting events. The resulting data are written to Data Summary Tapes (DST) which contain detailed information of the event. At this stage, the average size of an hadronic event is 60 kbytes. To improve the quality of the real data, a new processing of DELANA is done, which uses the results of the first calibration and alignment. This reprocessing ('DSTFIX') can be done on the detailed DST without reprocessing of the raw data. In addition, this rerun on DST instead on raw data allows to improve the precision of the simulated data. The DST size is latter reduced by a factor three or ten in size by summarizing the information of individual detector components ('short' DST or 'mini' DST respectively). This reduction is sufficient for most of physics analysis. In the analysis presented here the 'Short' DST was used.

The physics analysis presented here is performed completely at the DELPHI computer facilities on SHIFT at CERN (Geneva, Switzerland), at the Lyon's Computer Center (France) and at IFIC (Valencia, Spain). They are powerful clusters of HP and AIX workstations. Running on both clusters, the events used in this work are processed using the PHDST [88] and SKELANA [89] package environments. Event information is extracted, processed according to the physics requirements of the analysis and finally compacted in *ntuples* [90]. Ntuples can be manipulated interactively by the Physics Analysis Workstation package PAW [91] and in batch by Fortran codes using the HBOOK environment [90]. All these steps are described in chapter 4. The information contained in the ntuples is finally converted in direct physical observables which are the input of a global fit allowing the direct determination of R_b (chapters 5 and 6).

3.2.6 Global tracking quality and global alignment

The momentum precision of the global tracking system in the barrel region is illustrated in figure figure 3.8.a, which shows the measured inverse momenta (which has a good Gaussian behavior) in dimuon events with acollinearity below 0.15° (45.6 GeV/c muons) and which tracks contain information from all the barrel detectors (VD, ID, TPC, OD). The distribution is fitted to the sum of two Gaussians. A width of $\sigma(1/p) = 0.57 \times 10^{-3}$ $(\mathrm{GeV/c})^{-1}$ is obtained for the narrower Gaussian. The tails of the distribution require the wider Gaussian with a width $\sigma(1/p) = 1.04 \times 10^{-3}$ $(\mathrm{GeV/c})^{-1}$ and with a peak value of about 8% with respect to the total peak. A similar plot for the forward region computed from tracks containing hits in at least the Closer layer of the VD and in FCB is shown in figure

3.8.b, where the measured precision is $\sigma(1/p) = 1.31 \times 10^{-3}$ $(\mathrm{GeV/c})^{-1}$.

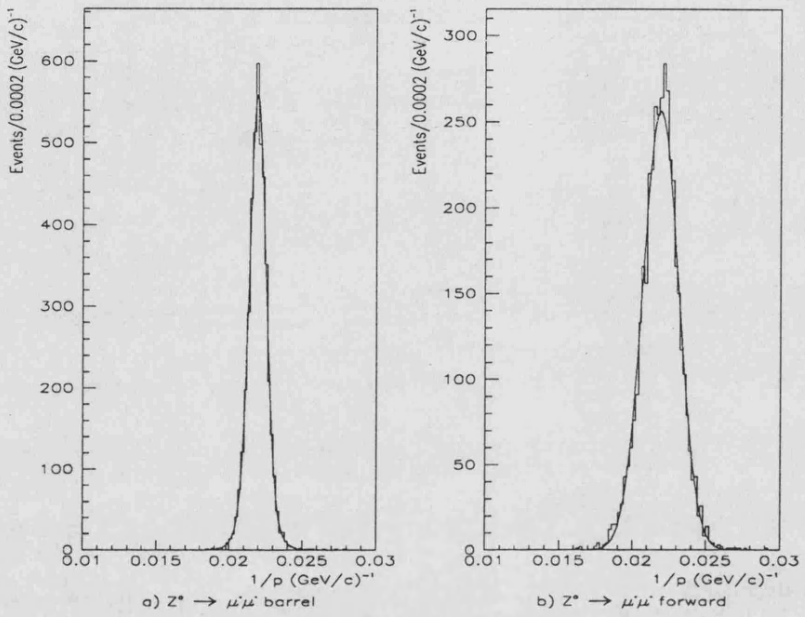

Figure 3.8: Inverse momentum distributions for collinear dimuon events: (a) tracks containing hits from VD, ID, TPC and OD; (b) tracks containing hits from VD and FCB at least.

The precisions obtained on the track parameters at other momenta can be estimated by comparing the simulated and reconstructed parameters in a sample of generated Z hadronic decays. The precision remains essentially constant over the barrel region for a given momentum but deteriorates in the forward regions of the detector [78].

The global alignment of the tracking chambers is performed mainly using dimuon events. For the barrel detectors, the OD is chosen as starting point since the wire positions are known to a precision of 30 μm from optical and mechanical surveys and the detector has a good time stability and a long lever arm with respect to the interaction point. The position of the VD with respect to the OD is then determined assuming the two muons from a single track. Then the ID and TPC are aligned using reference tracks formed by the VD and OD, imposing a fixed momentum but relaxing the collinearity constraint. FCA and FCB are aligned from the extrapolation of muon reconstructed tracks in the TPC to the forward region.

Figure 3.9 shows a typical hadronic Z decay reconstruction in DELPHI using the tracking chambers. The plot shows the VD, ID and TPC detectors in the $R\phi$ and yz planes in four different views of the same event.

plane showing the full event reconstruction in the DELPHI barrel. and dashed lines the corresponding extrapolations

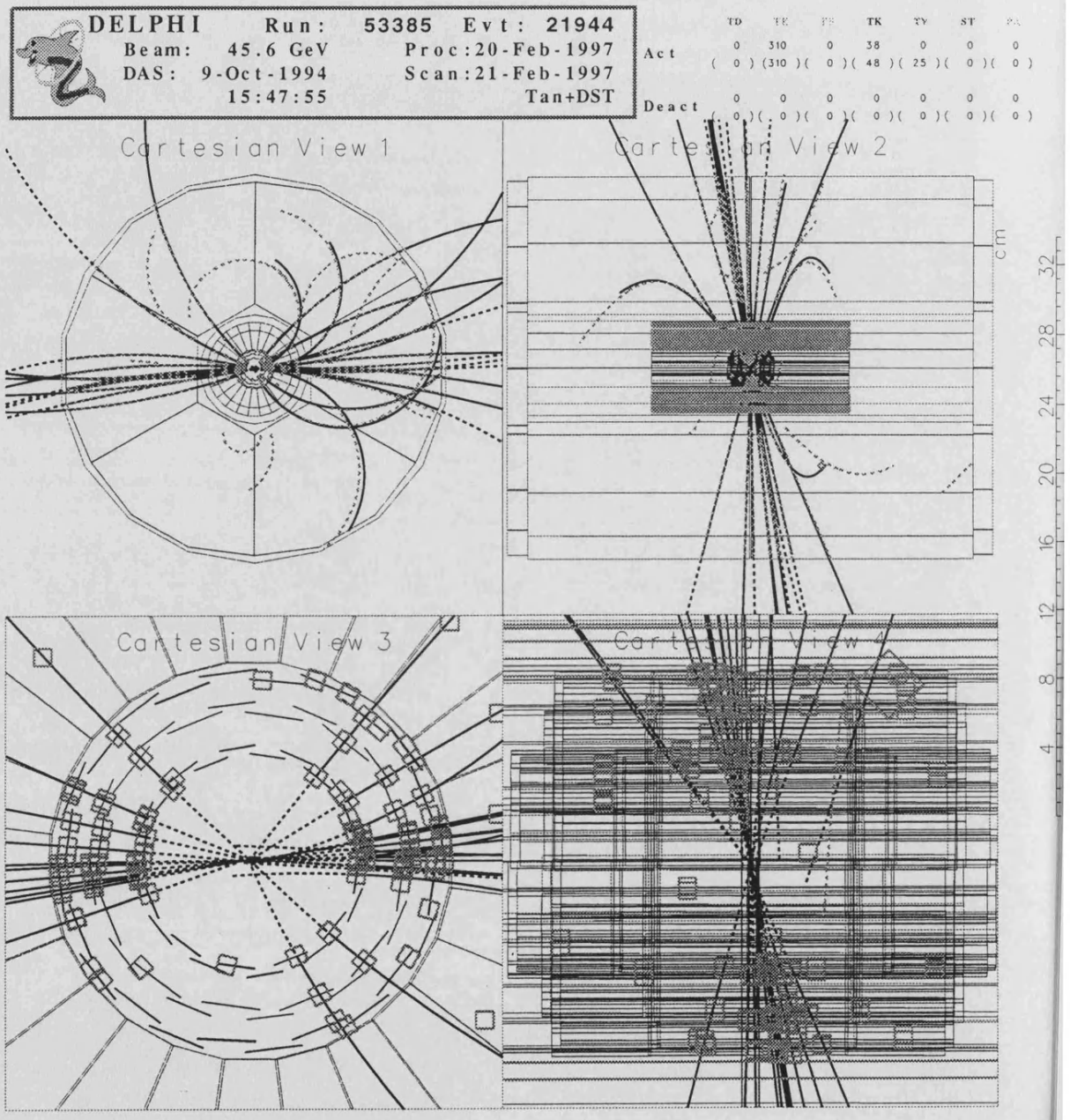

Figure 3.9: Multihadronic event display showing the track fitting (solid lines) through VD, ID and TPC together with the track extrapolation to the interaction point (dashed lines). Squares and points are single hits in the detectors. The Cartesian views correspond to: (1) $R\phi$ plane, (2) yz plane, (3) zoom in the $R\phi$ plane of the VD region, (4) zoom in the yz plane of the VD region.

3.2.7 Physics and detector simulation

In almost all of the high energy physics analyses, Monte Carlo studies play an important role. That is the case of the measurement presented here. As it will be shown through this report, although the dependence of the analysis on Monte Carlo simulation is small it is important in order to evaluate some backgrounds and small correction factors, as well as the systematic significance of the measurement. Therefore, the simulation program should provide events as close as possible to real raw data. In the standard DELPHI simulation program, DELSIM [92], Z decays are firstly generated according to a particular physics process, $e^+e^- \rightarrow q\bar{q}$ in our case. This is done using external generators, like JETSET [32], HERWIG [33] and ARIADNE [34] (see chapter 1 for differences between them). The generators are tuned using the big amount of relevant data collected in the past years in the experiments at LEP and the information on bottom and charm hadrons is updated to account for the new experimental measurements. In this way it is possible now to tune the event generators which simulate the hadronization and decays of different quarks with high precision. The corresponding study performed by the DELPHI experiment is published in [93]. Secondly, generated particles are passed through the DELPHI detector producing hits in active detector components, taking into account the information from the DELPHI detector data base CARGO, the magnetic field and the possibility for secondary interactions. At this level, simulation data has the same structure as raw data, and can then be processed with DELANA to produce the DST by following exactly the same procedure as for the real data. All these efforts will result in a good observed agreement between data and simulation in all the distributions relevant for the R_b analysis reported here.

Chapter 4

Tagging $Z \rightarrow b\bar{b}$ events in DELPHI

As it was pointed out in chapter 1, one of the key points for the precise determination of R_b is the design of an efficient and pure classifier of the $Z \rightarrow b\bar{b}$ decays in the complex mixing of $Z \rightarrow$ *hadrons* produced at LEP 1. This chapter is just devoted to the detailed description of the classifiers developed by DELPHI, which try to use in a consistent way the maximum available information provided by the experimental setup.

4.1 Track and event selection

The starting point for flavour tagging is the selection of good hadronic Z decays. In order to perform this selection, we have adopted standard cuts (namely *TEAM 4*) of the DELPHI experiment [94]. Firstly, charged particles are accepted if:

- their polar angle is between 20^o and 160^o,
- their track length is $>$ 30.0 cm in the TPC,
- their momentum is $>$ 400 MeV/c with a relative error less than 100%,
- their impact parameter (see section 4.5) relative to the interaction point is $<$ 4.0 cm in the plane perpendicular to the beam direction, and $<$ 10.0 cm along the beam direction.

Events were selected by requiring:

- at least 5 reconstructed charged particles,
- the summed energy of the charged particles had to be larger than 12% of the total center-of-mass energy,
- thrust axis satisfying $|\cos\theta_{thrust}| < 0.95$, where θ_{thrust} is the polar angle of the event thrust axis (section 4.4).

With these cuts the efficiency to select hadronic events was about 95% with all backgrounds (mainly from $\tau^+\tau^-$ pairs but also from $\gamma\gamma$ collisions) below 0.1%, without any significant bias in the flavour composition of the sample. Additional requirements on detector availability (provided by the slow control system) were required. The ratio of the $Z \to b\bar{b}$ cross-section to the total hadronic cross-section varies very little at center-of-mass energies around the Z mass. Thus no selection on the center-of-mass energy has been made.

The tagging is defined only from a subsample of physical *tight two-dimensional (2D)* and *tight three-dimensional (3D)* tracks required to have been produced near the interaction point. In addition to the *TEAM 4* cuts, *tight 2D* tracks have to satisfy the following conditions:

- hits in at least 2 of the 3 $R\phi$ layers of the VD;
- the $R\phi$ impact parameter (section 4.5) with respect to the main event vertex (section 4.4) less than 0.30 cm;
- the track was not associated to a reconstructed K^0, Λ or e^+e^- pair from photon conversion (see below).

Tight 3D tracks require further the following conditions:

- hits in at least 1 of the 2 z layers of the VD;
- the impact parameter with respect to the main event vertex in z less than 1.0 cm;
- no error code in the 3D impact parameter routine (section 4.5);
- the track-jet abscissa (section 4.5.2) less than 2.0 cm.

It happens that for a small fraction of the accepted events (around 0.1%) no tight tracks are found in none hemisphere. The event is then rejected because no tagging information is available in that case.

Finally, due to the limited angular acceptance of the microvertex detector an additional event polar angle acceptance cut is needed. A cut at 0.65 on $|\cos\theta_{thrust}|$ was imposed. The physical reason for this hard cut instead of a softer cut (for instance at 0.75) is to reduce and control as much as possible hemisphere tagging correlations from VD edge effects (chapter 6). No additional cut on the number of jets in the event is performed. With all these cuts the global efficiency to select hadronic events was about 60%.

As said above, selected tracks are required not to be associated to a reconstructed K^0, Λ or e^+e^- pair from photon conversion (V^0's). Candidate V^0 decays in hadronic events are found by considering all pairs of oppositely charged particles and then reconstructing the vertex using similar techniques to the ones described below in

this chapter. V^0 candidates are found according to the standard DELPHI algorithm described in the first reference of [78]. The reconstructed invariant mass distributions for the 1994 sample of 'tight' K^0 and $\Lambda(\bar{\Lambda})$ are shown in figures 4.1.a and 4.1.b respectively. The efficiency reconstruction depends on the V^0 momentum as it can be seen in figures 4.1.c and 4.1.d. The average over momentum spectrum of 'tight' K^0 selection is about 36% with a contamination of 3%. The same for 'tight' $\Lambda(\bar{\Lambda})$ selection is 30% with a contamination of about 10%. There is no protection against short range Σ^+ and Σ^-. Also there is a small, but non vanishing probability that charged pions and kaons decay inside the beam pipe.

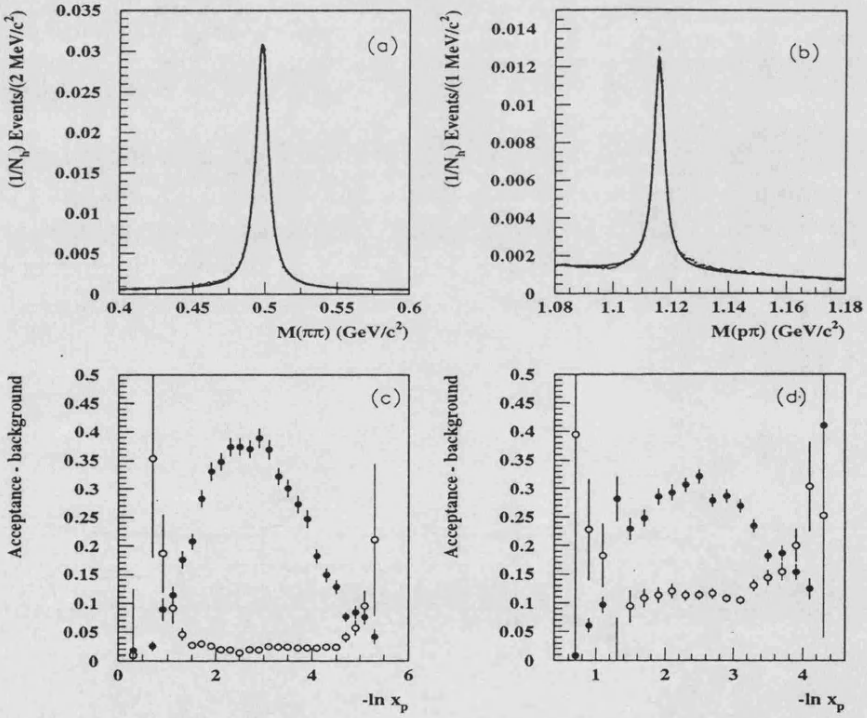

Figure 4.1: Invariant mass distribution for the tight (a) K^0 and (b) $\Lambda(\bar{\Lambda})$ samples, normalized to the total number of hadronic events; the line shows a fit to a Breit-Wigner shape for the mass plus a linear background. Efficiency (closed circles) and background fraction (open circles) as a function of $-\ln x_p = -\ln p/p_{beam}$ for tight (c) K^0 and (d) $\Lambda(\bar{\Lambda})$ samples. The mass cuts are $0.35 < m_{\pi\pi} < 0.65$ GeV/c^2 and $1.3 < m_{p\pi}$ GeV/c^2 for Λ^0, with $0.02 <$ probability to have decayed within the fitted distance < 0.95 for both cases.

4.2 The data and Monte Carlo samples

The total number of accepted hadronic Z decays from the 1991 to the 1995 runs of the LEP collider[1], before and after the angular acceptance cut, is summarized in table 4.1. The 1994 and 1995 data have been reprocessed with a the reconstruction program (DELANA) that greatly enhances the tracking efficiency and resolution with respect to the one used for the 1991 to 1993 data. The data from the earlier years (1991-1993) are still under reprocessing with this new reconstruction program, and therefore the older reconstruction algorithm was used for these data.

Table 4.1: Number of hadronic Z decays accepted for the analysis in each year of operation, before and after $|\cos\theta_{thrust}| < 0.65$ cut.

Year	1991	1992	1993	1994	1995	Total
Before $\|\cos\theta_{thrust}\|$ cut	247277	691658	698557	1370354	664676	3672522
After $\|\cos\theta_{thrust}\|$ cut	150635	421741	425796	828168	400482	2226822

Samples about three times the data statistics of $Z \to q\bar{q}$ events has been simulated using the Lund parton shower Monte Carlo JETSET 7.3 [32] and the DELPHI detector simulation DELSIM [92]. The simulated events have been passed through the same analysis chain as the real events. The total number of accepted simulated hadronic Z decays is shown in table 4.2. In addition, dedicated samples of $Z \to b\bar{b}$ events have been generated (table 4.3).

Table 4.2: Number of hadronic Z decays accepted after $|\cos\theta_{thrust}| < 0.65$ cut in simulation for the analysis in each year.

Year	1991	1992	1993	1994	1995	Total
	210013	1599895	1217802	2465416	557850	6050976

Table 4.3: Number of equivalent hadronic Z decays accepted after $|\cos\theta_{thrust}| < 0.65$ cut of dedicated $Z \to b\bar{b}$ events for each year.

Year	1991	1992	1993	1994	1995	Total
	-	1420295	1451752	2371936	949487	6193470

[1]The used processing of the data are the last available at the moment when this work was written: 91F1, 92D2, 93C1, 94C2 and 95D2.

The event selection was designed to have the same acceptance for any quark flavour. There is, however, a small bias caused by the charged track multiplicity requirement: b quark events have a higher average multiplicity, and hence a higher efficiency for selection, than the other flavours. This flavour bias increases the value of R_b in the selected event sample. The bias towards $Z \rightarrow b\bar{b}$ events in the selected sample was estimated from simulation and was found to be small (table 4.4). To estimate this bias, the following expression was used:

$$\delta R_b = \frac{R_b f_b}{R_b f_b + (1 - R_b) f_{udsc}} - R_b \tag{4.1}$$

were R_b here is the generated value of R_b in the simulation and f_b and f_{udsc} are the efficiencies to select b and $udsc$ events respectively. In order to reduce Monte Carlo statistical errors in the evaluation of δR_b, the $Z \rightarrow q\bar{q}$ samples were used to evaluate f_{udsc}, but also the dedicated $Z \rightarrow b\bar{b}$ samples were used to estimate f_b. To compute the statistical significance of δR_b, error propagation on (4.1) was applied.

The background in the hadronic event selection is dominated by $\tau^+\tau^-$ pairs, and changes slightly the fraction of $b\bar{b}$ events in the sample. The bias towards $Z \rightarrow b\bar{b}$ events, as estimated from simulation, depends mainly on the number of charged tracks required in the hadronic selection. For 5 tracks, it is -0.00046, where the corresponding error is dominated by systematics, being negligible compared with the acceptance bias error. The bias and background are corrected for when measuring R_b, and the systematic error is due to the uncertainty in the simulation of the track multiplicity distribution and to the limited amount of Monte Carlo simulation. However, the former is negligible compared to the latter one, which is given in table 4.4 for the different data samples.

Table 4.4: The bias towards $Z \rightarrow b\bar{b}$ events in the selected sample estimated from simulation. This bias is defined as the difference of the fraction of $b\bar{b}$ events in the selected events with respect to its true value.

Year	1991-1993	1994	1995
	$(0.66 \pm 1.12) \times 10^{-3}$	$(0.69 \pm 0.13) \times 10^{-3}$	$(1.18 \pm 0.26) \times 10^{-3}$

The parameters used in JETSET were optimized by DELPHI [93], in particular some parameters to which the determination of R_b is sensitive. Between them are:

- fragmentation function for heavy flavours, taken as Peterson et al. [36];
- the production fractions of weakly decaying charmed hadrons in $c\bar{c}$ events;
- the lifetimes of the charmed hadrons;
- the average charged decay multiplicities of the charmed hadrons;

- the production rates of b and c quarks via gluon splitting;
- the production rates of K^0's and hyperons.

Other fundamental parameters like the production fractions, lifetimes and the average charged decay multiplicities of the B hadrons are also optimized, although the determination of R_b reported here has a small sensitivity to them. The central values of all these parameters and their uncertainties used when evaluating systematic errors are given in chapter 6.

4.3 The multivariate tagging algorithm

Tagging events containing b quarks is based on reconstructing as precisely as possible the position of the primary Z boson decay, the track parameters of the outgoing particles with respect to the reconstructed vertex and applying an algorithm optimizing the use of this information. This chapter describes in detail all these steps, which were firstly proposed in [95] and recently improved in [96].

The tagging algorithm is based on the large mass and relatively long lifetime of the b quark (typically 1.6 ps) and some event shape properties of their decays. All the available information is combined using multivariate techniques. The lifetime information exploits the large and positive signed impact parameters of tracks coming from B decays together with a search for secondary vertices and their invariant masses. Finally, the lifetime information is combined with the event shape properties of the B decays like large transverse momentum of the tracks with respect to the jet axis, rapidity distributions and the boosted sphericity.

For each single variable z^i, the probability $p_q(z^i)$ to observe a value of z^i for a hemisphere of flavour q is given by the content $y_q(z^i)$ of the corresponding bin in the density distribution of this variable for flavour q:

$$p_q(z^i) = \frac{y_q(z^i)}{N_q^{tot}} \tag{4.2}$$

where N_q^{tot} is the total number of events in the q flavour distribution. The density distribution $y_q(z^i)$ is modelized by a *training sample* of simulated events that is different and tuned for each data set period[2]. The probability that the observed set $\left\{z^1, z^2, ..., z^N\right\}$ comes from a given quark flavour uds, c and b is

$$\mathcal{P}_{uds} = \frac{3\prod_{\lambda=1}^{N} p_{uds}(z^\lambda)}{3\prod_{\lambda=1}^{N} p_{uds}(z^\lambda) + \prod_{\lambda=1}^{N} p_c(z^\lambda) + \prod_{\lambda=1}^{N} p_b(z^\lambda)}$$

$$\mathcal{P}_c = \frac{\prod_{\lambda=1}^{N} p_c(z^\lambda)}{3\prod_{\lambda=1}^{N} p_{uds}(z^\lambda) + \prod_{\lambda=1}^{N} p_c(z^\lambda) + \prod_{\lambda=1}^{N} p_b(z^\lambda)}$$

[2]In addition, to reduce statistical fluctuations, Gaussian and exponential fits are performed for some tail distributions.

$$\mathcal{P}_b = \frac{\prod_{\lambda=1}^{N} p_b(z^\lambda)}{3\prod_{\lambda=1}^{N} p_{uds}(z^\lambda) + \prod_{\lambda=1}^{N} p_c(z^\lambda) + \prod_{\lambda=1}^{N} p_b(z^\lambda)} \tag{4.3}$$

respectively, being N the total number of variables used. The empirical factor 3 assigned to *uds* reflects the fact that this flavour is the sum of the three lighter flavours u, d and s, which are taken together because their distributions are very similar. With this formulation the five flavours have the same weight.

This method of combining the probabilities may not be optimal. It should be realized that the individual probabilities are obtained independently, but they are in fact all correlated. Thus there is no statistically correct way to combine them, and several techniques could be tried. However, this choice was proven to be the best of several tried.

What counts when comparing flavours are ratios of probabilities or their logarithmic differences. For this reason, we have introduced three estimators

$$\begin{aligned} \mathcal{L}_{uds} &= \frac{2\ln\mathcal{P}_{uds} - \ln\mathcal{P}_c - \ln\mathcal{P}_b}{3} \\ \mathcal{L}_c &= \frac{2\ln\mathcal{P}_c - \ln\mathcal{P}_{uds} - \ln\mathcal{P}_b}{3} \\ \mathcal{L}_b &= \frac{2\ln\mathcal{P}_b - \ln\mathcal{P}_{uds} - \ln\mathcal{P}_c}{3} \end{aligned} \tag{4.4}$$

called *flavour likelihoods*, which are the basis of the classification. The event can be classified according to the corresponding positive flavour likelihood (only one is positive), being the absolute value of the likelihood a sensitive indicator of the tag purity. Based on this value, each tag can be subdivided into categories according to a set of given cuts.

4.4 The hemisphere primary vertex finder

A primary vertex fit serves to estimate the position of the e^+e^- interaction point. In a first step we determine an *event vertex*, whose purpose will be to see if a track originates from the production point region and can be selected as a tight track as described in section 4.1. The position of the event vertex is computed using an iterative procedure which starts with all the charged particles of the event having an impact parameter in $R\phi$ with respect to the beam spot position less than 4.0 cm (very soft cut), by minimizing the full 3D least squares ansatz [97]:

$$\mathcal{M} = \sum_{j=1} \vec{\delta}_{a,j}^{\,T} \tilde{G}_j \vec{\delta}_{a,j} + \sum_{j=1} \left\{ \frac{(b_{x,j} - V_x)^2}{\sigma^2_{b_{x,j}}} + \frac{(b_{y,j} - V_y)^2}{\sigma^2_{b_{y,j}}} \right\}. \tag{4.5}$$

In equation (4.5), $\vec{\delta}_{a,j}$ is the vector of closest approach in space of the track to the candidate vertex $\vec{V}$ and $\tilde{G}_j$ is the weight matrix of track j. The second term of (4.5) corresponds to the inclusion of the beam spot position $(b_{x,j}, b_{y,j})$ and dimensions

$(\sigma^2_{b_{x,j}}, \sigma^2_{b_{y,j}})$ as a constraint of the vertex fit. This constraint is meaningful only in the $R\phi$ plane. At each iteration, a search for the track with maximum contribution to the full 3D least squares ansatz above a threshold of 10.0 is performed. If found, the track is removed and a new vertex fit is attempted until no track is removed. If no tracks are finally left, the beam spot position is used as estimate of the vertex. Since the beam spot position is used as a starting reference point, in principle all the tracks can be rejected from the fit. For these events the beam spot center is taken as the event main vertex and the covariance matrix corresponds to the beam spot size. The fraction of such events is around 1%.

The beam spot is defined as the interaction region of the electron and positron beams. To follow variations during the LEP fill, its position is determined for every cartridge written by the DAS corresponding to about 200 sequential hadronic events. The x and y positions are found with typical uncertainties of about 9 μm and 4 μm respectively. The width along the x coordinate varies with time but a typical value is 100 to 120 μm with an error of 7 μm. The beam spot is small, which improves the accuracy of the event by event primary vertex fit and therefore the efficiency for tagging b quark events.

However, the fact that this primary vertex shares tracks from both hemispheres introduces tagging correlations between the hemispheres:

- if one B hadron has a long decay length, it will be almost certainly tagged. However, it will degrade the resolution of the primary vertex, making it less likely that the second B hadron will be tagged;
- if two hemispheres share a common primary vertex and if its error happens to be large, the B hadrons will be less likely to be tagged as b;
- if the primary vertex is pulled towards one of the B hadrons (because it includes decay tracks), the decay range of that B hadron will be underestimated, while that of the other B will be overestimated.

These problems can almost be eliminated if a primary vertex is computed separately for each hemisphere. It should be remarked that the price to pay for this independence is a small decrease in tagging efficiency. However, the reduction of hemisphere correlations has been proven to be one of the most important points of the analysis.

Back-to-back hemispheres are defined by classifying particles into two subsets using the event thrust axis. The thrust axis $\vec{T}$ is defined to maximize the ratio [32]

$$\frac{\sum_a \mid \vec{p}_a \cdot \vec{T} \mid}{\sum_a \mid \vec{p}_a \mid} \tag{4.6}$$

where $\mid \vec{T} \mid = 1$. Index a runs over all the final state particles and $\vec{p}_a$ is the momenta of each particle. The maximal value found is known as event thrust. Particles are distributed into jets using the JADE algorithm [32] with $y_{cut} = 0.01$, and the

jet direction was given by the jet thrust axis. Then particles are assigned to the hemisphere of the jet they belong to.

From this list of particles, an *hemisphere primary vertex* is now evaluated. Tracks with wrong associations to hits in the VD, from secondary decays of long lived particles or from interactions in the detector material, may spoil the reconstruction of the vertex. To minimize the presence of these tracks, in a first step all the previously identified tight tracks of the hemisphere are used for the hemisphere vertex fit, taking as approximative solution the global event vertex previously computed. Then a selection of tracks is performed by requiring an $R\phi$ impact parameter less than 0.30 cm and less than 2.5 cm in z with respect to the vertex obtained in this first step. In the second step, with the selected tracks a new vertex fit is performed. If the fit probability of the full 3D least squares ansatz of equation (4.5) is less than 0.05, the particle with the most important contribution is removed, and a new vertex iteration is attempted. If no tracks are left in the fit (this happens on simulation in about 4% of hemispheres), the event vertex is taken. From this fast algorithm the hemisphere vertex position, as well as the full covariance matrix, are determined.

Figure 4.2 shows the difference between the reconstructed and generated vertex positions in the x, y and z directions for light, charm and b hemispheres for the 1994 simulation. By comparison, table 4.5 summarizes the RMS of the obtained distributions for the 1994 and 1993 simulations. In 1994, for light quark events the RMS of the distribution in the x direction is about 60 μm and for b quarks it is around 125 μm; in the y direction it is around 10 μm for both, uds and b quarks. Therefore, the y primary vertex resolution is similar for uds and b quarks, because the tight beam spot constraint in that component. However compared to uds hemispheres, the x resolution for b quarks shows: a) higher RMS, which is the result of the exclusion in the vertex fit of secondary tracks reducing the track multiplicity of the fit together with a poorer beam spot determination (compared to the y component); b) larger tails, because of the inclusion in the fit of some secondary tracks. In the z component similar arguments to the x component can be applied, with the additional consideration that the beam spot in z is not a real constraint in the vertex fit. Before 1994 the VD did not provide measurements of the z coordinate. Table 4.5 shows the factor about eight of gain in z resolution for b hemispheres from 1993 to 1994, as a consequence of the upgrade of the microvertex detector with z readout. In the x coordinate the resolution before 1994 is slightly poorer and it is similar for the y coordinate.

Figure 4.3.a-c shows the differences between the reconstructed primary vertex and the beam spot. For the 1994 data, the RMS of the x, y and z distributions are 133.1 μm, 3.3 μm and 7050 μm respectively, compared with 130.9 μm, 3.0 μm and 7109 μm obtained from the Monte Carlo simulation of the experiment. Figure 4.3.d-f shows also the error obtained from the hemisphere vertex fit. The large tail of the z component is mainly due to badly measured tracks in z and the poor beam spot determination in that component.

Finally, figure 4.4 shows the differences between two hemisphere vertex positions

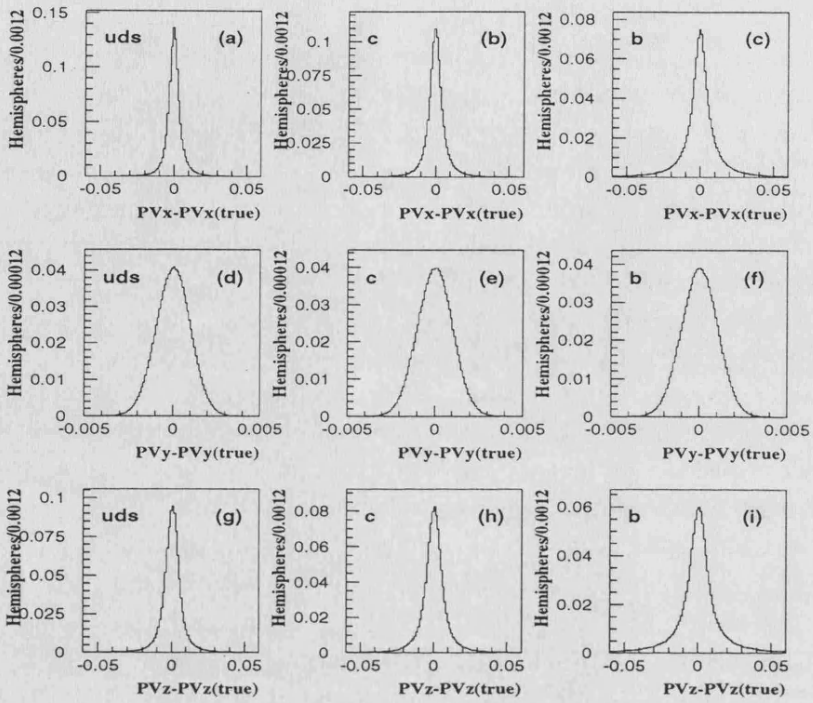

Figure 4.2: Difference between the reconstructed and generated hemisphere vertex positions in the x, y and z directions for light quarks, charm quarks and b quarks in the 1994 simulation. Horizontal scale is in cm.

in data and simulation for 1994, and table 4.6 summarizes the RMS of the distributions. As previously, the x and z distributions have larger tails because of the inclusion of secondary tracks and the poorer beam spot constraint.

4.5 Impact parameter reconstruction

Since the experimental track precision in the three spatial dimensions are comparable (when VD hits in $R\phi$ and z have been associated to the track), normal 3D metric for impact parameter reconstruction can be used. It has been found that weighting the $R\phi$ and z coordinates to take into account the differences in accuracy do not bring significant improvements with respect to the standard 3D calculations.

Conceptually, the impact parameter is the distance of closest approach between a track and the interaction point. The trajectory is represented by an helix. The usual convention is to take for the starting point of the helix a point $\vec{P}_0$ which is the perigee with respect to the origin of the DELPHI reference frame. The trajectory is defined through the usual five helix parameters $(h_0^{xy}, \Delta_z^0, \theta_0, \phi_0, 1/\rho)$ taken at perigee

Table 4.5: RMS of the distributions of differences between the reconstructed and generated vertex positions in the x, y and z directions for light quarks, charm quarks and b quarks for 1994 and 1993 simulation.

Distribution	1994 Simulation	1993 Simulation
PVx-PVx(true) *uds*	56.6 μm	69.5 μm
PVx-PVx(true) c	73.8 μm	87.9 μm
PVx-PVx(true) b	125.3 μm	144.7 μm
PVy-PVy(true) *uds*	9.8 μm	9.9 μm
PVy-PVy(true) c	10.0 μm	10.0 μm
PVy-PVy(true) b	10.3 μm	10.3 μm
PVz-PVz(true) *uds*	85.2 μm	783.0 μm
PVz-PVz(true) c	99.0 μm	803.5 μm
PVz-PVz(true) b	147.4 μm	875.0 μm

Table 4.6: RMS of the distributions of differences between the two reconstructed hemisphere vertex positions in the x, y and z directions for 1994 simulation and real data.

Distribution	1994 Simulation	1994 Data
PVx1-PVx2	91.1 μm	90.3 μm
PVy1-PVy2	3.8 μm	4.3 μm
PVz1-PVz2	155.4 μm	161.6 μm

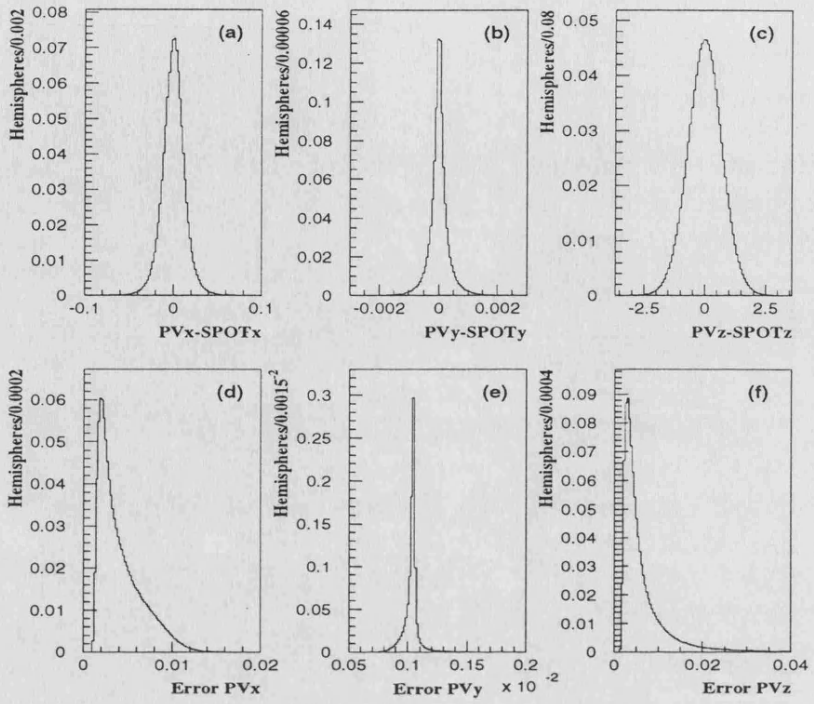

Figure 4.3: Vertex positions with respect to the beam spot and their errors in the x, y and z directions for the 1994 data. Horizontal scale is in cm.

$\vec{P}_0$. The coordinates of $\vec{P}_0$ are therefore $(h_0^{xy} \sin\phi_0, -h_0^{xy} \cos\phi_0, \Delta_z^0)$. The point $\vec{P}_0$ defines an origin on the helix. The position of another point of abscissa s (path length of the helix) can be calculated directly knowing the direction $\vec{T}_0$ (defined by ϕ_0 and θ_0) at $\vec{P}_0$ and the curvature $1/\rho$.

We approximate the interaction point by the hemisphere primary vertex, represented on figure 4.5 by the point $\vec{V}$. The value of $s = (\vec{V} - \vec{P}_0) \cdot \vec{T}_0$, defines a new point $\vec{P}_a$ (see section 4.5.3) which is the point of closest approach of the track with respect to the interaction point $\vec{V}$. The *3D impact parameter magnitude* will be therefore $\delta_a = \mid \vec{P}_a - \vec{V} \mid$.

4.5.1 Signed impact parameter

The decay point of the b quark must lie along the flight path of the heavy hadron. The purpose of attributing a sign to the impact parameter is to recognize that situation. One assumes that the direction $\vec{J}$ of the most energetic jet represents the quark direction. The line of direction $\vec{J}$, attached to the vertex $\vec{V}$, approximates the line of flight of the quark. A first interesting quantity is the *projected impact*

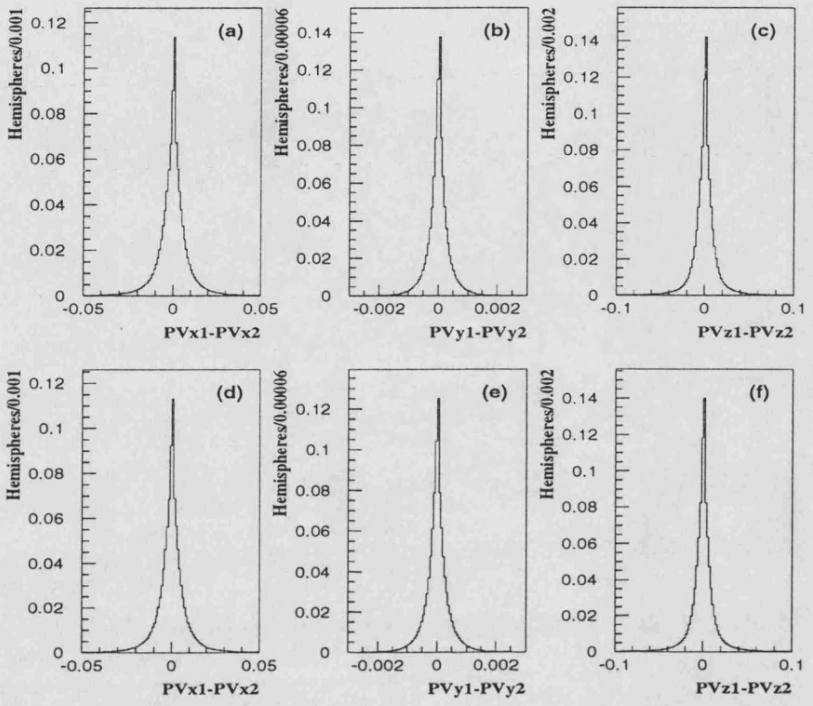

Figure 4.4: Difference between the two hemisphere vertex positions in the x, y and z directions for 1994 simulation (a,b,c) and data (d,e,f). Horizontal scale is in cm.

parameter on the jet axis

$$q_J = \overrightarrow{P_a V} \cdot \vec{J}. \tag{4.7}$$

However, it is more useful to calculate the closest approach distance between the quark line of flight and the track. This can be done by minimizing the square distance $\mid \overrightarrow{RQ} \mid^2$ between two points $\vec{Q}$ and $\vec{R}$ belonging to the quark and particle lines respectively (figure 4.5). At the minimum, $\vec{Q}$ and $\vec{R}$ are conveniently represented by their abscissas s_J and s_t taken each one relatively to their origin: $\vec{V}$ for the quark line and $\vec{P}_a$ for the track. When the particle is a b product, the values of s_J and s_t are positive. For that reason, we assign to the track impact parameter δ_a the sign of s_J. The expression of s_J is derived in section 4.5.2[3].

[3] We may have taken as well s_t.

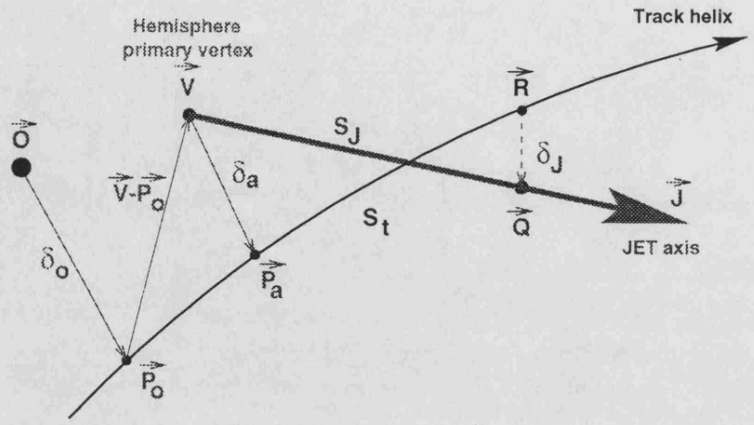

Figure 4.5: Definition of the signed impact parameter and the track-jet distance.

4.5.2 Track-jet distance in space

The quantity $\delta_J = |\overrightarrow{RQ}|$ is the closest approach distance between the quark line and the track. The interest of δ_J is to be only sensitive to cascade decays of the b quark. In the limit of no errors, the quark and the track would intersect exactly when the particle is produced either at the interaction point or at the first generation decay. Therefore, only second generation decays would produce non vanishing values of δ_J.

Mathematically, the problem of finding the point of closest approach between a line and a helix in space is transcendental and an iterative procedure is needed. The procedure has only been applied to tight 3D tracks. For 2D tracks, it is meaningless.

We start by approximating the track as a line defined by the point $\vec{P}_a$ of closest approach of the track to the hemisphere vertex, plus its direction, $\vec{T}_a$. The same for the line of the jet axis, where the origin is the hemisphere primary vertex $\vec{V}$. We then solve for the arc length s_t along the track which corresponds to the point of closest approach between the linearized track and the jet axis. The solution is given by

$$s_t = (\vec{V} - \vec{P}_a) \cdot \left[\frac{\vec{T}_a - \vec{J}\left(\vec{T}_a \cdot \vec{J}\right)}{1 - \left(\vec{T}_a \cdot \vec{J}\right)^2} \right]. \tag{4.8}$$

The assumption of the helix to its tangent may become not accurate when s_t is not small compared to the radius of curvature. In this case, a new origin $\vec{P}$ of abscissa s_t with tangent $\vec{T}$ replaces the old point represented by $\vec{P}_a$ and $\vec{T}_a$. The change of origin is explicited in section 4.5.3, and equation (4.8) is again solved. The total path from $\vec{P}_a$ is updated and the process is iterated until the path length change is small. This takes generally one iteration and a maximum of four. By following this procedure, the track point $\vec{R}$ of closest approach track-jet is obtained as $\vec{R} = \vec{P} + s_t\vec{T}$ with $\vec{P}$, $\vec{T}$ and s_t taken from the last iteration. The corresponding point $\vec{Q}$ on the

jet axis is then determined from the relation $\vec{Q} = \vec{V} + s_J\vec{J}$, where s_J is defined by

$$s_J = (\vec{V} - \vec{P}_a) \cdot \left[\frac{\vec{T}\left(\vec{T}\cdot\vec{J}\right) - \vec{J}}{1 - \left(\vec{T}\cdot\vec{J}\right)^2} \right]. \tag{4.9}$$

The quantity s_J is just the distance on the jet line between $\vec{V}$ and $\vec{Q}$ (*track-jet abscissa*). The vector $\overrightarrow{RQ}$ can then be written as

$$\overrightarrow{RQ} = \vec{\delta}_a - \left[\frac{\vec{\delta}_a\vec{U}}{|\vec{U}|}\vec{U} + \frac{\vec{\delta}_a\vec{V}}{|\vec{V}|}\vec{V} \right] \tag{4.10}$$

where $\vec{U} = (\vec{T} + \vec{J})/2$ and $\vec{V} = (\vec{T} - \vec{J})/2$. The *track-jet distance* δ_J is therefore given by the simple formula

$$\delta_J^2 = \delta_a^2 - \frac{\left[\vec{\delta}_a \cdot \vec{U}\right]^2}{|\vec{U}|^2} - \frac{\left[\vec{\delta}_a \cdot \vec{V}\right]^2}{|\vec{V}|^2}. \tag{4.11}$$

The δ_J distance verifies the condition $\delta_J < |\delta_a|$.

4.5.3 The track helix linearization

For the 3D determination of the impact parameter and the track-jet distance, it is necessary to propagate the track parameters to a new point at the arc length s in space, using a linear approximation of the track.

Given the unitary vector of the tangent $\vec{T}_0 = (T_{x,0}, T_{y,0}, T_{z,0})$ at the point $\vec{P}_0 = (P_{x,0}, P_{y,0}, P_{z,0})$, the tangent parameters $\vec{T}_1$ of the same helix at the arc length s in space are given by the formulae

$$\begin{aligned} T_{x,1} &= T_{x,0}\cos\beta - T_{y,0}\sin\beta \\ T_{y,1} &= T_{x,0}\sin\beta + T_{y,0}\cos\beta \\ T_{z,1} &= T_{z,0}. \end{aligned} \tag{4.12}$$

$\beta = s\sqrt{T_{x,0}^2 + T_{y,0}^2}/\rho$ represents the rotation of the helix in the $R\phi$ projection between $\vec{P}_0$ and $\vec{P}_1$ and ρ is the projected signed radius. The point $\vec{P}_1$ is defined by

$$\begin{aligned} P_{x,1} &= P_{x,0} + \rho\frac{T_{x,0}\sin\beta - T_{y,0}(1-\cos\beta)}{\sqrt{T_{x,0}^2 + T_{y,0}^2}} \\ P_{y,1} &= P_{y,0} + \rho\frac{T_{y,0}\sin\beta + T_{x,0}(1-\cos\beta)}{\sqrt{T_{x,0}^2 + T_{y,0}^2}} \\ P_{z,1} &= P_{z,0} + sT_{z,0}. \end{aligned} \tag{4.13}$$

4.5.4 Signed impact parameter in two dimensions

When the experimental track precision in $R\phi$ is much higher than in z (which corresponds to the case when $R\phi$ VD hits have been associated to the track but not in z), a standard 2D impact parameter reconstruction must be adopted, what is the case for all data taken in 1991, 1992, 1993 and a small fraction of tracks in 1994 and 1995.

Taking as starting point the track parameters at perigee (point of closest approach to the DELPHI origin), the 2D impact parameter with respect to the hemisphere vertex projected on the $R\phi$ plane is

$$\eta_a = h_0^{xy} + (V_y \cos\phi_0 - V_x \sin\phi_0) - \frac{(V_x \cos\phi_0 + V_y \sin\phi_0)^2}{2\rho} \tag{4.14}$$

where ρ is the signed curvature of the track projected on the $R\phi$ plane. The notation η_a is adopted to avoid confusion with the 3D impact parameter δ_a. The first term of expression (4.14) corresponds to a coordinate change from the origin of DELPHI to the reconstructed hemisphere primary vertex and the second one is a correction due to the track curvature. Similarly, the impact parameter in z can be estimated according to the expression

$$\Delta_z^a = \Delta_z^0 - V_z + \frac{V_x \cos\phi_0 + V_y \sin\phi_0}{\tan\theta_0}. \tag{4.15}$$

The principle of signing the impact parameters in two dimensions is similar to the case of three dimensions. The impact parameter in $R\phi$ projected on the jet axis can be estimated as

$$q_J = \eta_a \sin\epsilon_J \tag{4.16}$$

where ϵ_J is the angle (projected on $R\phi$) of the trajectory at perigee with the jet direction. Note that q_J is positive for decay products of B and D hadrons traveling in the downstream direction of the jet.

4.5.5 Impact parameter errors

The impact parameter is the minimal distance from the trajectory to the primary vertex. The error on this quantity has therefore two components. The first one is due to the track extrapolation error at the DELPHI origin. The second one, which has a smaller contribution, is due to the primary vertex itself. The accuracy on the primary vertex depends on the beam spot size and the accuracy of the tracks included.

Sources of errors on the track parameters at the perigee

The contribution of the trajectory measurement and its extrapolation to the interaction region can be estimated from the apparent distance between the tracks from

$Z \rightarrow \mu^+\mu^-$ decays, where multiple scattering is negligible (in this case there is no primary vertex contribution). In the $R\phi$ plane a track extrapolation error of 20 μm is measured. In the Rz plane, the precision varies as a function of θ. For $\theta = 90^0$ tracks, the extrapolation error is 34 μm. At lower momenta, the track fit and extrapolation error can be estimated using tracks with negative impact parameters, which have little contamination from particles produced in b decays. This is done by subtracting the vertex position uncertainty in quadrature. The errors on the impact parameters h_0^{xy} and Δ_z^0 are parameterized as

$$\sigma^2_{IP_{R\phi}} = \left(\frac{\alpha_{MS}}{p\sin^{3/2}\theta}\right)^2 + \sigma^2_{0,R\phi} \qquad \sigma^2_{IP_z} = \left(\frac{\alpha'_{MS}}{p\sin^{5/2}\theta}\right)^2 + \sigma^2_{0,Rz} \tag{4.17}$$

where α_{MS} (α'_{MS}) is a multiple scattering coefficient (in μm GeV/c) and p is the track momentum. In both expressions, the first term is the multiple scattering contribution and the second one the intrinsic resolution of the tracking system in the absence of multiple scattering. Figure 4.6.a shows the fit of $\sigma^2_{IP_{R\phi}}$ as a function of $p\sin^{3/2}\theta$. The contribution of the event vertex position uncertainty is shown by the lower curve. Parameterizing the extrapolation uncertainty as above gives $\alpha_{MS} = 60$ μm GeV/c and $\sigma_{0,R\phi} = 20$ μm.

The extrapolation in Rz depends strongly on the polar angle of the track. Two effects contribute to the precision for non perpendicular tracks. The first one is the varying point precision hit in z which affects the measurement error; the second one is the larger path through the material which increases the multiple scattering error. Figure 4.6.b shows the extrapolation error in Rz as a function of momentum for $45° < \theta < 55°$ (upper curve) and $80° < \theta < 90°$ (lower curve). The measurement error values are 96 μm and 39 μm respectively, matching well with the result obtained from the dimuon miss distance at the same angles. The multiple scattering coefficient α'_{MS} is 151 μm GeV/c and 71 μm GeV/c respectively. The low amount of material (about $0.5X_0$) per layer in the VD reduces the degradation of the precision for low momentum tracks.

The improvement achieved by adding the z VD information can be seen by comparing the impact parameter resolution in the Rz plane for nearly perpendicular tracks ($70° < \theta < 110°$) above 6 GeV/c, without and with z hits. Adding the z hits gives approximately an improvement factor of 20 in the Rz impact parameter precision.

2D impact parameter errors with respect to the hemisphere vertex

At the level of individual tracks, the error on the impact parameters η_a and Δ_z^a are obtained by differentiating equations (4.14) and (4.15). The calculation requires to propagate the track impact parameters at perigee (h_0^{xy} and Δ_z^0) to the new reference point, the hemisphere primary vertex $\vec{V}$. As this point is close to the DELPHI origin, the propagation has little effect and equation (4.14) can be taken at first order. For

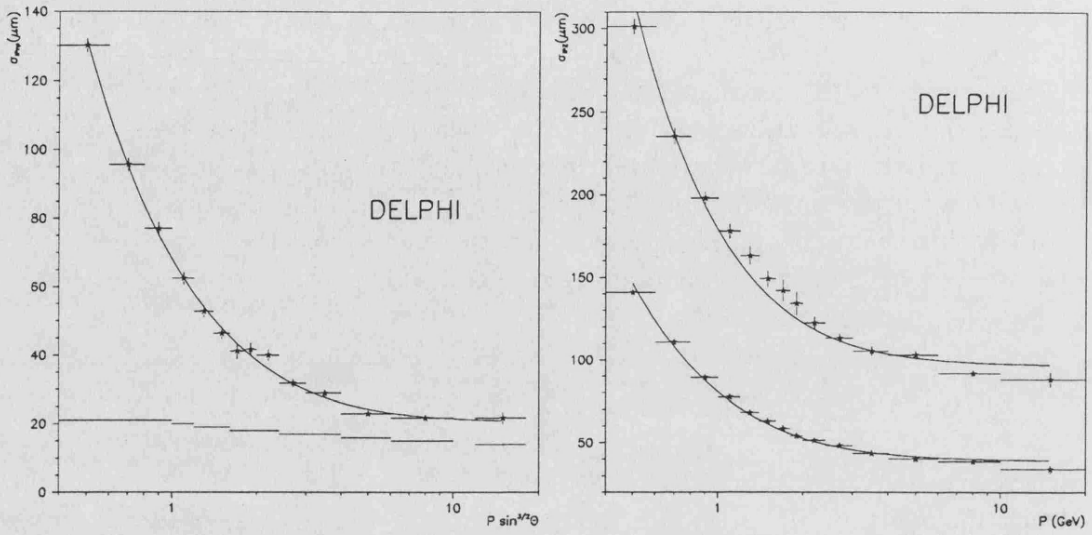

(a) (b)

Figure 4.6: (a) Error on the $R\phi$ impact parameter h_0^{xy} measured as a function of $p\sin^{3/2}\theta$, where p is the particle momentum. The full line is a fit to $60/p\sin^{3/2}\theta \oplus 20$. The contribution due to the vertex position uncertainty was already subtracted and is shown by the bottom curve. (b) Error on the z impact parameter Δ_z^0, measured as a function of p. The two curves correspond to tracks with $80° < \theta < 90°$ and with $45° < \theta < 55°$, respectively. The full lines are a fit to $71/p \oplus 39$ and $151/p \oplus 96$.

the $R\phi$ component, the error on h_0^{xy} must be added to the contribution due to the error on the (x, y) coordinates of $\vec{V}$:

$$\sigma_{\eta_a}^2 = \sigma_{h_0^{xy}}^2 + \sin^2\phi_0\sigma_{V_x}^2 + \cos^2\phi_0\sigma_{V_y}^2 - 2\sin\phi_0\cos\phi_0 cov(V_x, V_y). \tag{4.18}$$

The z component error $\sigma_{\Delta_z^a}$ is derived from equation (4.15):

$$\sigma_{\Delta_z^a}^2 = \sigma_{\Delta_z^0}^2 + \sigma_{V_z}^2(\cos^2\phi_0\sigma_{V_x}^2 + \sin^2\phi_0\sigma_{V_y}^2)/\tan^2\theta_0 + \sin 2\phi_0 cov(V_x, V_y)/\tan^2\theta_0 +$$
$$2[\cos\phi_0 cov(V_x, V_z) + \sin\phi_0 cov(V_y, V_z)]/\tan\theta_0. \tag{4.19}$$

A similar equation is derived for the covariance $cov(\eta_a, \Delta_z^a)$. The correlation due to the fact that the track could be included in the vertex fit is neglected. The error on q_J is then straightforward. There is an additional error coming from the angular uncertainty on the jet axis direction.

3D impact parameter errors with respect to the hemisphere vertex

One advantage to compute the impact parameter in space, instead of in $R\phi$ and Rz projections separately, is that the potential $R\phi - Rz$ correlation in the track parameters is automatically included. However, the error of the impact parameter in space is more complicated to estimate. For convenience, we express $\vec{\delta}_a$ in a local helix frame in the vicinity of the reconstructed hemisphere primary vertex $\vec{V}$, defined by three unitary vectors: $\hat{t}$ and $\hat{n}$ are the tangent and normal (on the $R\phi$ plane) to the track in the $R\phi$ projection and $\hat{k}$ is a vector along the z direction. The vector $\vec{\delta}_a$ can be expressed as a function of η_a and Δ_z^a:

$$\vec{\delta}_a = \eta_a \hat{n} + \Delta_z^a \hat{k}. \tag{4.20}$$

It is convenient to define an unit vector $\hat{d}_a$ in the direction of $\vec{\delta}_a$ by $\vec{\delta}_a = \delta_a \hat{d}_a$. For small displacements in the interaction region, the contributions due to errors on track angles can be ignored. The error σ_a on δ_a can be expressed by

$$\sigma_a^2 = \left(\hat{d}_a \cdot \hat{n}\right)^2 \sigma_{\eta_a}^2 + \left(\hat{d}_a \cdot \hat{k}\right)^2 \sigma_{\Delta_z^a}^2 + 2\left(\hat{d}_a \cdot \hat{n}\right)\left(\hat{d}_a \cdot \hat{k}\right) cov(\eta_a, \Delta_z^a). \tag{4.21}$$

The quantities σ_{η_a}, $\sigma_{\Delta_z^a}$ and $cov(\eta_a, \Delta_z^a)$ are given by equations (4.18) and (4.19). The track-vertex correlation effects were again neglected.

The procedure followed to estimate the error on the track-jet distance δ_J (σ_{δ_J}) is similar to the one described before for the impact parameter in space. The additional contribution to be considered in the error propagation is the angular uncertainty on the jet axis determination. The jet direction uncertainty can be written as

$$d\vec{J} = d\alpha_J \hat{n}_J + d\beta_J \hat{e}_J \tag{4.22}$$

where $\hat{n}_J$ and $\hat{e}_J$ are two orthonormal vectors both perpendicular to the jet axis $\vec{J}$; $d\alpha_J$ and $d\beta_J$ represent small displacements along the 'north' and 'est' directions given by $\hat{n}_J$ and $\hat{e}_J$ respectively. These small displacements are connected to the angular uncertainties in the jet axis measurement. It could be approximated that the mean values of both displacements are similar and equal to the jet axis resolution σ_{jet}. In $Z \rightarrow b\bar{b}$ events, typical resolutions in the estimate of the B hadron direction of about 70 mrad are obtained, improving to about 50 mrad for jet energies above 10 GeV. The error on δ_J can then be determined applying error propagation to the expression (4.11). However, a simplest expression for δ_J can be obtained if we take as reference point of the track $\vec{P}_a$ instead of $\vec{P}_0$. In that case $\vec{\delta}_a \cdot \vec{T}_a = 0$ and expression (4.11) is simplified to

$$\delta_J^2 = \delta_a^2 - \frac{q_J^2}{1 - \left(\vec{T} \cdot \vec{J}\right)^2}. \tag{4.23}$$

The final expression for σ_{δ_J} can easily be obtained after a little of algebra from equations (4.7), (4.20), (4.22) and (4.23).

The errors associated to the projected impact parameter on the jet axis q_J (σ_{q_J}) and on the track-jet abscissa s_J (σ_J) are calculated using exactly the same procedure as for the track-jet distance error.

4.5.6 Impact parameter significance

The ratio between the impact parameter and its error gives the *statistical significance* of the measured impact parameter. Figure 4.7 represents the significance, $S = \delta_a/\sigma_a$ in 1994 for (a) tight 3D tracks and (b) tight 2D tracks for data and Monte Carlo simulation. For simulation, the composition of *uds*, *c* and *b* quarks is shown. The large positive tail is the lifetime signal. The negative half of the distribution measures the resolution of the impact parameter reconstruction, arising from inaccurate track reconstruction (this sample of tracks is mainly produced at the interaction point and have no true impact parameter). This resolution effect should be equally positive and negative. In both cases, 3D and 2D metric, the negative part of the resolution is well fitted to the sum of four Gaussians plus one exponential function. These fits are a direct measure of the resolution function $\mathcal{R}(S)$ for the impact parameter significance.

Unfortunately a complete, physically motivated parameterization of the non-Gaussian tail does not exist since there are many sources of completely different nature which produce it. They include unavoidable mistakes in the track search algorithm producing large impact parameters, interactions of the particles with the detector material, decays of long-lived particles (K^0, Λ), presence of secondary vertices, etc. That is why the parameterization is rather complex and arbitrary. The non-Gaussian tail depends significantly on the criteria which are used for the selection of tracks and events.

4.6 Tracking tuning

The accuracy of the R_b measurement relies on a close agreement between the observed data distributions and those predicted by the detailed detector simulation. The *physical* events generated [32] are passed through a complex and detailed simulation of the DELPHI detector [92]. In a second step, these simulated raw data are analyzed through the same reconstruction programs [84] as the data. However, after this procedure some disagreements remain between data and simulation in the individual track resolution and in the primary vertex description. They are not drastically large but nevertheless can spoil the precise determination of R_b.

Both the generation of the intrinsic physical parameters and the simulation of the detector response must be as realistic as possible. In studies of *b* quark events based on the separation of their origin and decay points, the charged track impact parameter resolution and the primary vertex reconstruction uncertainty are the most crucial part of the detector response. The main features to reproduce are then

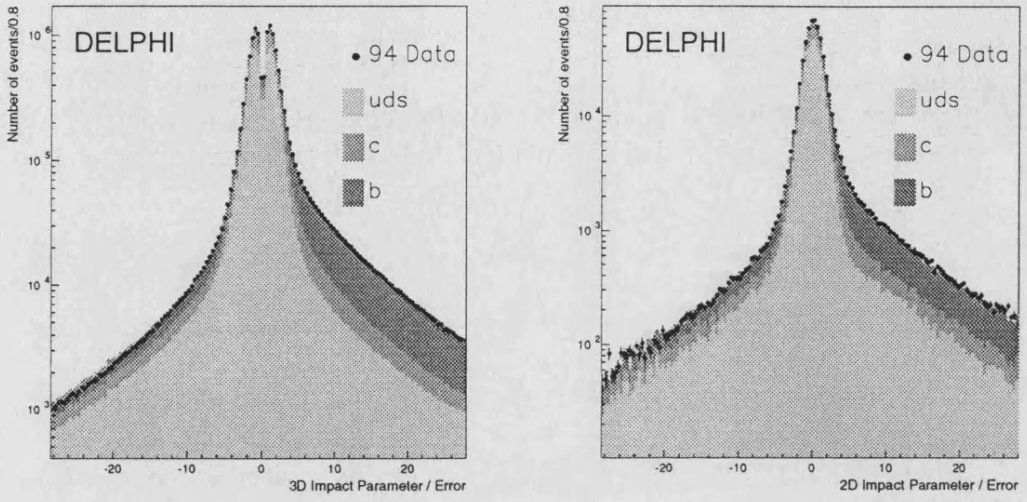

(a) (b)

Figure 4.7: Signed impact parameter over the error (significance) with respect the hemisphere vertex in the 1994 period for (a) 3D tight tracks and (b) 2D tight tracks.

the resolution function $\mathcal{R}(S)$ of the impact parameter significance S and the mean number of VD hits associated to tracks.

The standard Monte Carlo simulation includes a vertex detector map, thus reproducing inefficient and dead regions. The remaining differences between data and simulation in the efficiency of assigning VD hits to tracks are small and they are due basically to residual effects that play a role in the track-hit association, such a discrepancies in outer tracking between data and simulation producing differences in the result of the pattern recognition algorithms.

However, in the standard Monte Carlo simulation the resolution function is found to be slightly different to the one measured in the data. The errors, calculated track by track, are the results of a fit of the trajectories inside the detectors. These errors represent not the true detector resolution but our understanding of it. Therefore, how reliable are these errors is crucial for an analysis based on lifetime. We shall describe a control mechanism which allows to check their validity and eventually to readjust them. The procedure used for the impact parameter tuning is described in detail in reference [98].

Tuning of $R\phi$ impact parameter errors

The error distributions of the reconstructed impact parameters h_0^{xy} and Δ_z^0 are parameterized by expressions (4.17). The parameters α_{MS} (α'_{MS}) and $\sigma_{0,R\phi}$ ($\sigma_{0,Rz}$),

called generally (a, b), depend on the pattern of the track measurements in the different parts of the tracking device. In the case of DELPHI, the track resolution is dominated by the VD (which improves the resolution by one order of magnitude). Thus, for tracks with hits in at least two $R\phi$ layers (tight tracks) we should take into account the dependence on the VD map of hits. For those tracks, figure 4.8 shows the resolution in $R\phi$ of the impact parameter versus the function $p^2 \sin^3\theta$. The superimposed adjusted curve from (4.17) gives a reasonable description of the track resolution.

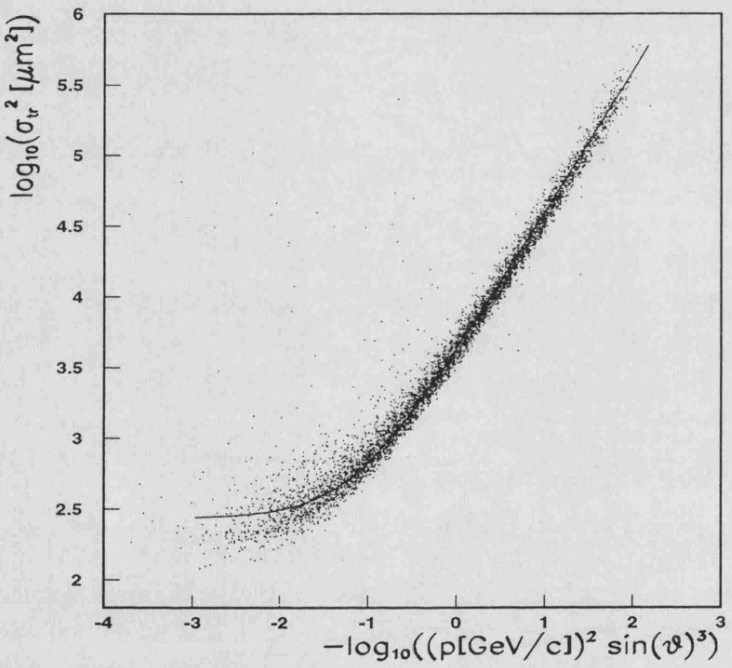

Figure 4.8: Resolution of the $R\phi$ track impact parameter h_0^{xy} versus $p^2 \sin^3\theta$ for tracks with hits in three $R\phi$ layers of the VD.

The determination of (a, b) from the error on the impact parameter h_0^{xy} (called in general σ_{res}) is merely the result of the fit shown in figure 4.8. However, σ_{res} reflects not the real precision of the tracking system but, as it was said before, our understanding of it (accuracy of the different parts of the detector and the material distribution inside it). In the case of primary particles, for which the true impact parameter is expected to be zero, any departure of the impact parameter from zero is due to the measurement error. The distribution of the impact parameters is then just the distribution of the errors σ_{obs}. If a sample of primary particles can be isolated, a comparison between σ_{obs} and σ_{res} can be performed.

The 'real' accuracy σ_{obs} is evaluated in the ideal case, for a given p and θ, by the variance of the observed distribution of the impact parameters, if it is described by a Gaussian. However, in the real data the 'true' impact parameter with respect to the origin cannot be determined directly: first, the true origin point is not known; second, the presence of tracks from secondary interactions in the material or from long-lived particles (B hadrons, K^0_s, hyperons, etc.). The 'true' impact parameter can be approximated from a sample of primary tracks as follows. Tight tracks with negative and small absolute values of significance are selected, in order to reduce the contribution from secondary tracks. An even more pure selection is achieved by requiring an event anti-b tag on a b tagging variable, for instance, the one described in section 4.7. The point of origin can be approximated by the reconstructed primary vertex, within errors. The parameterization of the distribution of observed impact parameters is then determined by a maximum likelihood fit. For each track entering in the fit, the probability density function is defined by

$$\begin{aligned} f(\eta_a) &= \frac{1}{\sqrt{2\pi}\sigma_{\eta_a}} \exp\left\{-\eta_a^2/(2\sigma_{\eta_a}^2)\right\} \\ \sigma_{\eta_a}^2 &= \sigma_{obs}^2(a,b) + \sigma_{PV}^2 \end{aligned} \tag{4.24}$$

where σ_{obs} is the function of (a,b) defined in (4.17) and σ_{PV} is the error corresponding to the uncertainty in the primary vertex position. In this $R\phi$ tuning, η_a is the 2D impact parameter defined in equation (4.14). This method to approximate the 'true' distribution is tested on simulation events by measuring (a,b) in the same way as in real data, and comparing the impact parameter distribution knowing the true origin. The values of (a,b) obtained in both cases are compatible within statistical errors, showing that the procedure is reliable and is not influenced by secondary tracks.

The two different estimates of the track resolution can be compared using the resolution error given by the track fit (σ_{res}) or using the observed distribution of the track impact parameters (σ_{obs}). Both estimates can be parameterized by the same function (4.17) with slightly different coefficients. The correction of the track resolution is performed in such a way that it combines the better average description of the resolution by σ_{obs} with the individual peculiarities of the track reconstruction which are kept in σ_{res}. The resolution error of each track in data is multiplied by the factor K^{RD}_{res} defined as

$$(K^{RD}_{res})^2 = \frac{(a^{RD}_{obs})^2 + (b^{RD}_{obs})^2 (p\sin^{3/2}\theta)^{-2}}{(a^{RD}_{res})^2 + (b^{RD}_{res})^2 (p\sin^{3/2}\theta)^{-2}}. \tag{4.25}$$

In this equation, $(a^{RD}_{obs}, b^{RD}_{obs})$ are the coefficients of the parameterization of σ_{obs}, $(a^{RD}_{res}, b^{RD}_{res})$ the coefficients of σ_{res} and RD denotes real data. The resolution error in the simulation can be similarly corrected multiplying the track impact parameter error by the factor K^{MC}_{res} calculated as

$$(K_{res}^{MC})^2 = \frac{(a_{obs}^{RD})^2 + (b_{obs}^{RD})^2 (p \sin^{3/2}\theta)^{-2}}{(a_{res}^{MC})^2 + (b_{res}^{MC})^2 (p \sin^{3/2}\theta)^{-2}} \tag{4.26}$$

being $(a_{res}^{MC}, b_{res}^{MC})$ the coefficients of the parameterization of σ_{res} in the simulation (MC).

Tuning of $R\phi$ track impact parameters in the simulation

However the track impact parameter in the simulation should be additionally smeared because the distribution of impact parameters itself differs from the data. The distribution of 'true' impact parameters can be parameterized by a Gaussian with the variance in the form of equation (4.17) with coefficients $(a_{obs}^{MC}, b_{obs}^{MC})$. The multiplication of the 'true' impact parameter by the value K_{obs}^{MC} defined as

$$(K_{obs}^{MC})^2 = \frac{(a_{obs}^{RD})^2 + (b_{obs}^{RD})^2 (p \sin^{3/2}\theta)^{-2}}{(a_{obs}^{MC})^2 + (b_{obs}^{MC})^2 (p \sin^{3/2}\theta)^{-2}} \tag{4.27}$$

transforms the variance σ_{obs}^{MC} of its distribution in σ_{obs}^{RD}. This transformation is equivalent to add the value $\eta_a^{true}(K_{obs}^{MC} - 1)$ to the track impact parameter, where η_a^{true} is the true impact parameter in the simulation.

After this transformation the variance of the impact parameter distribution is forced to be the same as in data. In addition, such a method of tuning has the following features: a) the smearing in simulation is done without additional randomization; b) the correction treats equivalently both primary and secondary tracks; c) because the values of $(a_{obs}^{RD}, b_{obs}^{RD})$ are determined as a function of the track azimuthal angle ϕ, after this correction the resolution in simulation acquires the same ϕ dependence as in data.

Non-Gaussian effects

The corrections described above assume that the impact parameter distribution can be parameterized by a Gaussian with variance σ_{obs}, which is only true for small values of significance. Therefore, the description of the non-Gaussian tail is poor, which implies that additional corrections are needed. For that, the parameterization of the resolution is changed to include more terms, in particular a second Gaussian function and an exponential one

$$f(\eta_a) = \frac{P_1}{\sqrt{2\pi}\sigma_{obs}} \exp\left\{-\eta_a^2/(2\sigma_{obs}^2)\right\} + \frac{P_2}{\sqrt{2\pi}K_{sg}\sigma_{obs}} \exp\left\{-\eta_a^2/(2K_{sg}^2\sigma_{obs}^2)\right\}$$

$$+ \frac{P_3 K_{exp}}{2\sigma_{obs}} \exp\left\{-K_{exp} \mid \eta_a \mid /\sigma_{obs})\right\} \tag{4.28}$$

with the constraint $P_1 + P_2 + P_3 = 1$. The impact parameter of tracks in the simulation is modified in the following way: first, the Gaussian correction is applied

to all tracks; second, for a fraction P_2 the tracks, the factor K_{obs}^{MC} is multiplied by K_{sg}; third, a fraction P_3 of tracks is exponentially smeared around their generation point with a slope K_{exp}. The fractions P_2 and P_3 are very small and do not exceed a few percent.

Rz impact parameter tuning

A similar tuning is performed independently for the z impact parameter Δ_z^a and only for the 1994-1995 data sets. The only significant difference between the $R\phi$ and Rz tuning is that in the last case the parameters (a, b) depend on θ. This dependence is determined by many factors of different origin like signal to noise ratio, Landau distributions and delta electron emission, the number of strips that collect the signal, etc. The resulting θ dependence is difficult to predict and it is obtained phenomenologically from the fit of $\sigma_{\Delta_z^a}$ resolution as a function of θ. In particular, θ dependences of a and b are parameterized by the following phenomenological functions [98]:

$$\begin{aligned} a^2 &= a_0^2 + a_1^2 \cot^2\theta \\ b &= \frac{b_0}{\sin\theta}. \end{aligned} \tag{4.29}$$

Figure 4.7 represents the significance, $S = \delta_a/\sigma_a$ for 1994 after the impact parameter tuning. It can be seen that the data and simulation agree reasonably well in a wide range of significance values, for both, 3D and 2D impact parameter reconstruction. The agreement is much better than it was before the tracking tuning [98]. For 3D, the agreement is successful even though the tuning was performed independently for $R\phi$ and Rz projections.

4.7 Probability of primary vertex decay products

The resolution function measured from negative impact parameter tracks can be used to extract the lifetime information of the positive impact parameter tracks by following the method firstly proposed by the ALEPH Collaboration in [99]. This is done by defining a probability function for the tracks

$$\mathcal{P}_T(S) = \int_{-\infty}^{-|S|} \mathcal{R}(s) ds. \tag{4.30}$$

In order to take into account the number of VD hits, separated resolution functions $\mathcal{R}(s)$ for each configuration (2 and 3 $R\phi$ hit layers; 0, 1 and 2 Rz hit layers) were considered. This integrated probability represents the probability that a measurement of the significance S is larger than the observed one. Given the measured track significance S, $\mathcal{P}_T(S)$ can be interpreted as the probability that the track is consistent with coming from the primary vertex.

The same principle can be used to combine probabilities for a set of N tracks. We can consider the individual track probability as defining a point inside an N-dimensional hypercube of unit volume. The differential probability for this point can be determined as the product of individual track probabilities, $\Pi = \Pi_{i=1}^{N} \mathcal{P}_T(S_i)$. The integrated probability is then the integral over this N-cube of all points having the same differential probability or less,

$$\mathcal{P}_N = \int_{(0,0,...,0)}^{\Pi_{i=1}^{N} x_i} dx_1 dx_2 ... dx_N = 1 - \int_{\Pi_{i=1}^{N} x_i}^{(1,1,...,1)} dx_1 dx_2 ... dx_N. \tag{4.31}$$

In order to compute the integral, it is better to express it in the form

$$\mathcal{P}_N = 1 - \int_{\Pi}^{1} \int_{\Pi/x_N}^{1} \int_{\Pi/(x_N x_{N-1})}^{1} ... \int_{\Pi/\Pi_{i=2}^{N} x_i}^{1} dx_1 dx_2 ... dx_N. \tag{4.32}$$

In the case of $N = 1$, we recover $\mathcal{P}_N = \Pi = \mathcal{P}_T$. For $N = 2$, $\mathcal{P}_N = \Pi(1 - \log \Pi)$. By induction it can be shown that for N we have

$$\mathcal{P}_N = \Pi \sum_{j=0}^{N-1} \frac{(-\ln \Pi)^j}{j!}. \tag{4.33}$$

By construction, a flat distribution of $\mathcal{P}_N$ is expected for a group of tracks from the primary vertex, provided that the significances are not correlated. If the group includes tracks from secondary vertices, the distribution has a peak at low values of $\mathcal{P}_N$. In the simulation the distribution of $\mathcal{P}_N$ for light quarks is approximately flat, while for b quarks it has a sharp peak at zero. For light quark events there is also a small peak (significantly lower than for b and c quarks) at low probability values due to residual tracks from V^0 decays or interactions in the detector material (like e^+e^- pairs).

4.8 Search for secondary vertices

The detection of secondary and tertiary vertices significantly separated from the primary vertex is a also signature of B hadrons. The signature, carries some independent information with respect to positive impact parameters, leading to different systematic sensitivity on R_b. We shall call secondary the particles produced at the B decay vertex and tertiary the particles originating from the charmed hadron which decays later. The two group of particles are disconnected in space, but the low decay multiplicity and short decay ranges together with the limited resolution of the tracking system limit the possibility of separation of the two vertices. Then it happens that decay products are in most of the cases merged into a single vertex and vertices could appear as single tracks.

In order to determine the presence of secondary and even tertiary vertices, a search for disconnected groups (that do not share tracks) of charged particles which

intersect in space at a sufficient distance from the primary vertex has been implemented. The search is hierarchical: multiplets of five or more particles are searched first. If none are found or among particles external to these multiplets, quadruplets are searched. Then the procedure is repeated for triplets, doublets and singlets (group reduced to a single particle).

The intersection $\vec{A}_{sc}$ of the group of tracks is defined from a geometrical fit similar to that of equation (4.5), but now without the inclusion of the beam spot constraint. The vertex fit probability and the proper decay length of the multiplet is the criteria used to accept the group. The decay length is defined as the distance between the hemisphere primary vertex and the secondary vertex candidate projected on the flight direction $\vec{J}_{sc}$, approximated by the total momentum direction of the multiplet. From the decay length, it is straightforward to compute the proper decay length of the multiplet by the expression $c\tau_0 = c\tau m_{sc}/p_{sc}$, where m_{sc} is the invariant mass of the vertex and p_{sc} its total momentum:

$$c\tau_0 = \overrightarrow{VA_{sc}} \cdot \vec{J}_{sc} m_{sc}/p_{sc}. \tag{4.34}$$

By definition, the distance is signed positive if the range goes in the same direction as the momentum of the multiplet.

Tight tracks involved in the secondary vertex search were required to pass further cuts. They had to have:

- positive impact parameter;
- a momentum p greater than 0.5 GeV/c; and
- a low probability (using equation 4.5) for the other tracks of the hemisphere to fit a main vertex (less than 1%). This condition is implemented to remove configurations with only one track, which affects essentially the *uds* flavour. In b hemispheres the multiplicity of secondary tracks is 5.5 in average and therefore the configuration with a single secondary track is rare. The condition improves slightly the purity of the selection.

Requirements used for the multiplet definition vary with multiplicity, being tighter for triplets and doublets:

- a fit probability $> 10\%$;
- a decay length > 1.0 mm (> 1.5 mm for doublets and triplets);
- a proper decay length > 0.2 mm (> 0.25 mm for doublets and triplets);
- for doublets and triplets, a vertex fit probability for the remaining non associated tracks of the hemisphere $< 10\%$.

For the tracks that have not been associated to none of the previous multiplets, a singlet search is performed at the last stage. Two situations are distinguished. In the first case a multiplet has already been found. There is a good chance for a b hemisphere, where two vertices (one secondary and one tertiary) are in principle present, to have only one charged particle attached to one vertex (this is often the case of a D^+). Then the vertices are not saturated, and information can still be provided by single tracks. The conditions in the search for such singlets are not severe:

- track momentum > 2.0 GeV/c;
- track significance $S > 3.0$;

The second situation is when no multiplets have been found. The configuration is disfavorable because the hemisphere is probably non b. But if it is b, it may happens that both the secondary and the tertiary vertex have only one charged particle attached or seen. For this reason, we look for pairs of singlets, by imposing tighter conditions than previously:

- angle of the track with respect to the most energetic jet of the hemisphere $< 30°$;
- track momentum > 2.0 GeV/c;
- an intersection of two tracks is computed, which allows to compute a proper decay length required to be > 0.20 mm;
- the fit probability of the pseudo-intersection should be greater than 1%, and the probability of the other tracks to be associated in a main vertex $< 1\%$.

As an example, figure 4.9 shows the distribution of the proper decay length and mass resulting from the search for quintuplets and quadruplets for a 1994 Monte Carlo subsample. For the same data set, table 4.7 summarizes the performances of the secondary vertex algorithm for each type of configuration. The reached purities of the different configurations are good with a 42.7% of hemispheres having at least one singlet or multiplet found, with a mean purity of 83.0%. For sextuplets, quintuplets and quadruplets having a non-negligible total efficiency of about 12%, the purity is really high, higher than 95%. This algorithm will help in tagging performances in the relevant region of high purity for the R_b analysis.

The algorithm described before provides finally a full list of candidates to secondary and tertiary vertices with their proper decay lengths and invariant masses. How these informations are combined to construct tagging variables will be described in section 4.10.

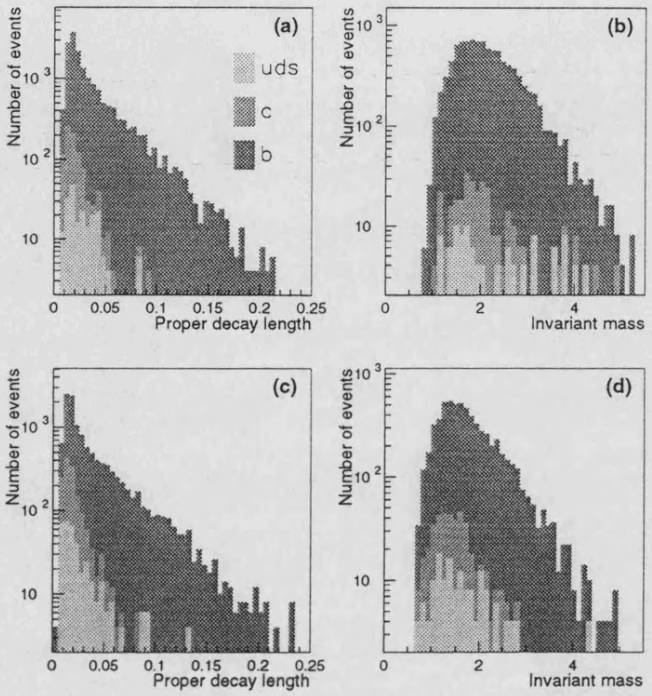

Figure 4.9: Results of the search for candidates to secondary vertices with five (a,b) and four (c,d) tracks for a 1994 simulation sample. The two most important physical quantities associated to the vertex (proper decay length $c\tau_0$ and invariant mass m_{sc}) are shown. The flavour composition of the selected vertices is also shown. Horizontal scale is in cm. A cut at 0.02 cm is performed on the proper decay length. This cut is already included in the invariant mass distributions.

4.9 Weights of B hadron decay products

Another technique to extract information from impact parameters is 'counting' direct secondary particles coming from B hadron decays, prompt as well as cascade. This 'counting' can be done assigning some kind of probability or weight to each track. In order to optimize the information provided by each individual track (lifetime as well as event shape properties) several probabilities or weights ω^i can be assigned to each particle as a function of:

- the rapidity y of the tight track, defined as

$$y = \frac{1}{2} \ln \left(\frac{E + p_{\parallel}}{E - p_{\parallel}} \right) \tag{4.35}$$

  where E is the energy of the track and $p_{\parallel}$ its longitudinal momentum with respect to the jet axis;

Table 4.7: b efficiencies and purities as a function of several multiplet and singlet configurations found by the secondary vertices search algorithm. These results are obtained from a simulated 1994 data sample.

Hemisphere condition	b purity(%)	b efficiency(%)
None	21.9	100.0
Sextuplets	98.8	3.4
Quintuplets	96.2	4.3
Quadruplets	92.4	4.5
Triplets	86.9	15.2
Doublets	77.9	14.7
Singlets	86.4	26.9
Multiplets	84.7	37.8
Singlets and no multiplets	71.8	4.9
No singlets and multiplets	77.8	15.8
Singlets and multiplets	90.4	22.0
Singlets or multiplets	83.0	42.7

- the momentum p of the tight track;
- the impact parameter magnitude over its error, i.e. the significance $S = \delta_a/\sigma_a$ for tight 3D tracks or $S = \eta_a/\sigma_{\eta_a}$ for tight 2D tracks;
- the track-jet abscissa over its error s_J/σ_J for tight 3D tracks and the projected impact parameter on the jet axis over its error q_J/σ_{q_J} for tight 2D tracks;
- the track-jet distance over its error $\delta_J/\sigma_{\delta_J}$ for tight 3D tracks.

The choice of these observables has a direct physical motivation. The rapidity y is an attempt to distinguish between leading and non-leading particles, as well as the momentum p. The significance S and s_J/σ_J (or q_J/σ_{q_J}) are designed to separate tracks originated from non-vanishing lifetime hadrons[4]. Finally the ratio $\delta_J/\sigma_{\delta_J}$ tries to distinguish between prompt secondary tracks and cascade tracks in B decays.

These weights are modelized using the Monte Carlo simulation and they are computed from the ratio of one-dimensional histograms for B decay products over the corresponding one-dimensional histogram for all tracks. In the case of S and s_J/σ_J the weights are computed from 2D histograms in order to include the correlation between both variables. The weights are normalized to its maximum value as it is shown in figure 4.10 for the 1994-1995 simulation data samples.

[4]In the following, the ratios δ_a/σ_a and s_J/σ_J will indicate the proper tight 3D track ratios as well as the corresponding to tight 2D tracks, i.e. η_a/σ_{η_a} and q_J/σ_{q_J} respectively.

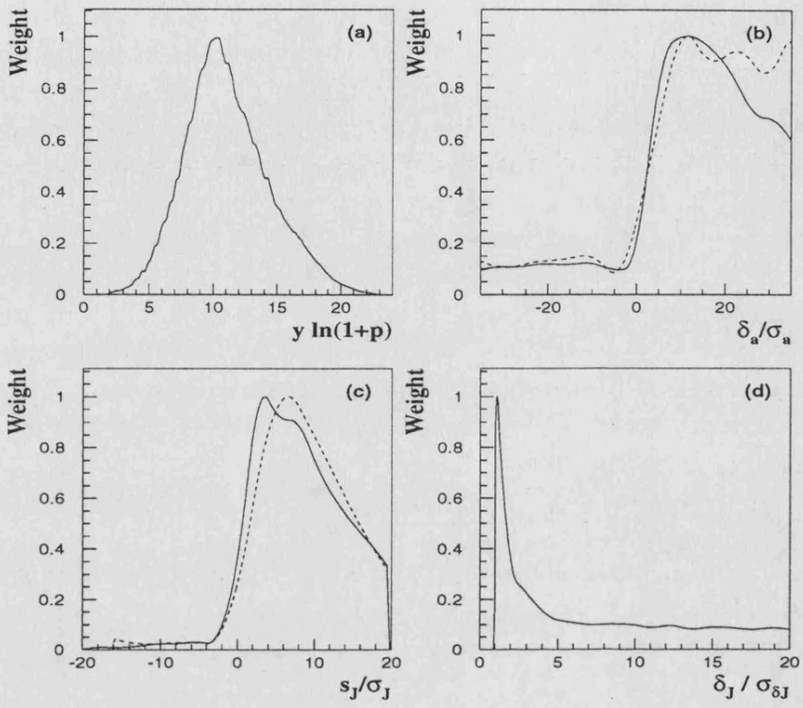

Figure 4.10: Single track weights of B decay products normalized to its maximum value as a function of: (a) the product of the rapidity by the logarithm of the momentum, $y \ln(1+p)$, for all the tight tracks; (b) the significance S for tight 2D (dotted line) and tight 3D (continuous line) tracks; (c) the track-jet abscissa over its error s_J/σ_J for tight 2D (dotted line) and tight 3D (continuous line) tracks; (d) the track-jet distance over its error $\delta_J/\sigma_{\delta_J}$ for tight 3D tracks.

From these individual track weights, two global track weights are computed in an attempt to combine the different informations:

$$\begin{aligned} \mathcal{W}_1^i &= \omega^i(y)\,\omega^i(p)\,\omega^i(S, s_J/\sigma_J) \\ \mathcal{W}_2^i &= \omega^i(y)\,\omega^i(p)\,\omega^i(\delta_J/\sigma_{\delta_J}). \end{aligned} \tag{4.36}$$

$\mathcal{W}_1^i$ and $\mathcal{W}_2^i$ share the rapidity and momentum dependence, but differ in the lifetime weight. The first one, $\mathcal{W}_1^i$, is sensitive to the impact parameter significance S and the normalized track jet abscissa s_J/σ_J. The second weight, $\mathcal{W}_2^i$, is sensitive to the track-jet significance $\delta_J/\sigma_{\delta_J}$. There is no strong physical reason for these combinations which may not be optimal, but they are the best of several tried. How these weights are used in tagging variables is described in section 4.10.

4.10 Definition of the tagging variables

From the ingredients described in previous sections, a set of 13 variables is computed independently in each hemisphere. Some of the variables described in the following were originally proposed in [95]. However, many new variables have been defined and other refined [96]. Here we perform a full description of all the variables.

Figures 4.11 to 4.13 display the distributions of these variables for *uds*, *c* and *b* flavours obtained from the simulated sample tuned for the 1994 DELPHI data. For the 1995 data sample the distribution of all variables is very similar. For 1991-1993 they are, of course, less discriminant but have the same shape. Figures are plotted with a logarithmic scale, and the contributions of the three flavours are on top of each other for readability. Real data are superimposed to show the quality of the Monte Carlo description of the data. For all data samples from 1991 to 1995 the agreement between data and simulation is good.

4.10.1 Variables from secondary vertex search

The following three variables summarize the results of the secondary vertex search described in section 4.8. They include multiplicities, masses and proper decay lengths, and are shown in figure 4.11.

Secondary vertex counter (*SumNSV*)

The *SumNSV* variable tries to count the number of secondary and tertiary tracks from the number of multiplets and singlets obtained in the secondary vertex search algorithm. It is given by:

$$SumNSV = \sum_{n=1}^{6} nN_n \tag{4.37}$$

where N_n is the number of multiplets with multiplicity n.

Secondary vertex proper decay length (*SumDSV*)

The variable *SumDSV* is similar to *SumNSV*. It sums the proper decay lengths of the multiplets weighted by their multiplicities:

$$SumDSV = c\tau_0^0 + \sum_{n=1}^{6} n\overline{c\tau_0^n} \tag{4.38}$$

where $\overline{c\tau_0^n}$ is the average proper decay length of the multiplets with multiplicity n found in the hemisphere. To the sum is added a default value $c\tau_0^0$. In the case when there is no singlets and multiplets *SumDSV* would be zero. The term $c\tau_0^0$ smears this peak at zero and introduces also some decay length information. $c\tau_0^0$ is a proper decay length computed for all the tracks of the most energetic jet of the

hemisphere verifying $p > 1.5$ GeV/c. Apart from this term, when one multiplet is found, *SumDSV* is the product of its proper decay length by its multiplicity.

Secondary vertex mass (*MaxMSV*)

The variable *MaxMSV* is the maximum invariant mass of:

- all the multiplets (multiplicity higher than one);
- all the possible combinations of pairs formed with all the multiplets and singlets. The underlying idea to consider pairs is that, if secondary and tertiary vertices are separated, they should be combined to make a B.

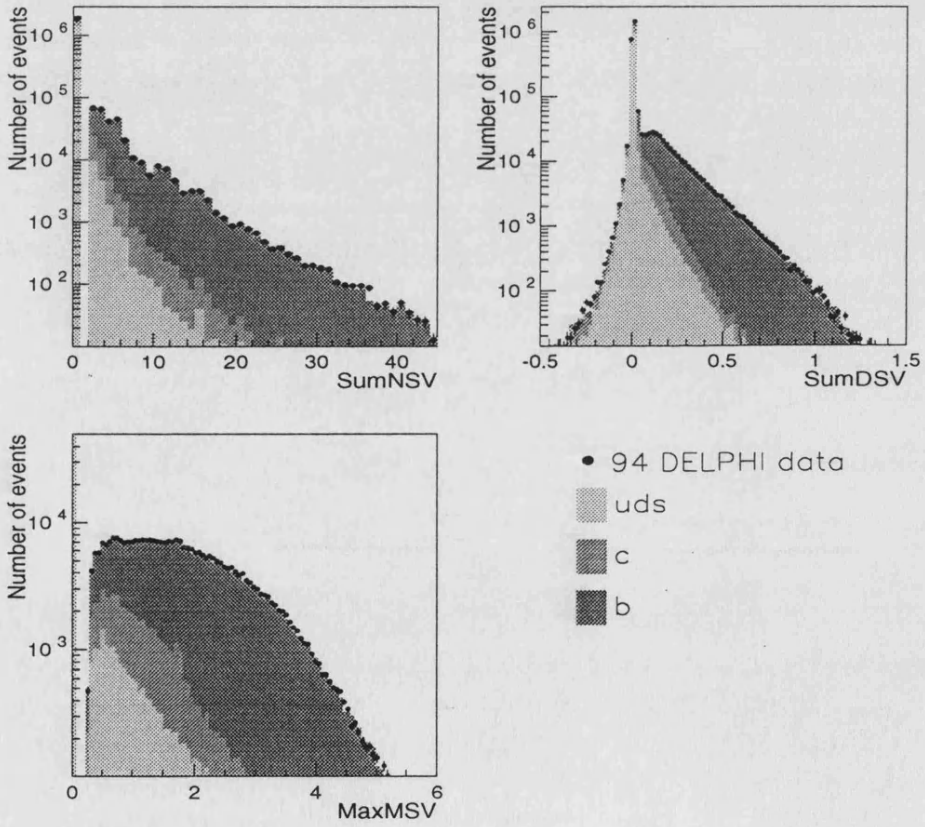

Figure 4.11: Distribution of b tagging variables from secondary vertex search for the 1994 data sample. Real data are superimposed to show the quality of the Monte Carlo description of the data. For simulation the contribution of uds, c and b flavour is also shown.

4.10.2 Variables using B decay weights

The next five variables are weighted counters of B hadron decay products and some of their characteristics. Figure 4.12 displays these variable distributions for *uds*, *c* and *b* flavours for the 1994 DELPHI data and simulation. The most selective by itself is Ω_1.

Weighted mass (ω_{mass})

This is an adaptation of a variable originally proposed by the ALEPH Collaboration [100]. Particles are first ordered by decreasing consistency to be a B decay product, the criteria being the $\mathcal{W}_1^i$ weight. They are iteratively combined, starting from the track of highest *b* consistency, until the invariant mass of the group exceeds 2.0 GeV/c. The value of ω_{mass} is defined as the track weight $\mathcal{W}_1^i$ of the last track added. For *b* hemispheres this can be high since the D hadron mass can be exceeded using only tracks from the B hadron decay; while for *c* hemispheres ω_{mass} is much smaller, since tracks from the primary vertex are needed to exceed the same cut-off. That mass cut helps in the rejection of *c* hemispheres in which the D hadron has an unusual long decay length.

Total weight 1 (Ω_1)

The variable Ω_1 is designed to count the total number of secondary particles and is computed as

$$\Omega_1 = \sum_i \mathcal{W}_1^i. \tag{4.39}$$

Total weighted $p_\perp$ ($\Omega_{p_\perp}$)

This variable is defined as the weighted sum

$$\Omega_{p_\perp} = \sum_i \mathcal{W}_1^i p_\perp^2. \tag{4.40}$$

The sum of $p_\perp^2$ weighted by the *b* probabilities intend to enhance the feature that *b* products have larger $p_\perp^2$ than the average, as described in chapter 1.

Total weighted p (Ω_p)

This is a weighted variable similar to the previous one, which intends to compute the sum of p for secondary particles:

$$\Omega_p = \sum_i \mathcal{W}_1^i p. \tag{4.41}$$

This sum intends to be large for the *b* flavour, because the B hadron carries most of the initial quark momentum (between 70% and 80%).

Total weight 2 (Ω_2)

This variable, specific for 3D tracking, is only defined for the 1994-1995 data samples. Like Ω_1, Ω_2 is designed for counting the total number of 'tertiary' tracks, since the weight $\mathcal{W}_2^i$ based on the track-jet distances is designed to favor these tracks. It is defined as:

$$\Omega_2 = \sum_i \mathcal{W}_2^i. \tag{4.42}$$

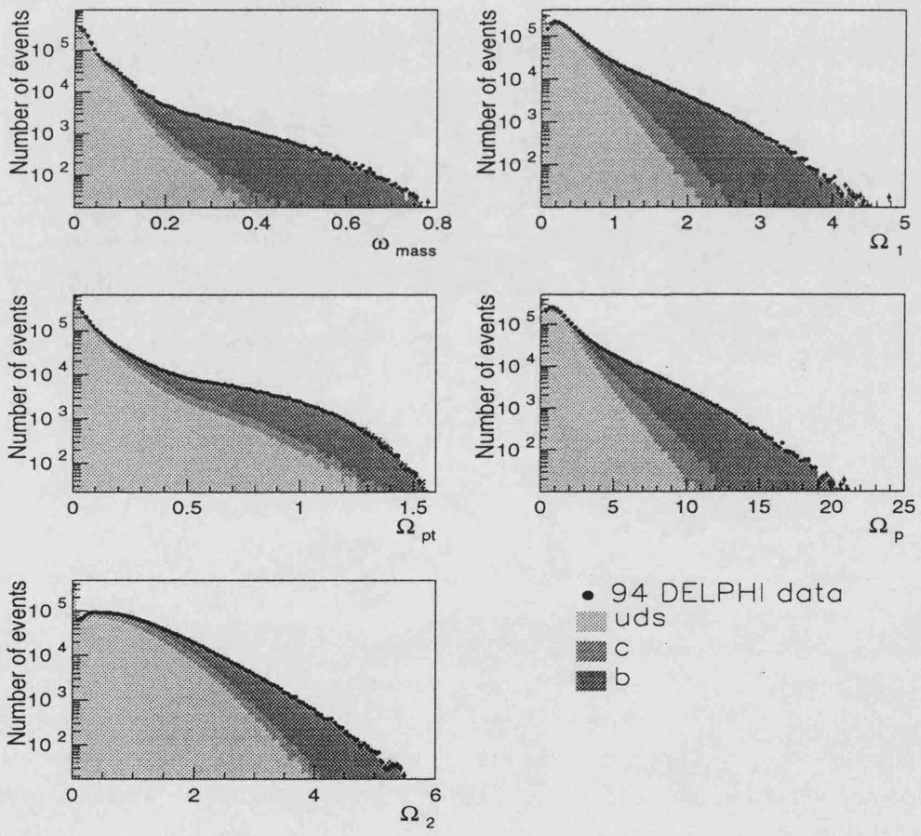

Figure 4.12: Distribution of b tagging variables from single track B decay weights for the 1994 data sample. Real data are superimposed to show the quality of the Monte Carlo description of the data. For simulation the contribution of uds, c and b flavour is also shown.

4.10.3 Miscellaneous variables

Figure 4.13 displays the distributions of the last five variables for uds, c and b flavours corresponding to the 1994 DELPHI data and simulation. They are described in the following.

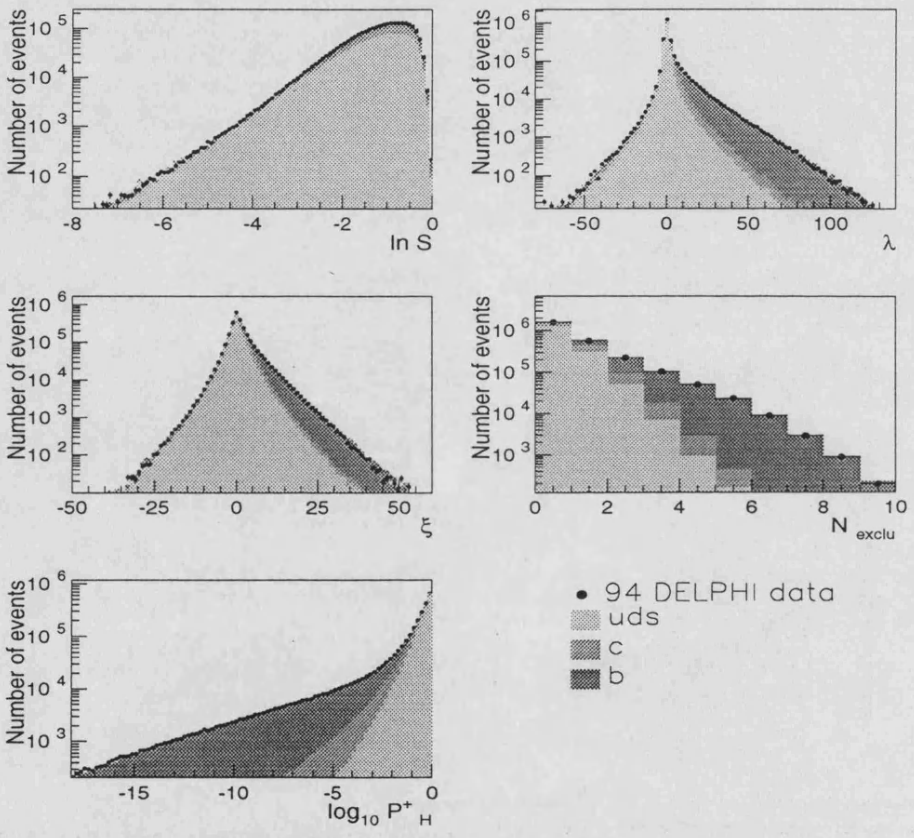

Figure 4.13: Distribution of several b tagging variables for the 1994 data sample: $\ln S$ is the boosted sphericity of the most energetic jet of the hemisphere, the normalized decay path λ, sum of projected impact parameter ξ, the number of excluded particles N_{exclu} in the primary vertex fit and the hemisphere primary vertex decay products probability ($\mathcal{P}_H^+$). Real data are superimposed to show the quality of the Monte Carlo description of the data. For simulation the contribution of uds, c and b flavour is also shown.

Boosted sphericity ($\ln S$)

This variable is the only one computed exclusively with four-momenta. The jet sphericity of the particles belonging to the most energetic jet in the hemisphere is

evaluated with respect to an estimated rest frame of a B hadron. The B hadron is assumed to move along the jet direction. A boost, along the jet direction, with a Lorentz γ parameter is needed to perform the transformation from the laboratory frame to the B rest frame. Monte Carlo studies show that at Z energies the optimum value is $\gamma \simeq 4$. The sphericity in this frame is expected to be larger for $b\bar{b}$ events than for the other flavours. The sphericity is defined as [29]

$$S = \frac{3\sum_a \mid \vec{p}_\perp^{\,a} \mid^2}{2\sum_a \mid \vec{p}^{\,a} \mid^2} \tag{4.43}$$

where $\vec{p}^{\,a}$ is the three momentum of the a^{th} particle and $\vec{p}_\perp^{\,a}$ is the transverse momentum taken relative to the axis which minimizes $\sum_a \mid \vec{p}_\perp^{\,a} \mid^2$ (local sphericity axis).

Normalized decay path (λ)

A 'pseudo' secondary vertex fit is attempted in the hemisphere. The most energetic jet of the hemisphere is again associated to the primary quark direction. Only particles making an angle of less than 20° with the jet axis, with an impact parameter with respect to the hemisphere primary vertex $\vec{V}$ of less than 3 mm in space are candidates to the secondary vertex. The fit provides the position $\vec{A}'_{sc}$ of a secondary vertex and its covariance matrix. If there is only one track remaining in the fit, $\vec{A}'_{sc}$ is taken as the intersection in the $R\phi$ projection or in space of this track and the jet axis passing through the main hemisphere vertex $\vec{V}$. If no track is found in the cone, the procedure is applied to the second most energetic jet.

An algebraic distance D along the jet direction $\vec{J}$ is defined for each hemisphere as

$$D = \overrightarrow{VA'_{sc}} \cdot \vec{J}. \tag{4.44}$$

Dividing by its error σ_D, the 'pseudo' normalized decay path variable λ could be defined as

$$\lambda = D/\sigma_D. \tag{4.45}$$

Sum of normalized track-jet abscissa or projected impact parameter (ξ)

The sum of the normalized track-jet abscissa is defined for tight 3D tracks as

$$\xi = \sum_i s^i_J/\sigma^i_J \tag{4.46}$$

and for tight 2D tracks it is replaced by the normalized projected impact parameter:

$$\xi = \sum_i q^i_J/\sigma_{q^i_J}. \tag{4.47}$$

The ξ distribution is expected to be centered at zero for the *uds* flavours while for *c* and *b* an asymmetry in the positive direction is expected, due to the fact that the decay products have track-jet abscissa or projected impact parameter positive.

Excluded particles (N_{exclu})

N_{exclu} is the number of excluded particles during the iterative procedure of the hemisphere vertex fit described in section 4.4. This variable, which is correlated to the weighted sum Ω_1, is highly selective by itself.

Hemisphere primary vertex probability ($\mathcal{P}_H^+$)

This variable was described with detail in section (4.7). Originally proposed by ALEPH [101], this probability was adapted to DELPHI on the basis of a common event vertex [102]. However, in this analysis, the recalculation of a primary vertex distinct for each hemisphere imposes to recompute the variable in order to redefine the significance S and the resolution function $\mathcal{R}(S)$. The analytical parameterization of the resolution function (taken from the negative part of the significance distribution in the simulation) was computed separately for tight 2D and 3D tracks, needing in both cases four Gaussians plus one exponential function. As tight 2D and 3D tracks may be found together in the same hemisphere, the individual track probabilities take into account the type of each track, and the calculation of the global probability $\mathcal{P}_N$ given in equation 4.33 can be done. To increase the selection power of the variable, only tracks with positive impact parameter (which contain the lifetime information) are included in $\mathcal{P}_N$.

4.11 Flavour confidences

In order to improve the performances of the multivariate technique, we have tried to incorporate the know-how of other multivariate-like techniques developed by DELPHI into a global multivariate classifier. Such a very interesting and elaborated technique, called *flavour confidences*, was proposed in reference [103]. Similarly to the multivariate approach, the confidence method is based not only on the track impact parameters but also on two kinematic variables, the track momentum and the angle with respect to the jet axis. No secondary vertices search is performed. The track information is used in a different way in both techniques, so the overlap between them is expected to be reduced and interesting gains in performances can be obtained in a combination. Like the variable $\mathcal{P}_H^+$ described in 4.10.3, these confidences have been adapted with respect to [103] to the reconstruction of separate primary vertices for hemispheres.

A probability function is build from simulation which gives the fraction of tracks which come from *b*, *c* and *uds* quarks in a 3-D bin of the three particle characteristics: impact parameter over its error δ_a/σ_a, momentum p and angle ϕ to the jet

axis. Kinematic effects in the decay of B hadrons, which produce correlations between the three quantities, are automatically taken into account by the 3-D binning. In the case of momentum and impact parameter an arc tangent transformation is made ($f(\delta_a/\sigma_a) = \tan^{-1}\frac{\delta_a}{10\sigma_a}$ and $g(p) = \tan^{-1}\log_{10} \mid p \mid$ respectively). This transformation of variables ensures that the variables are bounded by $\pm\pi/2$ and makes the distribution somewhat more uniform. The selected angle ranges for each flavour are given in table 4.8. They were chosen in order to have similar statistics in each bin. The distributions are computed separately for each VD hit configuration and were finally smoothed in order to reduce statistical fluctuations in the bin contents.

Table 4.8: The selected ϕ angle ranges. They were chosen in order to have similar statistics in each bin.

Bin number	Phi range
1	$0° - 1.4°$
2	$1.4° - 3.1°$
3	$3.1° - 5.1°$
4	$5.1° - 7.3°$
5	$7.3° - 9.9°$
6	$9.9° - 14.1°$
7	$14.1^0 - 21.6°$
8	$21.6° - 37.9°$
9	$37.9° - 180.0°$

For each single track an individual flavour confidence is computed as

$$C_q(\delta_a/\sigma_a, p, \phi) = \frac{f_q(\delta_a/\sigma_a, p, \phi)}{f_{uds}(\delta_a/\sigma_a, p, \phi) + f_c(\delta_a/\sigma_a, p, \phi) + f_b(\delta_a/\sigma_a, p, \phi)} \tag{4.48}$$

where

$$f_q(\delta_a/\sigma_a, p, \phi) = \frac{N_q(\delta_a/\sigma_a, p, \phi)}{N_q^{total}}. \tag{4.49}$$

$N_q(\delta_a/\sigma_a, p, \phi)$ is the number of events in the bin $(\delta_a/\sigma_a, p, \phi)$ with initial quark flavour q (taken from simulation) and N_q^{total} is the total number summed over all bins. C_q is 1/3 when there is no b enhancement. Figure 4.14 shows, in the case of the 1994-1995 simulation, the zones of high b confidences for tight 3D tracks for the 9 individual ϕ ranges. In this figure, the fraction of tracks in each bin which come from b quarks is represented by the box size. The population size in each of the nine plots are similar. It can be seen that tracks with low angle with respect the jet axis have little b enhancement, while those in bin 5 can give very large weights.

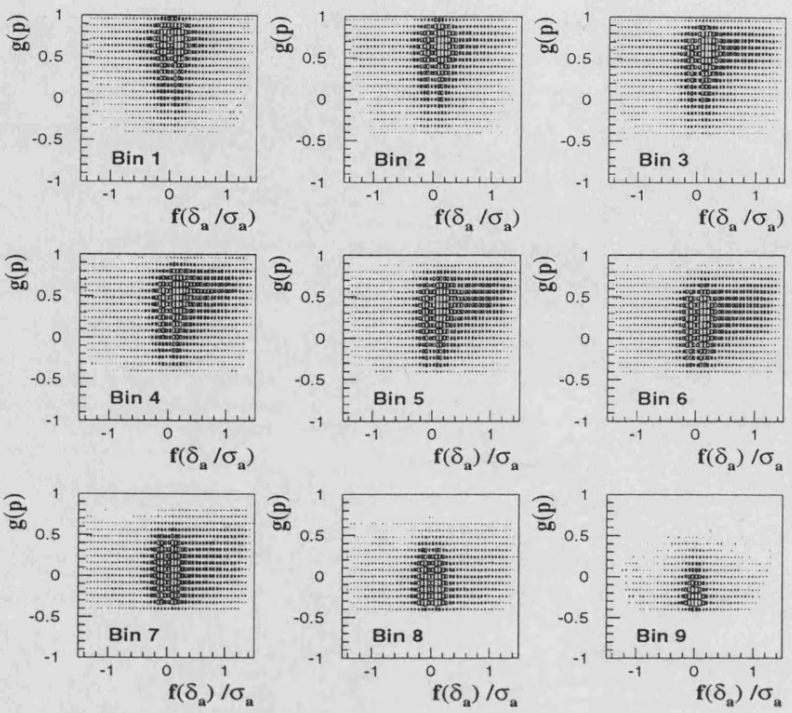

Figure 4.14: Density plots for b track confidences for tight 3D tracks in b events for the 1994 simulation. Each plot corresponds to a range of ϕ between track and jet as given in the text. The abscissa and ordinates are transformations of δ_a/σ_a and p. The fraction of tracks in each bin which come from b quarks is represented by the box size.

The individual flavour confidences must be combined to make the hemisphere tag:

$$\begin{aligned} \mathcal{CONF}_{uds} &= \frac{3\prod_i \mathcal{C}^i_{uds}}{3\prod_i \mathcal{C}^i_{uds} + \prod_i \mathcal{C}^i_c + \prod_i \mathcal{C}^i_b} \\ \mathcal{CONF}_c &= \frac{\prod_i \mathcal{C}^i_c}{3\prod_i \mathcal{C}^i_{uds} + \prod_i \mathcal{C}^i_c + \prod_i \mathcal{C}^i_b} \\ \mathcal{CONF}_b &= \frac{\prod_i \mathcal{C}^i_b}{3\prod_i \mathcal{C}^i_{uds} + \prod_i \mathcal{C}^i_c + \prod_i \mathcal{C}^i_b} \end{aligned} \tag{4.50}$$

$\mathcal{C}^i_q$ being the q-flavour confidence for track i. The factor 3 has the same physical motivation as in equations (4.3).

As was stated in section 4.3, this method of combination may be not optimal, and in addition correlations between tracks are neglected. However it has one very useful feature. If there is a track which carries no information about the flavour of

the event it will have equal confidences for each of the three hypotheses. Therefore all tracks can be included and the maximum information is extracted. Figure 4.15 displays the distribution of the hemisphere confidences for *uds*, *c* and *b* flavours for the 1994 DELPHI data and simulation.

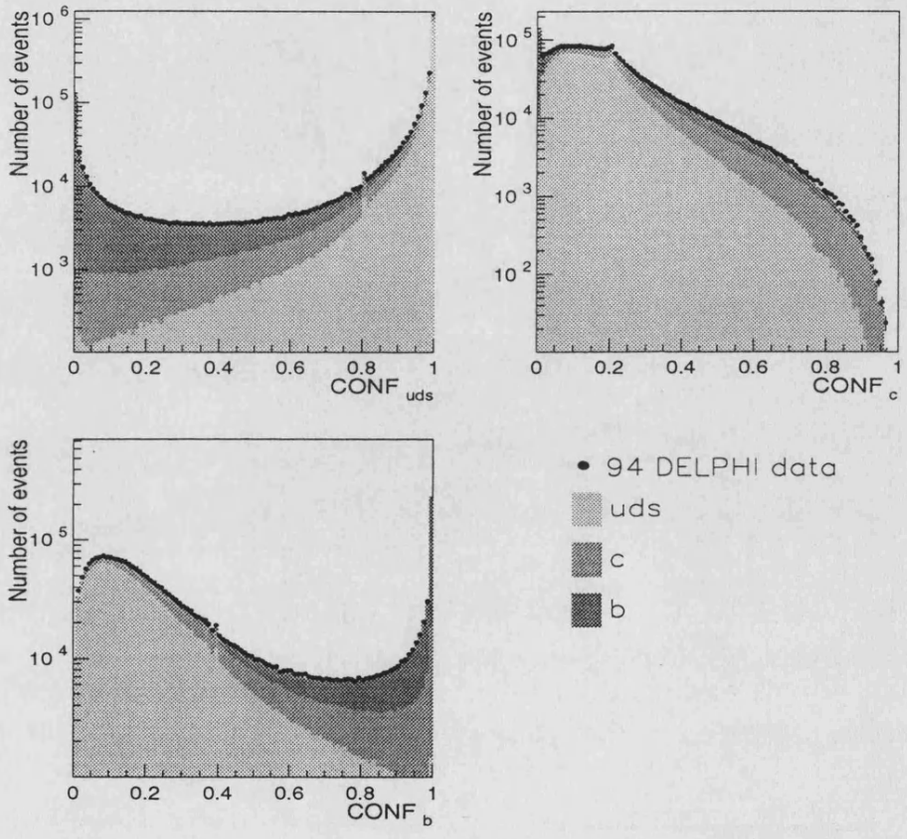

Figure 4.15: Distribution of *uds*,*c* and *b* confidences in 1994 simulation and data. Real data are superimposed to show the quality of the Monte Carlo description of the data. For simulation the contribution of *uds*, *c* and *b* flavour is also shown.

4.12 Combined multivariate/flavour confidences tagging

The two tags, multivariate and flavour confidences, can be combined using a simple linear combination for each flavour. In order to be homogeneous with the multivariate flavour likelihoods $\mathcal{L}_{uds}$, $\mathcal{L}_c$ and $\mathcal{L}_b$, we have to take the logarithm of the

difference to unity of the each flavour confidence:

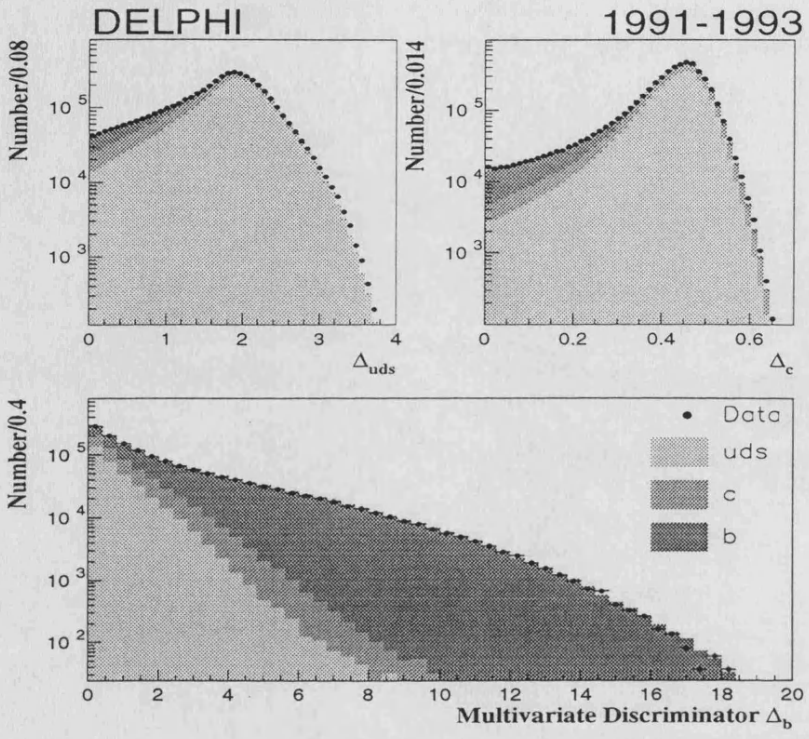

Figure 4.16: Distribution of the multivariate discriminator Δ in the *uds*, *c* and *b* tags for all the 1991 to 1993 data and simulation. The different types of shading show the different flavour contributions to the simulated event sample. The simulation distributions are normalized to the data statistics. Only the positive part of Δ_q is shown.

$$\begin{aligned} \Delta_{uds} &= (1-\alpha)\mathcal{L}_{uds} - \alpha \ln(1 - \mathcal{CONF}_{uds}) \\ \Delta_c &= (1-\alpha)\mathcal{L}_c - \alpha \ln(1 - \mathcal{CONF}_c) \\ \Delta_b &= (1-\alpha)\mathcal{L}_b - \alpha \ln(1 - \mathcal{CONF}_b). \end{aligned} \tag{4.51}$$

The quantities Δ_{uds}, Δ_c and Δ_b are called *flavour multivariate discriminators* and are the basis of the classification. This way to combine has been proven to be the best of several tried. It could also be possible to optimize a different value of α for each flavour, but it happens that in practice the same value optimize the three flavours. The quoted value was $\alpha = 0.8$. The apparently high ratio $\alpha/(1-\alpha) = 4$ is due to the fact that the range definition of the multivariate flavour likelihoods is higher than the corresponding to the flavour confidences ($\mathcal{L}_{uds}$, $\mathcal{L}_c$ and $\mathcal{L}_b$ are calculated from the 13 variables described in section 4.10, while the flavour confidences are

based on the 3 variables of section 4.11). It corresponds approximatively to an equal weight of the two components. Figures 4.16 and 4.17 show the distributions of the flavour multivariate discriminators for all the 1991 to 1993 and 1994-1995 data and simulation separately. It can be seen that the agreement between data and Monte Carlo is good, thanks to the very fine physics and detector tuning of the simulation. It proves that the simulation describes properly the performance of the multivariate tag, so reliable estimations of systematic errors can be quoted.

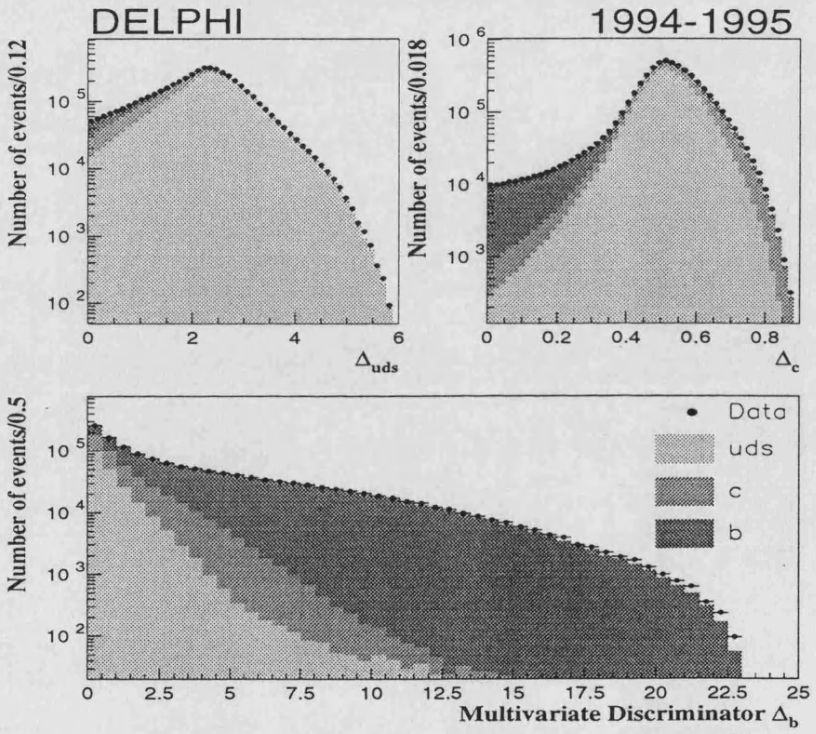

Figure 4.17: Distribution of the multivariate discriminator Δ in the *uds*, *c* and *b* tags for all the 1994-1995 data and simulation. The different types of shading show the different flavour contributions to the simulated event sample. The simulation distributions are normalized to the data statistics. Only the positive part of Δ_q is shown.

4.13 Tagging performances

The efficiency of the hemisphere *b* tag as a function of the *b* purity for each data set is given in figure 4.18. Figure 4.19 plots for the three tags the *background efficiencies* versus the tag efficiency. The background efficiencies are the probabilities to classify the wrong flavours in a given tag. Results have been averaged and presented

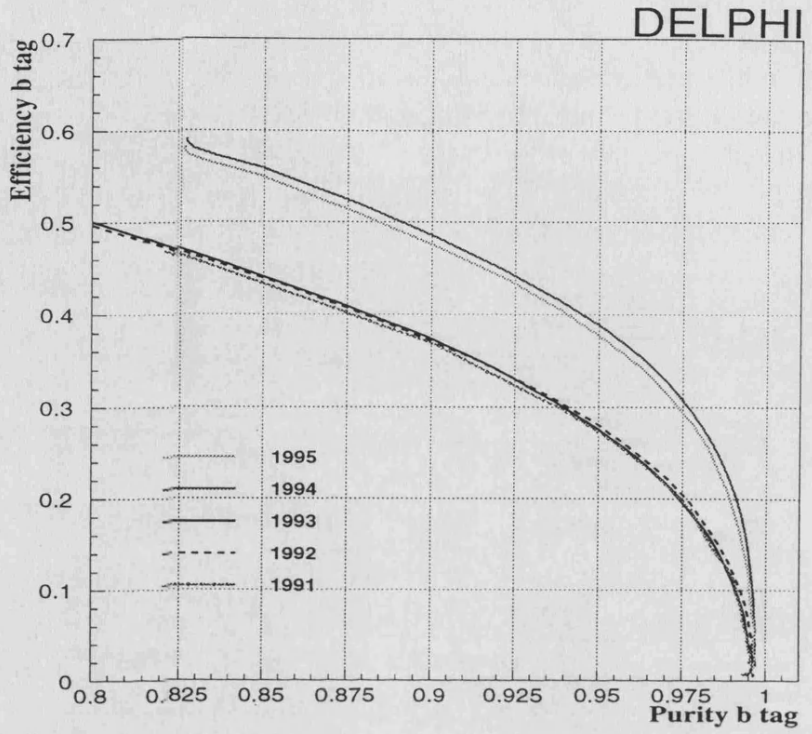

Figure 4.18: The hemisphere b efficiency obtained as a function of the b purity in tagging hemispheres with the multivariate technique for each year.

separately for the 1991-1993 and 1994-1995 periods, since the different microvertex setup leads to different tagging performances. The plots are obtained for hemispheres within an angular acceptance of 0.65 on $|\cos\theta_{thrust}|$. From figure 4.18, for purities of 90%, the efficiency is approximately 48% in 1994-1995 and about 37% in 1991-1993. At 95% purity, efficiencies are about 38% and 28% respectively. At 98% purity, the efficiencies drop to about 28% and 18%. Reading figure 4.19, for a 20% b efficiency, the mistag probabilities are: a) in 1994-1995, less than 0.02% for uds quarks and 0.2% for c quarks, and b) in 1991-1993, about 0.04% for uds and 0.6% for c quarks. Therefore very high purities can be reached in the b identification with relatively important b efficiencies.

It should be stressed that this tool provides also uds and c tags. Their performances are by far poorer than for the b tag. For instance, for a 15% uds tag efficiency, the background efficiencies are about 5% for c quarks and less than 1% for b quarks, for all data. For a 15% c tag efficiency, the background efficiencies are less than 5% for both uds and b quarks in 1994-1995 data. In the 1991-1993 data, and for the same efficiency, the uds background is about 7% and the b background less than 7%. Figure 4.20 shows the efficiencies of the hemisphere uds and c tags

as a function of the corresponding purities for each data sample. Interesting is the improvement in c performances of the 1994-1995 data sample with respect to the 1991-1993. These tags can be used alone or combined between them and with the powerful b tag. For example, the quality of the uds and c tags can be improved by reducing b contamination by imposing extra cuts on the b multivariate discriminator $\mathcal{L}_b$.

However, although the uds and the c tags are poor when compared to the b tag ones, both tags can help in the rejection of b tag backgrounds for the precise R_b determination. Moreover, and what it is more interesting, they are a fundamental part of the technique used to self-calibrate the tagging (chapters 5 and 6), reducing dependences on simulation models and therefore reducing important systematic uncertainties affecting the R_b determination.

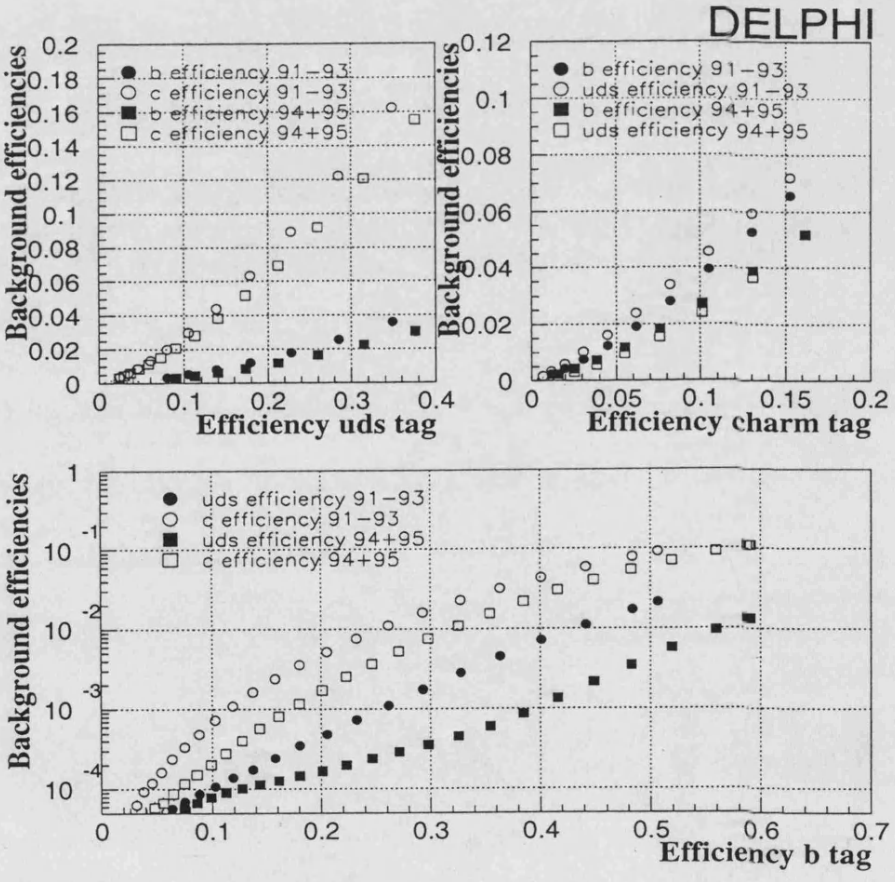

Figure 4.19: The hemisphere backgrounds in each flavour tag as a function of the corresponding flavour efficiency with the multivariate technique. The quoted performances are shown for 1991-1993 and 1994-1995 data separately due to the different tagging performances and the different microvertex detector setup.

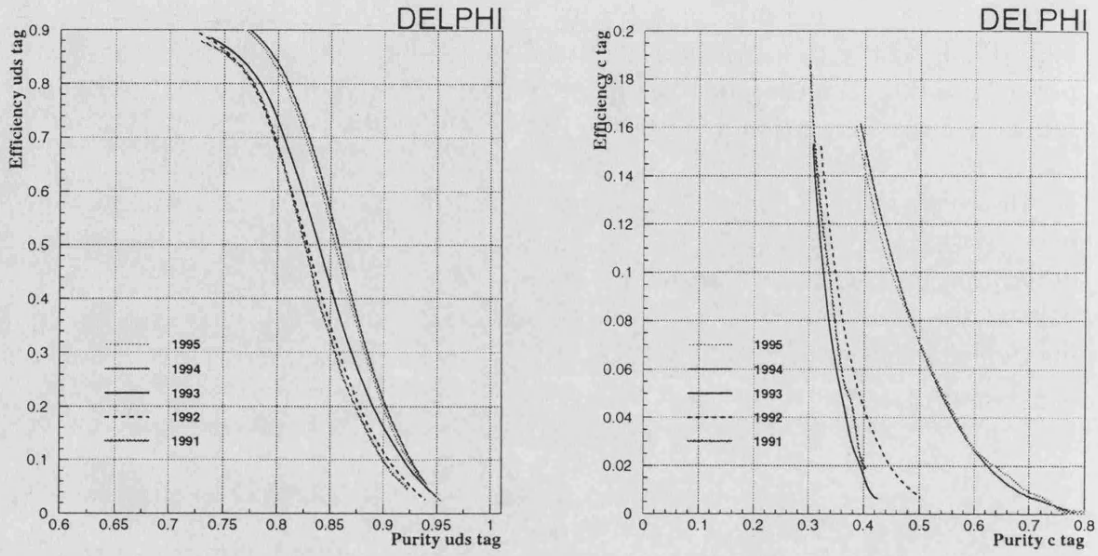

(a) (b)

Figure 4.20: The hemisphere *uds* and *c* efficiency obtained as a function of the *uds* and *c* purity in tagging hemispheres with the multivariate technique for each data taking period.

Figures 4.21 and 4.22 show the event display with a full tracking reconstruction in DELPHI of two clearly identified b and *uds* events respectively. The plots show the VD, ID and TPC detectors in the $R\phi$ and yz planes in four different views of the same event. As it was described in chapter 1, the presence of tracks coming from two secondary vertices and tracks produced in fragmentation coming from the primary vertex is very clear in the b tagged event. In the case of the *uds* event, only tracks produced in the primary vertex are detected. In addition it can also be seen the difference in charged track multiplicity and event shape topology. The tracks used for the vertex fits have hits in at least two layers of the VD.

4.14 The combined impact parameter tag

In this last section we describe briefly a tagging technique, which is not part of the multivariate technique, developed by DELPHI in order to improve the accuracy on R_b. This method, called combined impact parameter tag, is the result of longstanding efforts within the Collaboration to obtain a simple and high efficiency/purity performance b tagging. Its discriminator, defined below in equation (4.53), will be used together with the multivariate discriminators Δ_{uds}, Δ_c and Δ_b to define several tagging categories in a high precision multiple tag (chapter 5) measurement of

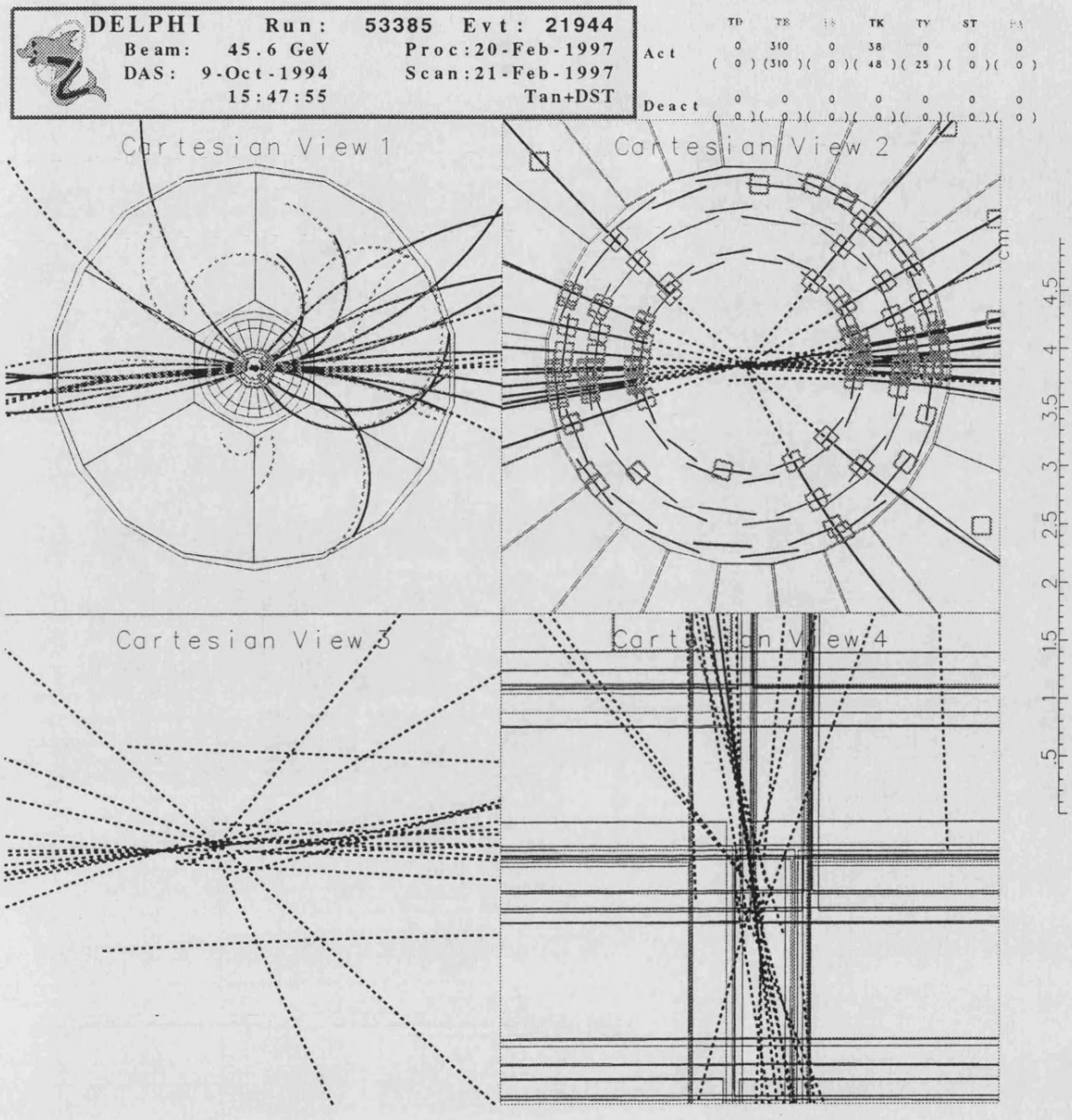

Figure 4.21: Event display of a b tagged event showing the track fitting (solid lines) through VD, ID and TPC together with the track extrapolation to the interaction point (dashed lines) and the primary and secondary vertex reconstruction. Squares and points are single hits in the detectors. The views correspond to: (Cartesian view 1) $R\phi$ plane, (Cartesian view 2) zoom in the $R\phi$ plane of the VD region, (Cartesian view 3) zoom in the $R\phi$ plane of the interaction region, (Cartesian view 4) zoom in the yz plane of the interaction region. The scale corresponds to the Cartesian views 3 and 4. Only tracks with VD hits are extrapolated.

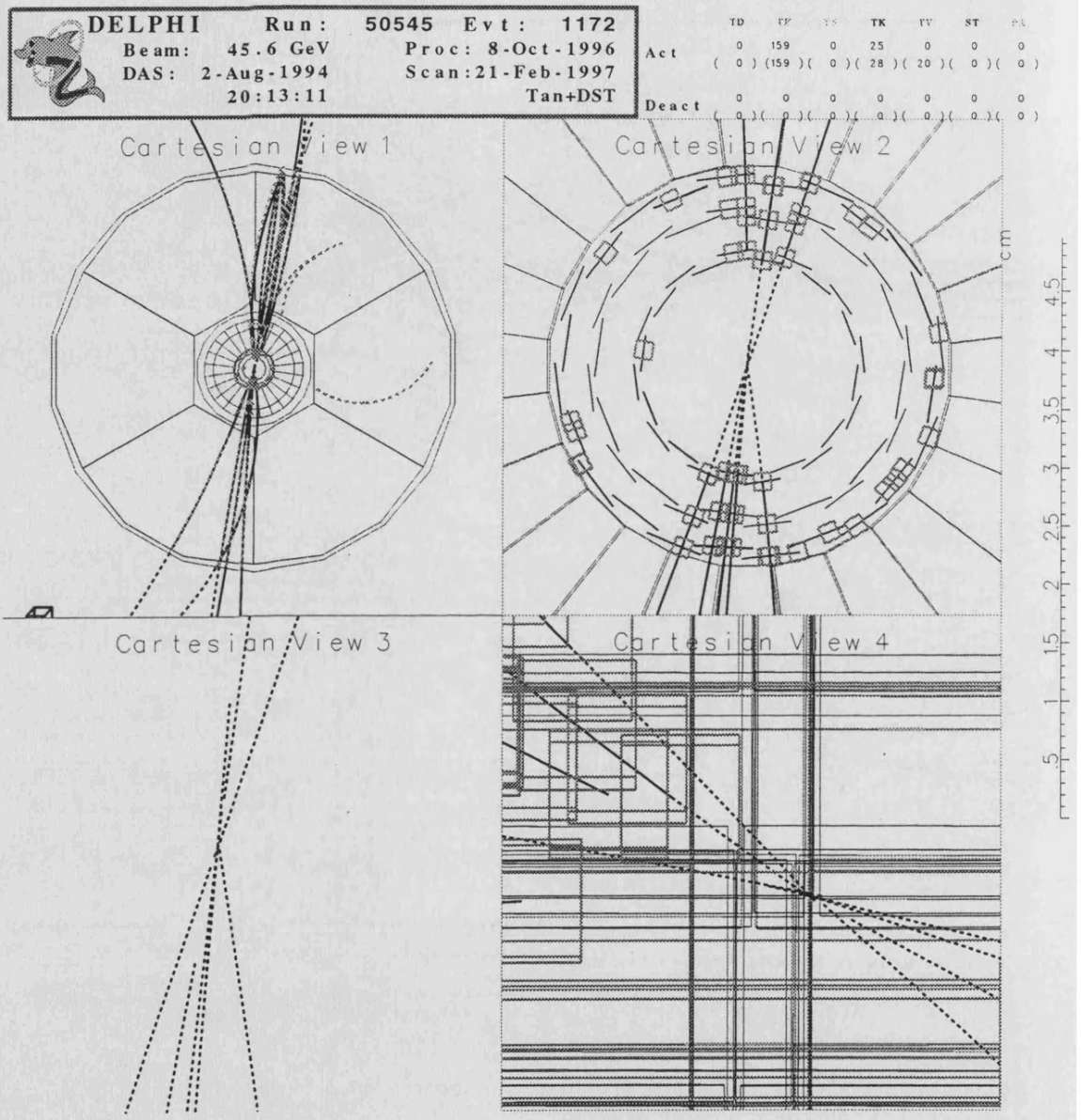

Figure 4.22: Same as previous figure but for an *uds* tagged event. Only tracks with VD hits are extrapolated.

R_b. The combined impact parameter tag will be used only to define the tagging category with the highest b purity, while the others are defined with the help of the multivariate discriminators. Besides its optimized performances for b separation in the high purity region, the combined impact parameter tag, being simpler than the multivariate algorithm, allows a better control of the charm and light quark background systematics (chapter 6).

This tagging method is described in detail in [104]. As the multivariate algorithm, it combines several decay characteristics of B hadrons. All discriminating variables are defined for jets (using JADE algorithm with y_{cut}=0.01) with reconstructed secondary vertices. Such a condition allows to use the specific properties of B hadrons for the tagging and also the separation of their decay products from the particles coming from b quark hadronization. The jets without reconstructed secondary vertices are not considered. In addition, the requirement of jets with reconstructed secondary vertices is a good selection by itself as it removes a significant part of the background. The purity of B hadrons in jets with secondary vertices is about 85% with a selection efficiency of almost 50%.

The reconstructed secondary vertex is required to contain at least two tracks not compatible with the primary vertex and to have $L/\sigma_L > 4$, where L is the distance from the primary to the secondary vertex and σ_L is its error. Each track included in the secondary vertex should have at least one hit in the VD and at least two tracks should have hits in both the $R\phi$ and the Rz planes of the VD.

The description of the four discriminating variables is as follows:

- The jet lifetime probability, $\mathcal{P}_j^+$, is constructed from the positively signed impact parameters of the tracks included in a jet and corresponds to the probability of a given group of tracks being compatible with the primary vertex, as described in section 4.7. For jets with B hadrons, this probability is very small due to the significant impact parameters of tracks from B decays. However, jets with c quarks can also have low values of $\mathcal{P}_j^+$ because of the non-zero lifetime of D mesons, which limits the performance of the lifetime tag. The distribution of $-\log_{10}(\mathcal{P}_j^+)$ for different quark flavours is shown in figure 4.23.a.

- The effective mass distribution of particles included in the secondary vertex, M_s, is shown in figure 4.23.b. The mass of the secondary vertex for c jets is limited by the mass of D mesons and above $M_s = 1.8\,\mathrm{GeV}/c^2$ the number of vertices in c jets decreases sharply, while that in b jets extends up to $5\,\mathrm{GeV}/c^2$.

- The rapidity distribution of tracks included in the secondary vertex with respect to the jet direction, R_s^{tr}, is shown in figure 4.23.c. Although a B hadron has on average higher energy than a D meson from a c jet, the rapidity of particles from a B decay is on average less than that from a c quark decay. This could be explained by the higher mass of the B hadron and the larger multiplicity of its decays. The secondary vertices in light quark jets are induced mainly by wrongly measured tracks. The wrong measurements occur

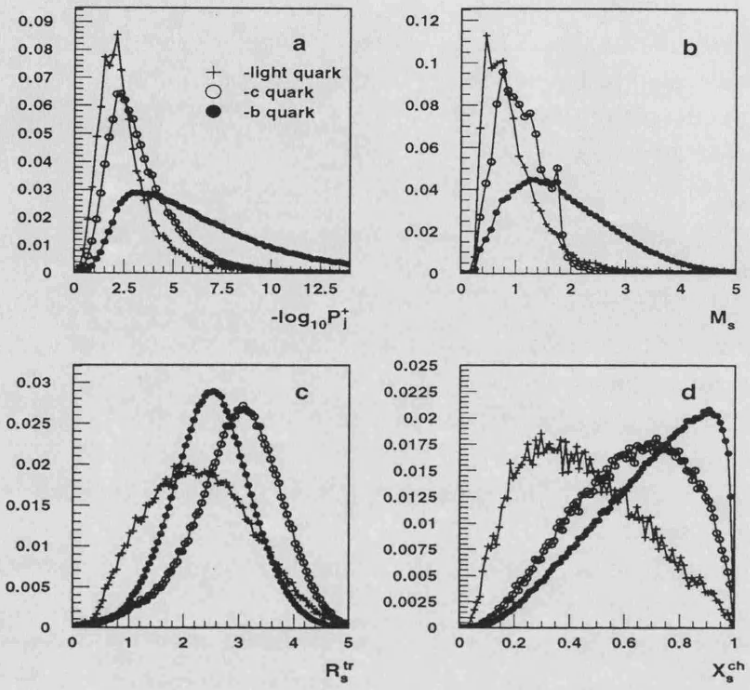

Figure 4.23: Distributions of discriminating variables used in the combined impact parameter tagging: (a) the jet lifetime probability, $\mathcal{P}_j^+$; (b) the effective mass distribution of particles included in the secondary vertex, M_s; (c) the rapidity distribution of tracks included in the secondary vertex with respect to the jet direction, R_s^{tr}; (d) the fraction of the charged energy distribution of a jet included in the secondary vertex, X_s^{ch}.

due to multiple scattering in the detector, interactions in the material, etc. so that tracks included in the secondary vertices of light quark jets are usually soft and their rapidity distribution is shifted to lower values.

- The fraction of the charged energy distribution of a jet included in the secondary vertex, X_s^{ch}, for different quark types is shown in figure 4.23.d. In the case of B hadrons, when almost all the particles included in the secondary vertex come from the B decay, the distribution of X_s^{ch} is determined by the fragmentation function $f(b \to B)$. The same is valid for c quark jets, where the distribution of X_s^{ch} is determined by $f(c \to D)$, which is softer than $f(b \to B)$. In light quark jets, the energy of the secondary vertex is much less than that in b quark jets.

The problem now is how to construct the combination of the different discriminating variables into a single tagging variable. First, we denote as $f^B(z)$ and $f^S(z)$

the probability density functions of the variable z for background and signal events respectively. We assume that the ratio $y = f^B(z)/f^S(z)$ is a monotonously decreasing function with increase of z. Then, if we select events in some band $[z_1, z_2]$, the addition of all events with $z > z_2$ can only increase the purity of the sample. The selection of events can then be realized with the condition $y < y_0$.

In the case of several independent discriminating variables $\left\{z^1, ..., z^N\right\}$, we can write

$$y = \frac{f^B(z^1, ..., z^N)}{f^S(z^1, ..., z^N)} = \prod_{i=1}^{N} \frac{f_i^B(z^i)}{f_i^S(z^i)} = \prod_{i=1}^{N} y_i \tag{4.52}$$

where $f_i^B(z^i)$, $f_i^S(z^i)$ are probability density functions for background and signal for the variable z^i and $y_i = f_i^B(z^i)/f_i^S(z^i)$. The events with $y < y_0$ are tagged as signal, where the cut value y_0 can be varied to select desired purity or efficiency of tagging.

As the two types of background (jets generated by c quarks and by uds quarks) are independent and have different distributions of discriminating variables, the combined variable to tag B hadrons in the jet with reconstructed secondary vertex is defined as

$$y = n_c \prod_i \frac{f_i^c(z^i)}{f_i^b(z^i)} + n_{uds} \prod_i \frac{f_i^{uds}(z^i)}{f_i^b(z^i)} = n_c \prod_i y_i^c + n_{uds} \prod_i y_i^{uds} \tag{4.53}$$

where n_c, n_{uds} is the normalized number of jets with a reconstructed secondary vertex in c and uds events respectively ($n_c + n_{uds} = 1$) and $f_i^{uds}(z^i)$, $f_i^c(z^i)$, $f_i^b(z^i)$ are probability density functions of the variable z^i in uds, c and b quark jets. The products in (4.53) run over all tagging variables of a given jet. The variable R_s^{tr} is defined for each particle included in the secondary vertex and so the corresponding ratio of probabilities for each particle enters in equation (4.53). For the transformations $y_i^c(z^i) = f_i^c(z^i)/f_i^b(z^i)$ and $y_i^{uds}(z^i) = f_i^{uds}(z^i)/f_i^b(z^i)$ we use smooth functions which are obtained from a fit of the ratios of the corresponding distributions.

The tagging procedure defined in such a way is simple and allows to include more discriminating variables. However, in practice the number of variables is limited to 4 because the application of the tagging method assumes that all variables are independent, and requires the choice of variables with reduced correlation. Alternatively, one can use a n-dimensional definition (similar to the one used in the flavour confidence tagging method of section 4.11 for the case of $n = 3$) to take into account the correlation of variables. But it is technically difficult for $n > 2$.

Figure 4.24 shows the tagging efficiency versus purity of the selected sample for different combinations of discriminating variables. It can be seen that the addition of each new variable improves the tagging performance. The variable X_s^{ch} is very weak and can hardly be used for tagging by itself. However, the addition of such variable improves the combined tagging. The overlap of background and signal for variable R_s^{tr} is also big, as it can be seen from figure 4.23, but due to large number

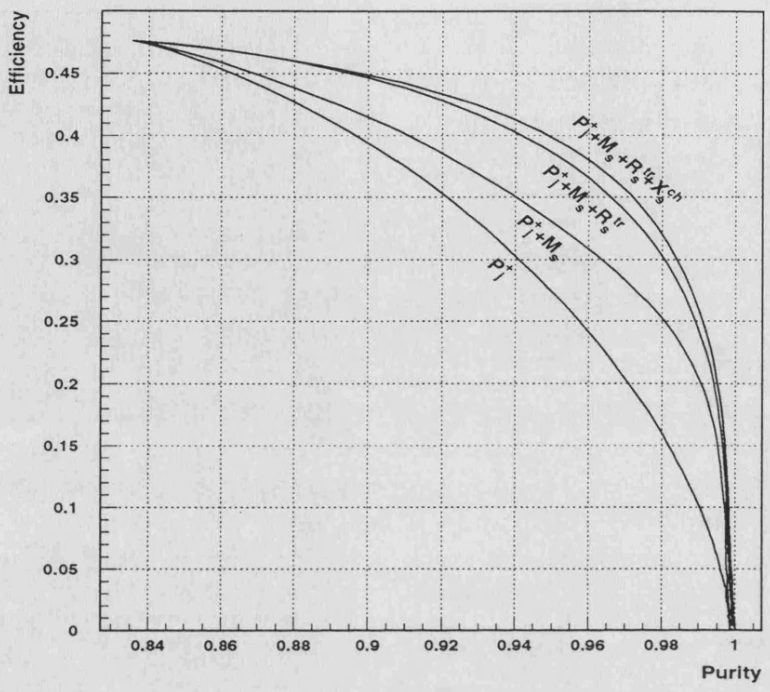

Figure 4.24: b tagging efficiency versus purity of selected sample of jets with reconstructed secondary vertices for different compositions of discriminating variables, with the combined impact parameter tagging.

of secondary tracks the gain in the tagging efficiency with the addition of R_s^{tr} is significant.

The combined tagging in comparison with the simple lifetime tag $\mathcal{P}_j^+$ suppresses the content of background by more than 3 times for a b tagging efficiency of 30% and about 6 times for a b tagging efficiency of 20%. A very pure b sample with purity greater than 99.5% can be obtained with the sizable b efficiency of 20%. These performances can be compared to those achieved for b quarks with the multivariate tagging, as shown in figure 4.18. It can be seen that they are slightly better in the high purity region, for instance 32% efficiency compared to 29% at 98% purity. At lower purity it is the opposite, as for example 47% compared to 55% at 85% efficiency[5]. This fact, together with the simpler technique, justify our choice of using the combined tag to define the category of highest purity and the multivariate tag to define all the other categories, in a multiple tag scheme R_b determination, as

[5]The differences in fact are smaller because these values were obtained with slightly different hadronic event selection in both cases: the multivariate technique required at least 5 charged tracks, compared to at least 6 in the combined impact parameter tag.

described in next chapter.

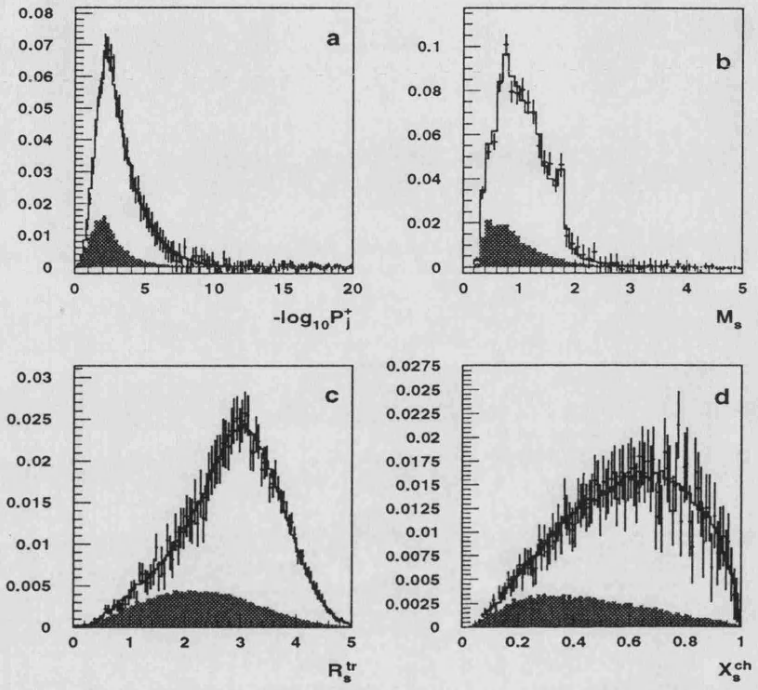

Figure 4.25: Distribution of discriminating variables for background (u, d, s, c) jets used in the combined impact parameter tag. The points with errors are from the data and histogram is the simulation prediction. The contribution of light quark jets is shown as the filled histograms.

All distributions for this tagging method are taken from simulation, so that a check of their agreement with data is important for its successful application. For a measurement of R_b, only the agreement of background distributions should be verified since the efficiency of b quark tagging is taken from data.

The high purity of the tagged sample allows the extraction from data of the distributions of the discriminating variables for background and the comparison of them with those used in the simulation. B hadrons in one hemisphere are tagged with a high purity of about 99% to give a clean and almost uncontaminated sample of B hadrons in the opposite hemisphere. The distributions of the discriminating variables in such hemispheres can be subtracted after appropriate normalization from the corresponding distributions in the untagged sample of jets with secondary vertices. The untagged sample contain large contamination from other quark flavours and thus the distributions of discriminating variables for background can be obtained.

The comparison of these distributions for data and simulation is shown in fig-

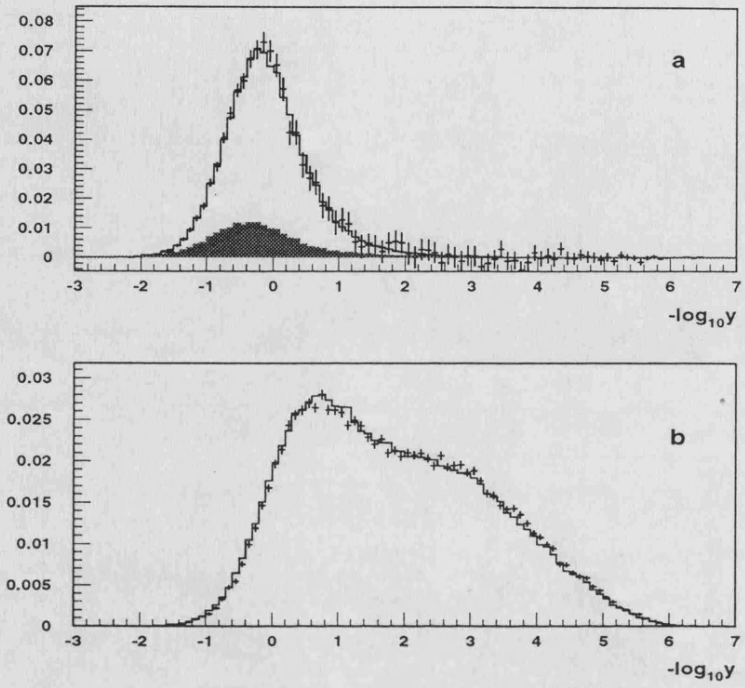

Figure 4.26: Distribution of the combined tagging variable $-\log_{10} y$ for (a) background (u, d, s, c) jets and (b) jets with b quarks. The points with errors are from the data and the histogram is the simulation prediction. The contribution of light quark jets is shown as the filled histogram in the upper figure.

ure 4.25. Good agreement in the background description for all the variables used in the tagging can be seen. The variable $-\log_{10} \mathcal{P}_j^+$ for background is sensitive to the track resolution and confirms that the applied tuning of resolution gives reasonable agreement between data and simulation. The distribution of the track rapidity depend on the modeling of the physics processes. Again a good agreement between data and simulation for background can be stated. Finally, figure 4.26 shows the comparison of the distributions for the combined tagging variable $-\log_{10} y$, where y is defined by (4.53). As before, for the multivariate tagging, it proves that the simulation describes properly the performance of the combined impact parameter tag, so reliable estimations of systematic errors can be quoted.

Chapter 5

How to measure R_b: the multiple tag scheme

This chapter is devoted to the description of the mathematical formalism that allows to measure precisely the branching ratio R_b using the flavour tagging techniques already described. We shall review several techniques and justify the choice of the so called *multiple tag* scheme that we have developed for that purpose. This method has the advantage to optimize the statistical error while minimizing at the same time the dependence on Monte Carlo simulation, reducing therefore also the systematic uncertainties.

The experimental determination of R_b is in principle easy. From a general point of view, tagging variables associated to a hadronic Z event can be summarized into a global event discriminator Θ. One can define a cut value (let us call it Θ_0) and associate to the $b\bar{b}$ class those events for which $\Theta > \Theta_0$, and to the complementary class (non $b\bar{b}$ events) those for which $\Theta \leq \Theta_0$. The fraction R^E of events classified as $b\bar{b}$ is

$$R^E = R_b \epsilon^b + (1 - R_b)\epsilon^{udsc} \tag{5.1}$$

where ϵ^b is the fraction of $b\bar{b}$ events classified as such and ϵ^{udsc} is the fraction of non-$b\bar{b}$ events classified as $b\bar{b}$ (b tag background efficiency). From this equation, one can determine R_b if ϵ^b and ϵ^{udsc} are computed from simulation.

Nevertheless, one can proceed more precisely as follows. The fraction of $b\bar{b}$ events can be determined from the data by means of a fit in the unknown parameter R_b through the expression

$$\mathcal{R}(\Theta) = R_b \varphi^b(\Theta) + (1 - R_b)\varphi^{udsc}(\Theta) \tag{5.2}$$

where $\mathcal{R}(\Theta)$ is the normalized distribution of the data mapped through the variable classifier Θ; $\varphi^b(\Theta)$ and $\varphi^{udsc}(\Theta)$ are the normalized distributions of the classes for $b\bar{b}$ and lighter quark events respectively, obtained by simulation.

The huge drawback of this *event single tag* scheme for the determination of R_b is the dependence on the simulation for the determination of ϵ^b and ϵ^{udsc} or $\varphi^b(\Theta)$ and

$\varphi^{udsc}(\Theta)$, introducing therefore large systematic uncertainties on R_b. This is not a problem when precisions on R_b at the level of 5-10% are required. This technique was used for the first LEP measurements of R_b, using tagging variables as:

- the high total and transverse momentum of leptons coming from semileptonic b decays [105, 106];
- event shape properties, as the boosted sphericity product [107]; and
- neural network outputs combining event shape properties [108].

In the lepton analyses, the number of prompt leptons in a sample of hadronic events is determined by the products $R_b Br(b \to l)$, $R_b Br(b \to c \to l)$ and $R_c Br(c \to l)$. The individual factors in the products can be isolated by a simultaneous consideration of the $(p, p_\perp)$ spectrum of single and dilepton events. In general, the fits are extended to include A^b_{FB}, A^c_{FB}, the average scaled energies of weakly decaying B and D hadrons $< x_E(c) >$ and $< x_E(b) >$ respectively, the average b mixing parameter $\bar{\chi}$ and R_c (the latest one because of the existence of prompt leptons from the decay $c \to l$). Errors arise from the assumed knowledge of lepton identification efficiencies and the contamination by instrumental backgrounds, as well as from semileptonic decay models, semileptonic branching ratios and b and c fragmentation models [109]. The small number of dilepton events limits also the statistical error. The combined errors obtained by the LEP Collaborations on R_b using this technique is about 2% [106, 6].

With the event shape variables and neural networks, R_b is measured from a fit to the data distribution of the event shape variable or neural network output respectively, by varying the b and non b contribution from simulation. The statistical error is improved with respect to the lepton analyses because there is no more restriction to a particular decay channel, but the systematic error is affected by large uncertainties in the fragmentation (in both the light and heavy flavour sectors), which reflect uncertainties in tagging efficiency for the event single tag method. These kind of analyses are statistically powerful, but rely on Monte Carlo simulation to describe the shape of b and *udsc* quark events and therefore results in large systematic errors. The combined LEP precision of this kind of analyses does not exceed some 3-4% [107, 108].

Therefore, the required high precision (better than 0.5%) asks for more refined techniques. The step forward in the high precision was done with the introduction of the double *hemisphere single tag* and the double *hemisphere multiple tag* schemes. The latest one that we have developed is the main subject of the present thesis.

5.1 Hemisphere single tag scheme

If with some criteria a pure b flavour sample can be selected in one hemisphere, it is possible to find the efficiency of this selection and the fraction of $b\bar{b}$ events

in the initial sample in an almost model independent way. It can be quoted by measuring the number of selected single hemispheres and the number of events in which both hemispheres were selected. In this way the dependence on simulation is largely reduced. This double tag technique or *hemisphere single tag* scheme uses two experimental facts, already described in previous chapters: i) in a hadronic decay, the Z boson always decays into a pair of quarks with identical flavour, and ii) due to the momentum conservation, the quarks produced (and the jets coming from them) fly in opposite directions. One can thus separate the event in two almost independent hemispheres by cutting it by a plane perpendicular to the event axis (for instance the event thrust axis), as it was done in chapter 4.

In practice the situation becomes more difficult because the background from the other flavours cannot be fully suppressed and thus it must be subtracted properly. Additional problems arise from the fact that the hemispheres are not absolutely independent and the tag in one hemisphere biases the efficiency in the other one, though this bias is small.

These statements may be expressed in the following form. If with some tag the efficiencies to select different flavours in one hemisphere are ϵ^b, ϵ^c and ϵ^{uds} and the efficiencies to select events in which both hemispheres are tagged are ϵ_d^b, ϵ_d^c and ϵ_d^{uds}, one can write:

$$R^H = \epsilon^b R_b + \epsilon^c R_c + \epsilon^{uds}(1 - R_b - R_c) \tag{5.3}$$

$$\begin{aligned} R^E &= \epsilon_d^b R_b + \epsilon_d^c R_c + \epsilon_d^{uds}(1 - R_b - R_c) \\ &= \epsilon^b \epsilon^b (1 + \rho_b) R_b + \epsilon^c \epsilon^c R_c + \epsilon^{uds}\epsilon^{uds}(1 - R_b - R_c). \end{aligned} \tag{5.4}$$

In these equations R^H is the fraction of tagged hemispheres, R^E the fraction of events in which both hemispheres are tagged and R_b and R_c the fractions of $Z \to b\bar{b}$ and $Z \to c\bar{c}$ events respectively in the initial hadronic sample. It is supposed that hadronic decays of the Z consist of $b\bar{b}$, $c\bar{c}$ and uds quark final states, so that the fraction of light quarks may be written as $R_{uds} \equiv (1 - R_b - R_c)$. The double tag efficiency for the b flavour, ϵ_d^b, is expressed as $\epsilon_d^b = \epsilon^b \epsilon^b (1 + \rho_b)$, which takes into account the correlation ρ_b between hemispheres. If for c and uds flavours the tagging efficiencies ϵ^c and ϵ^{uds} are small enough, the corresponding correlations do not influence R_b and ϵ^b and thus may be neglected in the equations above. From equations (5.3) and (5.4), the fraction R_b and the tagging efficiency ϵ^b can be extracted, provided that the values ϵ^c, ϵ^{uds}, ρ_b and R_c are known:

$$R_b = \frac{\left(R^H - R_c(\epsilon^c - \epsilon^{uds}) - \epsilon^{uds}\right)^2}{R^E - R_c(\epsilon^c - \epsilon^{uds})^2 + \epsilon^{uds}\epsilon^{uds} - 2R^H\epsilon^{uds} - \rho_b R_b\left(\epsilon^b - \epsilon^b\epsilon^b\right)} \tag{5.5}$$

$$\epsilon^b = \frac{R^H - R_c(\epsilon^c - \epsilon^{uds}) - \epsilon^{uds}}{R^E - R_c\epsilon^c(\epsilon^c - \epsilon^{uds}) - R^H\epsilon^{uds} - \rho_b R_b\left(\epsilon^b - \epsilon^b\epsilon^b\right)}. \tag{5.6}$$

The value of R_c can be taken from electroweak theory or other measurements, while ϵ^c, ϵ^{uds} and ρ_b are extracted from the simulation. R_b and ϵ^b cannot be extracted

directly, being coupled through the correlation term ρ_b. Since this term is small, they can be easily solved iteratively. If the b purity of the tagged sample is high, the dependence on simulation is small and may be included in the systematic uncertainties. For the correct assignment of the statistical error to the measured values of R_b and ϵ^b, the correlation of the variables R^H and R^E, which are not independent, must be taken into account. It can be computed numerically from a simple Monte Carlo model of the experiment. But in fact, these errors are basically determined by the statistical error of R^E.

5.2 Hemisphere multiple tag scheme

In the hemisphere single tag scheme, hemispheres are tagged simply as b and non-b. This leads to two equations (5.3 and 5.4) with six unknowns, R_b, ϵ^b, R_c, ϵ^{uds}, ϵ^c and ρ_b. Three of them, ϵ^{uds}, ϵ^c and ρ_b, are then taken from simulation and R_c is fixed to the Standard Model value. If the number of equations for physical observables were larger than the number of unknowns, the latter could be extracted directly from the data, and the simulation would be required only to estimate systematic errors and the influence of hemisphere correlations. That is the principle of our *hemisphere multiple tag (multitag)* scheme which is described in the following.

5.2.1 The efficiency matrix

The multiple tag scheme involves the fit of a matrix of observables. More complex but more powerful than the single tag scheme, it is based on the same principles. In this frame one can measure R_b together with the hemisphere efficiencies, not only inside but also outside of the b sector. The tagging probabilities are grouped into an *efficiency matrix.*

In this case, we assume that the tagging algorithm is able to classify the hadronic hemispheres, containing $F = 3$ classes or flavours (uds, c and b), into T mutually exclusive tagging categories or tags. Applying the tag to both sides of the event, we get a symmetric matrix n_{IJ}, number of events classified as I and J for hemispheres 1 and 2 respectively, the elements of the matrix verifying the normalization condition

$$\sum_{IJ} n_{IJ} = N_{had} \tag{5.7}$$

where N_{had} is the total number of selected hadronic events. Dividing n_{IJ} by N_{had} one obtains the matrix of observables d_{IJ}, verifying the condition

$$\sum_{IJ} d_{IJ} = 1. \tag{5.8}$$

Let ϵ_I^q be the efficiency matrix element, i.e. the probability to tag a hemisphere of flavour q in the category I. The bidimensional array ϵ_I^q is the same for both hemispheres as in section 5.1 (this hypothesis will be experimentally verified in section

5.2.7). Therefore, the same flavour index could be associated to both hemispheres. However, the quark and the antiquark might appear in the same hemisphere when a very hard gluon is radiated, producing correlation effects that will be studied in section 5.2.6. If the hemispheres are independent, the fraction of double tagged events d_{IJ} can be parameterized as

$$d_{IJ} = \sum_q \epsilon_I^q \epsilon_J^q R_q, \quad I, J = 1, ..., T \tag{5.9}$$

where R_q is the sample hadronic fraction for flavour q. The elements of the efficiency matrix and the hadronic fractions have to be compatible with the constraints

$$\sum_I \epsilon_I^q = 1, \quad q = uds,\ c,\ b \tag{5.10}$$

and

$$\sum_q R_q = 1. \tag{5.11}$$

Equation (5.10) has the physical meaning that all hemispheres are tagged in one of the T tags.

5.2.2 Extraction of the efficiency matrix and R_q

To resolve the problem of the R_q and ϵ_I^q determination for a given matrix n_{IJ}, we can apply least squares principle for classified data [110] by defining the objective function

$$\chi^2 = \sum_{IJ} \sum_{I'J'} (n_{IJ} - N_{had} d_{IJ}) \tilde{V}^{-1} (n_{I'J'} - N_{had} d_{I'J'}) \tag{5.12}$$

where $\tilde{V}$ is the covariance matrix associated to n_{IJ}, which is multinomially distributed [110]. Because of the normalization condition (5.7), the matrix $\tilde{V}$ is singular and cannot be inverted. The least squares principle as formulated by equation (5.12) is therefore not applicable to this case. However, if we omit one of the observations, for example d_{TT}, as it is redundant, the remaining observables have an associated covariance matrix $\tilde{V}^*$ which is regular. $\tilde{V}^*$ is simply $\tilde{V}$ without the T row and column. Then we can reformulate the least squares principle as

$$\chi^2 = \sum_{(I,J)\neq(T,T)} \sum_{(I',J')\neq(T,T)} (n_{IJ} - N_{had} d_{IJ}) (\tilde{V}^*)^{-1} (n_{I'J'} - N_{had} d_{I'J'}) \tag{5.13}$$

being

$$(\tilde{V}^*)^{-1} = \frac{1}{N_{had}} \begin{pmatrix} d_{11}^{-1} + d_{TT}^{-1} & d_{TT}^{-1} & \dots & d_{TT}^{-1} \\ d_{TT}^{-1} & d_{12}^{-1} + d_{TT}^{-1} & \dots & d_{TT}^{-1} \\ \cdot & \cdot & \cdot & \cdot \\ \cdot & \cdot & \cdot & \cdot \\ \cdot & \cdot & \cdot & \cdot \\ d_{TT}^{-1} & d_{TT}^{-1} & \dots & d_{T(T-1)}^{-1} + d_{TT}^{-1} \end{pmatrix}. \tag{5.14}$$

In the above χ^2 expression, the double sum can be written as

$$\chi^2 = \sum_{(I,J)\neq(T,T)} \frac{(n_{IJ} - N_{had}d_{IJ})^2}{N_{had}d_{IJ}} +$$

$$\frac{1}{N_{had}d_{TT}} \sum_{(I,J)\neq(T,T)} \sum_{(I',J')\neq(T,T)} (n_{IJ} - N_{had}d_{IJ})(n_{I'J'} - N_{had}d_{I'J'}) =$$

$$= \sum_{(I,J)\neq(T,T)} \frac{(n_{IJ} - N_{had}d_{IJ})^2}{n_{IJ}} + \frac{1}{n_{TT}} \left[\sum_{(I,J)\neq(T,T)} (n_{IJ} - N_{had}d_{IJ}) \right]^2 =$$

$$= \sum_{(I,J)\neq(T,T)} \frac{(n_{IJ} - N_{had}d_{IJ})^2}{n_{IJ}} + \frac{1}{n_{TT}} (n_{TT} - N_{had}d_{TT})^2 \tag{5.15}$$

or more simply

$$\chi^2 = \sum_{IJ} \frac{(n_{IJ} - N_{had}d_{IJ})^2}{n_{IJ}}. \tag{5.16}$$

Expression (5.16) restores the symmetry for all T tags. This expression could have been written down at once, from the assumption that the number of events n_{IJ} is Poisson distributed with mean and variance equal to $N_{had}d_{IJ}$. The algebra above, taken from [110], thus demonstrates the mathematical equivalence between two different points of view, the first considering $T(T+1)/2$ (dependent) multinomially distributed variables conditioned on their sum N_{had}, the second considering $T(T+1)/2$ independent Poisson variables. In other words, although our matrix of observables n_{IJ} is distributed by following a multinomial distribution, each of its elements can be considered as statistically independent according to a Poisson distribution. This consequence is very important when one needs to estimate statistical errors on the parameters fitted in (5.16), because one does not need to consider potential correlation effects between the observables.

In principle, the minimization of χ^2 in equation (5.16) allows the simultaneous determination of the efficiency matrix ϵ_I^q and the R_q fractions. As said previously, the fit solution has to be compatible with the (5.10) and (5.11) constraints. No solution

exists if the number of observables N_o is less than the number of unknowns N_u. For any given F and T, provided the normalization conditions (5.8), (5.10) and (5.11), the number of observables and unknowns are $N_o = T(T+1)/2-1$ and $N_u = TF-1$ respectively. The number of degrees of freedom is therefore $\nu = N_o - N_u$.

In our case with *uds*, *c* and *b* flavours (F=3), T must be at least 6. The value of χ^2_{min} for ν degrees of freedom can be used to estimate the quality of the fit.

Equivalent formalism

This formalism can be rewritten in an equivalent way by following the pattern of the single tag scheme, in which the observables are the fractions of single and double b tags R_I^H and R_{IJ}^E, while in the multiple tag scheme only double tag fractions d_{IJ} are considered. Extending the single tag formalism to T tags, leads to

$$R_I^H = \epsilon_I^b R_b + \epsilon_I^c R_c + \epsilon_I^{uds}(1 - R_b - R_c) \quad (5.17)$$

$$R_{IJ}^E = \epsilon_I^b \epsilon_J^b R_b + \epsilon_I^c \epsilon_J^c R_c + \epsilon_I^{uds} \epsilon_J^{uds}(1 - R_b - R_c) \quad (5.18)$$

where $R_I^H = n_I/2N_{had}$ is the fraction of hemispheres tagged in category I, and $R_{IJ}^E = d_{IJ}$ is the fraction of events doubly tagged in categories I and J. In equations (5.17) hemisphere correlations were neglected. Since the two sets of observables are related by T closure relations

$$R_I^H = \sum_J R_{IJ}^E \quad (5.19)$$

the way to fit out R_I^H and R_{IJ}^E simultaneously is to exclude from the fit the elements belonging to one of the categories. The convention is to exclude the last category which is called *no-tag*. Excluding the elements of the no-tag category leaves $T-1$ and $T(T-1)/2$ observables of types R_I^H and R_{IJ}^E respectively, i.e. a total of $N_o = T(T+1)/2 - 1$ as before. With that formulation n_{IJ} and n_I are not statistically independent. The solution is to adjust in the fit, instead of R_I^H, the quantities

$$2R_I'^H = 2R_I^H - \sum_{K=1}^{T-1} R_{IK}^E(1+\delta_{IK}) = \left[n_I - \sum_{K=1}^{T-1} n_{IK}(1+\delta_{IK})\right]/N_{had}. \quad (5.20)$$

The advantage of this presentation is to avoid the introduction of unitary constraints (5.10) and (5.11). The formulation is mathematically equivalent to the previous one. The multiple tag scheme appears therefore as a natural generalization of the single tag scheme.

5.2.3 The degeneracy problem

Unfortunately, the minimum of equation (5.16) is not unique due to a rotation degeneracy. In fact, if a vector

$$\vec{V}_I = (\epsilon_I^{uds}\sqrt{R_{uds}}, \epsilon_I^c\sqrt{R_c}, \epsilon_I^b\sqrt{R_b}) \tag{5.21}$$

is introduced for each tag, the expected fraction of double tagged events can be expressed as a scalar product $d_{IJ} = \vec{V}_I \cdot \vec{V}_J$, which is invariant under rotations in the vector space.

Let us define a vector sum $\vec{U} = \sum_I \vec{V}_I = (\sqrt{R_{uds}}, \sqrt{R_c}, \sqrt{R_b})$ in a 3D frame, where the three axes correspond to pure *uds*, *c* and *b* states. The vector $\vec{U}$, of unit length, and the set of $\vec{V}_I$ can be viewed as a rigid body. Mathematically this means that the rotation matrix $\tilde{\mathcal{R}}$ is an orthonormal matrix with $F = 3$ degrees of freedom. Once a particular solution has been found, other solutions may be generated by moving this rigid body according to the three degrees of freedom. Two degrees of freedom could be the position (Θ,Ψ dip and azimuth angles) of the extremity of $\vec{U}$ on a sphere of unit radius, the remaining one an internal rotation ξ around the $\vec{U}$ axis. The flavour fractions are then

$$R_{uds} = \cos^2\Theta\cos^2\Psi\ , \quad R_c = \cos^2\Theta\sin^2\Psi\ , \quad R_b = \sin^2\Theta. \tag{5.22}$$

From a given particular solution $\vec{V}_I$, one can generate equivalent solutions $\vec{V}'_I$ as

$$V_I'^r = \sum_q \mathcal{R}_{rq} V_I^q \tag{5.23}$$

with $r = uds,\ c,\ b$. $\tilde{\mathcal{R}}$ is the orthonormal matrix parameterizing the rotation with (Θ,Ψ,ξ) as free parameters. If we sum over I in equation (5.23) we obtain

$$\sqrt{R'_r} = \sum_q \mathcal{R}_{rq}\sqrt{R_q}. \tag{5.24}$$

From equations (5.21), (5.23) and (5.24) it is straightforward to prove that

$$\epsilon_I'^r = \frac{\sum_q \mathcal{R}_{rq}\epsilon_I^q\sqrt{R_q}}{\sum_q \mathcal{R}_{rq}\sqrt{R_q}}. \tag{5.25}$$

It can be easily shown taking into account the orthonormality condition of matrix $\tilde{\mathcal{R}}$ that $\epsilon_I'^r$ and R'_r verify the same relations (5.10) and (5.11) as ϵ_I^q and R_q.

The allowed range of (Θ,Ψ,ξ) is limited by two factors. All the ϵ_I^q and R_q elements should be non negative since they are probabilities. Thus, the set of $\vec{V}_I$ vectors should remain in the first octant. When a pure tagging is reached for a given flavour, some of the $\vec{V}_I$ vectors, corresponding to the enriched sample, become practically aligned with a flavour axis. In the limit of three vectors almost aligned with the different axes, the rigid body becomes locked. It happens then that the domain of rotations is indeed strongly limited, and the R_q range is actually bound to an interval of a few percent (compared to a few per mil of the required precision on R_b).

5.2.4 The way out

The way to solve the degeneracy is to introduce in the fit (5.16) at least $F = 3$ parameters *well chosen* which can be taken from simulation, theory or external measurements. The exact meaning of *well chosen* parameters is defined by two requirements: first, the total impact on R_b (total error on R_b, including statistical and systematic uncertainties) of the parameters should be minimal; second, they are independent. The independence of these parameters can be studied looking at expressions (5.24) and (5.25). Two possible solutions, among many others, were investigated.

Asymptotic purity approach

The simplest way to resolve the problem is to fix parameters from simulation. However, it was important at the beginning of this analysis to remain as independent as possible from simulation (the Monte Carlo was then not able to reproduce accurately the data). This requirement imposed to find other solutions. The most interesting strategy is the following: the degeneracy is broken in the b sector if some of the ϵ_I^b parameters can be estimated independently (at least 2 in the case of 3 flavours). The third degree of degeneracy can be removed by fixing R_{uds} or R_c. If X_I^b are estimates of the ϵ_I^b parameters and σ_I their errors, a modified objective function χ^2_*, introducing a degeneracy breaking term, can be written as

$$\chi^2_* = \chi^2 + \sum_I \frac{(\epsilon_I^b - X_I^b)^2}{\sigma_I^2} \tag{5.26}$$

where the I index only runs over the considered X_I^b.

The X_I^b estimates can be obtained by the technique we proposed originally in [95]. From the set of $n_I(\Theta)$ observables, which represent the number of hemispheres classified into tag I in one hemisphere provided that the opposite side was tagged as b with a Θ value of the b tagging variable, one computes the fractions

$$\mathcal{F}_I(\Theta) = \frac{n_I(\Theta)}{\sum_J n_J(\Theta)}. \tag{5.27}$$

The $\mathcal{F}_I(\Theta)$ fractions represent hence the fraction of each hemisphere tagged as I when the opposite side was tagged as b with a Θ value of the b tagging variable. They can also be expressed as

$$\mathcal{F}_I(\Theta) = \epsilon_I^b + \xi_I(\Theta) \tag{5.28}$$

with the residue $\xi_I(\Theta)$

$$\xi_I(\Theta) = (\epsilon_I^{uds} - \epsilon_I^b)\mathcal{F}_{uds}(\Theta) + (\epsilon_I^c - \epsilon_I^b)\mathcal{F}_c(\Theta). \tag{5.29}$$

$\mathcal{F}_{uds}(\Theta)$ and $\mathcal{F}_c(\Theta)$ are the uds and c backgrounds in the b tagged hemisphere, and they are independent of the I index. From (5.28) and (5.29), the asymptotic value

of $\mathcal{F}_I(\Theta)$ is ϵ_I^b, provided that high purity is achieved in the b tagged hemisphere for hard cuts on Θ, as is the case of the b tagging algorithms described in chapter 4. The X_I^b estimates are therefore the asymptotic values of the $\mathcal{F}_I(\Theta)$ distributions.

The recalculated number of degrees of freedom will be now $\nu' = \nu + \kappa$, where κ is the number of independent estimates injected in the fit, generally $\kappa = T - 1$. Therefore, for our case of $F = 3$, T must be at least 4 instead of 6.

In order to extract the asymptotic value of $\mathcal{F}_I(\Theta)$, an analytical parameterization of the $\xi_I(\Theta)$ distributions must be used. It was found that the parameterization which best describes the whole range of the contamination distributions $\mathcal{F}_{uds}(\Theta)$ and $\mathcal{F}_c(\Theta)$ for the DELPHI data is the product of an exponential with a Gaussian function. The fitting of the approaches to the asymptotes of the $\mathcal{F}_I(\Theta)$ distributions with $T = 6$ requires a minimum of 6 extra parameters in addition to R_b and the 15 efficiencies ϵ_I^q. The introduction of these auxiliary parameters increases significantly the statistical error.

The problem with the minimization of (5.26) is to evaluate properly the systematic errors of the X_I^b estimates, included in σ_I. This difficulty can be avoided by combining the two fits into one and minimizing the global objective χ_*^2 function defined as

$$\chi_*^2 = \chi^2 + \sum_{I,\Theta} \frac{\left\{\mathcal{F}_I(\Theta) - \epsilon_I^b - \xi_I(\Theta)\right\}^2}{\sigma^2_{f_I(\Theta)}}. \tag{5.30}$$

This allows the simultaneous determination of the efficiency matrix, the hemisphere background distributions $\mathcal{F}_{uds}(\Theta)$ and $\mathcal{F}_c(\Theta)$, and R_b. The $\sigma_{f_I(\Theta)}$ are the experimental errors on $\mathcal{F}_I(\Theta)$ for each bin of Θ. With this function and in the absence of correlations, a degeneracy in the *udsc* sector is still present but it can be removed, for instance, by fixing R_c to the Standard Model value. As it can be seen from equation (5.22), this constraint has no direct effect on R_b and therefore, neglecting background effects in the estimation of X_I^b, R_b does not depend explicitly on R_c.

High purity approach

When a very pure and efficient tagging is reached for a given flavour in one tagging category or tag, the corresponding $\vec{V}_I$ vector becomes practically aligned with the flavour axis and the backgrounds from the other flavours are very small. The well chosen parameters which should be taken from the simulation, in order to break the degeneracy, are then the small *uds* and *c* backgrounds of a b-tight tagging category and R_c, like in the case of the single tag scheme. As it will be shown later, the systematic impact of these parameters on R_b decreases when the purity of the b-tight tag increases, but the statistical impact increases. Due to this interplay, an optimal b purity needs to be found for the b-tight tag (see chapter 6). Fixing $F = 3$ parameters, the minimum number of required categories diminishes again from 6 to 4.

High versus asymptotic purity approaches

The method which finally we have adopted to provide the precise measurement of R_b is the high purity multiple tag scheme. The reasons for this choice are summarized in the following, and they are numerically shown in chapter 6.

From a historical point of view, the understanding of the DELPHI detector has improved considerably from the beginning of data taking in 1989 to the last LEP 1 period in 1995. At the beginning, the standard DELPHI Monte Carlo simulation was not able to reproduce accurately the data, and the underlying idea to perform the measurement of R_b was to be as independent as possible from the simulation. For this reason, we have first developed the asymptotic purity approach using as tagging technique the multivariate algorithm described in chapter 4. With this method, the only inputs from Monte Carlo were the hemisphere tagging correlations (as described below) and the shape (parameterization) of the *uds* and *c* quark backgrounds $\mathcal{F}_{uds}(\Theta)$ and $\mathcal{F}_c(\Theta)$ as a function of the multivariate discriminator $\Theta = \Delta_b$. The parameters themselves were fitted to data. This method was applied and published for the 1991-1993 DELPHI data [111, 112]. Because of the small dependence on simulation, this analysis has low systematics compared to the standard lifetime analyses using the same data [63]. However, it is statistically limited due to the large number of free parameters required for the fit of R_b. New solutions were then needed to achieve the required precision.

With the advent in DELPHI of the very fine tuning of the physics and tracking resolution as described in chapter 4, the high purity approach becomes a good solution to improve precision. This requires to define the b-tight category by an algorithm providing high purity and efficiency but being at the same time as simple as possible in order to have reliable determinations of charm and light quark background systematics (chapter 6). That was possible using the combined impact parameter tag described in chapter 4. Therefore, the step forward to improve precision was the combination of optimized tagging algorithms with a multiple tag determination of R_b, which generalizes the single tag scheme.

5.2.5 Definition of the hemisphere tags

Even though the minimum number of tags needed to measure R_b is now $T = 4$, the choice of $T = 6$ was made in order to overconstrain the problem and to minimize the error. The definition of the six hemisphere tags is given in table 5.1. They are constructed in an attempt to isolate the desired quark with acceptable efficiency and reduced backgrounds. The basis of the definition of the tags is the combined impact parameter variable y and the multivariate discriminators Δ_b, Δ_c and Δ_{uds}, described in chapter 4. The tags or categories are defined to be mutually exclusive and they are ordered by decreasing b purity. Three of the six categories are designed to identify b quarks, one c quarks and also one *uds* quarks. The remaining tag (no-tag) contains all hadronic hemispheres not considered in one of the previous

tags, in order to verify experimentally the condition (5.10). The tags are defined as follows. Firstly, b-tight tagged hemispheres are selected by the condition $y \leq y_0$. The highest priority is assigned to the combined impact parameter tagging, for the reasons pointed out above as well as in chapter 4. Among the remaining hemispheres, only the multivariate criteria is used for tagging them as b-standard, b-loose, charm and uds and following this order or priority. Finally, the left over are included in the no-tag category.

Table 5.1: Definition of the hemisphere tags.

Tagging category or tag	Condition	Priority/Number of tag
b-tight	$y \leq y_0$	1
b-standard	$\Delta_b > \Delta_{b,0}^{up}$	2
b-loose	$\Delta_b > \Delta_{b,0}^{low}$	3
charm	$\Delta_c > \Delta_{c,0}$	4
uds	$\Delta_{uds} > \Delta_{uds,0}$	5
no-tag	left over	6

The b-tight category has the strongest influence on the R_b measurement. The value of y_0 determines the systematic and statistical impact on R_b of the backgrounds and signal efficiencies in the b-tight tag ($\epsilon_{b-tight}^{uds}$, $\epsilon_{b-tight}^{c}$ and $\epsilon_{b-tight}^{b}$). Due to the interplay between both sources of errors, its optimal value is determined by the minimal total error of R_b as a function of y_0. The cut $-\log_{10} y_0$ is finally fixed at 1.2 to minimize the total error. All other cuts are chosen in order to obtain good efficiencies with reasonable backgrounds in the affected tags; they were taken to be $\Delta_{b,0}^{up}$=3.5, $\Delta_{b,0}^{low}$=1.2, $\Delta_{c,0}$=0.65 and $\Delta_{uds,0}$=3.2. The Monte Carlo expectations for the efficiencies are given, separately for 1994 and 1995, in table 5.2. This table features the specificities for the six tags (note that most of *uds* and *c* hemispheres enter in the no-tag category) and is a measure of the performance of tagging techniques, all working simultaneously. In this analysis of R_b, only the charm and light quark backgrounds of the b-tight category are taken from simulation. Therefore only the light and charm quark systematic errors of the combined impact parameter tag are necessary for this measurement of R_b. All the other efficiencies are measured directly from the data and can be used as a powerful cross-check of the analysis.

Compared with the single tag scheme in which only b-tight tagged hemispheres are used, in this multiple tag analysis all hadronic hemispheres are classified, allowing the statistical accuracy to be increased. The systematic uncertainty on R_b due to background and hemisphere correlations is also improved.

For 1992-1993 data, the combined impact parameter tag was not still available when this report was written, and the b-tight tag was defined also in terms of the multivariate discriminators, with the condition $\Delta_b \geq \Delta_{b,0}^{b-tight}$. To minimize the total error, $\Delta_{b,0}^{b-tight}$ is taken to be 5.0. All other tags are defined similarly as in 1994-

Table 5.2: Monte Carlo results for the tagging efficiencies at the nominal cuts for the 1994-1995 data.

	1994			1995		
Tag	ϵ^{uds}	ϵ^{c}	ϵ^{b}	ϵ^{uds}	ϵ^{c}	ϵ^{b}
b-tight	0.00052	0.00407	0.28404	0.00049	0.00376	0.27453
b-standard	0.00131	0.02782	0.15751	0.00120	0.02678	0.15558
b-loose	0.01200	0.07877	0.15108	0.01212	0.07812	0.15380
charm	0.05174	0.16143	0.05171	0.05415	0.16128	0.05295
uds	0.12054	0.03123	0.00488	0.11678	0.03083	0.00479
no-tag	0.81390	0.69667	0.35078	0.81525	0.69923	0.35835

1995, but the cut values were chosen slightly different due to differences in the range definition of the discriminators. In this case, the cut values were $\Delta_{b,0}^{up}$=2.8, $\Delta_{b,0}^{low}$=1.4, $\Delta_{c,0}$=0.45 and $\Delta_{uds,0}$=2.3. The Monte Carlo expectations for the efficiencies are given in table 5.3.

Table 5.3: Monte Carlo results for the tagging efficiencies at the nominal cuts for the 1992-1993 data.

	1992-1993		
Tag	ϵ^{uds}	ϵ^{c}	ϵ^{b}
b-tight	0.00054	0.00445	0.19245
b-standard	0.00425	0.02754	0.17076
b-loose	0.01691	0.05993	0.14333
charm	0.07196	0.15246	0.06568
uds	0.14642	0.04818	0.00895
no-tag	0.75992	0.70743	0.41883

5.2.6 Hemisphere-hemisphere tagging correlations

The previous definition of the hemisphere tags attempts also to keep the tag correlations between the hemispheres as small and transparent as possible. For that reason, the tags are constructed for each hemisphere using only its information. In particular, as it was largely explained in chapter 4, the Z decay vertex is reconstructed independently in the two hemispheres. Intrinsic correlations are still possible between the two sides due to the physics of the Z decay, such as for instance, the correlations in the momenta of the two B hadrons and the correlations produced by hard gluon emission (QCD effects).

The b tagging efficiency rises with the momentum of B hadrons. Gluons emitted at large angles with respect to the quarks affect the energy of both quarks (figure 5.1.a), leading to a positive correlation. In about 2% of the events both b quarks are boosted into the same hemisphere, recoiling against a hard gluon (figure 5.1.b). This leads to a negative correlation, since only one hemisphere will tag.

Other correlations are associated with tag efficiency dependence on the orientation of the event thrust axis with respect to the detector and by the fact that the two hemisphere vertices share the information on the beam size (angular effects). The two particles in an event are typically nearly back-to-back. This leads to a positive correlation due to the polar angle. The multiple scattering contribution to the VD resolution increases with decreasing polar angle and close to the end of the VD some tracks get lost outside its acceptance. There are also some minor effects connected with the azimuthal angle. Due to the flatness of the beam spot at LEP, the resolution is better for horizontal than for vertical jets and owing to inefficient or badly aligned modules the detector is not completely homogeneous.

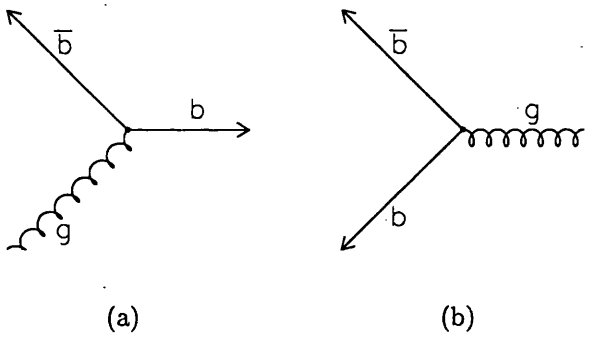

Figure 5.1: Hemisphere correlations due to QCD effects: (a) gluon emitted at large angles leading to a positive correlation; (b) recoiling hard gluon displacing the two quarks into the same hemisphere, leading to a negative correlation.

Other possible sources of correlations are basically eliminated by computing the tagging variables separately in each hemisphere, including a separated primary vertex reconstruction in each hemisphere. In particular, the large effects detailed in section 4.4. Furthermore, when using a common primary vertex, the Monte Carlo prediction for the correlation is found to be strongly dependent on the mean B hadron energy and charged decay multiplicity. This dependence arises since these quantities affect the ratio between the number of charged tracks coming from the B hadron decay and the number of particles coming from fragmentation. This uncertainty is strongly reduced by reconstructing the primary vertex separately in each hemisphere. In general, the production point finder reduces dependences on the b

physics inputs of the Monte Carlo simulation, so it reduces systematic uncertainties derived from them.

To take properly into account hemisphere-hemisphere correlations, equation (5.9) must be modified as

$$d_{IJ} = \sum_q \epsilon_I^q \epsilon_J^q (1 + \rho_{IJ}^q) R_q \qquad I, J = 1, ..., T \tag{5.31}$$

where ρ_{IJ}^q is the correlation correction factor defined as

$$\rho_{IJ}^q = \frac{\epsilon_{IJ}^q}{\epsilon_I^q \epsilon_J^q} - 1. \tag{5.32}$$

ϵ_{IJ}^q is the efficiency for flavour q that the event is tagged as I in one hemisphere and as J in the other one. Correlation coefficients verify the condition

$$\epsilon_J^q = \sum_I \epsilon_I^q \epsilon_J^q (1 + \rho_{IJ}^q), \quad q = uds, c, b; \quad J = 1, ..., T \tag{5.33}$$

or simplifying

$$\sum_I \epsilon_I^q \epsilon_J^q \rho_{IJ}^q = 0, \quad q = uds, c, b; \quad J = 1, ..., T. \tag{5.34}$$

Equation (5.17) could be modified in the same way. To include the correlation in the asymptotic approach given in equations (5.26), (5.28) and (5.30), one has to replace ϵ_I^b by $\epsilon_I^b[1 + \rho_I^b(\Theta)]$, where $\rho_I^b(\Theta)$ is defined now as

$$\rho_I^b(\Theta) = \frac{\epsilon_{d,I}^b(\Theta)}{\epsilon_I^b \epsilon^b(\Theta)} - 1. \tag{5.35}$$

In equation (5.35), $\epsilon_{d,I}^b(\Theta)$ is the efficiency that the event will be tagged as I in one hemisphere and as b in the other one with a Θ value of the tagging variable; $\epsilon^b(\Theta)$ is the efficiency to tag a hemisphere as b with the same Θ value. Correlation coefficients for charm and lighter quarks in (5.29) can be safely neglected.

5.2.7 Hemisphere equivalence

The hypothesis of hemisphere equivalence stated before, mathematically corresponds to the symmetry of the $\tilde{n}$ matrix,

$$n_{IJ} - n_{JI} = 0, \quad I, J = 1, ..., T. \tag{5.36}$$

We have verified this hypothesis using a χ^2 test formulated as [110, 113]

$$\sum_{I<J} \frac{(n_{IJ} - n_{JI})^2}{n_{IJ} + n_{JI}} \tag{5.37}$$

with $\frac{1}{2}T(T-1)$ degrees of freedom. Table 5.4 summarizes the results of the test applied to all the data sets. It is therefore concluded that the hypothesis of hemisphere equivalence is acceptable inside the given statistical limit of the samples.

Table 5.4: Hemisphere definition equivalence confidence level for all the analysed data sets.

Data		
1992-1993	1994	1995
63.1%	70.5%	59.5%

5.2.8 General formulation of the problem

The set of observables, that is, the matrix n_{IJ} with I,J = 1,...,T, is defined as the observed number of hadronic events tagged as I and J for hemispheres 1 and 2 respectively, and verifies (5.7). The corresponding expected fraction of events d_{IJ} can be written as given by equation (5.31), where the flavour fractions R_q satisfy the unitary condition (5.11). Assuming that all the hadronic hemispheres are classified in one tag, the conditions (5.10) and (5.34) are satisfied. The $T(T+1)/2-1$ independent measurements are therefore described by the following set of unknown independent parameters: $(F-1)$ flavour fractions, $F(T-1)$ efficiencies and $FT(T-1)/2$ correlation coefficients.

There are $FT(T-1)/2$ independent correlation coefficients instead of $FT(T+1)/2$ because equation (5.34) provides FT relations between the ρ^q_{IJ} correlations and the ϵ^q_I efficiencies. The correlation coefficients are in practice small or not significant. They can be therefore borrowed from a reliable simulation of the experiment. However, since the ρ^q_{IJ} and ϵ^q_I are related by the FT (18 for $T=6$ and $F=3$) closure relations (5.34), it is possible to let float in the fit as many correlation coefficients. We choose to let float the coefficients connected with the last no-tag category (I or J equal to $T=6$) and to take from simulation the others (I and $J \neq T$). The no-tag correlation coefficients have been chosen to be fitted because this tag has the most complex selection criteria, and therefore is the most difficult to be accurately reproduced by the simulation of the experiment.

At this level, the fit of the n_{IJ} observables is not possible because of the rotation degeneracy described in section 5.2.3. This problem can be avoided if some additional constraints are used. In the high purity *multiple tag* scheme presented here, the problem is resolved by taking from simulation the backgrounds of one of the tags and fixing R_c to its electroweak theory prediction. Systematic errors on R_b due to these three factors can be reduced if the corresponding category has a high b purity (b-tight tag). The systematic error will reflect the uncertainties in the simulation calculations of the background efficiencies of the b-tight tag, $\epsilon^{uds}_{b-tight}$

and $\epsilon^c_{b-tight}$, and the correlations ρ^q_{IJ} with $I, J \neq T$. The result will be given as a function of the assumed value of R_c. As already pointed, the choice of $T = 6$ tags was made in order to overconstrain the problem and to minimize the error. The number of independent observables is therefore 20 with 14 independent unknowns: 13 efficiencies and R_b. There are 45 independent correlations elements to be taken from simulation. Only a few of them will have sensitivity on the measurement, as it will be shown in chapter 6.

The technical implementation of the fit was done using the NAG scientific library [114], with a Lagrange Multiplier algorithm to consider the constraints of the problem [110, 114]. The estimation of the statistical error was performed using a $\chi^2 = \chi^2_{min} + 1$ confidence interval method [7].

Chapter 6

The measurement of R_b

In this chapter we will describe the full R_b measurement using the multiple tag scheme described in the previous chapter, as well as some cross-checks of the results. The 1991 data were not included in the analysis because their negligible statistical weight compared to all the LEP 1 statistics. The 1994 and 1995 data were analyzed separately [115] and the 1992-1993 data were merged into a single sample. It was however verified that the separated analysis of the 1992 and 1993 data does not change the final results.

6.1 Fit results

6.1.1 High purity multiple tag scheme

In the framework of the high purity and multiple tag approach, R_b was measured for many different values of b efficiency and purity of the b-tight category. The minimum total error was obtained for a cut on the variable $-\log_{10} y \geq 1.2$ for 1994-1995 data, and $\Delta_b \geq 5.0$ for 1992-1993. At these chosen working points, the tagging efficiencies for uds and c quarks in the b-tight tag were estimated using the simulation to be

$$\begin{aligned} \epsilon^{uds}_{b-tight} &= 0.00052 \pm 0.00001 \\ \epsilon^{c}_{b-tight} &= 0.00407 \pm 0.00007, \end{aligned} \tag{6.1}$$

$$\begin{aligned} \epsilon^{uds}_{b-tight} &= 0.00049 \pm 0.00003 \\ \epsilon^{c}_{b-tight} &= 0.00376 \pm 0.00014 \end{aligned} \tag{6.2}$$

and

$$\begin{aligned} \epsilon^{uds}_{b-tight} &= 0.00054 \pm 0.00001 \\ \epsilon^{c}_{b-tight} &= 0.00445 \pm 0.00007 \end{aligned} \tag{6.3}$$

for 1994, 1995 and 1992-1993 data respectively. The errors are only due to the limited amount of simulated data (see table 4.2). The fifteen correlation coefficients ρ^q_{IJ} for b quarks, estimated from the simulation, are given in table 6.1. For charm and light quarks they are shown in table 6.2. All these coefficients are small or compatible with zero. Only 14 of the 45 correlation coefficients are significant to the analysis as it will be shown later on (tables 6.9, 6.10 and 6.11).

Table 6.1: Monte Carlo estimations of the fifteen b correlation coefficients for the three data sets at the nominal cuts. Errors are only statistical.

b correlations	1994	1995	1992-1993
$\rho^b_{b-tight,b-tight}$	0.0187 ± 0.0027	0.0235 ± 0.0044	0.0327 ± 0.0033
$\rho^b_{b-tight,b-standard}$	0.0036 ± 0.0027	-0.0006 ± 0.0044	0.0141 ± 0.0027
$\rho^b_{b-tight,b-loose}$	-0.0020 ± 0.0028	-0.0032 ± 0.0044	-0.0039 ± 0.0031
$\rho^b_{b-tight,charm}$	0.0104 ± 0.0053	-0.0025 ± 0.0083	-0.0107 ± 0.0048
$\rho^b_{b-tight,uds}$	0.0254 ± 0.0180	0.0599 ± 0.0293	0.0601 ± 0.0140
$\rho^b_{b-standard,b-standard}$	0.0047 ± 0.0050	0.0077 ± 0.0079	0.0121 ± 0.0037
$\rho^b_{b-standard,b-loose}$	-0.0003 ± 0.0042	0.0122 ± 0.0065	0.0052 ± 0.0033
$\rho^b_{b-standard,charm}$	-0.0094 ± 0.0077	-0.0162 ± 0.0120	0.0001 ± 0.0052
$\rho^b_{b-standard,uds}$	0.0896 ± 0.0270	0.0439 ± 0.0421	0.0066 ± 0.0148
$\rho^b_{b-loose,b-loose}$	0.0144 ± 0.0052	0.0081 ± 0.0080	0.0015 ± 0.0044
$\rho^b_{b-loose,charm}$	-0.0139 ± 0.0079	0.0115 ± 0.0122	0.0018 ± 0.0058
$\rho^b_{b-loose,uds}$	-0.0177 ± 0.0266	-0.0513 ± 0.0408	-0.0044 ± 0.0163
$\rho^b_{charm,charm}$	0.0233 ± 0.0154	0.0483 ± 0.0238	0.0002 ± 0.0096
$\rho^b_{charm,uds}$	-0.0998 ± 0.0460	0.0056 ± 0.0753	0.0009 ± 0.0253
$\rho^b_{uds,uds}$	0.2655 ± 0.1827	-0.2044 ± 0.2297	-0.0911 ± 0.0681

The experimentally measured numbers n_{IJ} of doubly tagged events which passed the $|\cos\theta_{thrust}|$ cut are given in table 6.3 for the 1994, 1995 and 1992-1993 data separately.

The fit of R_b and the efficiencies to these numbers gives the results

$$R_b = 0.21617 \pm 0.00100(stat.) \tag{6.4}$$

with $\chi^2/ndof = 4.76/6$ for 1994,

$$R_b = 0.21688 \pm 0.00144(stat.) \tag{6.5}$$

with $\chi^2/ndof = 4.32/6$ for 1995, and

$$R_b = 0.21631 \pm 0.00150(stat.) \tag{6.6}$$

with $\chi^2/ndof = 3.10/6$ for 1992-1993. The errors are only statistical. These results have been corrected for event selection bias and τ background. The efficiencies

Table 6.2: Monte Carlo estimations of the fifteen c and uds correlation coefficients for the three data sets. Errors are only statistical.

c correlations	1994	1995	1992-1993
$\rho^c_{b-tight,b-tight}$	-0.4561 ± 0.2719	2.9926 ± 1.2625	-0.2167 ± 0.2094
$\rho^c_{b-tight,b-standard}$	0.0376 ± 0.1414	-0.2373 ± 0.2014	-0.0136 ± 0.0913
$\rho^c_{b-tight,b-loose}$	0.0169 ± 0.0808	0.0186 ± 0.1316	0.0622 ± 0.0630
$\rho^c_{b-tight,charm}$	-0.0220 ± 0.0528	-0.0582 ± 0.0844	0.0171 ± 0.0366
$\rho^c_{b-tight,uds}$	-0.1378 ± 0.1213	-0.0728 ± 0.2041	-0.0142 ± 0.0681
$\rho^c_{b-standard,b-standard}$	0.1816 ± 0.0589	0.0209 ± 0.0869	0.0330 ± 0.0375
$\rho^c_{b-standard,b-loose}$	0.0300 ± 0.0307	0.0689 ± 0.0488	-0.0009 ± 0.0238
$\rho^c_{b-standard,charm}$	-0.0469 ± 0.0197	-0.0169 ± 0.0312	0.0201 ± 0.0142
$\rho^c_{b-standard,uds}$	-0.0474 ± 0.0482	0.0153 ± 0.0779	0.0275 ± 0.0270
$\rho^c_{b-loose,b-loose}$	0.0042 ± 0.0190	0.0544 ± 0.0300	0.0145 ± 0.0170
$\rho^c_{b-loose,charm}$	-0.0015 ± 0.0114	0.0365 ± 0.0178	0.0043 ± 0.0094
$\rho^c_{b-loose,uds}$	0.0164 ± 0.0285	-0.0444 ± 0.0430	0.0135 ± 0.0178
$\rho^c_{charm,charm}$	0.0350 ± 0.0093	0.0151 ± 0.0141	-0.0005 ± 0.0065
$\rho^c_{charm,uds}$	0.0538 ± 0.0192	0.0889 ± 0.0299	0.0026 ± 0.0105
$\rho^c_{uds,uds}$	-0.0359 ± 0.0468	0.2033 ± 0.0811	0.0017 ± 0.0209
uds correlations	1994	1995	1992-1993
$\rho^{uds}_{b-tight,b-tight}$	0.0000 ± 0.7071	0.0000 ± 0.7071	5.9780 ± 3.4890
$\rho^{uds}_{b-tight,b-standard}$	2.3950 ± 2.0985	0.0000 ± 0.7071	0.0532 ± 0.4297
$\rho^{uds}_{b-tight,b-loose}$	0.1242 ± 0.3948	-0.1640 ± 0.6016	-0.1367 ± 0.1917
$\rho^{uds}_{b-tight,charm}$	0.1491 ± 0.1856	0.1309 ± 0.2828	-0.0768 ± 0.0926
$\rho^{uds}_{b-tight,uds}$	0.0259 ± 0.1108	-0.0598 ± 0.1706	-0.0004 ± 0.0644
$\rho^{uds}_{b-standard,b-standard}$	-0.0548 ± 0.6683	0.0000 ± 0.7071	-0.2607 ± 0.1141
$\rho^{uds}_{b-standard,b-loose}$	-0.1674 ± 0.1951	0.1536 ± 0.3620	0.1447 ± 0.0692
$\rho^{uds}_{b-standard,charm}$	-0.0161 ± 0.0988	0.3996 ± 0.1813	0.0549 ± 0.0311
$\rho^{uds}_{b-standard,uds}$	0.0680 ± 0.0645	-0.0696 ± 0.0985	0.0013 ± 0.0203
$\rho^{uds}_{b-loose,b-loose}$	0.1052 ± 0.0705	-0.0267 ± 0.1004	-0.0439 ± 0.0316
$\rho^{uds}_{b-loose,charm}$	-0.0175 ± 0.0307	0.0608 ± 0.0474	0.0243 ± 0.0150
$\rho^{uds}_{b-loose,uds}$	0.0019 ± 0.0195	0.0285 ± 0.0306	0.0291 ± 0.0101
$\rho^{uds}_{charm,charm}$	0.0556 ± 0.0156	0.0650 ± 0.0231	0.0118 ± 0.0075
$\rho^{uds}_{charm,uds}$	0.0219 ± 0.0091	0.0314 ± 0.0140	-0.0058 ± 0.0046
$\rho^{uds}_{uds,uds}$	0.0778 ± 0.0067	0.0869 ± 0.0107	0.0519 ± 0.0037

Table 6.3: Measured numbers of doubly tagged events at the nominal cuts, passing the $|\cos\theta_{thrust}|$ cut.

			1994			
Tag	b-tight	b-standard	b-loose	charm	uds	no-tag
b-tight	15809					
b-standard	17048	4656				
b-loose	16006	9091	5050			
charm	5918	4396	7619	7218		
uds	667	778	2619	10436	9474	
no-tag	36111	25453	43026	91054	110430	405309
			1995			
Tag	b-tight	b-standard	b-loose	charm	uds	no-tag
b-tight	7804					
b-standard	7752	1965				
b-loose	7695	4266	2394			
charm	3005	2088	3832	3860		
uds	290	331	1262	5321	4241	
no-tag	17937	11785	20680	46621	51309	196044
			1992-1993			
Tag	b-tight	b-standard	b-loose	charm	uds	no-tag
b-tight	15809					
b-standard	17048	4656				
b-loose	16006	9091	5050			
charm	5918	4396	7619	7218		
uds	667	778	2619	10436	9474	
no-tag	36111	25453	43026	91054	110430	405309

obtained from the same fits within statistical errors are shown in table 6.4. They can be compared with the simulation predictions of tables 5.2 and 5.3. For a complete comparison an estimate of the systematic errors must be included.

Table 6.4: Tagging efficiencies with their statistical errors for data as measured from the fit at the nominal cuts. For a complete comparison of the fit results with the simulation an estimate of the systematic error must be included. The efficiencies $\epsilon^{uds}_{b-tight}$ and $\epsilon^{c}_{b-tight}$ were assumed from the Monte Carlo simulation of the experiment.

		1994	
Tag	ϵ^{uds}	ϵ^{c}	ϵ^{b}
b-tight	0.00052	0.00407	0.2950 ± 0.0012
b-standard	0.0016 ± 0.0002	0.0262 ± 0.0015	0.1593 ± 0.0007
b-loose	0.0119 ± 0.0004	0.0799 ± 0.0020	0.1498 ± 0.0008
charm	0.0638 ± 0.0005	0.1754 ± 0.0016	0.0536 ± 0.0006
uds	0.1308 ± 0.0005	0.0331 ± 0.0016	0.0052 ± 0.0002
no-tag	0.7914 ± 0.0008	0.6814 ± 0.0035	0.3371 ± 0.0013
		1995	
Tag	ϵ^{uds}	ϵ^{c}	ϵ^{b}
b-tight	0.00049	0.00376	0.2962 ± 0.0017
b-standard	0.0016 ± 0.0002	0.0244 ± 0.0024	0.1492 ± 0.0010
b-loose	0.0130 ± 0.0006	0.0735 ± 0.0029	0.1498 ± 0.0012
charm	0.0690 ± 0.0008	0.1825 ± 0.0024	0.0560 ± 0.0009
uds	0.1254 ± 0.0007	0.0350 ± 0.0024	0.0044 ± 0.0003
no-tag	0.7906 ± 0.0012	0.6808 ± 0.0052	0.3444 ± 0.0019
		1992-1993	
Tag	ϵ^{uds}	ϵ^{c}	ϵ^{b}
b-tight	0.00054	0.00445	0.1869 ± 0.0012
b-standard	0.0053 ± 0.0004	0.0242 ± 0.0023	0.1642 ± 0.0008
b-loose	0.0190 ± 0.0005	0.0549 ± 0.0027	0.1457 ± 0.0009
charm	0.0788 ± 0.0007	0.1600 ± 0.0023	0.0710 ± 0.0009
uds	0.1566 ± 0.0006	0.0518 ± 0.0025	0.0090 ± 0.0004
no-tag	0.7397 ± 0.0012	0.7047 ± 0.0049	0.4231 ± 0.0016

The essential tagging efficiency $\epsilon^{b}_{b-tight}$ was found to be 0.2950 ± 0.0012, 0.2962 ± 0.0017 and 0.1869 ± 0.0012 for 1994, 1995 and 1992-1993 respectively, compared to the simulation estimate of 0.284, 0.275 and 0.192. The purity at the working point for these measurements is 98.4%, 98.6% and 97.3%. The real data 1994 (1995) are about 4% (7%) more efficient than simulation in this category. However, in 1992-1993 the real data are about 3% less efficient. These differences are due to the non perfect simulation of the b physics (B hadron production and its decay modes). The physics

tuning of the 1994-1995 simulation was slightly different to the one done for the 1992-1993 sample, what explains the different sign of the discrepancy. This is just one justification of the use of the double tagging technique (hemisphere tagging instead of event tagging), as said in chapter 5. In fact, as in the case of the comparison of table 6.4 with tables 5.2 and 5.3, one needs to consider in the comparison all uncertainties in the simulation of b physics (see section 6.2). For instance, the B hadron decay multiplicity used in the 1994-1995 simulation is consistent with a recent measurement of the DELPHI Collaboration [116], but disagrees slightly with the central value proposed in [109]. By reweighting the simulation inside the error proposed in [109], an excellent agreement between data and simulation for all the b efficiencies can be obtained, showing the strong effect of the b physics simulation on the b efficiencies. In addition, there are other sources of b physics inputs, like B lifetimes, b fragmentation and B branching ratios having also strong effects on the b efficiencies. However, as it will be shown, because of the separate primary vertices and the direct measurement of the b efficiencies from data, the effects of these physics systematics are finally very small.

6.1.2 Single tag scheme

The measurement of R_b was repeated using the single tag scheme at the same cut value defining the b-tight tag as previously, $-\log_{10} y \geq 1.2$. In this case the background efficiencies ϵ^{uds} and ϵ^{c} are given by (6.1), (6.2) and (6.3), and the correlation ρ_b is given by the term $\rho^b_{b-tight,b-tight}$ of table 6.1. The following results were obtained:

$$\begin{aligned} R_b &= 0.21737 \pm 0.00123(stat.), \\ R_b &= 0.21662 \pm 0.00175(stat.), \\ R_b &= 0.21696 \pm 0.00190(stat.) \end{aligned} \tag{6.7}$$

for 1994, 1995 and 1992-1993 respectively. As before, the errors are only statistical. In this case, the ϵ^b tagging efficiency was found to be 0.2936 ± 0.0017, 0.2964 ± 0.0024 and 0.1865 ± 0.0016 for 1994, 1995 and 1992-1993 data respectively. As before, the real data 1994 (1995) are about 4% (7%) more efficient than simulation, and for 1992-1993 the real data are about 3% less efficient than simulation.

The measurement of R_b using the single tag scheme was also performed at various values of the y_0 cut, i.e. at many values of ϵ^b. The minimum total error in the 1994-1995 data analysis was obtained for a cut on the variable $-\log_{10} y \geq 1.0$. At this chosen working point, the tagging efficiencies for uds and c quarks according to the simulation were found to be

$$\begin{aligned} \epsilon^{uds} &= 0.00064 \pm 0.00001 \\ \epsilon^{c} &= 0.00603 \pm 0.00008 \end{aligned} \tag{6.8}$$

in 1994 and

$$\begin{aligned} \epsilon^{uds} &= 0.00064 \pm 0.00001 \\ \epsilon^{c} &= 0.00603 \pm 0.00008 \end{aligned} \tag{6.9}$$

in 1995. The hemisphere correlation was estimated to be

$$\rho_b = 0.0176 \pm 0.0024 \tag{6.10}$$

$$\rho_b = 0.0194 \pm 0.0040 \tag{6.11}$$

for 1994 and 1995 respectively. The errors are only due to the limited Monte Carlo statistics. Using the above values of the efficiencies and correlations, the measured values of R_b were

$$R_b = 0.21685 \pm 0.00119(stat.) \tag{6.12}$$

and

$$R_b = 0.21620 \pm 0.00163(stat.) \tag{6.13}$$

for 1994 and 1995 respectively. The ϵ^b tagging efficiency was found to be 0.3192 ± 0.0017 and 0.3220 ± 0.0024 for 1994 and 1995 data respectively, compared to the simulation estimate of 0.309 and 0.299. As before, the real data 1994 (1995) are about 3% (8%) more efficient than simulation. In the upper part of figure 6.1, the ratio of b tagging efficiency in 1994 real data and in simulation is given as a function of the b efficiency.

As a cross-check of this measurement, a comparison of R_b as a function of the b efficiency is given in the lower part of figure 6.1 for the 1994 single tag analysis. The measured value of R_b is stable over a wide range of b purities and therefore of the efficiencies and of the correlation.

6.1.3 Multiple tag scheme with asymptotic approach

As another cross-check on all these results, the R_b measurement was again repeated for all the data sets using the multiple tag scheme with the asymptotic approach described in chapter 5. The cuts defining the b-tight category were chosen to be $-\log_{10} y \geq 1.0$ for 1994-1995 and $\Delta_b \geq 5.0$ for 1992-1993. Figure 6.2 shows the $\mathcal{F}_I(\Theta)$ distributions for the 1994-1995 data with $\Theta = \Delta_b$, being Δ_b the multivariate discriminator in the opposite hemisphere (to the one classified I) when this hemisphere is b tagged. Superimposed are the separate contributions of uds, c and b flavours as predicted from simulation. In each category the uds and c backgrounds

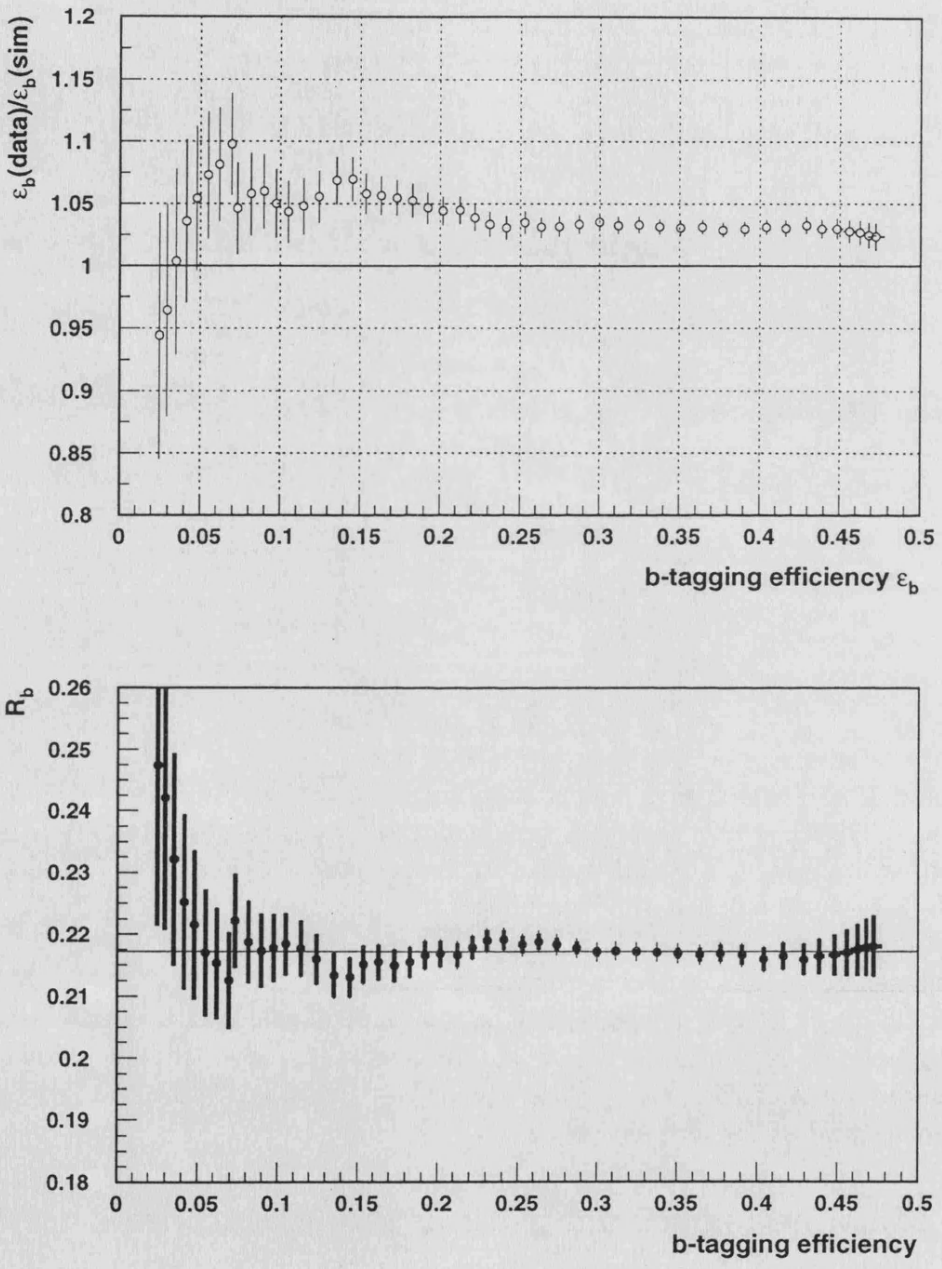

Figure 6.1: Single tag scheme: above, ratio of the b efficiency ϵ^b measured in 1994 real data and the one generated in the simulation as a function of the b efficiency; below, measured value of R_b with its total error as a function of the b efficiency for 1994 data. The horizontal line corresponds to the value measured at the reference point, $-\log_{10} y \geq 1.0$, that corresponds to $\epsilon^b = 31.92\%$.

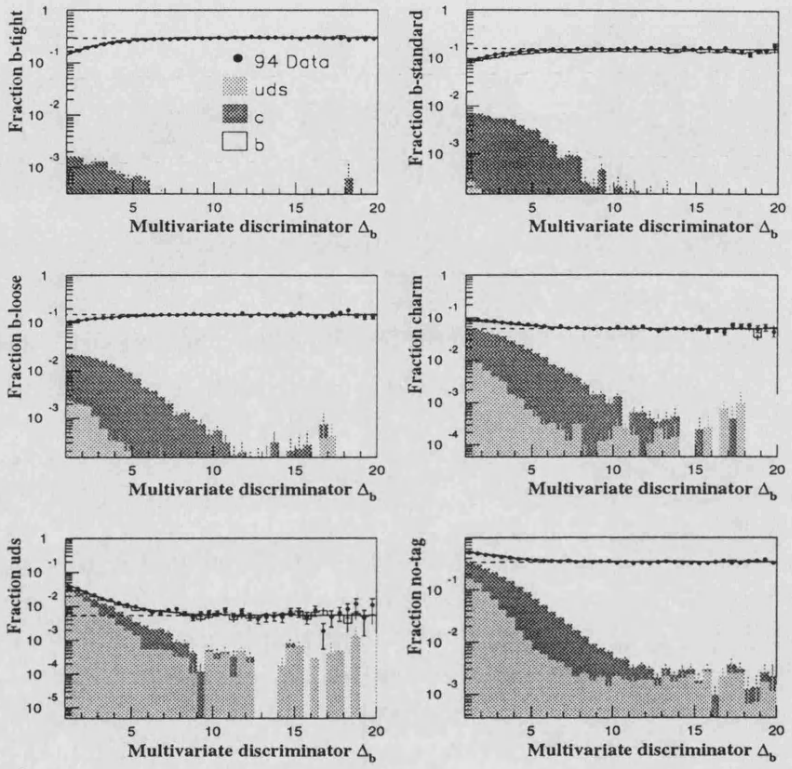

Figure 6.2: Distributions of category fractions $\mathcal{F}_I(\Delta_b)$ for the 1994-1995 data. The horizontal lines show the fitted ϵ_I^b from real data. The distributions for simulation are superimposed, together with the contributions of *uds*, *c* and *b* quarks. To show the small backgrounds in the region of hard cuts, a log scale has been chosen which goes down to one per mil of the efficiency.

$\xi_I(\Delta_b)$ have been fitted independently by the product of an exponential with a Gaussian function, as explained in section 5.2.4.

The no-tag, uds and charm tags contain the smallest fractions of *b* hemispheres, as can be seen from the higher *uds* and *c* backgrounds in the distributions of $\mathcal{F}_I(\Delta_b)$ for these tags; to achieve high *b* purity requires tighter cuts in the discriminator than in the other tags. However, these tags have little weight in the evaluation of R_b. No significant irreducible *uds* and *c* background is observed in the asymptotic regions of the b-tight, b-standard and b-loose distributions, which are the most significant for the R_b extraction. Effects of remaining background are small and can be included in the systematic uncertainties.

The fit of R_b, the efficiencies ϵ_I^q and the parameters describing the background distributions $\mathcal{F}_{uds}(\Delta_b)$ and $\mathcal{F}_c(\Delta_b)$ in the *b* tagged hemisphere, gives the results

$$R_b = 0.21616 \pm 0.00188(stat.) \tag{6.14}$$

with $\chi^2/ndof = 249.5/257$ for 1994,

$$R_b = 0.21500 \pm 0.00295(stat.) \tag{6.15}$$

with $\chi^2/ndof = 254.2/257$ for 1995, and

$$R_b = 0.21640 \pm 0.00258(stat.) \tag{6.16}$$

with $\chi^2/ndof = 293.3/257$ for 1992-1993. The errors are only statistical.

The $\epsilon^b_{b-tight}$ tagging efficiency was now found to be 0.2955±0.0013, 0.2972±0.0021 and 0.1869 ± 0.0011 for 1994, 1995 and 1992-1993 data respectively, compared to the simulation estimate of 0.284, 0.275 and 0.192.

Table 6.5 compares the values of R_b and of the major efficiency $\epsilon^b_{b-tight}$ for the three schemes and the three periods of data taking. All the results presented here, using the single tag and multiple tag (with both, high purity and asymptotic approaches) schemes agree well inside statistical differences (in this table, the cut defining the b-tight category for 1994-1995 is $-\log_{10} y \geq 1.2$). By far the method providing the best statistical precision is the multiple tag scheme with high purity approach. In addition, it reduces the systematic errors due to hemisphere correlations and charm contamination, compared to the single tag scheme. This is the reason why we finally adopt this analysis method to produce the final R_b result and therefore to study in detail the systematic errors, as it will be done in the following section. All other measurements must be seen as cross-checks. A study of the systematics for the asymptotic approach for the 1992-1993 data is given in references [111, 112].

6.2 Systematic errors

The systematic errors are due to the quantities estimated from simulation: event selection bias, light and charm quark backgrounds in the b-tight tag and hemisphere correlations. The event selection error was estimated already in chapter 4. In the following we discuss the two other sources of uncertainties, for the high purity multiple tag and single tag schemes. For the later one it was performed only for the 1994 data.

6.2.1 Light and charm quark efficiency uncertainties

Light and charm quark efficiency uncertainties are due to several sources which are studied in the following: charm physics systematics, rate of long lived light hadrons, $b\bar{b}$ and $c\bar{c}$ production from gluon splitting, detector effects (tracking) and the statistical accuracy of the simulation. All these uncertainties on the background

Table 6.5: Comparison of the fitted values of R_b and of the major efficiency $\epsilon^b_{b-tight}$ with their statistical errors for the three methods of analysis (high purity multiple tag, single tag and asymptotic approach) and the three periods of data taking.

Scheme	R_b		
	1994	1995	1992-1993
High purity multiple tag	0.2162 ± 0.0010	0.2169 ± 0.0014	0.2163 ± 0.0015
Single tag	0.2174 ± 0.0012	0.2166 ± 0.0018	0.2170 ± 0.0019
Asymptotic approach	0.2162 ± 0.0019	0.2150 ± 0.0030	0.2164 ± 0.0026
	$\epsilon^b_{b-tight}$		
	1994	1995	1992-1993
High purity multiple tag	0.2950 ± 0.0012	0.2962 ± 0.0017	0.1869 ± 0.0012
Single tag	0.2936 ± 0.0017	0.2964 ± 0.0024	0.1865 ± 0.0016
Asymptotic approach	0.2955 ± 0.0013	0.2972 ± 0.0021	0.1869 ± 0.0011

efficiencies except detector effects and Monte Carlo statistics were calculated by varying the simulation physics inputs within their experimental ranges around their central values as given below, using for that purpose a reweighting technique in the Monte Carlo samples. For all physics assumptions the recommendations of the LEP Heavy Flavour Working Group (LEPHFWG) [109] have been followed.

The detailed breakdown of the relative errors on ϵ^{uds} and ϵ^c are given in table 6.6 for the 1994 analysis. and the cut $-\log_{10} y \geq 1.0$ defining the b-tight tag, which is the cut value minimizing the error in the single tag analysis. As we shall see later, the optimal cut for the high purity multiple tag scheme is $-\log_{10} y \geq 1.2$ instead of 1.0. Errors given in previous table have to be reevaluated to account for this harder cut. The sensitivity of R_b to light and charm quark uncertainties is the same in the two methods, but since the harder cut reduces the uds and c background efficiencies by factors of about 1.2 and 1.5 respectively, finally the systematic error on R_b is smaller. The upper part of table 6.7 summarizes for the 1994-1995 analysis, the relative systematic errors on $\epsilon^{uds}_{b-tight}$, $\epsilon^c_{b-tight}$ and the corresponding systematic error on R_b. Errors have been added in quadrature. The last line (MC statistics) corresponds to the statistical error on $\epsilon^{uds}_{b-tight}$, $\epsilon^c_{b-tight}$ and its impact on R_b. Table 6.8 reports the breakdown of light and charm quark uncertainties for the 1992-1993 analysis.

We describe now how errors due to charm physics systematics, rate of long lived light hadrons, $b\bar{b}$ and $c\bar{c}$ production from gluon splitting and detector effects have been evaluated.

Table 6.6: Single tag scheme: relative systematic errors on the light and charm quark efficiencies at cut $-\log_{10} y \geq 1.0$.

Source of systematics	Range	$\Delta\epsilon^{uds}/\epsilon^{uds}$	$\Delta\epsilon^{c}/\epsilon^{c}$
Detector resolution		± 0.052	± 0.022
Detector efficiency		± 0.016	± 0.014
K^0	Tuned JETSET$\pm$10%	± 0.013	
Hyperons	Tuned JETSET$\pm$10%	± 0.002	
Photon conversions	$\pm$50%	± 0.006	
Gluon splitting $g \to c\bar{c}$	$(2.38 \pm 0.48)\%$	± 0.043	± 0.005
Gluon splitting $g \to b\bar{b}/g \to c\bar{c}$	0.13 ± 0.04	± 0.173	± 0.020
D^+ fraction in $c\bar{c}$ events	0.233 ± 0.028		± 0.031
D_s fraction in $c\bar{c}$ events	0.102 ± 0.037		∓ 0.009
$c-baryon$ fraction in $c\bar{c}$ events	0.065 ± 0.029		∓ 0.022
D decay multiplicity	2.39 ± 0.14		± 0.022
$Br(D \to K^0 X)$	0.46 ± 0.06		± 0.051
D^0 lifetime	0.415 ± 0.004 ps		± 0.005
D^+ lifetime	1.057 ± 0.015 ps		± 0.007
D_s lifetime	0.447 ± 0.017 ps		± 0.003
Λ_c lifetime	0.206 ± 0.012 ps		± 0.000
$\langle x_E(c) \rangle$	0.484 ± 0.008		± 0.009
Total charm physics			± 0.069
Total $udsc$ background systematics		± 0.206	± 0.079
MC statistics		± 0.037	± 0.019

Table 6.7: Multiple tag scheme: relative light and charm quark systematics at cut $-\log_{10} y \geq 1.2$ for the 1994-1995 data.

Source	$\Delta\epsilon^{uds}_{b-tight}/\epsilon^{uds}_{b-tight}$	$\Delta\epsilon^{c}_{b-tight}/\epsilon^{c}_{b-tight}$	$\Delta R_b \times 10^4$
Tracking effects	± 0.054	± 0.022	$\pm 1.57/1.40$
K^0, hyperons, photons	± 0.014		$\mp 0.26/0.28$
$g \to c\bar{c}$: $(2.38 \pm 0.48)\%$ per event	± 0.159	± 0.024	$\mp 3.63/3.36$
$g \to b\bar{b}/g \to c\bar{c}$: 0.13 ± 0.04	± 0.144	± 0.021	$\mp 3.27/3.05$
Charm physics		± 0.066	$\mp 3.13/2.75$
Total $udsc$ background systematics	± 0.222	± 0.076	$\pm 6.02/5.50$
MC statistics (1994/1995)	$\pm 0.025/0.055$	$\pm 0.017/0.037$	$\pm 0.96/1.90$

Table 6.8: Multiple tag scheme: relative light and charm quark systematics for the 1992-1993 data.

Source	$\Delta\epsilon^{uds}_{b-tight}/\epsilon^{uds}_{b-tight}$	$\Delta\epsilon^{c}_{b-tight}/\epsilon^{c}_{b-tight}$	$\Delta R_b \times 10^4$
Tracking effects	± 0.017	± 0.065	± 5.25
K^0, hyperons, photons	± 0.053		∓ 1.81
$g \to c\bar{c}$: $(2.38 \pm 0.48)\%$ per event	± 0.035	± 0.006	∓ 1.32
$g \to b\bar{b}/g \to c\bar{c}$: 0.13 ± 0.04	± 0.151	± 0.022	∓ 5.58
Charm physics		± 0.131	∓ 10.53
Total *udsc* background systematics	± 0.165	± 0.148	± 13.21
MC statistics	± 0.024	± 0.015	± 1.48

Charm physics systematics

There are many physics effects which lead to an uncertainty in the charm background:

- The tagging efficiencies of weakly-decaying charmed hadrons are substantially different owing to large differences in lifetime. Therefore their relative abundances in $Z \to c\bar{c}$ events affect the charm tagging efficiency. The errors on the D^+, D_s and $c-baryon$ fractions in $c\bar{c}$ events, and their correlation matrix are used to evaluate the uncertainty on the charm efficiency. The D^0 fraction is considered as $f(D^0) = 1 - f(D^+) - f(D_s) - f(c-baryon)$. Therefore, when varying the fractions in the Monte Carlo, the variation of each of the three channels is always compensated by the D^0 fraction. The charmed hadron production rates are obtained as it is described in reference [109]. LEP data provide measurements of [117, 118, 119]:

$$\begin{aligned} R_c f(D^0) Br(D^0 \to K^-\pi^+) \\ R_c f(D^+) Br(D^+ \to K^-\pi^+\pi^+) \\ R_c f(D_s) Br(D_s^+ \to \phi\pi^+) \\ R_c f(\Lambda_c) Br(\Lambda_c^+ \to pK^-\pi^+). \end{aligned} \tag{6.17}$$

These measurements are then combined using the errors (or the covariance matrix) with the measured values of the charmed hadron branching ratios:

$$\begin{aligned} Br(D^0 \to K^-\pi^+) \\ Br(D^+ \to K^-\pi^+\pi^+) \\ Br(D_s^+ \to \phi\pi^+)/Br(D^0 \to K^-\pi^+) \\ Br(\Lambda_c^+ \to pK^-\pi^+). \end{aligned} \tag{6.18}$$

All of them are taken from the Particle Data Group [7], except for the case of $Br(D_s^+ \to \phi\pi^+)/Br(D^0 \to K^-\pi^+)$ which is taken from a model independent CLEO analysis [120]. This ratio is taken instead of the direct $Br(D_s^+ \to \phi\pi^+)$ because it is free of theoretical assumptions. Finally, an additional constraint is added on the heavy baryon production. It is assumed that $f(c-baryon)/f(\Lambda_c) = 1.15 \pm 0.05$. All this information is merged with a least squares minimization, leaving as free parameters $f(D^+)$, $f(D_s)$, $f(c-baryon)$, R_c, $f(c-baryon)/f(\Lambda_c)$ and the four branching ratios listed above [109]. Results and errors obtained for the fractions are $f(D^+) = 0.233 \pm 0.028$, $f(D_s) = 0.102 \pm 0.037$ and $f(c-baryon) = 0.065 \pm 0.029$. The correlation between $f(D^+)$ and $f(D_s)$ and $f(c-baryon)$ is measured to be -0.36 and -0.24 respectively. The correlation between $f(D_s)$ and $f(c-baryon)$ is -0.14.

- Different decay modes of a given charmed hadron can have different tagging efficiencies. Unfortunately, the complete set of measurements of the exclusive branching ratios does not exist for any hadron type. Since the tags basically extract the information from charged tracks, decay modes can be classified into topological channels, according to the number of charged products. This classification should account for the most part of the differences in efficiency. The most accurate measurement of the inclusive topological branching ratios of D^+, D^0 and D_s mesons are from the MARK III Collaboration [121]. In order to calculate the resulting error on the D decay multiplicity, each channel is varied by its uncertainty except for the largest one, which is used to balance the various shifts. The errors extracted for each channel are then combined using their correlation coefficients [109] in order to estimate the separated D^+, D^0 and D_s decay multiplicities. The error due to the D decay multiplicity is then the sum in quadrature of the separate uncertainties weighted by their relative contributions. The average D decay multiplicity value finally obtained is 2.39 ± 0.14. The MARK III measurements include K_s^0 decay products, which at LEP are generally not associated to a secondary vertex. There is therefore an additional uncertainty from the branching ratio $Br(D \to K_s^0\, X)$ which is taken from the Particle Data Group [7], and it has an average value of 0.46 ± 0.06.

- The lifetime of charm hadrons are taken from the Particle Data Group [7] and are listed in table 6.6.

- Charm fragmentation: parameters should be varied to give a range of the mean scaled energy of charmed hadrons consistent with LEP results, $\langle x_E(c)\rangle = 0.484 \pm 0.008$ [109]. The exact definition of the mean scaled energy is $\langle x_E(c)\rangle = E_{hadron}/E_{beam}$, where E_{hadron} refers to the weakly decaying charmed hadron. Previous value is a combination of measurements made at LEP with leptons, D mesons and D^{*+} mesons. Each of these analyses provides a measurement of $\langle x_E(c)\rangle$ for a particular mixture of charmed hadrons. The different results are

corrected to the weakly decaying level, and then combined to obtain the above result. The fragmentation function from the model of Peterson et al. [36] with one free parameter is used. This parameter is varied in order to assess the uncertainty due to the measured value of $\langle x_E(c) \rangle$.

Rate of long lived light hadrons

The total production rate of long lived light hadrons (K^0, Λ and other weakly-decaying hyperons) affects the backgrounds in lifetime based tags. These rates were measured by DELPHI and then the fragmentation models were tuned accordingly. As an estimate of the error due to these sources a 10% variation around their central values is used. Photon conversions were varied around their central values in simulation by 50%. These uncertainties are conservatively suggested by the remaining differences found between the rate for data and Monte Carlo simulation.

Gluon splitting

As described in chapter 1, the presence of a B or D hadron in a multihadronic final state is a signature of a primary production of $b\bar{b}$ or $c\bar{c}$ respectively. However, $b\bar{b}$ and $c\bar{c}$ pair quarks can also be produced from gluon radiation $g \to q\bar{q}$ in light quark events (but also in $c\bar{c}$ and $b\bar{b}$ events, although much more suppressed). Therefore, the rates of $b\bar{b}$ and $c\bar{c}$ production from gluon splitting is an additional source of systematic uncertainties in the evaluation of the *uds* and *c* efficiencies. The average number of $c\bar{c}$ quark pairs produced per multihadron event by the gluon splitting process $g \to c\bar{c}$ has been measured by OPAL to be $(2.38 \pm 0.48) \times 10^{-2}$ [122]. This measurement uses the JETSET Monte Carlo to model the very soft energy spectrum of heavy flavour hadrons from gluon splitting. This result is consistent with perturbative QCD calculations [123] and with the prediction of the JETSET Monte Carlo. The $g \to c\bar{c}$ rate in Monte Carlo was adjusted to the OPAL value, and the $g \to b\bar{b}$ rate, for which no published measurements are available, was adjusted to be 0.13 ± 0.04 of the $g \to c\bar{c}$ rate, based on theoretical expectations [123]:

$$\frac{f(g \to b\bar{b})}{f(g \to c\bar{c})} = \frac{m_c^2}{m_b^2} = 0.13 \pm 0.04. \tag{6.19}$$

The $g \to b\bar{b}$ rate was therefore taken $(0.31 \pm 0.11) \times 10^{-2}$. The $g \to c\bar{c}$ rate and the $g \to c\bar{c}/g \to b\bar{b}$ ratio were varied separately within the indicated ranges.

The assumed value of the $g \to b\bar{b}$ rate is compatible with two recent measurements from ALEPH [124] and DELPHI [125]. These measurements are both based on a search for b tagged jets in 4-jet events, providing an average result of $f(g \to b\bar{b}) = (0.246 \pm 0.092) \times 10^{-2}$. This average takes into account correlated systematic errors between both measurements.

Tracking effects

To estimate the uncertainties on $\epsilon^{uds}_{b-tight}$ and $\epsilon^{c}_{b-tight}$ due to detector effects in 1994-1995, four *tests* were carried out:

- To estimate the effect of the resolution, the simulation was rerun with a tuning of the tracking which described the data much poorly than the default one (about 4% relative difference in the light and charm quark efficiencies).
- A second test for the effect of the detector resolution on $\epsilon^{c}_{b-tight}$ was to use the calibration file for data in the simulation. This method was preferred for $\epsilon^{c}_{b-tight}$ since it directly tests the difference between the data and the simulation. It gave results consistent with the first test method. For $\epsilon^{uds}_{b-tight}$ it cannot be used, as it artificially modifies the tagging rate due to statistical fluctuations.
- To estimate the effect of correlations between tracks included in the tagging calculation, the difference in tagging rate between data and simulation using tracks with negative impact parameters was taken as the uncertainty on $\epsilon^{uds}_{b-tight}$.
- The track efficiency in the simulation was varied by the amount of the residual difference between the data and the Monte Carlo.

The errors obtained with the first, third and fourth tests were added in quadrature to obtain the final detector uncertainty on $\epsilon^{uds}_{b-tight}$. For $\epsilon^{c}_{b-tight}$ only the second and fourth tests were used. This procedure to assign uncertainties from detector effects is assumed to give a conservative estimate of the truth effect.

For 1992-1993 a simpler method was used. A value of R_b was obtained without applying the tracking resolution tuning described in chapter 4, and the result was compared with the standard measurement applying this fine tuning. The difference was assigned as a largely conservative estimate of the error due to detector resolution effects.

6.2.2 Hemisphere correlation uncertainties

The third main source of systematics, due to hemisphere correlations, is the more complex. As previously pointed out, one has to take into account for the extraction of R_b that the two hemispheres in an event are not completely uncorrelated. The ρ^{q}_{IJ} hemisphere correlations are estimated from simulation, but only of few of them has an impact on R_b. They are given with their sensitivities in the second column of tables 6.9, 6.10 and 6.11 for 1994, 1995 and 1992-1993 respectively, where the errors are due to simulation statistics. The sensitivity is defined as the relative change on R_b due to a change of a given correlation, $\frac{\Delta R_b}{R_b \Delta \rho^{q}_{IJ}}$. Only 14 correlations out of 45 are given in the table, whose have sensitivities to R_b higher than 0.010. The sensitivity of the measurement of R_b to $\rho^{b}_{b-tight,b-tight}$ is 0.805 in 1994, 0.798 in 1995 and 0.714

in 1992-1993, to be compared to unity in the single tag analysis. However, as shown in the tables, there are other correlations with non negligible sensitivities (two of them above 0.10 in 1994-1995 for instance), which have no counterpart in the single tag analysis. Finally, as explained in section 5.2.8, correlations containing the no-tag category (I or $J = N_T$) were determined from the data fit, so they have a negligible sensitivity on the analysis.

Systematic errors on ρ^q_{IJ} can be separated into three main sources:

- errors arising from uncertainties in *uds*, *c* and *b* simulation,
- errors due to the vertex detector acceptance, and
- errors due to gluon radiation effects.

Finally we should add the contribution of the statistical error on correlation coefficients, due to the limited statistics of the simulation sample (MC statistics). This uncertainty was obtained numerically from a 'toy' simulation of the experiment based on the central values and the statistical errors of ρ^q_{IJ} as quoted from the standard Monte Carlo samples.

Effects from *uds*, *c* and *b* physics simulation

Varying the *uds*, *c* and *b* physics simulation parameters (besides its direct effect on $\epsilon^{uds}_{b-tight}$, $\epsilon^{c}_{b-tight}$ and $\epsilon^{b}_{b-tight}$, though for $\epsilon^{b}_{b-tight}$ it is unimportant since it is fitted on data) can influence the size of the correlations and then the R_b measurement.

For each variation of these physical parameters, each simulated event is reweighted. Then the correlation coefficients are recalculated and their new values injected in the fit of the real data, allowing a new determination of R_b. The observed change on R_b is assigned as the systematic error due to the parameter. However due to the use of separate hemisphere primary vertices, the effects of these physics systematics were found to be extremely small. In the case of the single tag analysis, the uncertainties on ρ_b at cut $-\log_{10} \geq 1.0$ in 1994 are summarized in the upper part of table 6.12. The upper part of table 6.13 summarizes the errors on R_b due to these physical uncertainties in the case of the multiple tag analysis. In this case, additional uncertainties are included due to charm physics, production of heavy quarks from gluon splitting and B hadron branching ratios.

Like in the case of $\epsilon^{uds}_{b-tight}$ and $\epsilon^{c}_{b-tight}$, uncertainties in the physical parameters used in the simulation of correlations are calculated by varying the physics inputs within their experimental ranges around their central values, according to the prescription given in reference [109]. They are briefly summarized below:

- The average charged decay multiplicity of the B hadrons is varied by ± 0.35. The size of the variation reflects the accuracy of the measurements by DELPHI [126] and OPAL [127], whose combination is 5.25 ± 0.35, excluding all decay tracks from K^0 and Λ. In the 1994-1995 the simulation input for the B decay

Table 6.9: Major b, c and uds correlations (MC global) with sensitivity > 0.010 on R_b at the nominal cuts for the 1994 analysis. Estimations on simulation (MC) and real data (Data) of the contributions due to angular ($\cos\theta_{thrust}$, ϕ_{thrust}) and gluon radiation effects (p_{jet}).

			$\cos\theta_{thrust}$		ϕ_{thrust}		p_{jet}	
	MC global	Sensitivity	MC	Data	MC	Data	MC	Data
			b correlations					
$\rho^b_{b-tight,b-tight}$	0.0187 ± 0.0027	0.805	0.0035	0.0030	0.0010	0.0013	0.0115	0.0130
$\rho^b_{b-tight,b-standard}$	0.0036 ± 0.0027	0.236	0.0010	-0.0003	0.0006	0.0009	-0.0000	-0.0001
$\rho^b_{b-tight,b-loose}$	-0.0020 ± 0.0028	0.140	0.0000	0.0002	-0.0011	0.0004	0.0042	0.0051
$\rho^b_{b-tight,charm}$	0.0104 ± 0.0053	-0.040	-0.0033	-0.0066	0.0034	0.0016	0.0055	0.0066
$\rho^b_{b-standard,b-standard}$	0.0047 ± 0.0050	-0.082	0.0028	0.0008	0.0007	0.0003	0.0083	0.0071
$\rho^b_{b-standard,b-loose}$	-0.0003 ± 0.0042	-0.072	0.0029	0.0012	0.0008	0.0008	0.0035	0.0037
$\rho^b_{b-standard,charm}$	-0.0094 ± 0.0077	0.028	-0.0114	-0.0045	0.0003	-0.0007	0.0047	0.0045
$\rho^b_{b-loose,b-loose}$	0.0144 ± 0.0052	-0.037	0.0034	0.0021	0.0016	0.0010	0.0022	0.0025
$\rho^b_{b-loose,charm}$	-0.0139 ± 0.0079	0.019	-0.0121	-0.0065	-0.0004	0.0002	0.0029	0.0035
			c correlations					
$\rho^c_{b-standard,charm}$	-0.0469 ± 0.0197	0.012	-0.0079	-0.0066	0.0024	0.0017	0.0124	0.0083
$\rho^c_{b-loose,charm}$	-0.0015 ± 0.0115	0.025	-0.0105	-0.0089	0.0013	-0.0013	0.0142	0.0193
$\rho^c_{charm,charm}$	0.0350 ± 0.0093	-0.015	0.0158	0.0092	0.0025	0.0009	0.0116	0.0148
			uds correlations					
$\rho^{uds}_{charm,uds}$	0.0219 ± 0.0091	0.020	0.0088	0.0135	-0.0000	-0.0001	0.0184	0.0172
$\rho^{uds}_{uds,uds}$	0.0778 ± 0.0067	0.022	0.0079	0.0079	0.0053	0.0022	0.0374	0.0276

Table 6.10: Same as previous table but for 1995 data.

	MC global	Sensitivity	$\cos\theta_{thrust}$		ϕ_{thrust}		p_{jet}	
			MC	Data	MC	Data	MC	Data
			b correlations					
$\rho^b_{b-tight,b-tight}$	0.0235 ± 0.0044	0.798	0.0029	0.0037	0.0019	0.0024	0.0114	0.0111
$\rho^b_{b-tight,b-standard}$	-0.0006 ± 0.0044	0.221	0.0016	0.0014	-0.0000	-0.0000	0.0107	0.0109
$\rho^b_{b-tight,b-loose}$	-0.0032 ± 0.0044	0.128	0.0001	0.0001	-0.0007	-0.0012	0.0056	0.0060
$\rho^b_{b-tight,charm}$	-0.0025 ± 0.0083	-0.058	-0.0035	-0.0081	0.0015	0.0010	0.0055	0.0068
$\rho^b_{b-standard,b-standard}$	0.0077 ± 0.0079	-0.074	0.0032	-0.0002	0.0010	0.0011	0.0094	0.0098
$\rho^b_{b-standard,b-loose}$	0.0122 ± 0.0065	-0.063	0.0036	-0.0003	0.0013	0.0010	0.0049	0.0057
$\rho^b_{b-standard,charm}$	-0.0162 ± 0.0120	0.030	-0.0121	-0.0009	-0.0003	0.0008	0.0053	0.0066
$\rho^b_{b-loose,b-loose}$	0.0081 ± 0.0080	-0.039	0.0047	0.0028	0.0020	0.0015	0.0031	0.0045
$\rho^b_{b-loose,charm}$	0.0115 ± 0.0122	0.021	-0.0140	-0.0091	-0.0006	0.0002	0.0036	0.0030
			c correlations					
$\rho^c_{b-standard,charm}$	-0.0162 ± 0.0312	0.014	-0.0078	-0.0067	0.0019	0.0000	0.0109	0.0078
$\rho^c_{b-loose,charm}$	0.0365 ± 0.0178	0.027	-0.0113	-0.0109	0.0010	-0.0002	0.0122	0.0080
$\rho^c_{charm,charm}$	0.0151 ± 0.0141	-0.025	0.0157	0.0098	0.0020	0.0006	0.0111	0.0142
			uds correlations					
$\rho^{uds}_{charm,uds}$	0.0314 ± 0.0140	0.011	0.0086	0.0096	0.0008	0.0004	0.0170	0.0152
$\rho^{uds}_{uds,uds}$	0.0869 ± 0.0107	0.018	0.0075	0.0076	0.0032	0.0040	0.0359	0.0265

Table 6.11: Same as previous tables but for the 1992-1993 data.

	MC global	Sensitivity	$\cos\theta_{thrust}$		ϕ_{thrust}		p_{jet}	
			MC	Data	MC	Data	MC	Data
			b correlations					
$\rho^b_{b-tight,b-tight}$	0.0327 ± 0.0033	0.714	0.0034	0.0024	0.0086	0.0116	0.0153	0.0135
$\rho^b_{b-tight,b-standard}$	0.0141 ± 0.0027	0.346	0.0005	0.0006	-0.0002	-0.0006	0.0098	0.0099
$\rho^b_{b-tight,b-loose}$	-0.0039 ± 0.0031	0.214	-0.0006	0.0001	-0.0012	0.0020	0.0048	0.0051
$\rho^b_{b-tight,charm}$	-0.0107 ± 0.0048	-0.066	-0.0007	-0.0010	0.0026	0.0017	-0.0010	-0.0018
$\rho^b_{b-standard,b-standard}$	0.0121 ± 0.0037	-0.116	0.0010	0.0011	0.0010	0.0018	0.0073	0.0079
$\rho^b_{b-standard,b-loose}$	0.0052 ± 0.0033	-0.110	0.0010	0.0016	0.0009	0.0010	0.0041	0.0047
$\rho^b_{b-standard,charm}$	0.0001 ± 0.0052	0.045	-0.0006	-0.0005	-0.0005	0.0003	0.0006	0.0007
$\rho^b_{b-loose,b-loose}$	0.0015 ± 0.0044	-0.065	0.0014	0.0006	0.0010	0.0004	0.0025	0.0030
$\rho^b_{b-loose,charm}$	0.0018 ± 0.0058	0.031	-0.0005	-0.0019	-0.0002	0.0001	0.0010	0.0016
			c correlations					
$\rho^c_{b-standard,charm}$	0.0201 ± 0.0142	0.016	0.0013	0.0021	0.0032	-0.0185	0.0118	0.0086
$\rho^c_{b-loose,charm}$	0.0043 ± 0.0094	0.023	0.0010	0.0013	0.0019	-0.0078	0.0093	0.0089
$\rho^c_{charm,charm}$	-0.0005 ± 0.0065	-0.012	0.0003	0.0007	0.0031	0.0011	0.0033	0.0051
			uds correlations					
$\rho^{uds}_{charm,uds}$	-0.0058 ± 0.0046	0.031	-0.0037	-0.0055	-0.0010	0.0009	0.0079	0.0072
$\rho^{uds}_{uds,uds}$	0.0519 ± 0.0037	0.035	0.0065	0.0074	0.0045	0.0071	0.0231	0.0199

multiplicity was 4.93 instead of 5.25. However, this simulation input value is consistent with a recent new precise DELPHI measurement 4.96 ± 0.06 [116], based on a comparison of tracks with positive and negative lifetime impact parameters in b tagged events. Consequently the simulation was not reweighted for the 5.25 value. To be conservative the error on this value was taken to be ± 0.35.

- The average lifetime of B hadrons was taken to be 1.55 ± 0.04. The size of the variation was chosen to be larger than the accuracy of the world average of [7] to allow for the uncertainty due to the different efficiencies for different B hadron species.

- The b quark fragmentation was varied similarly as for the c quark fragmentation by applying a weight to each simulated event using the fragmentation function of Peterson et al. [36] in order to insure that the average scaled energy of the weakly decaying B hadron $\langle x_E(b) \rangle$ was 0.702 ± 0.008. This central value and range of variation reflects the accuracy of $\langle x_E(b) \rangle$ measured by LEP experiments [128]. The error quoted contains both statistical and systematic uncertainties. The largest uncertainty comes from the modeling of the shape of the fragmentation functions, both due to excited states and to the fragmentation function used. The fragmentation function is defined with respect to the non-observable variable $z = (E+p)_{\parallel,hadron}/(E+p)_{\parallel,quark}$ (see chapter 1). Monte Carlo must be used to translate z into x, and the weighting of the Monte Carlo must be applied in terms of z. Because of this, the value of the fragmentation parameter depends on the Monte Carlo used to do this correction, and it is therefore a strongly model dependent quantity. The derivation of the mean scaled energy from this function is however much less sensitive to these modeling issues. All these statements are also true for the charm fragmentation studied previously. Finally, because of the extremely small resulting error on R_b, weighting in terms of x instead of z leads to negligible differences.

- The production fractions of the B hadron species were taken from the Particle Data Group [7].

Isolation of correlation sources due to angular effects

Correlations are also affected by errors which are not related to simulation, such as the angular effects that are discussed below. However, when a source of correlation ρ^b_{IJ} can be isolated and measured in real and simulated data, it is possible to extract the contribution of this source to the systematic error on R_b. This done, as explained later, by a comparison of their effect in data and simulation.

To isolate the contribution of a single physical source to the correlations, a generic variable η which quantifies the physical effect is defined, and calculated

Table 6.12: Systematic errors on the hemisphere correlation ρ_b in the single tag analysis for the 1994 analysis.

Source of systematics	$\Delta\rho \times 10^3$
Two b quarks in one hemisphere: $\pm 30\%$	± 0.3
b fragmentation $\langle x_E(b)\rangle$: 0.702 ± 0.008	± 0.1
B decay multiplicity: 5.25 ± 0.35	± 1.0
Average B lifetime: 1.55 ± 0.04 ps	± 0.2
Total b physics correlation error	± 1.1
Angular effects	± 1.2
Gluon radiation	± 1.0
MC statistics	± 2.3

Table 6.13: Systematic errors due to hemisphere correlations for the multiple tag analysis.

Source	$\Delta R_b \times 10^4$	
	1994-1995	1992-1993
Two b quarks in same hemisphere: $\pm 30\%$	∓ 0.84	∓ 2.68
$g \to c\bar{c}$: $(2.38 \pm 0.48)\%$ per event	∓ 0.05	∓ 0.06
$g \to b\bar{b}/g \to c\bar{c}$: 0.13 ± 0.04	∓ 0.05	∓ 0.06
b fragmentation $\langle x_E(b)\rangle$: 0.702 ± 0.008	∓ 0.53	∓ 1.54
B decay multiplicity: 5.25 ± 0.35	∓ 2.01	∓ 4.49
B_s fraction: 0.112 ± 0.019	∓ 0.56	∓ 0.35
Λ_b fraction: 0.132 ± 0.041	∓ 0.55	∓ 3.18
Average B lifetime: 1.55 ± 0.04 ps	∓ 0.02	∓ 0.05
Charm physics	∓ 0.32	∓ 0.42
Total uds, c and b physics correlation error	∓ 2.40	∓ 6.34
Angular effects	$\pm 1.26/3.40$	± 6.34
Gluon radiation	$\pm 2.54/1.72$	± 1.82
MC statistics	$\pm 5.52/9.23$	± 6.41

independently in each hemisphere. For example, the angular acceptance correlation is studied using the polar angle of the B hadron which decays in a given hemisphere. For a variable η, we can define a probability function $\epsilon^b_{same}(\eta)$ to tag the B hadron as b, and the probability $\epsilon^b_{oppo}(\eta)$ to tag also the other B hadron as b in the opposite hemisphere. The B hadron tagging efficiency is then measured in the same and opposite hemispheres as a function of η. The convolution of these two efficiency functions gives the correlation effect due only to this variable, but averaging out all other correlation sources. The single source of correlation is calculated from local double tag efficiency, together with the single tag efficiency ϵ^b. This procedure uses the fact that the value of the test variable is correlated between the hemispheres, i.e. if one hemisphere has a cosine of its polar angle at z the other one has it at $-z$. The contribution from variable η to ρ_b in the single tag analysis can then be determined through the following expression

$$\rho^{\eta}_b = \frac{\sum_\eta f_b(\eta)\epsilon^b_{same}(\eta)\epsilon^b_{oppo}(\eta)}{\left[\sum_\eta f_b(\eta)\epsilon^b_{same}(\eta)\right]^2} - 1 \tag{6.20}$$

where $f_b(\eta)$ is the distribution of b hemispheres (normalized to unity) as a function of η; $\epsilon^b_{same}(\eta)$ and $\epsilon^b_{oppo}(\eta)$ are the efficiencies to tag a hemisphere of flavour b in the same and opposite hemispheres as a function of η respectively. Knowing the sources to the correlation ρ_b, the systematic error on its value can be estimated. For each correlation component an approximate correlation is defined using experimental observables. For example, the polar angle of the B hadron is replaced with the polar angle of the event thrust axis of the hemisphere associated with that hadron. The variables used to isolate the correlation sources are: the cosine of the polar angle, $cos\theta_{thrust}$, and the azimuthal angle, ϕ_{thrust}, of the thrust axis to describe the angular effects due to the vertex detector and p_{jet} (as described below) to study the QCD/gluon radiation effects. If the tagging efficiency in one hemisphere depends on the value of these testing variables in the same or opposite hemisphere, non-zero correlations are expected for these sources.

In the multiple tag analysis, expression (6.20) generalizes as follows:

$$\rho^{q,\eta}_{IJ} = \frac{\sum_\eta f_q(\eta)\left[\epsilon^q_{I,same}(\eta)\epsilon^q_{J,oppo}(\eta) + \epsilon^q_{J,same}(\eta)\epsilon^q_{I,oppo}(\eta)\right]}{2\left[\sum_\eta f_q(\eta)\epsilon^q_{I,same}(\eta)\right]\left[\sum_\eta f_q(\eta)\epsilon^q_{J,same}(\eta)\right]} - 1 \tag{6.21}$$

where $f_q(\eta)$ is the distribution of q hemispheres as a function of the variable η and $\epsilon^q_{I,same}(\eta)$ and $\epsilon^q_{J,oppo}(\eta)$ are the efficiencies, functions of η, to classify the same and opposite hemispheres in the categories I and J respectively for the flavour q.

The contribution $\rho^{q,\eta}_{IJ}$ can easily be computed for Monte Carlo because the flavour q is known. However, comparison of data and Monte Carlo requires the experimental isolation of this flavour also in the data. An approached flavour isolation was obtained for uds and b quarks using a soft multivariate tag. No c quark selection could

be achieved due to the small c event statistics and the rather poor c quark purification. However this was proven not to be a problem because of the small sensitivity of R_b to c correlations. In 1994-1995, the *uds* and b selections were performed imposing the soft cuts $\Delta_{uds} > 1.5$ and $\Delta_b > -0.5$ respectively on the opposite hemisphere to the tested one, in order to avoid an artificial bias. The resulting hemisphere b efficiencies were 11.7%, 35.5% and 79.2% for *uds*, c and b flavours respectively (56.9% b purity). The hemisphere *uds* efficiencies were 82.4%, 52.3% and 15.0% for *uds*, c and b flavours respectively (80.3% *uds* purity). Figures 6.3, 6.4 and 6.5 compare the efficiencies $\epsilon^q_{l,same}(\eta)$ and $\epsilon^q_{l,oppo}(\eta)$ for 1994 data and simulation for the polar and azimuthal angles for all events and with b and *uds* flavour enrichment in opposite hemisphere respectively. Only the b-tight, b-standard, charm and uds tags are shown. To remove global differences in efficiencies between data and simulation, which are meaningless in this analysis because of efficiencies are measured directly from data, the mean efficiency in data was normalized to the one obtained in simulation. In 1992-1993, the *uds* and b selections were quoted imposing the cuts $\Delta_{uds} > 1.4$ and $\Delta_b > -0.2$ respectively. The resulting hemisphere b efficiencies were 13.0%, 30.8% and 73.4% for *uds*, c and b flavours respectively (54.6% b purity). The hemisphere *uds* efficiencies were 75.1%, 50.2% and 15.9% for *uds*, c and b flavours respectively (79.5% *uds* purity).

The efficiencies $\epsilon^q_{l,same}(\eta)$ and $\epsilon^q_{l,oppo}(\eta)$ are obtained as the ratio of l tagged q hemispheres with respect to all q hemispheres as a function of η computed in the same and opposite hemispheres respectively after enrichment. For the *uds* and b enrichment the hemisphere was taken as q only if it passed the soft cut in the opposite hemisphere to the one where η was calculated. The normalized distributions $f_q(\eta)$ are similarly computed from the opposite hemisphere. In the case of figure 6.3 (no enrichment), they are simply the fraction of hemispheres classified as l in the same and opposite hemispheres.

From figures 6.3, 6.4 and 6.5, can be seen the good Monte Carlo description of the data, especially for the case of b categories, which is a result of the fine tuning of the tracking system. The obtained agreement for 1995 and 1992-1993 data is similar, although it is a little poorer in the latest data set. This will be reflected in larger systematic errors due to angular effects on hemisphere correlations.

The correlation was then calculated using equation (6.21). The result was scaled by the ratio of the correlations in pure q events and in the selected *uds* and b events obtained from simulation; c correlations were obtained by scaling on all events. This correction was done in order to remove backgrounds in the selected samples as well as to correct for any bias caused by the soft cuts. However, the obtained correction factors were small.

Since the primary vertex is reconstructed separately in each hemisphere, it can only contribute to correlations via the LEP interaction region, which is common to both hemispheres. As this interaction region is highly elliptical in the $R\phi$ plane, it tends to make the tagging efficiency ϕ dependent. Any resulting correlation is therefore contained in the contribution estimated using the ϕ_{thrust} variable.

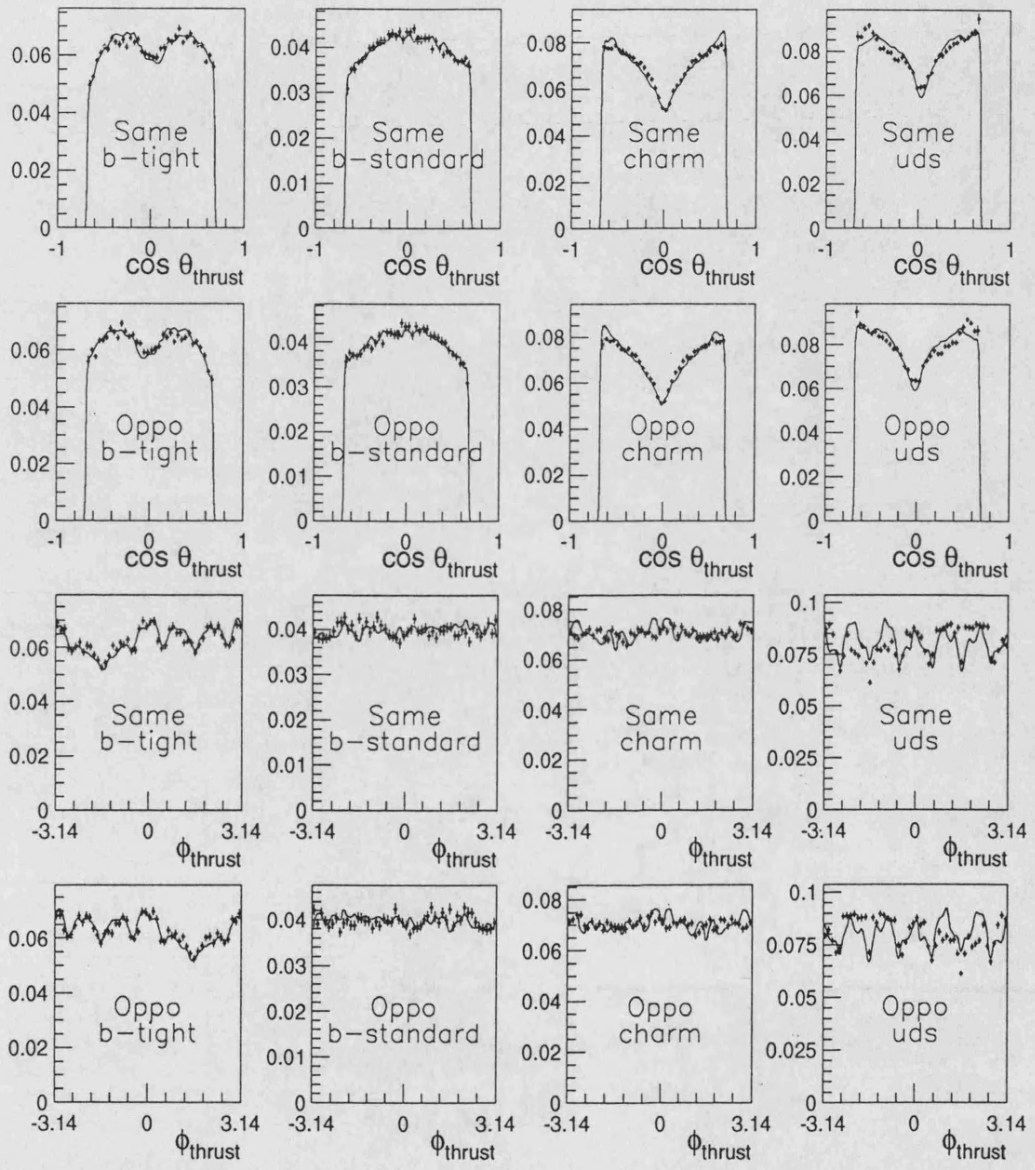

Figure 6.3: Comparison of the $\epsilon^q_{I,same}(\eta)$ and $\epsilon^q_{I,oppo}(\eta)$ efficiencies for data (points) and simulation (continuous line) in 1994 for the polar and azimuthal angles for all events. Only the b-tight, b-standard, charm and uds tags are shown. To remove global differences in efficiencies between data and simulation, which are meaningless in this analysis because of efficiencies are measured directly from data, the mean efficiency in data was normalized to the one obtained in simulation. Similar plots are obtained for the 1995 and 1992-1993 data samples.

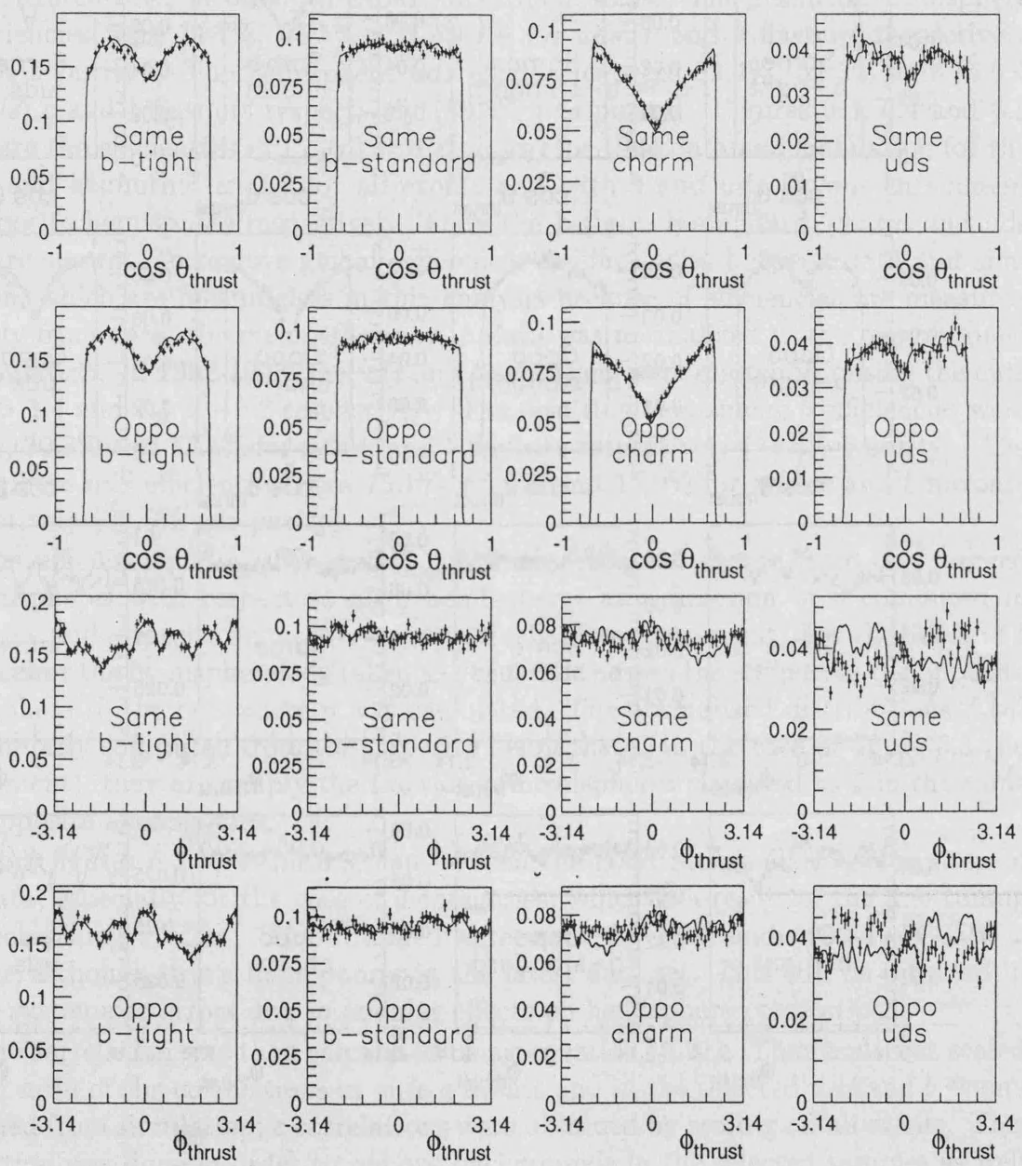

Figure 6.4: Same as figure 6.3 but with b flavour selection in opposite hemisphere (see text).

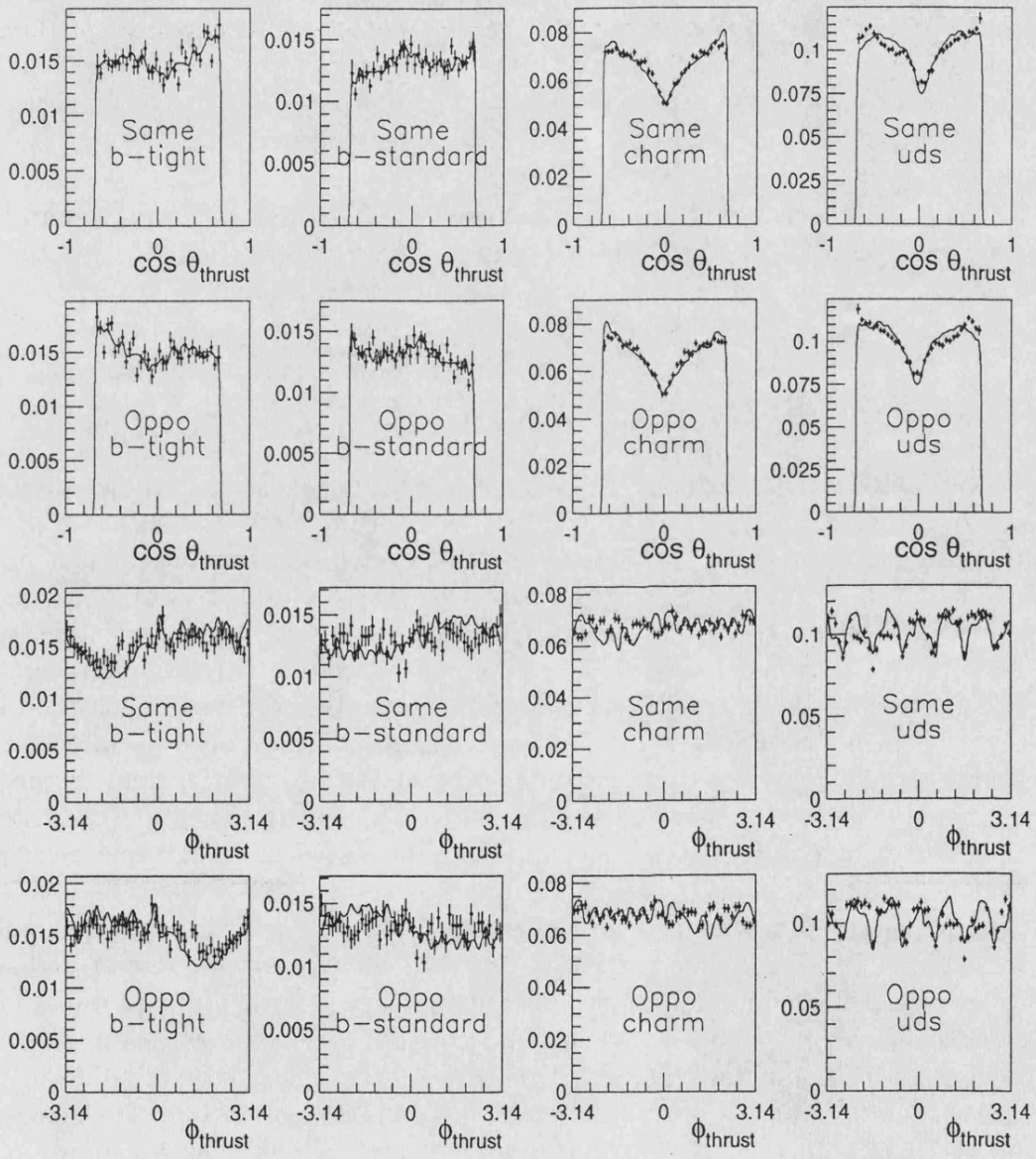

Figure 6.5: Same as figure 6.3 but with uds flavour selection in opposite hemisphere (see text).

Isolation of correlation sources due to gluon radiation (QCD) effects

We have not included in the list of *uds*, *c* and *b* effects the contribution of gluon radiation. We put it apart, because It can be isolated like angular effects (allowing comparison between simulated and real data), provided that a suitable variable η sensitive to gluon radiation is defined. Hard gluon radiation, as already pointed out, is one of the major sources of correlations, as it reduces the momentum of B hadrons (decreasing therefore the tagging efficiency) and eventually could leave them in the same hemisphere. The procedure to isolate correlations due to QCD effects is the same as for $cos\theta_{thrust}$ and ϕ_{thrust}. The third sensitive variable, called p_{jet}, is defined as follows.

The JADE jet algorithm [32] was forced to find three jets. The jet momenta were then rescaled to verify the energy-momentum conservation. If θ_{ij} is the angle between jets i and j, the recalculated energy for jet k is [129]:

$$E_k = \sqrt{s}\frac{\sin\theta_{ij}}{\sin\theta_{12}+\sin\theta_{23}+\sin\theta_{13}}. \tag{6.22}$$

If after this rescaling, y_3 (JADE)[1] is smaller than 0.005 the event is defined as two-jet. Let us take now p_j to be the momentum of the fastest jet divided by the beam energy[2]. The test variable p_{jet} is then introduced as $p_{jet} = (3p_j - 2)^2$. It varies between 0 and 1, and due to the square is a bit flatter than p_j. For the hemisphere that contains the fastest jet (one-jet hemisphere), p_{jet} was then signed to be positive and for the other hemisphere p_{jet} was signed negative (two-jet hemisphere). In the case of two jet events, the sign of p_{jet} is randomized. Since the p_{jet} distribution is different for *b* and *udsc* events, the soft flavour selection in the opposite hemisphere is now fundamental. As an additional complication, the two sources for QCD correlations act differently on the p_{jet} distribution. If the two *b* quarks are one in each hemisphere, the one-jet hemisphere represents the faster and thus better tagged *b*. If the two *b* quarks are boosted into the same hemisphere, the one-jet side contains only a gluon. The systematic error induced by events with both *b* quarks in one hemisphere was tested by varying their amount in simulation by 30%, as suggested by a comparison of the JETSET parton shower and second order matrix element simulations. For the systematic error of gluon radiation, the testing variable p_{jet} was used when comparing data and simulation.

Figure 6.6 compares the $\epsilon^q_{l,same}(\eta)$ and $\epsilon^q_{l,oppo}(\eta)$ efficiencies for data and simulation in 1994 for p_{jet} with *b* and *uds* flavour selections in opposite hemisphere. As previously, only the b-tight, b-standard, charm and uds tags are shown and the efficiencies in data are normalized to the one obtained in simulation.

The correlation from B momentum correlation (gluon radiation) was then calculated using equation (6.21) and rescaled like for the angular variables $cos\theta_{thrust}$

[1] y_3 (JADE) is the value of y_{cut} that sets the transition from 2 to 3 jets using the JADE algorithm.

[2] p_j is therefore defined between 2/3 and 1.

and ϕ_{thrust}.

Correlation errors on R_b due to angular effects and gluon radiation

Tables 6.9, 6.10 and 6.11 summarize the results of this procedure for each of the testing variables and 1994, 1995 and 1992-1993 periods. They compare between real and simulated data, the evaluated contributions of a source (at the nominal cuts) to correlation coefficients having a sensitivity higher than 0.01 on R_b. Figure 6.7 shows the total correlation for the b-tight tag (by far the one with biggest impact on R_b) as a function of the cut value for each 1994-1995 data sample, together with each of the three components and their sum, for data and simulation. It can be seen that the three variables considered above account for most of the global correlation and other correlation sources (apart of the contributions due to physics inputs) have a negligible effect on the correlation systematics. In any case the observed differences between the global correlation and the sum of components are compatible with the statistical error on the estimation of the global correlation. For the 1992-1993 analysis, the agreement between the total correlation and the sum of components is poorer than for the 1994-1995 analysis, which is due to a higher contribution from *uds*, *c* and *b* physics sources (see table 6.13).

The final step, after having estimated the correlation coefficients due to a given source, is to estimate the corresponding error on R_b. For that purpose, we perform two fits on real data. The first fit uses for the correlation matrices ρ_{IJ}^{uds}, ρ_{IJ}^{c} and ρ_{IJ}^{b} the estimations obtained for the source on simulation; the second uses the estimations obtained from real data. For both cases the main elements are given in the tables 6.9, 6.10 and 6.11 (MC and Data columns). The R_b values are compared and the difference is assigned as the systematic error related to the source, due to differences between simulation and data. The errors for the three sources were added quadratically and the quoted uncertainties are listed at the bottom of table 6.13. It must be stressed that this systematic error cannot be attributed only to differences between data and Monte Carlo for the particular flavour, but they can also be due to imperfections of the flavour isolation and scaling. It was also checked that the scaling correction on the correlation coefficients does not affect significantly the quoted systematic error on R_b.

Single tag analysis

In the single tag analysis, to obtain the systematic error on the correlation estimate from the simulation, a very similar procedure was followed. The fraction of tagged events was measured as a function of the relevant variable η both in data and simulation. From this, the correlation due to that single variable was calculated. The larger of either the difference between the data and simulation measurements or the statistical error on this difference was taken as the error estimate for this correlation source.

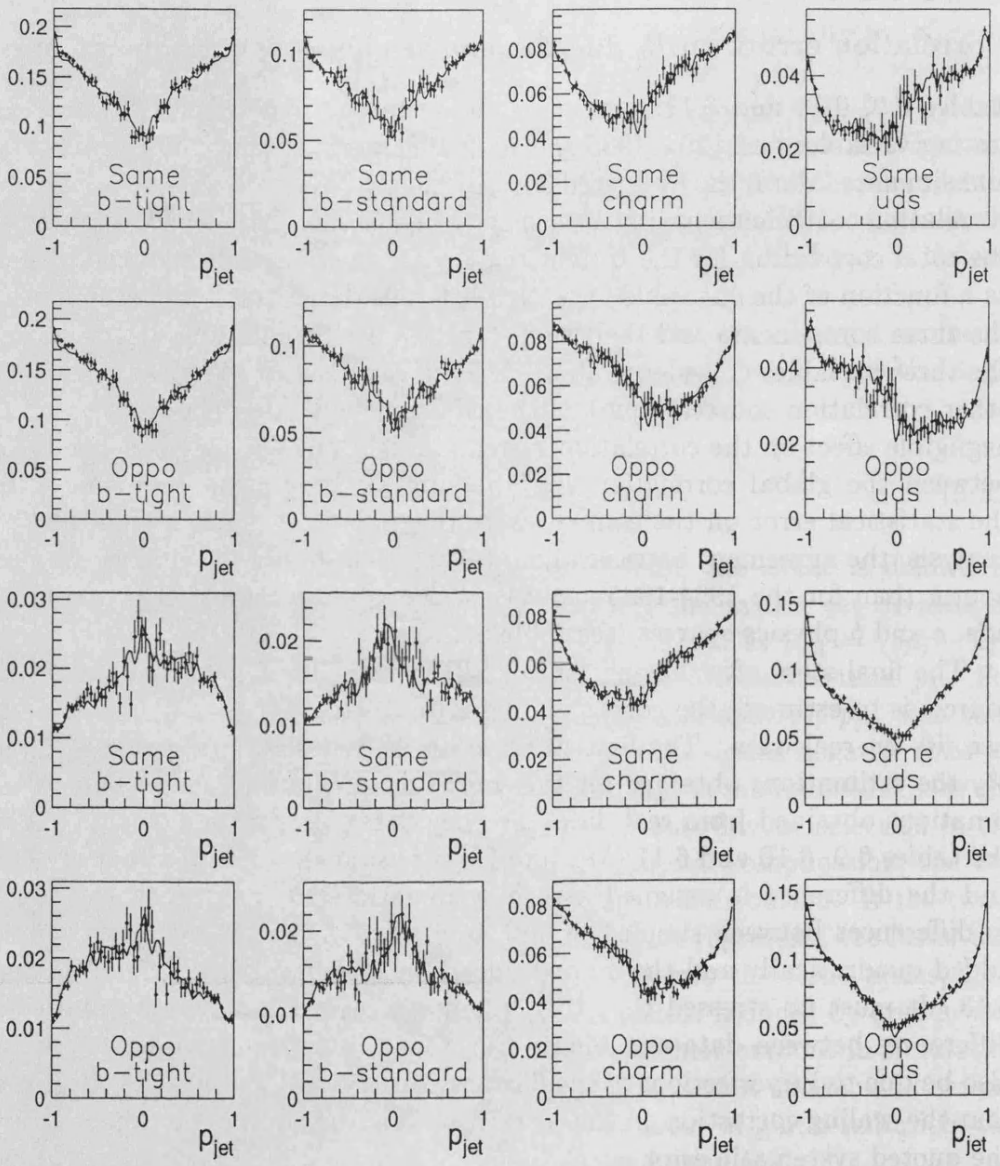

Figure 6.6: Comparison of the $\epsilon^q_{l,same}(\eta)$ and $\epsilon^q_{l,oppo}(\eta)$ efficiencies for data (points) and simulation (continuous line) in 1994 for p_{jet} with b (first eight plots) and uds (the rest) flavour selections in opposite hemisphere (see text). Only the b-tight, b-standard, charm and uds tags are shown. To remove global differences in efficiencies between data and simulation, which are meaningless in this analysis because of efficiencies are measured directly from data, the mean efficiency in data was normalized to the one obtained in simulation. Similar plots are obtained for the 1995 and 1992-1993 data samples.

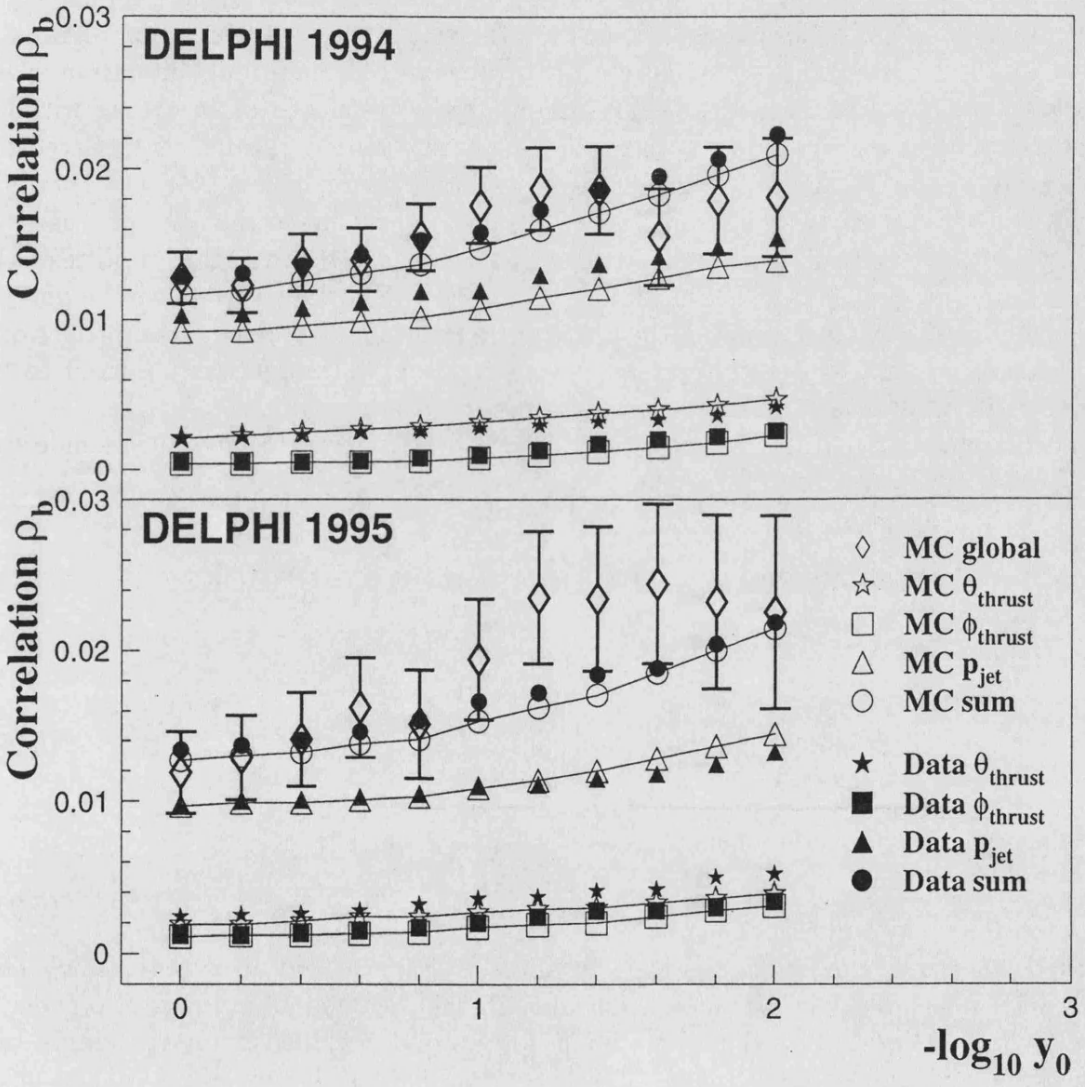

Figure 6.7: Global correlation (ρ_b or $\rho^b_{b-tight,b-tight}$) for the b-tight tag as a function of the cut value $-\log_{10} y_0$ for the 1994 and 1995 analyses, together with each of the three main correlation components and their sum, for data and simulation. Points are bin to bin correlated.

For the angular variables all events have been used. Because the initial angular distributions are identical for b and light quark events no bias was introduced. It was, however, verified that the conclusions did not change if a soft b tag was required in the hemisphere opposite to the tested one. For the QCD effects, systematic uncertainties were quoted as explained above using soft b confidence cut. The only difference was that, in an attempt to remove from p_{jet} the contribution coming from the two b quarks contained in the same hemisphere, the one-jet hemisphere was only used if it passed a soft b tag. On the two-jet side, the soft b tag was not applied since it changes the ratio of events with a fast b and a soft gluon and vice versa. Figure 6.8 shows the correlation ρ_b obtained with this procedure in data and simulation. Also shown is the correlation obtained from an unbiased sample of $b\bar{b}$ events without events that have both b quarks in one hemisphere. Good agreement is observed for the three samples, inside the rather large statistical errors. This plot was obtained with a slightly different hadronic selection and b enrichment that the one used in the multiple tag analysis. For this reason the value of the correlation is not exactly the same for both analyses. It should be stressed that the soft tag on the one-jet hemisphere to remove from p_{jet} the contribution due to the two b quarks in the same hemisphere changes slightly the correlation component, but it was observed to be basically insignificant on the quoted systematic error error.

The angular and QCD correlation uncertainties quoted for the 1994 single tag analysis are summarized at the bottom of table 6.12.

6.3 Final results and consistency checks

In summary, the final results are

$$R_b = 0.21617 \pm 0.00100(stat.) \pm 0.00091(syst.) - 0.024 \times (R_c - 0.172) \quad (6.23)$$

for 1994 and

$$R_b = 0.21688 \pm 0.00144(stat.) \pm 0.00121(syst.) - 0.024 \times (R_c - 0.172) \quad (6.24)$$

for 1995, where the first errors are statistical and the second ones systematic. The explicit dependence of this measurement with the assumed R_c value is also given.

The 1994 result must be compared to the one obtained from the single tag scheme:

$$R_b = 0.21685 \pm 0.00119(stat.) \pm 0.00096(syst.) - 0.033 \times (R_c - 0.172). \quad (6.25)$$

The multiple tag scheme improves the statistical error as well as the systematic uncertainties from light and charm quark backgrounds and hemisphere correlations. The explicit dependence on R_c is also smaller.

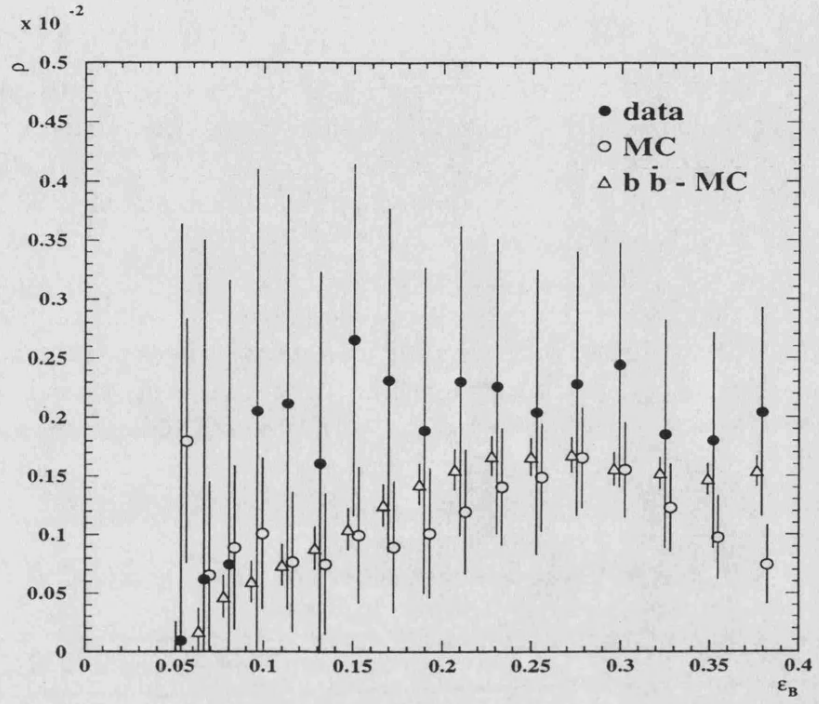

Figure 6.8: Single hemisphere correlation ρ_b due to gluon radiation as a function of the b tagging efficiency. The closed and open circles show data and simulation respectively, selected as described in the text. The open triangles show an unbiased sample of simulated $b\bar{b}$ events which do not contain two b quarks in one hemisphere.

The 1994 and 1995 multiple tag results are compatible and can be combined, with the following assumptions:

- all statistical errors are assumed to be independent;
- the errors in the hemisphere correlations due to gluon radiation are assumed to be fully correlated, but those from angular effects are taken uncorrelated, since dead VD modules are repaired year by year and the polar and azimuthal tracking tuning dependence is performed independently for each year. In addition, the VD alignment [82] was done separately for both years;
- the errors due to *uds*, *c* and *b* physics simulation inputs are assumed to be fully correlated, as well as the errors on the estimate of light and charm quark efficiencies due to detector effects.

With these assumptions, using a combining method similar to the one described in [130, 131], the result for the combined 1994-1995 data is:

$$R_b = 0.21639 \pm 0.00082(stat.) \pm 0.00085(syst.) - 0.024 \times (R_c - 0.172). \quad (6.26)$$

As said previously, the b hemisphere tagging efficiency $\epsilon^b_{b-tight}$ was found to be 0.2950 ± 0.0012 (0.2962 ± 0.0017) for 1994 (1995) data, compared to the simulation estimate of 0.284 (0.275). The real data are about 4% (7%) more efficient than simulation. The purity at the working point for this measurement is 98.5%.

Figure 6.9 shows the stability of the combined 1994-1995 R_b result as a function of the cut on $-\log_{10} y$ defining the b-tight tag, together with the change of the contributions to the total error. It can be observed that at small values of the cut the measurement is dominated by systematic uncertainties in the charm background, whilst at large values of the cut it suffers from rather large statistical errors. The smallest error is obtained at cut $-\log_{10} y \geq 1.2$. As an indication, a cut at 0.0 corresponds to an efficiency/purity working point of 44.0%/91.6%, and the value 2.0 to 21.0%/99.4%. The measured value of R_b is therefore stable over a wide range of the b efficiencies, purities and correlations.

The final result for the 1992-1993 data is

$$R_b = 0.21631 \pm 0.00150(stat.) \pm 0.00174(syst.) - 0.042 \times (R_c - 0.172). \quad (6.27)$$

The b hemisphere tagging efficiency was found to be 0.1869 ± 0.0012, compared to the simulation estimate of 0.192. The real data are in this case about 3% less efficient than simulation. The purity at the working point for this measurement is 97.3%.

Figure 6.10 shows the stability of the 1992-1993 R_b result as a function of the cut on the multivariate discriminator Δ_b defining the b-tight tag, together with the change of the contributions to the total error. The best error is obtained here for $\Delta_b \geq 5.0$. The cut at 3.0 corresponds to an efficiency/purity of 33.4%/91.2%, compared to 11.2%/98.6% at cut 6.5.

The 1994-1995 and 1992-1993 results are also compatible and can be combined with the same assumptions as previously, with the only difference that the errors due to detector effects on the estimate of light and charm quark efficiencies (tracking) can now be assumed uncorrelated because of the completely different vertex detector setup. The 1992-1995 combined result is therefore

$$R_b = 0.21638 \pm 0.00076(stat.) \pm 0.00087(syst.) - 0.025 \times (R_c - 0.172). \quad (6.28)$$

Applying the small (+0.0002) correction for photon exchange yields for the ratio of partial widths:

$$R^0_b = 0.21658 \pm 0.00076(stat.) \pm 0.00087(syst.) - 0.025 \times (R_c - 0.172). \quad (6.29)$$

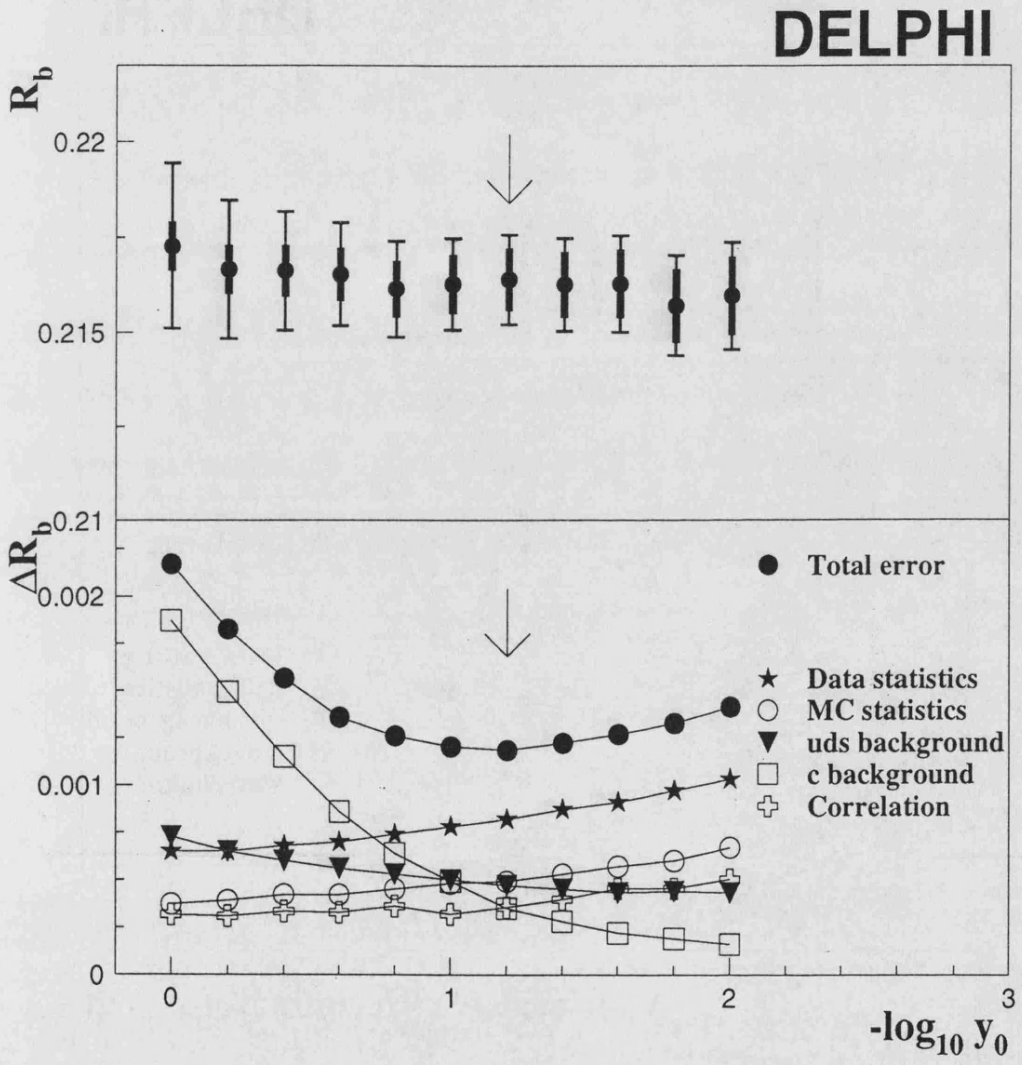

Figure 6.9: Multiple tag scheme: stability of the R_b result as a function of the cut $\log_{10} y_0$ defining the b-tight tag, together with the change of the contributions to the total error for the 1994-1995 analysis. The best error is obtained at cut 1.2. In the upper plot the thick error bar represents the statistical uncertainty and the narrow one is the total error.

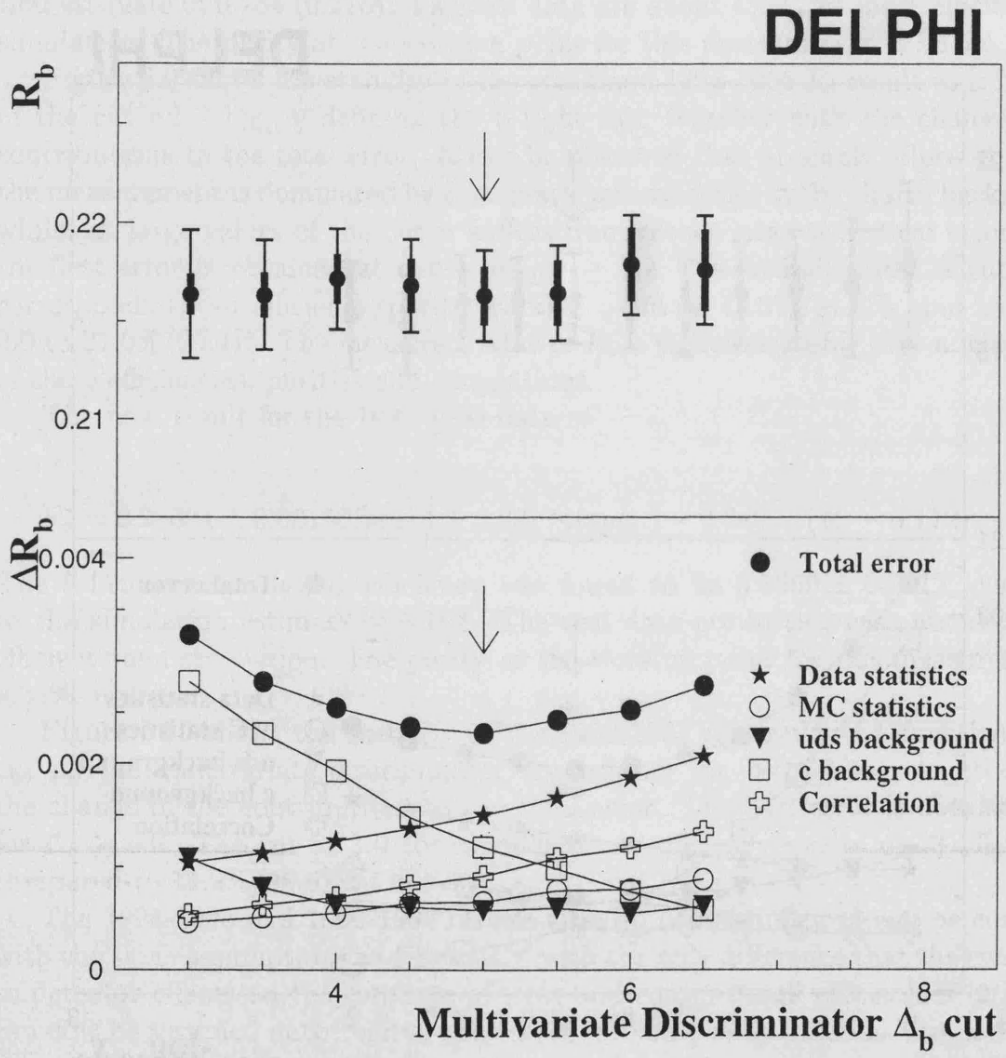

Figure 6.10: Multiple tag scheme: stability of the R_b result as a function of the multivariate discriminator cut defining the b-tight tag for 1992-1993 data, together with the change of the contributions to the total error. The best error is obtained at cut 5.0. In the upper plot the thick error bar represents the statistical uncertainty and the narrow one is the total error.

For this number, all center-of-mass energies at which LEP has run have been combined. Figure 6.11 shows the stability of R_b as a function of all other cuts $\Delta_{b,0}^{up}$, $\Delta_{b,0}^{low}$, $\Delta_{c,0}$ and $\Delta_{uds,0}$ defining the hemisphere tags. Table 6.14 reports the full breakdown of the error on this measurement, for the partial 1994-1995 combination, the 1992-1993 analysis and finally the full combination over the full LEP 1 statistics. Table 6.15 details the breakdown of the charm physics uncertainties.

Table 6.14: Breakdown of the error on R_b at the nominal cuts for the multiple tag analysis.

Source	ΔR_b		
	1994-1995	1992-1993	1992-1995
Data statistics	± 0.00082	± 0.00150	± 0.00076
MC statistics	± 0.00048	± 0.00066	± 0.00043
Event selection	± 0.00012	± 0.00012	± 0.00011
Tracking	± 0.00015	± 0.00052	± 0.00015
K^0, Λ^0, photons, etc.	∓ 0.00003	∓ 0.00018	∓ 0.00005
$g \to c\bar{c}$: $(2.38 \pm 0.48)\%$ per event	∓ 0.00035	∓ 0.00013	∓ 0.00032
$g \to b\bar{b}/g \to c\bar{c}$: 0.13 ± 0.04	∓ 0.00032	∓ 0.00056	∓ 0.00036
Charm physics	± 0.00030	± 0.00105	± 0.00042
Two b quarks in same hemisphere: $\pm 30\%$	∓ 0.00008	∓ 0.00027	∓ 0.00011
b fragmentation $\langle x_E(b) \rangle$: 0.702 ± 0.008	∓ 0.00006	∓ 0.00015	∓ 0.00007
B decay multiplicity: 5.25 ± 0.35	∓ 0.00020	∓ 0.00045	∓ 0.00024
B_s fraction: 0.112 ± 0.019	∓ 0.00006	∓ 0.00004	∓ 0.00006
Λ_b fraction: 0.132 ± 0.041	∓ 0.00006	∓ 0.00032	∓ 0.00010
Average B lifetime: 1.55 ± 0.04 ps	∓ 0.00000	∓ 0.00001	∓ 0.00000
Angular effects	± 0.00014	± 0.00061	± 0.00015
Gluon radiation	± 0.00023	± 0.00018	± 0.00022
Total systematic error	± 0.00085	± 0.00174	± 0.00087
Total error	± 0.00118	± 0.00230	± 0.00114

The breakdown of the error for the chosen cut on $-\log_{10} y$ for the single tag analysis for the 1994 data is given in table 6.16. If one compares the multiple and single tag results for 1994 from tables 6.14 and 6.16, it is clear that the multiple tag scheme improves the statistical accuracy and reduces the systematic errors due to hemisphere correlations and *uds* and charm contamination.

Clearly the multiple tag measurement is highly correlated with the one obtained with the single tag measurement, and both are consistent. In order to quantify the compatibility, the measurement of R_b was performed at cut $-\log_{10} y \geq 1.0$ using the multiple and single tag methods for the 1994 and 1995 samples. The multiple tag approach provided the results $R_b = 0.21615 \pm 0.00095(stat.)$ and $R_b = 0.21653 \pm 0.00136(stat.)$ for the 1994 and 1995 data respectively. With the single tag scheme

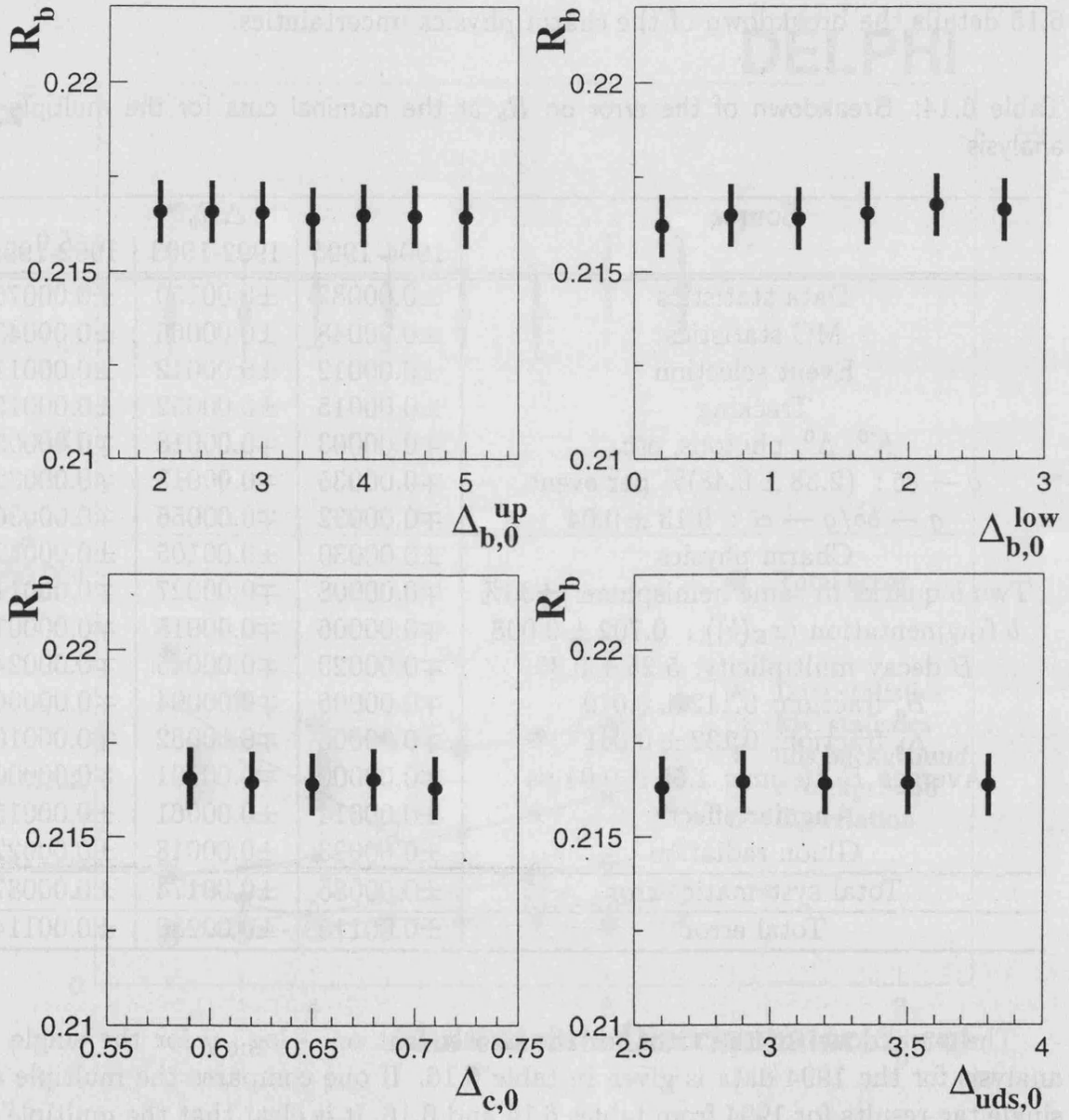

Figure 6.11: Stability of the R_b result as a function of the cuts $\Delta_{b,0}^{up}$, $\Delta_{b,0}^{low}$, $\Delta_{c,0}$ and $\Delta_{uds,0}$ defining the b-standard, b-loose, charm and uds hemisphere tags. Only the statistical errors are shown.

Table 6.15: Detailed breakdown of charm physics systematic error on R_b at the nominal cuts for the multiple tag analysis.

Source	ΔR_b		
	1994-1995	1992-1993	1992-1995
D^+ fraction in $c\bar{c}$ events: 0.233 ± 0.028	∓ 0.00014	∓ 0.00034	∓ 0.00017
D_s fraction in $c\bar{c}$ events: 0.102 ± 0.037	∓ 0.00004	∓ 0.00003	∓ 0.00004
$c-baryon$ fraction in $c\bar{c}$ events: 0.065 ± 0.029	± 0.00010	± 0.00022	± 0.00012
D decay multiplicity: 2.39 ± 0.14	∓ 0.00010	∓ 0.00076	∓ 0.00020
$Br(D \to K^0 X)$: 0.46 ± 0.06	± 0.00022	± 0.00024	± 0.00022
D^0 lifetime: 0.415 ± 0.004 ps	∓ 0.00002	∓ 0.00002	∓ 0.00002
D^+ lifetime: 1.057 ± 0.015 ps	∓ 0.00003	∓ 0.00003	∓ 0.00003
D_s lifetime: 0.447 ± 0.017 ps	∓ 0.00001	∓ 0.00004	∓ 0.00001
Λ_c lifetime: 0.206 ± 0.012 ps	∓ 0.00000	∓ 0.00001	∓ 0.00000
$\langle x_E(c) \rangle$: 0.484 ± 0.008	∓ 0.00004	∓ 0.00055	∓ 0.00011

Table 6.16: Sources of errors for the measurement of R_b using the single tag scheme for 1994 data.

Source	ΔR_b
Data statistics	± 0.00119
Light quark efficiency	± 0.00050
Charm efficiency	± 0.00050
Hemisphere correlation	± 0.00041
MC statistics	± 0.00051
Event selection	± 0.00014
Total	± 0.00154

the results were $R_b = 0.21685 \pm 0.00119(stat.)$ and $R_b = 0.21620 \pm 0.00163(stat.)$, well in agreement (within statistical differences) with the former results.

However, the difference between these R_b results is not only due to their statistical differences. The sensitivity of both approaches to light and charm quark efficiency uncertainties is the same, and therefore the systematic errors due to *uds* and *c* backgrounds are fully correlated. However, the sensitivities to correlations are different. In fact, the sensitivity of the multiple tag measurement to $\rho^b_{b-tight,b-tight}$ at cut $-\log_{10} y \geq 1.0$ is 0.838, compared to the sensitivity of unity of the single tag analysis. In this way, the correlation error as obtained in the single tag analysis, $\Delta\rho^b_{b-tight,b-tight} = \pm 0.0030$ (± 0.0043) in 1994 (1995) induces an error on R_b of 0.00065 (0.00092) and 0.00055 (0.00078) for the single tag and multiple tag methods respectively. Therefore, the part of the error due to correlations which is uncorrelated between the multiple and the single tag analyses is 0.00036 (0.00049). Combining this error with the statistical difference, we obtain a difference between the multiple and single tag measurements of -0.00070 ± 0.00080 ($+0.00033 \pm 0.00102$). Therefore they are well compatible.

Furthermore, it was checked that the error on $\rho^b_{b-tight,b-tight}$ found with the procedure followed in the single tag analysis agreed well with that obtained in the multiple tag analysis. Flavour isolation, p_{jet} definition and error assignment were done in slightly different ways.

Finally, the comparison of the high purity multiple tag with the asymptotic approach results of table 6.5 must be also seen as a cross-check of the measurement.

6.4 Energy dependence

In 1995, data were taken at three different center-of-mass energies, $\sqrt{s} = 89.44$, 91.28 and 92.97 GeV, and in 1993 at $\sqrt{s} = 89.49$, 91.25 and 93.08 GeV. As photon exchange and $\gamma - Z$ interference are strongly suppressed at energies close to the Z resonance, $R_b(\sqrt{s})$ is predicted to be almost constant in the Standard Model. However, if R_b is affected by the interference of the Z with a Z' almost degenerate in mass, as suggested by Caravaglios and Ross [132], some energy dependence can be expected if the mass and width of the Z' are not exactly equal to those of the Z. Since the *b* tagging efficiency varies only very little within the energy range considered here, no complicated single to double tag comparison is needed to measure $\frac{R_b(\sqrt{s})}{R_b(M_Z)}$. Instead, simply the ratio of the fraction of tagged events can be used, with very small corrections due to changes in the *b* tagging efficiency and almost negligible corrections due to background. These corrections were calculated using the Monte Carlo simulation.

The measurement was performed using event tagging instead of hemisphere tagging. For 1995 the combined impact parameter tag $-\log_{10} y$ was used, and for 1993 the probability of primary vertex decay products $-\log_{10} P_E$ as defined in chapter 4 was taken instead. Several different values of the event variable cut were used, and

a minimum statistical error was found at a b purity of 79% (70%) for 1995 (1993).

In 1995, at the value of the cut, the b tagging efficiency varied by a relative amount of $\pm 0.1\%$ with respect to that at the Z peak and was about 81%, while the efficiency to tag c (uds) events was about 21% (2%). The following ratios were found [115]:

$$\begin{aligned} R_- &= \frac{R_b(89.44\,\mathrm{GeV})}{R_b(91.28\,\mathrm{GeV})} = 0.9870 \pm 0.0114 \\ R_+ &= \frac{R_b(92.97\,\mathrm{GeV})}{R_b(91.28\,\mathrm{GeV})} = 1.0056 \pm 0.0096. \end{aligned} \tag{6.30}$$

In 1993, the b tagging efficiency varied by a relative amount of $\pm 0.5\%$ with respect to that at the Z peak and was about 70%, while the efficiency to tag c (uds) events was about 20% (4%). To avoid any systematic uncertainties due to time dependence of the b tagging efficiency, the data taken in the first part of the year, where LEP ran only at $\sqrt{s} = 91.25$ GeV, on the Z peak, were neglected. With these requirements the following ratios were found [112]:

$$\begin{aligned} R_- &= \frac{R_b(89.49\,\mathrm{GeV})}{R_b(91.25\,\mathrm{GeV})} = 0.982 \pm 0.015 \\ R_+ &= \frac{R_b(93.08\,\mathrm{GeV})}{R_b(91.25\,\mathrm{GeV})} = 0.997 \pm 0.016. \end{aligned} \tag{6.31}$$

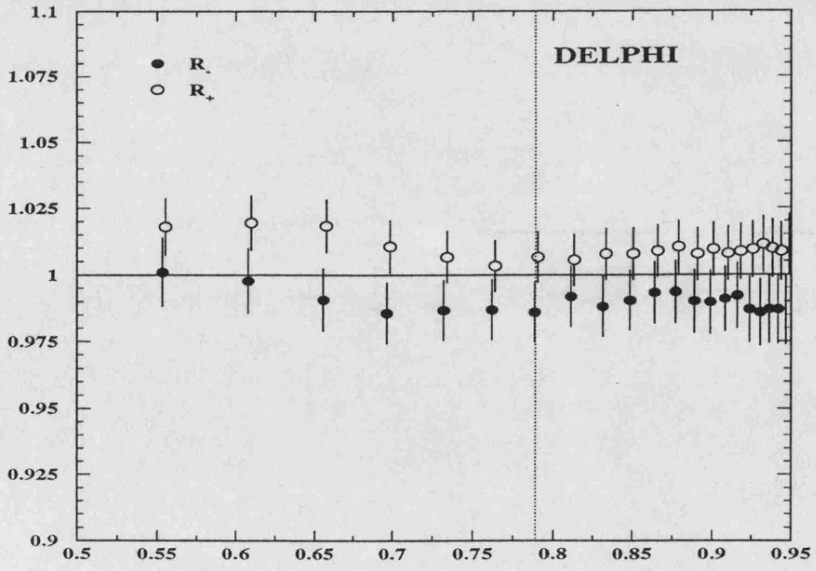

Figure 6.12: Ratio of the off-peak and on-peak R_b values as a function of the b purity for the 1995 data. The vertical dotted line marks the cut used for the central values.

In (6.30) and (6.31) the errors are statistical only, including the limited Monte Carlo statistics at the off-peak points. All systematic uncertainties were found

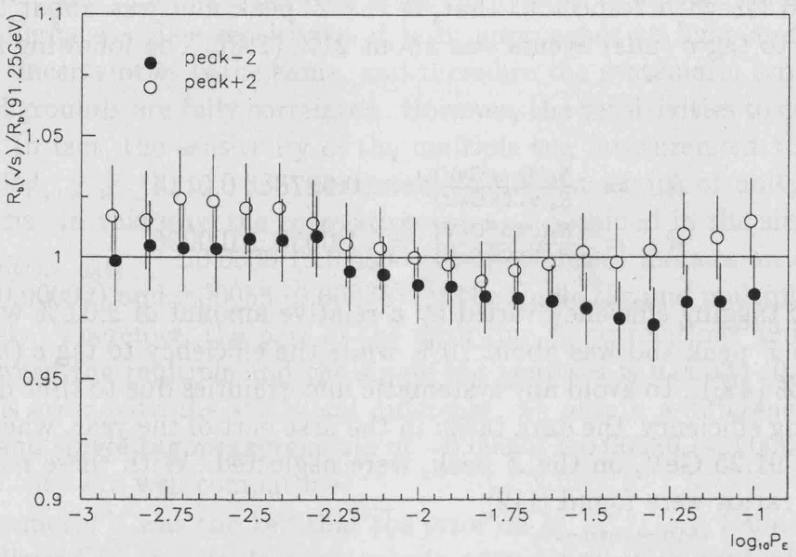

Figure 6.13: Ratio of the off-peak and on-peak R_b values as a function of the cut value for the 1993 data. The vertical dotted line marks the cut used for the central values.

to be negligible. Figures 6.12 and 6.13 show the stability of these measurements as a function of the b purity and the probability cut for the 1995 and 1993 runs respectively.

Combining both values yields:

$$\begin{aligned} R_- &= \frac{R_b(89.46\,\text{GeV})}{R_b(91.27\,\text{GeV})} = 0.9852 \pm 0.0091 \\ R_+ &= \frac{R_b(93.00\,\text{GeV})}{R_b(91.27\,\text{GeV})} = 1.0033 \pm 0.0082. \end{aligned} \tag{6.32}$$

The Standard Model predicts a ratio of 0.997 (0.998) for R_- (R_+). Figure 6.14 compares the result with the Standard Model prediction. The values at higher energies are taken from [133]. Results are therefore compatible with the Standard Model prediction.

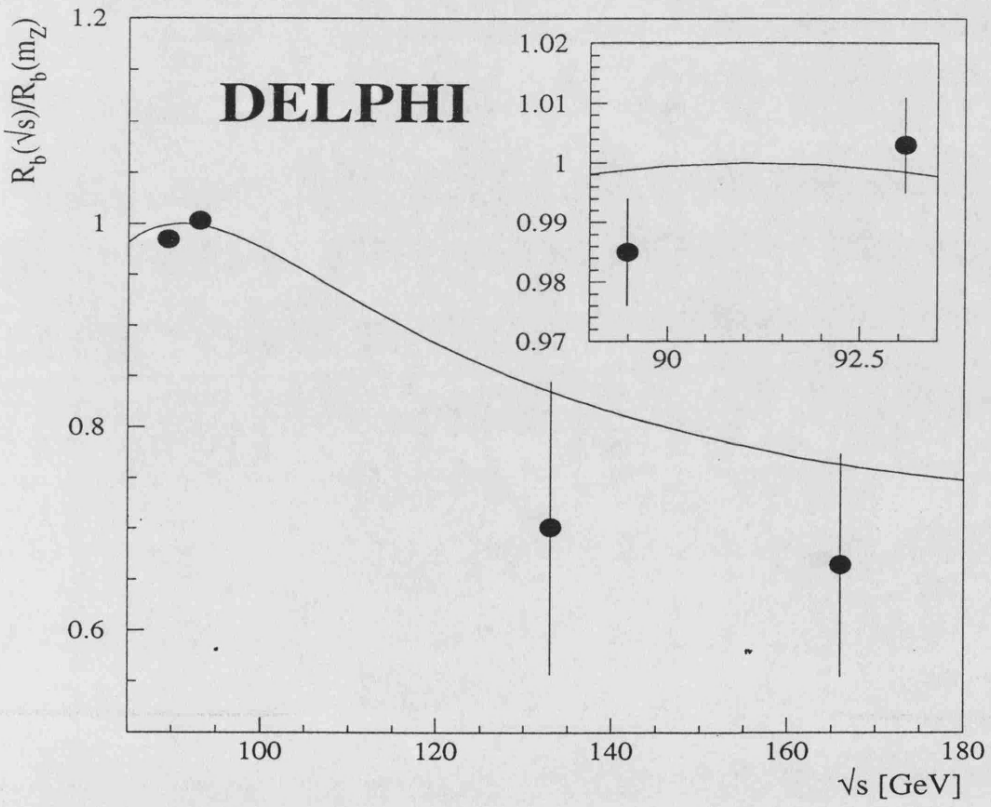

Figure 6.14: Ratio of the off-peak and on-peak R_b values as a function of $\sqrt{s}$. The solid line shows the Standard Model prediction.

Chapter 7

Conclusions

This thesis has reported the high precision measurement of $R_b^0 = \Gamma(Z \to b\bar{b})/\Gamma(Z \to hadrons)$ performed with the DELPHI detector at CERN's LEP collider using the full LEP 1 statistics, taken between the 1991 and 1995 years. A total of about 4.2M hadronic Z decays were recorded and analyzed. About 60% of these data were taken with a high precision double sided silicon microvertex detector, and all the rest with a single sided silicon detector providing high resolution only in the plane transverse to the colliding beams. Experimentally, R_b^0 can be obtained with only very small corrections from the ratio of cross-sections $R_b = \sigma(e^+e^- \to b\bar{b})/\sigma(e^+e^- \to hadrons)$. These small corrections are due to the photon propagation contribution.

R_b^0 is currently the object of a particular interest. Most electroweak and QCD radiative corrections cancel in the ratio, leaving R_b^0 sensitive essentially to corrections to the $Z \to b\bar{b}$ vertex, like the large CKM coupling to the top quark. Due to the high quality of the agreement between the Standard Model and most of precise observations, together with the recent top quark discovery and its direct mass measurement, the parameters of the Standard Model become better constrained. A precise measurement of R_b^0 at 0.5% level tests thus not only the Minimal Standard Model but also the presence of novel radiative vertex corrections. In this way, R_b^0 is currently one of the most interesting windows in the search for new physics.

Two different analyses based on double hemisphere tag methods have been performed. All of them relies on high purity/efficiency hemisphere b tagging techniques. The features included in the tagging algorithms are the long lifetime and the mass of B hadrons. The lifetime information was extracted from tracks having large impact parameters and reconstructed secondary vertices. The mass behavior was exploited using the effective invariant mass of reconstructed secondary vertices and event shape properties. In the different tagging techniques, the input quantities were combined using multivariate methods.

In the hemisphere single tag scheme with combined impact parameter tag, hemispheres (defined by the plane perpendicular to the event thrust axis) are tagged as b or non-b. In the combined tag, hemispheres were selected using tracks having large impact parameters in jets with reconstructed secondary vertices. The pure lifetime

information can then be combined with additional information like the effective mass, the rapidity and the charged energy of particles included in the secondary vertex. The comparison of the single and double tag rates allows the determination of R_b together with the b tagging efficiency, assuming R_c from electroweak theory and taking the uds and c efficiencies of the b tag and the hemisphere-hemisphere tagging efficiency correlation from Monte Carlo simulation. Correcting by photon exchange, the analysis of the 1994 data provided the result

$$R_b^0 = 0.21717 \pm 0.00119(stat.) \pm 0.00096(syst.) - 0.033 \times (R_c - 0.172)$$

where the first error is statistical and the second one systematic. The explicit dependence on R_c is also given.

In the hemisphere multiple tag scheme, also called multivariate analysis, the combined impact parameter tag is combined with two multivariate flavour tagging algorithms including impact parameter, secondary vertex and event shape information. Here hemispheres are classified between six mutually exclusive tagging categories or tags ordered by decreasing b purity: b-tight, b-standard, b-loose, charm, uds and no-tag. There are 20 different observables (combinations of two hemisphere tags) and 17 unknowns: R_b, R_c and 15 uds, c and b tagging efficiencies. As before, R_c is assumed from electroweak theory and the uds and c efficiencies of the b-tight tag and the hemisphere correlations are estimated using the Monte Carlo simulation of the experiment. The 1994 result is now

$$R_b^0 = 0.21637 \pm 0.00100(stat.) \pm 0.00091(syst.) - 0.024 \times (R_c - 0.172).$$

Compared with the combined impact parameter analysis in which only b-tight tagged hemispheres are used (single tag scheme), all hadronic hemispheres are tagged in the multivariate analysis (multiple tag scheme), allowing the statistical accuracy to be increased. The systematic uncertainty on R_b due to light and charm quark backgrounds is also improved because of the harder cut on the b-tight tagged hemispheres, which reduces in a factor 1.2 and 1.5 respectively the uds and c backgrounds, with the subsequent reduction in systematics uncertainties. The systematic errors due to hemisphere correlations are also smaller because now there are 45 independent correlation coefficients (of which only 14 are relevant to the analysis) instead of one as in the single tag scheme, some of them with opposite sign effects (sensitivities) on R_b, with a reduction in the systematic error. In addition, due to the smaller charm background, the explicit dependence on R_c is also smaller. This global reduction of the error at this level of precision becomes crucial.

An independent single tag analysis was also carried out by DELPHI on data collected in 1994, using purely vertex information for the tagging of b quarks [115]. For the tagging, a search for secondary vertices was made independently inside event hemispheres. In order to tag $Z \to b\bar{b}$ events, the output of a neural network [134] was used, with five input variables based only on the properties of the secondary vertices found. They were 1) decay length significance L/σ_L; 2) the number of unique tracks

in the secondary vertex; 3) the number of tracks in the primary vertex that were not also associated to a secondary; 4) the number of tracks in common to both the secondary and primary vertices and 5) the vertex rapidity. The variables were carefully chosen for both their flavour discriminating power and their low cross-correlation. Both the light and charm quark efficiencies were extracted from the simulation and their systematic errors as for the previous analyses. The hemisphere correlation in b events for this analysis was estimated also from the simulation. Contributions to the systematic error from both geometrical effects and physics modeling are estimated similarly to the single and multiple tag schemes and are detailed in [115]. The b purity at the best cut was 95.1% and the b tagging efficiency was 26.3%. Finally R_b is calculated to be:

$$R_b^0 = 0.2156 \pm 0.0014(stat.) \pm 0.0015(syst.) - 0.087 \times (R_c - 0.172).$$

The multivariate analysis was also used to analyze the 1995 and 1992-1993 data, giving respectively the following results:

$$R_b^0 = 0.21708 \pm 0.00144(stat.) \pm 0.00121(syst.) - 0.024 \times (R_c - 0.172)$$

and

$$R_b^0 = 0.21651 \pm 0.00150(stat.) \pm 0.00174(syst.) - 0.042 \times (R_c - 0.172).$$

All previous results are compatible inside statistical differences. Since the multivariate analysis has the smallest total error, it is taken as the DELPHI result. The 1992-1995 combined preliminary result yields for the ratio of partial widths:

$$\boxed{R_b^0 = 0.21658 \pm 0.00076(stat.) \pm 0.00087(syst.) - 0.025 \times (R_c - 0.172)}$$

For this number, all center-of-mass energies at which LEP has run have been combined.

The multivariate analysis relies heavily on the single tag analysis with combined impact parameter tag, which acts as the b-tight tag. The results are therefore highly correlated between each other, and cannot be used independently. However, the secondary vertex tag is not included in the multiple tag analysis, and therefore its result can be combined with the previous one taking into account correlated errors. Before this, the statistical correlation between both analyses needs to be estimated. This remains to be done. So at the moment the secondary vertex result must be seen as an independent cross-check of the multivariate result.

The result is in agreement with those of other precise measurements performed at LEP/SLC colliders, which are briefly described below. The precision on R_b depends fundamentally on the vertex detector characteristics, which are compared for the different experiments in table 7.1. In that table, the following characteristics

are given: the coordinates $R\phi$ and Rz used for track, impact parameter and vertex reconstruction, the number of silicon layers, the radius of the most internal and external layers, the $R\phi$ and Rz (if available) impact parameter resolution and the primary vertex reconstruction resolution. Meanwhile ALEPH and DELPHI reconstruct the primary vertex independently for each hemisphere using tracks from that hemisphere (reducing largely hemisphere tagging correlations), L3 and OPAL have a common event primary vertex. Due to the small stable SLC beams, in SLD the x and y coordinates of the primary vertex are measured from the average of impact parameters. The average is obtained from tracks in approximately 30 sequential hadronic events. The z coordinate of the primary vertex is determined as at LEP from each event separately.

Table 7.1: Vertex detector characteristics for all the LEP/SLC experiments. The following data are provided: the coordinates used ($R\phi$,Rz), the number of silicon layers, the radius of the most internal and external layers, the $R\phi$ and Rz (if available) impact parameter resolution and the primary vertex (PV) reconstruction resolution.

	Experiment				
	ALEPH	DELPHI	L3	OPAL	SLD
Coordinates used	$R\phi$,Rz	$R\phi$,Rz	$R\phi$,Rz	$R\phi$	$R\phi$,Rz
Number of layers	2	3	2	2	3
Radius of layers (cm)	6.5/11.3	6.3/11	6.4/7.3	6.1/7.5	2.9/4.1
$R\phi$ IP resolution (μm)	25	20	30	18	13
Rz IP resolution (μm)	25	30	30		24
PV resolution x (μm)	58	22	42	40	6.4
PV resolution y (μm)	10	10	10	10	6.4
PV resolution z (μm)	60	22	42		15

The ALEPH Collaboration has recently presented two precise measurements of R_b which are similar to the ones presented here, both using the full LEP 1 statistics recorded by the experiment between 1992 and 1995. The first analysis uses a double tag method with single tag scheme and a tag based on lifetime and mass [100]. The lifetime-mass tagging algorithm computes jet lifetime probabilities $\mathcal{P}_j^+$ from the three-dimensional impact parameter significance of charged tracks. To improve the rejection of c hemispheres in this pure lifetime technique, it is combined with other tag exploiting the B/D hadron mass difference, as in the DELPHI tags. However, here no secondary vertex is reconstructed and the mass tag is constructed as follows. The tracks in each jet are ordered by decreasing inconsistency with the primary vertex, until their invariant mass exceeds 1.8 GeV/c^2. For each jet, the mass tag variable is defined to be the track probability μ_J of the last track added. For a hemisphere, the mass tag variable μ_H is defined to be the value of μ_J for the jet with smallest value of μ_J (the most b like jet in that hemisphere). The two tags are

then combined using the linear combination $\mathcal{B}_{tag} = -(0.7 \log_{10} \mathcal{P}_H^+ + 0.3 \log_{10} \mu_H)$. The distribution of this variable for the different flavours is shown in figure 7.1. The primary vertex is reconstructed separately for each hemisphere, so reducing hemisphere correlations.

The second analysis uses a multiple tag scheme[1] [135]. In this analysis, the lifetime-mass tag is complemented by four other mutually exclusive tags. Two of the tags are designed to tag b events, one is designed to select c events and one designed to select uds events. These tags are constructed using two neural networks, identified high total and transverse momentum leptons and finally impact parameter probabilities for tracks with rapidity cuts to enrich in c events. One neural net is designed to select b quark hemispheres [139], with 25 event shape quantities as inputs. The second neural net is trained to select c quark hemispheres, with one lifetime and 19 event shape quantities. As in the case of DELPHI, this measurement improves largely the precision of the single tag scheme and it is highly correlated with it, and therefore it is taken as the ALEPH number. The efficiency and purity of the lifetime-mass tag at the nominal cut used in this analysis is given in table 7.2, where it is compared with those of the other experiments. The final result together with a breakdown of the error is given in table 7.3.

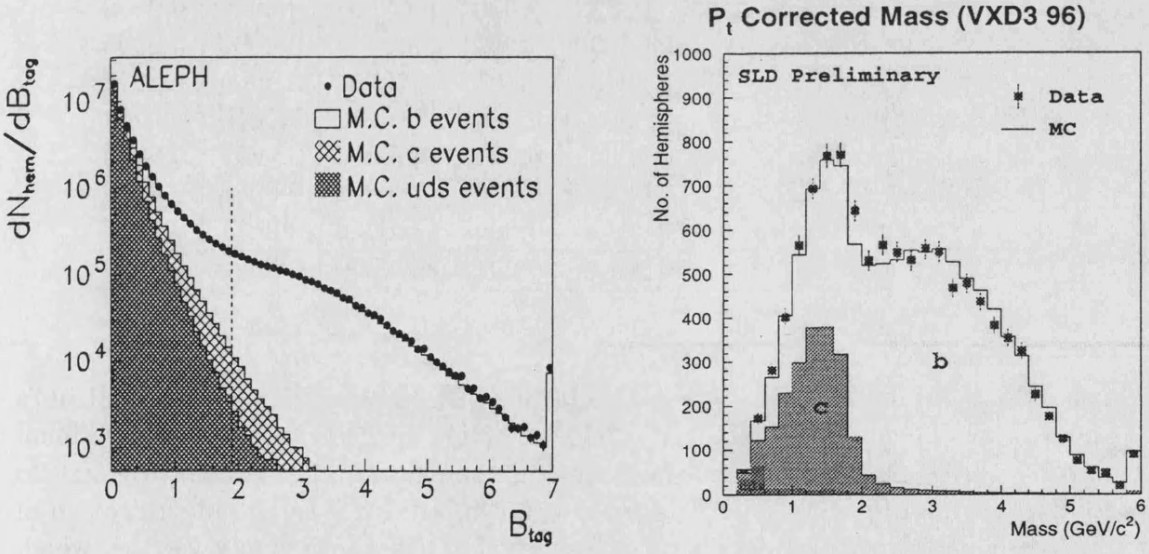

Figure 7.1: Distribution of the b tagging variables $\mathcal{B}_{tag}$ (left) and the corrected mass $\mathcal{M}$ (right) for data (points) and Monte Carlo breakdown of the b, c and uds contributions (histograms) used by the ALEPH and SLD experiments.

The SLD Collaboration has a measurement of R_b using a double tag method with single tag scheme and a vertex mass tag [138]. The measurement is performed using

[1] In fact, they use the multiple tag scheme equivalent formalism described in chapter 5.

Table 7.2: b tagging performances for all the LEP/SLC experiments. The efficiencies and purities are given at the nominal cuts defining the b tags for which the backgrounds are estimated from the simulation of the experiments. As it can be seen, DELPHI is the experiment with the best working purity, having simultaneously the best efficiency of all LEP experiments.

	Experiment				
	ALEPH	DELPHI	L3	OPAL	SLD
b purity (%)	98.1	98.5	86.4	90.5	97.6
b efficiency (%)	19.2	29.6	23.7	23.1	47.9

Table 7.3: R_b^0 results for the five LEP/SLC experiments together with an error breakdown.

	Experiment				
	ALEPH	DELPHI	L3	OPAL	SLD
R_b^0	0.2159	0.2166	0.2179	0.2178	0.2124
Data Statistics	0.0009	0.0008	0.0015	0.0014	0.0024
Monte Carlo statistics	0.0005	0.0004	0.0008	0.0003	0.0009
Event selection	0.0002	0.0001		0.0003	0.0003
Detector resolution	0.0005	0.0002	0.0004	0.0004	0.0011
Hemisphere correlations	0.0003	0.0003	0.0011	0.0010	0.0004
udsc physics	0.0005	0.0005	0.0022	0.0009	0.0005
Gluon splitting	0.0007	0.0005	0.0002	0.0006	0.0006
Total systematics	0.0011	0.0009	0.0026	0.0017	0.0017
Total error	0.0014	0.0011	0.0030	0.0022	0.0029

a sample of 200K hadronic Z decays collected with the experiment at the SLAC's SLD collider during the years 1993-1996. The tag utilizes the three-dimensional abilities of the SLD CCD pixel detector and the small and stable SLC beams to obtain a high b tagging efficiency/purity, a shown in table 7.2. The identification of vertices is performed using a topological vertexing procedure. Only vertices which are significantly displaced from the primary vertex are considered to be possible B hadron decay vertices. From all charged tracks included in the secondary vertex, the effective invariant vertex mass M is then calculated. The b tagging performance of this vertex mass tag can still be improved by applying a kinematic correction to the calculated invariant mass. Due to the loss of neutral particles in the decay, the secondary vertex flight path and the secondary vertex momentum vector are typically acollinear. In order to compensate for the acollinearity they correct the invariant mass using the minimum missing momentum $P_\perp$ transverse to the secondary vertex

flight path. The vertex mass tag is finally defined as $\mathcal{M} = \sqrt{P_\perp^2 + M^2} + \mid P_\perp \mid$. The ability to make this correction is specific to SLD due to the small and stable beam spot of the SLC collider and the high resolution vertexing. The distribution of $\mathcal{M}$ is shown in figure 7.1. By requiring $\mathcal{M} > 2$ GeV/c^2, the obtained b performances are the ones given in table 7.2. The quoted result together with a breakdown of the error is given in table 7.3.

The analyses performed by the L3 and OPAL Collaborations are also based on a double tag method with single tag scheme. In the case of L3, b hemispheres are selected using tracks having large impact parameters, computing lifetime probabilities $\mathcal{P}_H^+$ which are called here discriminant D, as shown in figure 7.2 [136]. In OPAL, hemispheres are selected only if they have reconstructed secondary vertices considerably displaced with respect to the primary vertex. The tagging variable is defined to be the decay length significance, which is shown in figure 7.2 [137]. The selection performances at the nominal cuts used to measure R_b are given in table 7.2. To help in precision, lifetime tags are here combined with lepton tags but always using double tagging techniques. After combination of results for the different double tag possibilities (lifetime-lifetime, lifetime-lepton and lepton-lepton), the quoted results with errors for both experiments are given in table 7.3.

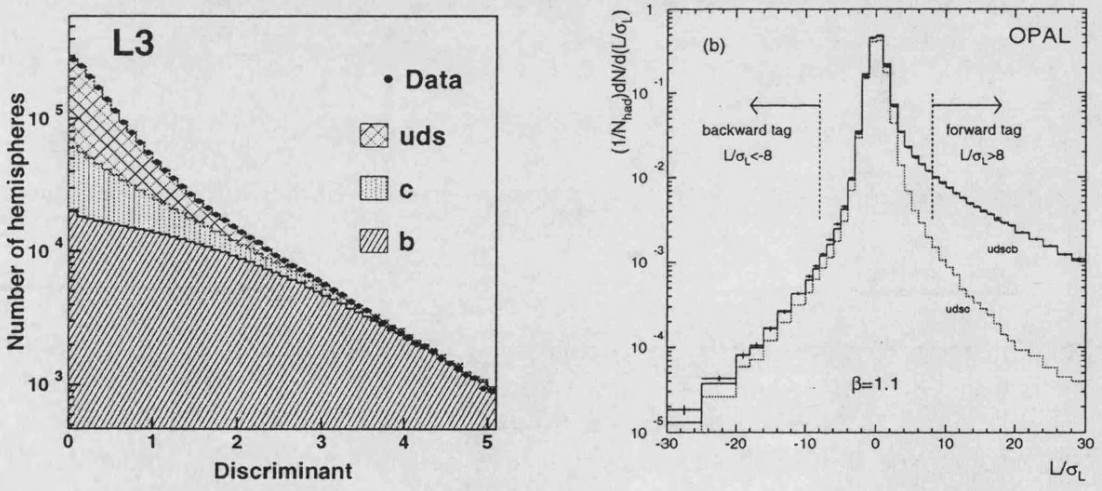

Figure 7.2: Distribution of the b tagging variables D (left) and L/σ_L (right) for data (points) and Monte Carlo breakdown of the b, c and uds contributions (histograms) used by the L3 and OPAL experiments.

The results obtained by the ALEPH, L3, OPAL and SLD experiments with the techniques previously outlined are compared with the DELPHI result in figure 7.3. It can be seen that the DELPHI result is currently the most precise single measurement.

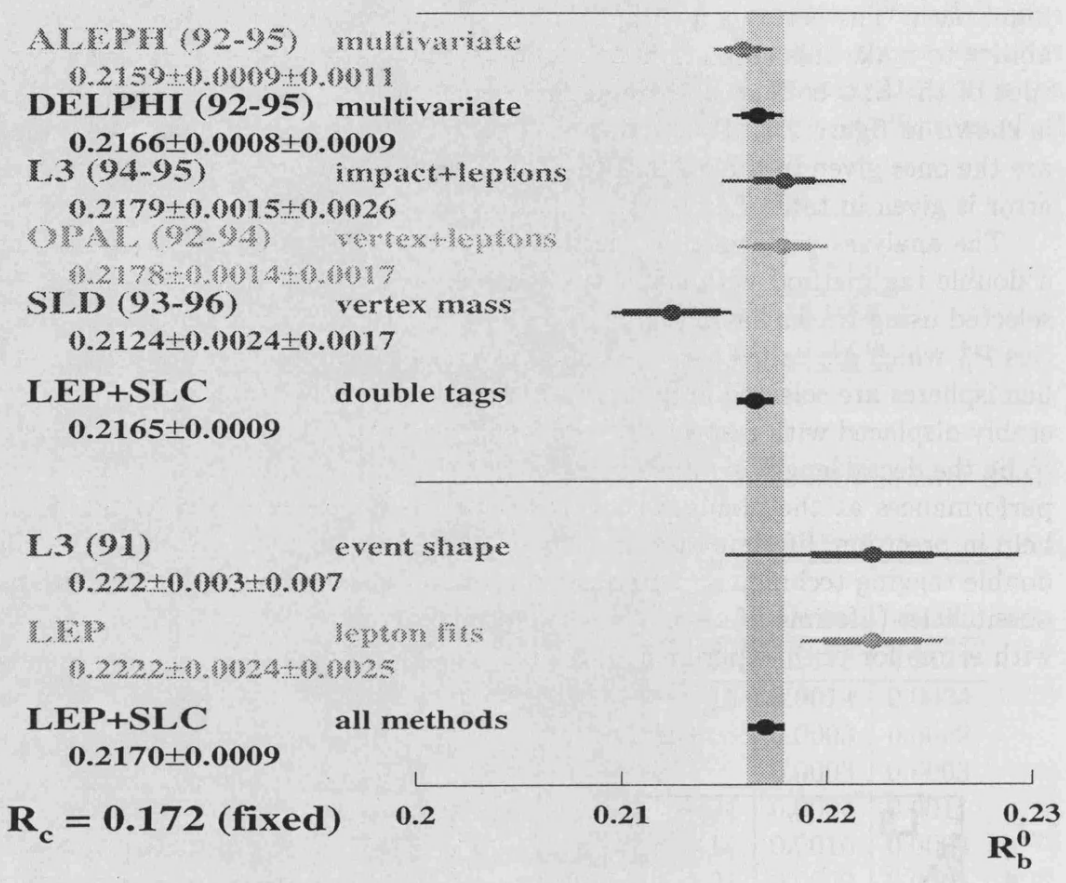

Figure 7.3: Summary of all LEP/SLC R_b^0 measurements together with the world average.

In this figure, two other measurements are shown, which are included in the global combination to quote the world average [6]. The first measurement is from L3 and it is based on a neural network with a total of 11 event shape variables [140]. With this tagging, R_b is measured from a fit to the data distribution of the neural net by varying the b and non-b contribution from simulation, using for that purpose an event single tag scheme (see chapter 5). The large error is dominated by systematic uncertainties in the fragmentation, which reflect uncertainties in tagging efficiencies for the event single tag method. The second measurement is from global lepton fits at LEP [39]. As said in chapter 1, lepton tagging relies on heavy quark semileptonic decays. The lepton momentum distributions for b and c quarks are rather similar, but the transverse momentum distribution from c decays is softer than that from b quark decays, allowing a separation between $b\bar{b}$ and $c\bar{c}$ events. Within leptonic channels, the upper limit of b tagging efficiency is low. It is twice the b semileptonic decay ratio (about 10% for e and μ separately). Momentum cuts and identification

efficiencies for inclusive leptons and muons lowers the limit to below 10% for about 90% purity. The number of prompt leptons in a sample of hadronic events is determined by the products $R_b BR(b \to l)$, $R_b BR(b \to c \to l)$ and $R_c BR(c \to l)$. The individual factors in the products can be isolated by a simultaneous consideration of the $(p, p_\perp)$ spectrum of single and dilepton events. By extending the maximum likehood fit to include the $cos\theta$ variation of the number of single and dilepton events, $A_{FB}^{0,b}$, $A_{FB}^{0,c}$ can in principle also be measured. As the momentum spectrum of the leptons is strongly affected by the heavy quark fragmentation, the parameters $\langle x_E(c) \rangle$ and $\langle x_E(b) \rangle$ can be extracted from these fits within the framework of a particular fragmentation model. Finally, the average b mixing parameter $\bar{\chi}$ can also be obtained. The choice of exactly which of these nine heavy flavour parameters have to be measured and which need to be taken from external sources comes from a balance between statistics and systematics. Only ALEPH performs a global fit with all nine quantities. DELPHI fixes $\langle x_E(c) \rangle$, $A_{FB}^{0,b}$ and $A_{FB}^{0,c}$ from external measurements and OPAL fixes additionally R_c. From the $(p, p_\perp)$ spectrum, L3 measures R_b and $BR(b \to l)$. The results obtained by the four LEP collaborations are published in reference [39], and their average is the one given in figure 7.3.

The global precision of each experiment (given in table 7.3 and figure 7.3) is a consequence of several factors. Between them, the method used to determine R_b (hemisphere multiple/single tag schemes), the b tagging performances and the good Monte Carlo simulation description of the data (which requires very fine understanding and tuning of physics and detector resolution) are the most critical. Thus tables 7.1 and 7.2 can be seen as fundamental parameters on R_b, which determine the results of table 7.3.

The good agreement of the DELPHI result with the Standard Model expectation $R_b^0 = 0.2158 \pm 0.0003$ [43], assuming a mass of the top quark of $m_t = 175.6 \pm 5.5\ GeV/c^2$ as measured directly at FNAL [9], is shown in figure 7.4. For R_c the combined world average $R_c^0 = 0.1734 \pm 0.0048$ [6] is taken, well compatible with the Standard Model prediction of 0.172. Figure 7.4 shows that if the Minimal Standard Model radiative corrections (dominated by top quark effects) were left out of the electroweak calculation, the expected result would be $R_b^0 = 0.2183 \pm 0.0001$, which corresponds to R_d^0 (down quark rate) for the top mass given before. Therefore, this measurement shows evidences at 0.53% precision level of the top quark dominated radiative vertex correction in the $Z \to b\bar{b}$ vertex.

The world average including all measurements shown in figure 7.3 is

$$R_b^0 = 0.2170 \pm 0.0009.$$

This number is about one standard deviation above the Minimal Standard Model prediction. The correlation of this result with R_c is measured to be 20%. The contours in the R_b^0-R_c^0 plane corresponding to 68%, 95% and 99% confidence levels assuming Gaussian systematic errors is shown in figure 7.5, together with the Minimal Standard Model prediction.

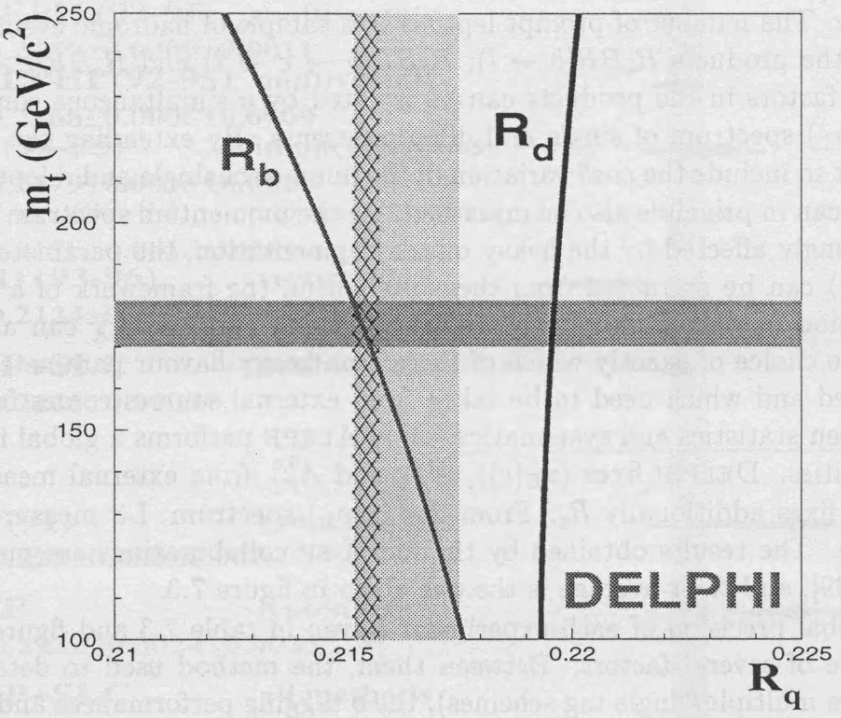

Figure 7.4: Comparison of the DELPHI R_b measurement (vertical band) with the Standard Model predictions of R_b and R_d as a function of the top quark mass. The top quark mass direct measurement from FNAL, $m_t = 175.6 \pm 5.5$ GeV/c^2 [9], is indicated by the horizontal band. The hatched vertical band corresponds to the Standard Model prediction of 0.2158 ± 0.0003. In this plot the combined world average $R_c^0 = 0.1734 \pm 0.0048$ [6] is assumed for R_c. A good agreement with the Standard Model prediction is observed.

Excluding of the world electroweak combination the L3 event shape analysis and the combined LEP result from global leptons fits[2], the result is

$$R_b^0 = 0.2165 \pm 0.0009.$$

This number agrees inside one standard deviation with the Minimal Standard Model prediction of $R_b^0 = 0.2158 \pm 0.0003$. Therefore, this measurement shows again evi-

[2]There are some reasons to do this. The event shape analysis from L3 is an old measurement using event single tag with very large systematic errors. The R_b value from the global lepton fits is potentially dangerous because in these fits there is a large correlation between R_b and $BR(b \to l)$ and the result is largely dependent on semileptonic decay models. In addition, the current measurements of $BR(b \to l)$ show some deviations from the expected results as well as some inconsistencies with the CLEO results [141], and it is therefore a potential source of additional systematics not yet under control.

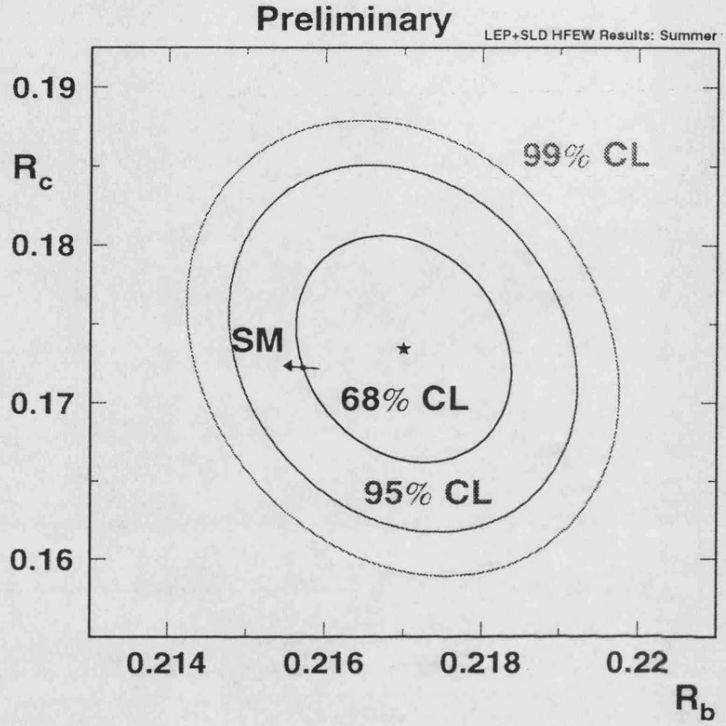

Figure 7.5: Contours in the R_b^0-R_c^0 plane derived from LEP and SLD data, corresponding to 68%, 95% and 99% confidence levels assuming Gaussian systematic errors. The Minimal Standard Model prediction for $m_t = 175.6 \pm 5.5$ GeV/c^2 is also shown. The arrow points in the direction of increasing values of m_t.

dences at 0.42% precision level of the top quark dominated radiative vertex correction in the $Z \to b\bar{b}$ vertex.

The evolution with time of the world average for R_b is shown in figure 7.6. The change in central value and its error is not only the consequence of the analysis of more data. The 1991 world result was based only on global lepton fits with rather limited amount of data. In 1992, lepton analyses with more data were presented, together with other event single tag analyses using event shape properties. It was in 1993 that for the first time precise measurements of R_b using double tagging techniques with lifetime tags were presented. The situation up to 1995 was improved only with the inclusion of more data. At that moment the discrepancy with the Standard Model prediction was serious, more than three standard deviations. In particular, the DELPHI result based on 1991-1993 data only was 2.2 standard deviations above the Standard Model prediction [112]. That was suggesting the need of new vertex corrections in the $Z \to b\bar{b}$ vertex, i.e. the presence of novel physics in the vertex. However, these measurements were systematically limited and the

charm background as well as hemisphere correlation systematics were a worry. Pure lifetime tag, with common event primary vertex, was not powerful enough to reject c events in the b tag and to have small hemisphere correlation efficiencies, in order to reduce systematic uncertainties. It was in Warsaw 1996 and Jerusalem 1997 that new data were analyzed with new techniques. The multiple tag measurements from ALEPH and DELPHI based on more powerful tags with better background rejection and smaller hemisphere correlations (thanks mainly to the independent reconstruction of the primary vertex for each hemisphere), allowed to increase the accuracy and to resolve successfully the question of the discrepancy of R_b with the Standard Model.

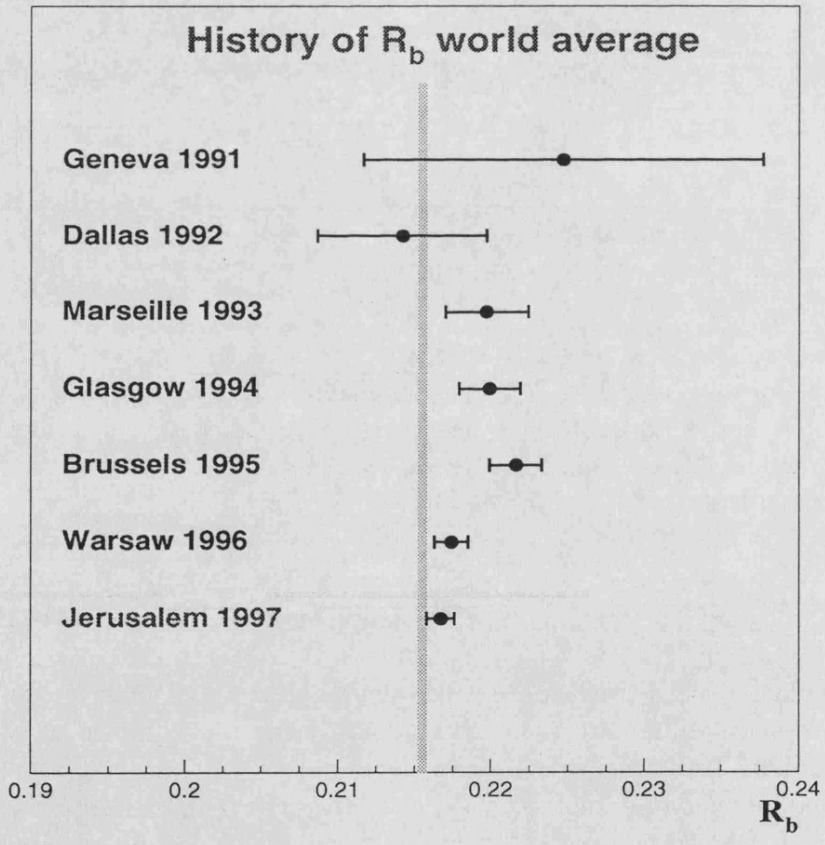

Figure 7.6: Variation of the R_b world average with time. Each value is obtained as the average using the values provided by the experiments at the Summer Conference (ICHEP) time of each year.

In figure 7.7 the global fitted result for R_b (including the L3 event shape and lepton fit results) (with R_c fixed to its Standard Model value) is plotted versus

$\sin^2\theta_W^{l,eff}$. The measurement of the leptonic ratio R_l provides a constraint (see section 2.8) that is shown also on the figure. If one assumes the Standard Model dependence of the partial widths on $\sin^2\theta_W^{l,eff}$ for light and charm quarks, and taking $\alpha_s(M_Z^2) = 0.118 \pm 0.003$ from the world average [7], R_l imposes a constraint on the two variables. A good agreement is seen for these three experimentally independent measurements, showing the consistency of the LEP/SLD data [6]. Excluding for R_b the L3 event shape and the LEP lepton fit results, the agreement is even better.

The DELPHI result presented here is still preliminary. The analysis is close to be finished, but still some work remains:

- In order to reduce the Monte Carlo statistical error on the measurement, the 1995 analysis will be repeated using a higher sample of simulated events, $Z \to q\bar{q}$ as well as $Z \to b\bar{b}$, which are now under processing.

- The 1992 and 1993 data used here do not use the last and more powerful DELANA processing which allows to increase the track reconstruction efficiency and resolution. This will allow to improve tagging performances in a large amount of the analyzed data, with the subsequent improvement on R_b. This will be accompanied by the generation of new Monte Carlo simulation samples with better tuning of physics and detector resolution parameters, given the better current understanding of the physics processes and the tracking system response during last years.

- The implementation and processing of the 1992-1993 data with the combined impact parameter tag defining the b-tight tag. This will allow also to improve precision for the 1992-1993 analysis.

- The statistical correlation between the multivariate and the secondary vertex analyses needs to be computed using Monte Carlo simulation. Due to the fact that a very large amount of Z decays ($\sim 100M$) is needed to determine the correlation with small uncertainty, the standard simulation of the experiment cannot be used. The strategy has been already designed and it is based on toy simulations on the tagging techniques rather than on a full simulation of DELPHI, which is not possible by technical reasons (CPU limitations).

In despite of that, the DELPHI result can also be improved using new inputs taken from very recent measurements for some fundamental parameters. If we take for the gluon splitting ratio into $b\bar{b}$ quark pairs, $f(g \to b\bar{b})$, the recent measurement $f(g \to b\bar{b}) = 0.246 \pm 0.092$ as given in chapter 6, instead of the input from theoretical calculation, $f(g \to b\bar{b}) = 0.31 \pm 0.11$, the central value of R_b increases only $+0.00019$, and the total systematic error changes from ± 0.00087 to ± 0.00083. If in addition the new DELPHI measurement of the B decay multiplicity, 4.96 ± 0.06, is used instead of the older one from DELPHI and OPAL, 5.25 ± 0.35, the corresponding systematic error changes from ± 0.00024 to ± 0.00004 without change in central value, and the

total systematic error is further reduced to ± 0.00080. The total precision of R_b would be now 0.00110, 0.51% relative. For the final DELPHI number these new inputs will be used.

With all of that, a precision better than 0.5% is feasible to be reached for the final DELPHI result.

LEP finished its data taking on the Z pole center-of-mass energy in November 1995, and no more runs are scheduled (except for calibration and alignment of the LEP detectors) in future. However, the experiments have not yet finished the analyses and their completions with the improved techniques will increase still the combined precision. On the contrary, more Z data is schedule at SLC collider. Therefore, a precision close to 0.3% for the world average could be reached in a rather close future.

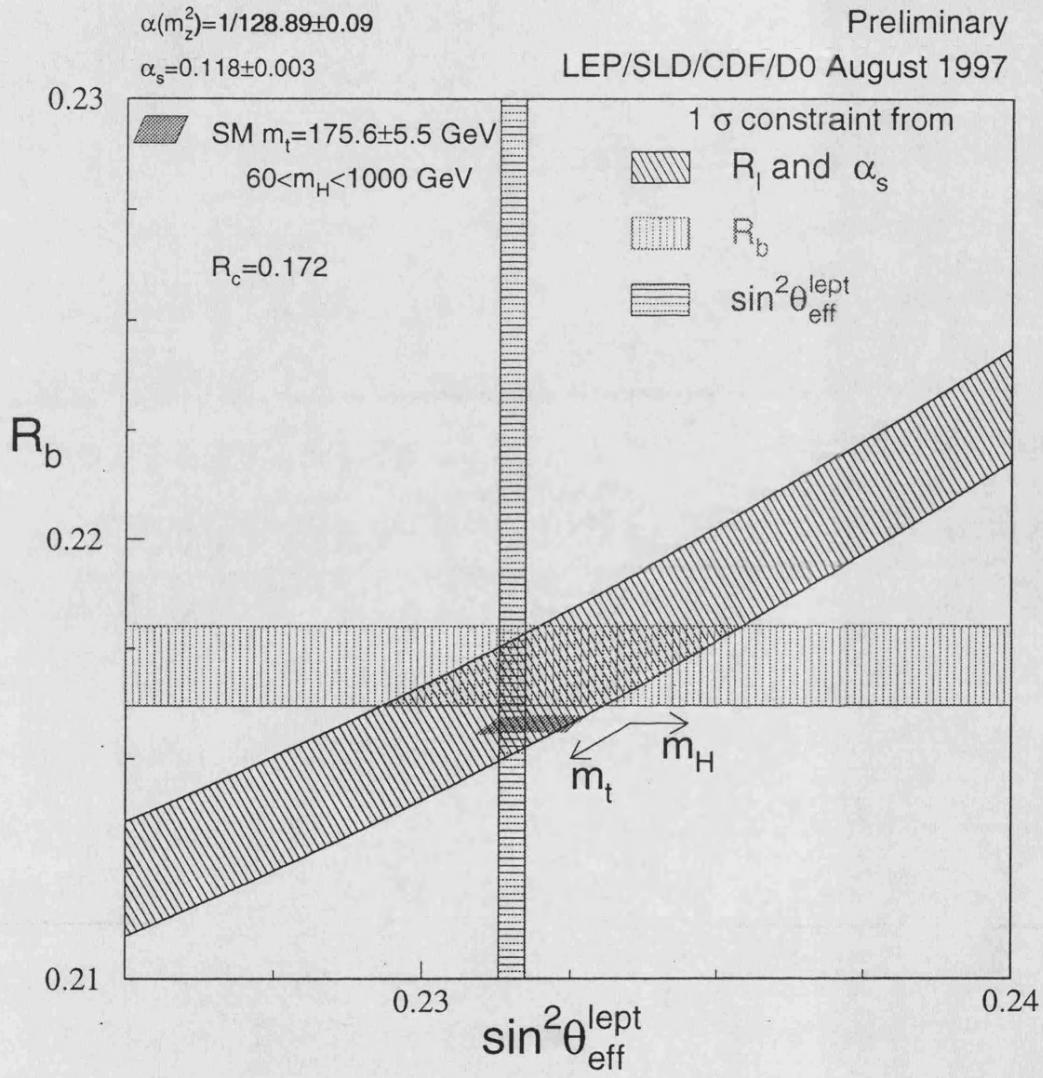

Figure 7.7: The LEP/SLD measurements of $\sin^2\theta_W^{l,eff}$ and R_b (assuming $R_c = 0.172$) and the Standard Model prediction. Also shown is the constraint resulting from measurement of R_l on these variables, assuming $\alpha_s(M_Z^2) = 0.118 \pm 0.003$, as well as the Standard Model dependence of light-quark partial width on $\sin^2\theta_W^{l,eff}$.

Bibliography

[1] See for example: V. Barger and R.J.N. Phillips, *Collider Physics*, Addison Wesley Publishers (1987).

[2] S.L Glashow, Nucl. Phys. **B22** (1961) 579.
S. Weinberg, Phys. Rev. Lett. **19** (1967) 1264.
A. Salam, Proc. of the 8th Nobel Symp., p.367, ed. N. Svartholm, Almqvist and Wiksell, Stockholm (1968).

[3] S.L Glashow, I. Iliopoulos, L. Maiani, Phys. Rev. **D2** (1970) 1285.

[4] N. Cabbibo, Phys. Rev. Lett. **10** (1963) 531.
M. Kobayashi, K. Maskawa, Prog. Theor. Phys. **49** (1973) 652.

[5] H.Y. Han, Y. Nambu, Phys. Rev. **139** (1965) 1006.
C. Bouchiat, I. Iliopoulos, Ph. Meyer, Phys. Lett. **B138** (1972) 652.

[6] The LEP Electroweak Working Group and the SLD Heavy Flavour Group, *A combination of preliminary LEP and SLD electroweak measurements and Constraints on the Standard Model*, Internal note LEPEWWG/97-02 and DELPHI 97-41 PHYS 726, Geneva (1997). References therein.

[7] M. Barnet et al. (Particle Data Group), Phys. Rev. **D54** (1996) 1.

[8] F. Abe et al. (CDF Collaboration), Phys. Rev. Lett. **74** (1995) 2626.
S. Abachi et al. (D0 Collaboration), Phys. Rev. Lett. **74** (1995) 2632.

[9] J. Abe et al. (CDF Collaboration), *Measurement of the top quark mass at CDF*, contributed paper to ICHEP'96, Warsaw (1996).
S. Abachi et al. (D0 Collaboration), *Measurement of the top mass from events with two isolated leptons produced in $p\bar{p}$ collisions at D0*, contributed paper to ICHEP'96, Warsaw (1996).
S. Abachi et al. (D0 Collaboration), *Measurement of the top mass from events with single isolated leptons produced in $p\bar{p}$ collisions at D0*, contributed paper to ICHEP'96, Warsaw (1996).
L. Lys, (CDF Collaboration), Proceedings ICHEP'96, Warsaw (1996), and FERMILAB-CONF-96/409-E.
E.W. Warnes, (D0 Collaboration), Proceedings ICHEP'96, Warsaw (1996), and FERMILAB-CONF-96/243-E.

[10] J. Yang et al., Astrophys. Jour. **281** (1984) 493.
J. Ellis and K.A. Olive, Phys. Lett. **B193** (1987) 525.

[11] Pauli rejected to print his lecture at a meeting of the American Physical Society where was firstly presented in public the idea of the neutrino. A posterior reference can be: W. Pauli, *Noyaux atomique*, VII Conseil de Physique Solvay 1933, Paris (1934), p. 324.

[12] F. Reines and C. Cowan, Phys. Rev. **92** (1953) 830.
C. Cowan, F. Reines, F. Harrison, H. Kruse and A. McGuire, Science **124** (1956) 103.

[13] J.I. Friedman and H.W. Kendall, Ann. Rev. Nucl. Science **22** (1972) 203.

[14] C.D. Anderson and S.H. Neddermeyer, Phys. Rev. **51** (1937) 894.

[15] G. Danby, J.M. Gaillard, K. Goulianos, L. Lederman, N. Mistry, M. Schwartz and J. Steinberger,Phys. Rev. Lett. **9** (1962) 36.

[16] J.D. Rochester, C.C. Butler, Nature **160** (1947) 855.

[17] J.J. Aubert et al., Phys. Rev. Lett. **33** (1974) 1404.
J.E. Augustin et al., Phys. Rev. Lett. **33** (1974) 1406.
B. Richter and S. Ting, Nobel Lectures, Stockholm (1977).

[18] M. Perl et al., Phys. Rev. Lett. **35** (1975) 1489.
M. Perl et al., Phys. Lett. **B63** (1976) 466.

[19] G. Goldhaber et al., Phys. Rev. Lett. **37** (1976) 255.

[20] S.W. Herb et al., Phys. Rev. Lett. **39** (1977) 252.

[21] D. Andrews et al., Phys. Rev. Lett. **45** (1980) 219.
S. Finicchiaro et al., Phys. Rev. Lett. **45** (1980) 222.

[22] F. Abe et al. (CDF Collaboration), Phys. Rev. Lett. **73** (1994) 225.

[23] For a review of gauge theories, see for example: I.J. Aitchison and A.J. Hey, *Gauge theories in particle physics*, Adam Hilger Ltd., Bristol (1981).

[24] P.W. Anderson, Phys. Rev. **110** (1958) 827; ibid., **130** (1963) 439.
Y. Nambu, Phys. Rev. **117** (1959) 648.
J. Schwinger, Phys. Rev. **125** (1962) 397.
P. Higgs, Phys. Rev. Lett. **12** (1964) 132.
F. Englert and R. Brout, Phys. Rev. Lett. **13** (1964) 321.
G.S. Guralnik, C.R. Hagen and T.W.B. Kibble, Phys. Rev. Lett. **13** (1964) 585.

[25] M. Kobayashi and M. Maskawa, Prog. Theor. Phys. **49** (1973) 652.

[26] F. J. Hasert et al., Phys. Lett. **B46** (1973) 121.

[27] R.E. Behrends, R.J. Finkelstein, A. Sirlin, Phys. Rev. **101** (1956) 866.

[28] G. Arnison et al. (UA1 Collaboration), Phys. Lett. **B122** (1983) 103.
M. Banner et al. (UA2 Collaboration), Phys. Lett. **B122** (1983) 473.
C. Rubbia, Nobel Lecture, Rev. Mod. Phys. **57** (1985) 699.

[29] Ed. G. Altarelli, R. Kleiss and C. Verzegnassi, *Z physics at LEP*, Vol.1, CERN 89-08, Geneva (1989). References therein.

[30] F. Abe et al. (CDF Collaboration), *Measurement of the W boson mass*, FERMILAB-PUB-95/033-E and FERMILAB-PUB-95/035-1995.
M. Demarteau et al., *Combining W mass measurements*, D0 NOTE 2115 and CDF/PHYS/CDF/PUBLIC/2552.
The LEP Electroweak W mass Working Group, *LEP WW cross-section and W mass for ICHEP'96*, Private comunication.

[31] M. Neubert, $\alpha_s(Q^2)$ *in* τ *decays*, Proceedings of the DPF'96 Meeting of the American Physical Society, Minneapolis (USA), World Scientific, Singapore (1996).
J. Casaus, *LEP results on* $\alpha_s(M_Z)$ *from* R_{had} *and event shape variables*, Proceedings of the XXX Rencontres de Moriond, QCD and High Energy Hadronic Interactions, Les Les Arcs (France), Ed. Frontieres, Gif-sur-Yvette (1995).
S. Bethke, Proceedings of the QCD '94 Conference, Montpellier, France, Nucl. Phys. **B** (Proc. Suppl.) **39B,C** (1995) 198.
J. Fuster, Proceedings of the XXII International Meeting on Fundamental Physics, Jaca (Spain, 1994).

[32] T. Sjöstrand, Comp. Phys. Comm. **82** (1994) 74.

[33] G. Marchesini et al., Comp. Phys. Comm. **67** (1992) 465.

[34] L. Lonnblad, Comp. Phys. Comm. **71** (1992) 15.

[35] B. Anderson, G. Gustafson and B. Söderberg, Zeit. Phys. **C20** (1983) 317.

[36] C. Peterson, D. Schlatter, I. Schmitt and P. Zerwas, Phys. Rev. **D27** (1983) 105.

[37] R.D. Field and R.P. Feynman, Nucl. Phys. **B136** (1978) 1.

[38] D. Amati and G. Veneziano, Phys. Lett. **B83** (1979) 87.
Ya.I. Azimov et al., Phys. Lett. **B165** (1985) 147.
Ya.I. Azimov et al., Zeit. Phys. **C27** (1985) 65.

[39] D. Buskulic et al. (ALEPH Collaboration), Zeit. Phys. **C62** (1994) 179.
D. Buskulic et al. (ALEPH Collaboration), Phys. Lett. **B384** (1996) 414.
P. Abreu et al. (DELPHI Collaboration), Zeit. Phys. **C66** (1995) 323.
O. Adriani et al. (L3 Collaboration), *L3 results on* R_b *and* $BR(b \to l)$ *for the Glasgow Conference*, L3 note 1625.
G. Alexander et al. (OPAL Collaboration), Zeit. Phys. **C70** (1996) 357.

[40] D. Buskulic et al. (ALEPH Collaboration), *Measurement of the partial decay width of the Z into* $c\bar{c}$ *quarks*, contributed paper to ICHEP'96, Warsaw (1996).
P. Abreu et al. (DELPHI Collaboration), *Summary of* R_c *measurements in DELPHI*, DELPHI 96-110 CONF 37, contributed paper to ICHEP'96, Warsaw (1996).

K. Ackerstaff et al. (OPAL Collaboration), CERN-PPE/97-093, submitted to Zeit. Phys. C.
K. Abe et al. (SLD Collaboration), *A preliminary measurement of R_c using the SLD detector*, SLAC-PUB-7594, contributed paper to ICHEP'97, Jerusalem (1997).

[41] D. Bardin, W. Hollik, G. Passarino, *Reports of the Working Group on Precision Calculations for the Z Resonance*, CERN 95-03, Geneva (1995). References therein.

[42] S. Cabrera, J. Fuster, S. Marti, *m_b at M_Z*, DELPHI 97-74 CONF 60, contributed paper to ICHEP'97, Jerusalem (1997).

[43] D. Bardin et al., Zeit. Phys. **C44** (1989) 493.
D. Bardin et al., Comp. Phys. Comm. **59** (1990) 303.
D. Bardin et al., Nucl. Phys. **B351** (1991) 1.
D. Bardin et al., Phys. Lett. **B255** (1991) 290.

[44] R. Barbieri et al., Phys. Lett. **B288** (1992) 95.
R. Barbieri et al., Nucl. Phys. **B409** (1993) 105.

[45] J. Fleischer, O.V. Tarasov and F. Jegerlehner, Phys. Lett. **B319** (1993) 249.

[46] A. Djouadi and C. Verzegnassi, Phys. Lett. **B195** (1987) 265.
K.G. Chetyrkin, J.H. Köhn and M. Steinhauser, *Reports of the Working Group on Precision Calculations for the Z Resonance*, CERN 95-03, Geneva (1995).

[47] F. Halzen, B. A. Kniehl, Nucl. Phys. **B353** (1991) 567.
A. Djouadi, P. Gambino, Phys. Rev. **D49** (1994) 3499.

[48] J. Bernabéu, A. Pich and A. Santamaria, Phys. Lett. **B200** (1988) 569.
J. Bernabéu, A. Pich and A. Santamaria, Nucl. Phys. **B363** (1991) 326.

[49] A. Akhundov, D. Bardin, T. Riemann, Nucl. Phys. **B276** (1986) 1.
W. Beenakker and W. Hollik, Zeit. Phys. **C40** (1988) 141.

[50] J. Fleischer et al., Phys. Lett. **B293** (1992) 437.
G. Buchalla and A. Buras, Nucl. Phys. **B398** (1990) 285.
G. Degrassi, Nucl. Phys. **B407** (1993) 271.
K.G. Chetyrkin, A. Kwiatkowski, M. Steinhauser, Mod. Phys. Lett. **A8** (1993) 2785.

[51] A. Denner, W. Hollik, B. Lampe, Zeit. Phys. **C60** (1993) 193.

[52] A. Kwiatkowski and M. Steinhauser, *Reports of the Working Group on Precision Calculations for the Z Resonance*, CERN 95-03, Geneva (1995).

[53] T. Appelquist and J. Carazzone, Phys. Rev. **D11** (1975) 2856.

[54] E. Blucher et al., *Report of the Working Group on High Luminosities at LEP*, CERN 91-02, Geneva (1991). References therein.

[55] Many good reviews on the effects of models beyond the Standard Theory on R_b are avalaible in the literature. See for example:
P. Bamert et al., *R_b and New Physics: A Comprehensive Analysis*, McGill University preprint McGill-96/04 hep-ph/9602438 (1996).
R.S. Chivukula, *Physics Beyond the Standard Model: Prospects and Perspectives*, Boston University preprint BUHEP-94-22 hep-ph/9409233 (1994).
F. Cornet, W. Hollik, W. Mösle, *The $Zb\bar{b}$ vertex: Implications for the Standard Model and beyond*, Karlsruhe preprint MPI-PhT/94-13 hep-ph/9408005 (1994).
X. Zhang and B.L. Young, *Non-Universal Correction to $Z \to b\bar{b}$ and flavour changing neutral current couplings*, Iowa State Univ. preprint AMES-HET-95-14 hep-hp/9501212 (1995).

[56] S. Weinberg, Phys. Rev. **D19** (1979) 1277.
L. Susskind, Phys. Rev. **D20** (1979) 2619.

[57] E. Eichten and K. Lane, Phys. Lett. **B90** (1980) 125.
S. Dimopoulos and L. Susskind, Nucl. Phys. **B155** (1979) 237.

[58] R.S. Chivukula, S.B. Selipsky, E.H. Simmons, Phys. Rev. Lett. **69** (1992) 575.
N. Kitazawa, Phys. Lett. **B313** (1993) 395.

[59] R.S. Chivukula, E. Gates, E.H. Simmons and J. Terning, Phys. Lett. **B311** (1993) 157.

[60] R.S. Chivukula, E.H. Simmons and J. Terning, Phys. Lett. **B331** (1994) 383.

[61] B. Holdom, Phys. Lett. **B259** (1991) 329.

[62] B. Holdom, Univ. of Toronto preprint UTPT-94-18 (1994).

[63] A. Blondel et al., *R_b and R_c?*, Proceedings of the XXXI Rencontres de Moriond, QCD and High Energy Hadronic Interactions, Les Arcs (France), Ed. Frontieres, Gif-sur-Yvette (1996); and CERN-PPE/96-91, Geneva (1996).

[64] R. Bamert, *R_b and heavy quark mixing*, McGill Univ. preprint McGill/96-21 hep-ph/9606227 v2 (1996).
R. Bamert, C.P. Burgess, J. Cline, D. London and E. Nardi, McGill Univ. preprint McGill/96-04 hep-ph/9602438 (1996).

[65] E. MA, Phys. Rev. **D53** (1996) 2276.
C.H.V. Chang, D. Chang and W.Y. Keung, National Tsing-Hua Univ. preprint NHUCU-HEP-96-1 hep-ph/9601326 (1996).
T. Yoshikawa, Hiroshima Univ. prepront HUPD-9528 hep-ph/9512251 (1995).

[66] J.F. Gunion, H.E. Haber, G.L. Kane and S. Dawson, *The Higgs Hunter's Guide*, Addison-Wesley, New York (1990).

[67] W. Hollik, Mod. Phys. Lett. **A5** (1990) 1909.

[68] A.K. Grant, Enrico Fermi Institute preprint EFI 94-24 (1994).

[69] H.E. Haber and G.L. Kane, Phys. Rep. **117**, Nos. 2-4 (1985) 75.

[70] L. Clavelli, *Light gluinos and* $\Gamma(Z \to b\bar{b})$, Univ. Alabama preprint UAHEP948 and hep-ph/9410343 (1994).

[71] J. Ellis et al., *Supersymmetry and* R_b *in the light of LEP 1.5*, CERN preprint CERN-TH/95-314 and hep-ph/9512288 (1995).

[72] W. de Boer et al., *Global fits of the SM and MSSM to electroweak precision data*, Karlsruhe preprint IEKP-KA/96-07 and hep-ph/9607286 (1996).

[73] T. Hebbeker et al., Phys. Lett. **B331** (1994) 165.

[74] T. Hebbeker, Phys. Rep. **217** (1992) 69.

[75] LEP design report, vol. 1, *The LEP injector chain*, CERN-LEP/TH/83-29, Geneva (1983).
LEP design report, vol. 2, *The LEP main ring*, CERN-LEP/TH/84-01, Geneva (1984).

[76] Ed. E. Blucher et al., *Report of the Working Group on High Luminosities at LEP*, CERN 91-02, Geneva (1991).

[77] L. Arnaudon et al., Phys. Lett. **B284** (1992) 97.

[78] P. Abreu et al. (DELPHI Collaboration), Nucl. Instr. and Meth. **A378** (1996) 57.
P. Aarnio et al. (DELPHI Collaboration), Nucl. Instr. and Meth. **A303** (1991) 233.
References therein.

[79] A.S. Schwarz, *Heavy flavour physics at colliders with silicon strip vertex detectors*, Phys. Rep. **238** (1994) 1.

[80] N. Bingefors et al., Nucl. Instr. and Meth. **A328** (1993) 447.

[81] V. Chabaud et al., Nucl. Instr. and Meth. **A368** (1996) 314.

[82] V. Chabaud et al., *Alignement of the DELPHI vertex detector*, DELPHI 95-177 MVX 10, Geneva (1995).

[83] V. Bocci et al., Nucl. Instr. and Meth. **A362** (1995) 361.

[84] *DELANA User's Guide*, DELPHI 89-44 PROG 137, Geneva (1989).

[85] *TANAGRA User's Guide*, DELPHI 87-95 PROG 98, Geneva (1987).

[86] A. Lipniacka, *Track quality in DELPHI*, DELPHI 95-7 TRACK 79, Geneva (1995). References therein.

[87] P. Billoir, Nucl. Instr. and Meth. **225** (1984) 352.

[88] V. Perevozchikov and N. Smirnov, *PHDST package description V.3.0*, DELPHI 92-118 PROG 189 Rev.3, Geneva (1992).

[89] T. Spassoff and N. Smirnov, *SKELANA User's Guide*, DELPHI Internal Manual, Geneva (1996).

[90] *HBOOK Manual.* CERN Program Library, Geneva.

[91] *PAW Manual.* CERN Program Library, Geneva.

[92] *DELSIM Reference Manual*, DELPHI 89-68 PROG 143, Geneva (1989).
DELSIM User's Guide, DELPHI 89-67 PROG 142, Geneva (1989).

[93] P. Abreu et al. (DELPHI Collaboration), Zeit. Phys. **C73** (1996) 11.

[94] P. Abreu et al. (DELPHI Collaboration), Nucl. Phys. **B417** (1994) 3.
P. Abreu et al. (DELPHI Collaboration), Nucl. Phys. **B367** (1991) 511.

[95] P. Billoir et al., Nucl. Instr. and Meth. **A360** (1995) 532.

[96] Ch. De la Vaissière and F. Martinez-Vidal, *Description and Performances of the DELPHI multivariate b-tagging*, DELPHI 97-134 PHYS 721, Geneva (1997).

[97] P. Billoir, R. Fruhwirth and M. Regler, Nucl. Instr. and Meth. **A241** (1985) 115.

[98] G. Borisov and C. Mariotti, Nucl. Instr. and Meth. **A372** (1996) 181.
G. Borisov and C. Mariotti, *Tuning of track impact parameter resolution of the Upgraded DELPHI detector*, DELPHI 97-95 PHYS 717, Geneva (1997).

[99] D. Brown and M. Frank, *Tagging b hadrons using track impact parameters*, ALEPH 92-135 PHYSIC 92-124, Geneva (1992).

[100] R. Barate at al., (ALEPH Collaboration), Phys. Lett. **B401** (1997) 150.

[101] D. Buskulic et al. (ALEPH Collaboration), Phys. Lett. **B313** (1993) 535.

[102] G. Borisov, *Lifetime Tag of events $Z \to b\bar{b}$ with the DELPHI detector. AABTAG program*, DELPHI 94-125 PROG 208, Geneva (1994).

[103] W. J. Murray, *Improved B tagging using Impact Parameters*, DELPHI 95-167 PHYS 581, Geneva (1995).

[104] G. Borisov, *Combined b-tagging*, DELPHI 97-94 PHYS 716, Geneva (1997).

[105] P. Abreu et al. (DELPHI Collaboration), Zeit. Phys. **C66** (1995) 323.

[106] D. Buskulic et al. (ALEPH Collaboration), Zeit. Phys. **C62** (1994) 179.
L3 Collaboration, *L3 results on R_b and $Br(b \to l)$ for the Glasgow Conference*, L3 Note 1625.
R. Akers et al. (OPAL Collaboration), Zeit. Phys. **C60** (1993) 199.

[107] P. Abreu et al. (DELPHI Collaboration), Phys. Lett. **B281** (1992) 383.

[108] D. Buskulic et al. (ALEPH Collaboration), Phys. Lett. **B313** (1993) 549.
P. Abreu et al. (DELPHI Collaboration), Phys. Lett. **B295** (1992) 383.
O. Adriani et al. (L3 Collaboration), Phys. Lett. **B307** (1993) 273.

[109] The LEP Electroweak Working Group, *Presentation of LEP electroweak heavy flavour results for Summer 1996 Conferences*, DELPHI 96-67 PHYS 627, Geneva (1996).
The LEP Electroweak Working Group, *A consistent treatment of systematic*

errors for LEP electroweak heavy flavour analyses, DELPHI 94-23 PHYS 357, Geneva (1994).
The LEP Electroweak Working Group, *Presentation of LEP electroweak heavy flavour results for Summer 1994 Conferences*, DELPHI 94-23/add PHYS 357, Geneva (1994).

[110] A.G. Frodesen, O. Skjeggestad and H. Tofte, *Probability and Statistics in Particle Physics*, Universitetsforlaget (1979).

[111] P. Abreu et al. (DELPHI Collaboration), Zeit. Phys. **C65** (1995) 555.

[112] P. Abreu et al. (DELPHI Collaboration), Zeit. Phys. **C70** (1996) 531.

[113] W.T. Eadie, D. Drijard, F.E. James, M. Roos and B. Sadoulet, *Statistical methods in experimental physics*, North-Holland, Amsterdam (1971).

[114] *NAGLIB Manual.* CERN Program Library, Geneva.

[115] G. Barker et al., *Measurement of the partial decay with* $R_b^0 = \Gamma_{b\bar{b}}/\Gamma_{had}$ *with the DELPHI detector at LEP*, DELPHI 97-106 CONF 88, contributed paper to ICHEP'97, Jerusalem (1997).

[116] C. Mariotti, *New measurement of the charged particle multiplicity of weakly decay B hadrons with the DELPHI detector at LEP*, DELPHI 97-125 CONF 106, contributed paper to ICHEP'97, Jerusalem (1997).

[117] G. Alexander et al. (OPAL Collaboration), Zeit. Phys. **C72** (1996) 1.

[118] P. Abreu et al. (DELPHI Collaboration), Zeit. Phys. **C69** (1996) 585.

[119] D. Buskulic et al. (ALEPH Collaboration), Zeit. Phys. **C69** (1996) 585.

[120] M. Artuso et al. (CLEO Collaboration), *Measurement of the branching fraction for* $D_s^- \to \phi\pi^-$, CLNS 95/1387, CLEO 95-23.

[121] D. Coffman et al. (MARK III Collaboration), Phys. Lett. **B263** (1991) 135.

[122] R. Akers et al. (OPAL Collaboration), Zeit. Phys. **C67** (1995) 27.
R. Akers et al. (OPAL Collaboration), Phys. Lett. **B353** (1995) 595.

[123] M.H.Seymour, Nucl. Phys. **B436** (1995) 163.

[124] D. Buskulic et al. (ALEPH Collaboration), *Measurement of the gluon splitting rate to* $b\bar{b}$ *in hadronic Z decays*, contributed paper to ICHEP'97, Jerusalem (1997).

[125] P. Abreu et al. (DELPHI Collaboration), CERN-PPE/97-39, submitted Phys. Lett. **B**.

[126] P. Abreu et al. (DELPHI Collaboration), Phys. Lett. **B347** (1995) 447.

[127] R. Akers et al. (OPAL Collaboration), Zeit. Phys. **C61** (1994) 209.

[128] D. Buskulic et al. (ALEPH Collaboration), Phys. Lett. **B357** (1995) 669.
D. Buskulic et al. (ALEPH Collaboration), Zeit. Phys. **C62** (1994) 179.
P. Abreu et al. (DELPHI Collaboration), Zeit. Phys. **C66** (1995) 323.

G. Alexander et al. (OPAL Collaboration), Phys. Lett. **B364** (1995) 93.
R. Akers et al. (OPAL Collaboration), Zeit. Phys. **C60** (1993) 199.

[129] S. Marti, *Estudi de la dependència energètica de les diferències entre jets de quarks i gluons utilitzant el detector DELPHI de LEP*, PhD. Thesis, Universitat de València (1995). Unpublished.

[130] L. Lyons and P. Clifford, Nucl. Instr. and Meth. **A270** (1988) 110.

[131] The LEP Experiments: ALEPH, DELPHI, L3 and OPAL, Nucl. Instr. and Meth. **A378** (1996) 101.

[132] F. Caravaglios and G. Ross, Phys. Lett. **B346** (1995) 159.

[133] P. Kluit, *A measurement of the cross sections and asymmetries for flavour tagged events at energies of 161 and 172 GeV and limits on new interactions*, DELPHI 97-93 CONF 78, contributed paper to ICHEP'97, Jerusalem (1997).

[134] A. Zell et al., *Stuttgart Neural Network Simulator*, University of Stuttgart, Institute for Parallel and Distributed High Performance Systems.

[135] R. Barate at al., (ALEPH Collaboration), Phys. Lett. **B401** (1997) 163.

[136] O. Adriani et al. (L3 Collaboration), *Measurement of the Z branching fraction into bottom quarks using double tag methods*, contributed paper to ICHEP'97, Jerusalem (1997).

[137] K. Ackerstaff et al. (OPAL Collaboration), Zeit. Phys. **C74** (1997) 1.

[138] K. Abe et al. (SLD Collaboration), *Measurement of R_b at SLD*, SLAC-PUB-96-7170, Proceedings of the XXXI Rencontres de Moriond, Electroweak Interactions and Unified Theories, Les Arcs (France), Ed. Frontieres, Gif-sur-Yvette (1996).
K. Abe et al. (SLD Collaboration), *A preliminary measurement of R_b using the upgrade SLD vertex detector*, SLAC-PUB-7585, contributed paper to ICHEP'97, Jerusalem (1997).

[139] D. Buskulic et al. (ALEPH Collaboration), Phys. Lett. **B313** (1993) 549.

[140] O. Adriani et al. (L3 Collaboration), Phys. Lett. **B307** (1993) 237.

[141] See for instance: M. Neubert, *B physics and CP violation* in 1995 European School of High Energy Physics, CERN 96-04, Geneva (1996).

UNIVERSITAT DE VALÈNCIA FACULTAD DE CIÈNCIES FÍSIQUES

Reunit el Tribunal que subscriu, en el dia de la data, acordà d'atorgar, per unanimitat, a aquesta Tesi Doctoral d'En/ Na/ N' FERNANDO MARTÍNEZ VIDAL la qualificació d APTO CUM LAUDE

València a 28 de NOVIEMBRE de 19 97

El Secretari,

El President,

UNIVERSITAT DE VALÈNCIA
BURJASSOT
FACULTAT DE CIÈNCIES FÍSIQUES